AD-A235 310

2

PL-TR-91-2031

# BOUNDARY LAYER PARAMETERIZATION FOR A GLOBAL SPECTRAL MODEL

L. Mahrt
M. Ek
J. Kim
A. A. M. Holtslag

Oregon State University
Department of Atmospheric Sciences
Corvallis, Oregon 97331-2209

DTIC
ELECTE
APR 29 1991
S B D

Final Report
1 October 1987 - 30 September 1990

27 January 1991

APPROVED FOR PUBLIC RELEASE; DISTRIBUTION UNLIMITED

PHILLIPS LABORATORY
AIR FORCE SYSTEMS COMMAND
HANSCOM AIR FORCE BASE, MASSACHUSETTS 01731-5000

DTIC FILE COPY

91 4 29 007

This technical report has been reviewed and is approved for publication.

Sam Chang
SAM CHANG
Contract Manager

Donald A Chisholm
DONALD A. CHISHOLM
Atmospheric Prediction Branch

FOR THE COMMANDER

Robert A. McClatchey
ROBERT A. McCLATCHEY, Director
Atmospheric Sciences Division

This report has been reviewed by the ESD Public Affairs Office (PA) and is releasable to the National Technical Information Service (NTIS).

Qualified requestors may obtain additional copies from the Defense Technical Information Center. All others should apply to the National Technical Information Service.

If your address has changed, or if you wish to be removed from the mailing list, or if the addressee is no longer employed by your organization, please notify OL-AA/PL(IMA), Hanscom AFB, MA 01731-5000. This will assist us in maintaining a current mailing list.

Do not return copies of this report unless contractual obligations or notices on a specific document require that it be returned.

# REPORT DOCUMENTATION PAGE

Form Approved
OMB No 0704-0188

[illegible]

**1. AGENCY USE ONLY** (Leave blank)

**2. REPORT DATE**
27-January-1991

**3. REPORT TYPE AND DATES COVERED**
Final (1 Oct 1987 - 30 Sep 1990)

**4. TITLE AND SUBTITLE**
Boundary Layer Parameterization for a Global Spectral Model

**5. FUNDING NUMBERS**
C - F19628-88-K-0001
PE 61102F
PR2310
TA G7
WU DA

**6. AUTHOR(S)**
L. Mahrt, M. Ek, J. Kim, A. A. M. Holtslag

**7. PERFORMING ORGANIZATION NAME(S) AND ADDRESS(ES)**
Department of Atmospheric Sciences
Oregon State University
Corvallis, Oregon 97331

**8. PERFORMING ORGANIZATION REPORT NUMBER**
None

**9. SPONSORING/MONITORING AGENCY NAME(S) AND ADDRESS(ES)**
Phillips Laboratory
Hanscom AFB, Massachusetts 01731

Contract monitor: Sam Chang/LYP

**10. SPONSORING/MONITORING AGENCY REPORT NUMBER**
PL-TR-91-2031

**11. SUPPLEMENTARY NOTES**
None

**12a. DISTRIBUTION/AVAILABILITY STATEMENT**
Approved for public release;
distribution unlimited

**12b. DISTRIBUTION CODE**

**13. ABSTRACT** (Maximum 200 words)

This report describes work on the AFGL atmospheric boundary-layer model conducted under contract number F19628-88-K-0001 from the Air Force Geophysics Laboratory. This model has been developed to provide turbulence parameterization schemes for a global spectral model. The research has led to new boundary-layer model developments, such as formulations for transport by clear air turbulence and transport due to topographically-forced gravity waves. The study of boundary-layer moisture regimes finds two asymptotic classes, drying and moistening, with the development of clouds found to be quite different for each class. A formulation for boundary-layer cloud cover is developed that includes important influences of turbulent scale and subgrid-mesoscale variations of relative humidity. The new surface roughness formulation allows the roughness length for momentum to be significantly larger than that for heat, accommodating recent observational evidence. An additional study examines the daytime evolution of the boundary-layer relative humidity and illustrates the complex interactions of the boundary layer, large-scale vertical motion and soil moisture.

**14. SUBJECT TERMS**
Atmospheric boundary layer, boundary-layer model, soil model, boundary-layer parameterization, surface energy balance, cloud cover parameterization, free atmospheric transport, surface fluxes, gravity wave drag.

**15. NUMBER OF PAGES**
216

**16. PRICE CODE**
n/a

**17. SECURITY CLASSIFICATION OF REPORT**
Unclassified

**18. SECURITY CLASSIFICATION OF THIS PAGE**
Unclassified

**19. SECURITY CLASSIFICATION OF ABSTRACT**
Unclassified

**20. LIMITATION OF ABSTRACT**
SAR

# Acknowledgements

The work on this contract was carried out by several scientists. Larry Mahrt provided the general guidance for model development. In addition to his own work on boundary-layer moisture regimes, he collaborated with Jinwon Kim on the research involving free atmospheric transport, and with Michael Ek on the boundary layer cloud cover formulation and model sensitivity testing. Bert Holtslag from KNMI, the Royal Netherlands Meteorological Institute, has previous experience with the boundary-layer model and helped with many improvements in the determination of surface fluxes and profile functions. Paul Ruscher and Hua-Lu Pan were involved in the early part of this contract and have provided valuable input in many aspects of model development. In addition to those people mentioned above, Nimal Gamage and Wayne Gibson also helped to write parts of the chapter describing the boundary-layer model physics and numerical methods. Special thanks go to Alice Gøttsche, Michael Krejci, and Chrislyn Scalley for their assistance in putting this report into final form.

Accession For
NTIS GRA&I ☒
DTIC TAB ■
Unannounced ☐
Justification

By
Distribution/
Availability Codes

| Dist | Avail and/or<br>Special |
|---|---|
| A-1 | |

# Table of Contents

Page

1. **Introduction** . . . . . . . . . . . . . . . . . . . . . . . . . . . . . . . . . . . . . . . . . . . . . 1

2. **Free Atmospheric Transport** . . . . . . . . . . . . . . . . . . . . . . . . . . . . . . . . . . 3

2.1. Momentum Transport by Gravity Waves (Kim and Mahrt) . . . . . . . . . . . . 3
  2.1.1. Introduction . . . . . . . . . . . . . . . . . . . . . . . . . . . . . . . . . . . . . 3
  2.1.2. Observed Flow . . . . . . . . . . . . . . . . . . . . . . . . . . . . . . . . . . . 5
  2.1.3. Observed wave momentum flux . . . . . . . . . . . . . . . . . . . . . . . . 7
  2.1.4. Wave equation . . . . . . . . . . . . . . . . . . . . . . . . . . . . . . . . . . . 8
  2.1.5. Wave breaking and wave stress supersaturation . . . . . . . . . . . . . 11
  2.1.6. Modelled wave momentum flux for ALPEX . . . . . . . . . . . . . . . . 17
  2.1.7. Effective mountain height . . . . . . . . . . . . . . . . . . . . . . . . . . . 18
  2.1.8. Upward turbulent heat flux in the wave breaking region . . . . . . . . 18
  2.1.9. Conclusions . . . . . . . . . . . . . . . . . . . . . . . . . . . . . . . . . . . . 21

2.2. Turbulent Transport in the Free Atmosphere and very stable Nocturnal Boundary Layer (Kim and Mahrt) . . . . . . . . . . . . . . . . . . . . . . . . . . . . . . . 35
  2.2.1. Introduction . . . . . . . . . . . . . . . . . . . . . . . . . . . . . . . . . . . . 35
  2.2.2. Data . . . . . . . . . . . . . . . . . . . . . . . . . . . . . . . . . . . . . . . . . 36
  2.2.3. Eddy diffusivities and the eddy Prandtl number . . . . . . . . . . . . . 37
  2.2.4. Comparison with the other clear air turbulence model . . . . . . . . . 40
  2.2.5. Turbulence in the free atmosphere: Column model simulations . . . . . 41
  2.2.6. Conclusions . . . . . . . . . . . . . . . . . . . . . . . . . . . . . . . . . . . . 45

3. **Boundary-Layer Moisture** . . . . . . . . . . . . . . . . . . . . . . . . . . . . . . . . . 61

3.1. Boundary-Layer Moisture Regimes (Mahrt) . . . . . . . . . . . . . . . . . . . . 61
  3.1.1. Introduction . . . . . . . . . . . . . . . . . . . . . . . . . . . . . . . . . . . . 61
  3.1.2. The data . . . . . . . . . . . . . . . . . . . . . . . . . . . . . . . . . . . . . . 62
  3.1.3. Moisture regimes . . . . . . . . . . . . . . . . . . . . . . . . . . . . . . . . . 64
  3.1.4. Moisture memory . . . . . . . . . . . . . . . . . . . . . . . . . . . . . . . . . 68
  3.1.5. Entrainment drying boundary layer . . . . . . . . . . . . . . . . . . . . . 71
  3.1.6. Moisture-temperature correlation . . . . . . . . . . . . . . . . . . . . . . . 75
  3.1.7. Moisture fronts and mesoscale variability . . . . . . . . . . . . . . . . . 76
  3.1.8. Conclusions . . . . . . . . . . . . . . . . . . . . . . . . . . . . . . . . . . . . 80

3.2. A Formulation for Boundary-Layer Cloud Cover (Ek and Mahrt) . . . . . . . . 103
  3.2.1. Introduction . . . . . . . . . . . . . . . . . . . . . . . . . . . . . . . . . . . . 103

3.2.2. Relative humidity models of cloud cover . . . . . . . . . . . . . . . . . 103
3.2.3. Relative humidity variance . . . . . . . . . . . . . . . . . . . . . . . . 106
3.2.4. Cloud transmission of solar radiation . . . . . . . . . . . . . . . . . . 111
3.2.5. Model tests . . . . . . . . . . . . . . . . . . . . . . . . . . . . . . . . 112
3.2.6. Conclusions . . . . . . . . . . . . . . . . . . . . . . . . . . . . . . . . 115

**4. Model Sensitivity Testing** . . . . . . . . . . . . . . . . . . . . . . . . . . 127

4.1. Surface Roughness Length (Holtslag and Ek) . . . . . . . . . . . . . . . . . 127
4.1.1. Introduction . . . . . . . . . . . . . . . . . . . . . . . . . . . . . . . 127
4.1.2. Data from HAPEX-MOBILHY . . . . . . . . . . . . . . . . . . . . . . . . . 128
4.1.3. Model description and parameter estimation . . . . . . . . . . . . . . . 129
4.1.4. Results . . . . . . . . . . . . . . . . . . . . . . . . . . . . . . . . . . 130
4.1.5. Summary and Discussion . . . . . . . . . . . . . . . . . . . . . . . . . . 132

4.2. Daytime Evolution of Boundary-Layer Relative Humidity (Ek and Mahrt) . . . . 139
4.2.1. Introduction . . . . . . . . . . . . . . . . . . . . . . . . . . . . . . . 139
4.2.2. Boundary-layer relative humidity . . . . . . . . . . . . . . . . . . . . . 140
4.2.3. Boundary-layer model sensitivity tests . . . . . . . . . . . . . . . . . . 142
4.2.4. Conclusions . . . . . . . . . . . . . . . . . . . . . . . . . . . . . . . . 144

**5. Boundary-Layer Model Physics and Numerical Methods (Ek and Mahrt)** . . 151
5.1. Introduction . . . . . . . . . . . . . . . . . . . . . . . . . . . . . . . . . 151
5.2. Model Equations and numerical methods . . . . . . . . . . . . . . . . . . . 152
5.2.1. Model equations . . . . . . . . . . . . . . . . . . . . . . . . . . . . . . 152
5.2.2. Computational procedures . . . . . . . . . . . . . . . . . . . . . . . . . 165
5.2.3. Diagrams of OSU1DPBL boundary-layer processes . . . . . . . . . . . . . . 168
5.2.4. OSU1DPBL flowchart . . . . . . . . . . . . . . . . . . . . . . . . . . . . 176
5.2.5. Finite differencing techniques . . . . . . . . . . . . . . . . . . . . . . 177
5.2.6. Modeling the snow cover . . . . . . . . . . . . . . . . . . . . . . . . . . 186
5.2.7. The radiation Richardson number . . . . . . . . . . . . . . . . . . . . . 189
5.2.8. Stable boundary layer . . . . . . . . . . . . . . . . . . . . . . . . . . . 191
5.2.9. Potential evaporation and surface temperature . . . . . . . . . . . . . . 191
5.2.10. Canopy resistance . . . . . . . . . . . . . . . . . . . . . . . . . . . . 196
5.2.11. References . . . . . . . . . . . . . . . . . . . . . . . . . . . . . . . . 197

**6. Concluding Remarks** . . . . . . . . . . . . . . . . . . . . . . . . . . . . . 202

Reports and Articles Prepared Under This Contract . . . . . . . . . . . . . . . . 204

# Chapter I

# Introduction

The research in this report can be described in terms of three classes of model development: 1) mixing and transport in the free atmosphere, 2) boundary-layer moisture regimes and cloud development and 3) the influence of surface conditions including surface roughness, soil and snow conditions.

A formulation for momentum transport due to topographically forced gravity waves was constructed by Jinwon Kim by generalizing the previous models of Lindzen and Smith (Chapter 2.1). Mr. Kim's work includes the first direct comparisons of formulations for gravity wave momentum transport with direct observations of fluxes. The modified formulation proved to be quite successful. The heat transport by gravity waves appears to be too small to measure with respect to sampling problems. For application to the global model, an existing data set for statistical surface topography must be acquired.

The companion formulation for transport by clear air turbulence was constructed by analyzing data from two field programs designed for such purposes, but never analyzed (Chapter 2.2). This chapter contains the first direct comparison of a free atmospheric mixing model with direct observations of turbulence fluxes. The formulation derived in this report is found to adequately describe the available data although the scatter is large for large stability, particularly for momentum transport. The formulation is tested in the one-dimensional model. The locally generated turbulence is found to be systematically significant on the underside of the nocturnal low-level jet. This turbulence can significantly influence the underlying nocturnal boundary layer.

The study of boundary-layer moisture regimes finds two asymptotic classes of boundary layers (Chapter 3.1). The *drying boundary layer* occurs with strong surface heating and rapid boundary-layer growth into dry air aloft. For this case, boundary-layer moisture is not well mixed and decreases with time. The *moistening boundary layer* is dominated by surface evapotranspiration. The development of clouds is expected to be quite different for these two types of boundary layers.

The formulation for boundary-layer cloud cover is developed using HAPEX data (Chapter 3.2). Analysis of this data indicates that inclusion of the influence of both turbulent scale and subgrid-mesoscale variations of relative humidity are necessary to correctly estimate the dependence of the spatially averaged cloud cover on the spatially averaged relative humidity. This implicitly introduces a stability dependence into the cloud cover formulation. The expression for transmission of radiation through the cloud is also important. Testing of the cloud cover formulation indicates more sensitivity to the large scale vertical motion than to the values of the coefficients in the formulation. Analysis of the cloud-enhancement of boundary-layer fluxes from the HAPEX data showed that the cloud influences on the boundary-layer transport was small for this data set. A new format for representing transport by boundary-layer clouds has been developed partly based on existing observational studies in the literature. However new data sets where cloud transport is more important must be obtained before such a model can be seriously considered.

The study on the roughness parameterization allows the roughness length for momentum to be significantly larger than that for heat to accommodate recent evidence accumulated from several field studies (Chapter 4.1). While the model is now more "modern", evaluation of the significance of the improvements with HAPEX data were inconclusive. This chapter will be revised significantly by Dr. A. A. M. Holtslag, at the Royal Netherlands Meteorological Center (KNMI) in The Netherlands before being submitting to a refereed journal.

An additional study was conducted to examine how the relative humidity field evolves in the modelled daytime boundary layer (Chapter 4.2). This evolution illustrates the complex interactions of the boundary layer, large scale vertical motion and soil moisture. These interactions can lead to unexpected developments with respect to potential cloud initiation. This chapter helps better understand the behavior of the model moisture structure and points out important interactions not previously anticipated. Also, studies on the suitability of the snow model were inconclusive due to the inability to find appropriate data sets and are not reported here.

Finally, the physics and numerical methods used in the boundary-layer model are summarized from the latest model user's guide and are presented in Chapter 5, followed by concluding remarks concerning boundary-layer parameterizations over land in Chapter 6.

# Chapter 2.1

## Momentum Transport by Gravity Waves

### 2.1.1. Introduction

Topographically generated internal gravity waves can transport significant momentum vertically in the atmosphere. The nondissipative nature of internal gravity waves (Eliassen and Palm. 1960) may allow the wave stress at the ground surface to be transferred far into the upper atmosphere where the density is small. Wave stress divergence associated with wave breaking acts as a drag on the mean flow at the wave breaking level. The impact of gravity wave drag is known to be important for large-scale motions on time scales longer than a week over continental areas during the wintertime (Palmer *et al.*, 1986). Spectral analyses show that the mesoscale variances are climatologically much larger over mountainous areas than over flat land surfaces or the ocean, and the observed differences are mostly due to gravity wave activity in the atmosphere (Jasperson *et al.*, 1990).

Momentum transfer by gravity waves can be locally important on smaller time scales above significant topography. Lilly *et al.* (1982), Hoinka (1985), and Brown (1983) found that the stress due to gravity-wave scale disturbances over mountainous areas sometimes exceeds several $N/m^2$ in the middle of the troposphere. This value is one or two orders of magnitude larger than typical turbulent stresses in the boundary layer. For a summary of the observed values of the gravity wave stress in previous studies, see Palmer *et al* (1986).

*Gravity wave drag* is usually parameterized in terms of solutions to the linear gravity wave equation with Kelvin-Helmholtz instability or convective instability as a criterion for wave breaking. The modelling study of Klemp and Lilly (1978) shows that a linearized two-dimensional model, combined with an adjustment of local flow with respect to Kelvin-Helmholtz instability, can simulate orographic gravity waves and associated momentum flux reasonably well. Inclusion of gravity wave drag parameterization has been shown to significantly improve the simulation of large-scale flow (Holton, 1982; Palmer *et al.*, 1986; McFarlane, 1987; Hunt, 1990). However, simple formulations of gravity wave momentum flux have, to our knowledge, not been directly compared to observed fluxes. Such comparisons must include the computation of the *effective* height of surface topography, the effects of nonlinear lower boundary condition (Smith, 1977), and the saturation and supersaturation conditions for the gravity wave stress (Lindzen, 1981, 1988). Direct comparison of gravity wave drag formulations with observed atmospheric fluxes is one of the main goals of this study.

Representation of the wave breaking process in the frame of linear gravity wave theory plays a central role in the parameterization of gravity wave drag. Lindzen (1981) introduces the wave stress saturation hypothesis assuming that the maximum amplitude of a gravity wave is limited by the onset of hydrodynamic instability. This wave stress saturation condition has been successfully employed in large-scale modelling studies (Palmer *et al.*, 1986). However, Smith (1977) and Lindzen (1988) suggest that some degree of convective instability can be maintained in wave breaking regions (wave stress supersaturation hypothesis). Lindzen's (1988) theory of supersaturation is derived for an isothermal atmosphere with constant wind speed. We will generalize Lindzen's wave stress supersaturation theory for application to vertically varying mean flows by introducing an *equivalent scale height* which replaces the scale height for an isothermal atmosphere.

Determination of the wave stress at the ground surface requires the value of the amplitude of the vertical displacement of a streamline at the ground surface (effective mountain height) which is usually assumed to be related to the height of the mountain (or the root-mean-square variance of subgrid scale orography for large-scale models). The vertical displacement of a streamline at the ground surface also depends on the flow conditions near the ground surface including the flow Froude number ($Fr$) defined as $Fr \equiv N_0\eta_0/U_0$ where $\eta_0$ is the height of the surface topography, and $N_0$ and $U_0$ are the buoyancy frequency and mean wind speed near the ground, respectively (Drazin, 1961; Pierrehumbert and Wyman, 1986). The nonlinear study of Drazin (1961) shows that as the Froude number increases, the flow near a three-dimensional obstacle becomes more two-dimensional; when the Froude number exceeds unity the vertical displacement of a streamline is essentially suppressed. Similar features are observed in the three-dimensional numerical modelling studies of Smolarkiewicz and Rotunno (1989). Blocking of the low level flow at the upstream from topography or pooling of cold air in a valley reduces the effective mountain height. However such processes are nonlinear and have no precise theoretical description. Stern and Pierrehumbert (1988) provide an estimate of the effective mountain height in terms of a critical Froude number based on two-dimensional modelling studies. In this study, we estimate the effective mountain height by fitting the gravity wave amplitude at the ground with the observed wave stress below the model-predicted wave breaking level.

The vertical heat flux by breaking gravity waves and associated turbulence may be locally important. Asymmetry of the streamlines due to wave steepening and nonlinear interactions between waves may induce some net wave heat flux. In addition wave breaking and associated turbulence can cause significant local turbulent heat flux. Earlier parameterizations of wave drag of Lindzen (1981) and Holton (1982) assume that the turbulent Prandtl number in the wave breaking region will be close to unity, i.e., heat and momentum transfer in the wave breaking region are of similar efficiency. Chao and Schoeberl (1984) suggest that streamlines will be nearly vertical in the wave breaking region in which case the local turbulent heat flux is near zero. Fritts and Dunkerton (1985) also suggest small net heat flux across the entire wave due to the upward turbulent heat flux in the convectively unstable wave breaking region. From rotating tank experiments Delisi and Orlanski (1975) and Dunkerton (1989) observe that wave breaking does not cause significant alteration of the initial stratification implying small net turbulent and wave heat flux.

The spatial variations of the turbulent heat flux will yield important information about the mechanisms of wave breaking. If wave breaking occurs mainly by Kelvin-Helmholtz instability, turbulent heat flux in the wave breaking region is expected to be downward. If wave breaking occurs by convective instability, the turbulent heat flux will be locally upward in the wave breaking region. This phenomenon can offset much of the downward heat flux due to wave-induced turbulence in the stably stratified regions. The observed turbulent heat flux is studied in Section 3 using aircraft data from ALPEX (the Alpine Experiment). In Section 8 we will formulate the upward turbulent heat flux in terms of wave-modified variables and compare with the observed turbulent heat flux.

Aircraft data collected on 6 and 25 March 1982 in ALPEX are analyzed in Sections 2 and 3 in order to study the most important characteristics of the disturbances generated by the underlying coastal range. The analysis will focus on wave momentum fluxes, wave breaking and resulting turbulent heat flux in the wave breaking region. A simple parameterization of the gravity wave drag is presented in Sections 4 and 5 using the solution to the linear gravity wave equation with first-order expansion of a nonlinear lower boundary condition presented in Smith (1977) combined with the generalized wave stress supersaturation condition. In section 6, the vertical profiles of wave momentum flux estimated for the ALPEX cases are compared with the observed wave momentum flux. Inference of the effective mountain height based on model comparisons with the data is presented in Section 7.

### 2.1.2. Observed flow

The NCAR ELECTRA aircraft flew over the coastal range of Northern Yugoslavia on 6 and 25 March 1982 in the north-east south-west direction, which is approximately parallel to the direction of the low level wind and perpendicular to the coastal range axis. The flights covered a region approximately 240 km wide, centered at the coastal ridge, in a layer 2.4-5.7 km above sea level. This study analyzes five flight legs at 2.4, 2.7, 3.3, 3.8, and 4.5 km above sea level for 6 March ALPEX and three flight legs at 3.3, 4.5, and 5.7 km above sea level for 25 March ALPEX.

The vertical structure of the mean wind, observed by radiosonde soundings at Zagreb, Yugoslavia, are quite different between the two days (Fig. 1a,c). On 6 March, a strong Bora flow near the ground surface leads to significant speed and directional shear. On 25 March, the wind speed increases monotonically in the vertical without significant change of wind direction within the troposphere. Detailed description of the flow on these two days is presented in Smith (1987) and Mahrt and Gamage (1987).

The vertical propagation of orographic gravity waves is influenced by the vertical variation of the wind component parallel to the *surface* wind (McFarlane, 1987) defined as

$$\mathbf{V_p}(z) \equiv \frac{<\mathbf{V}(z), \mathbf{V_0}>}{|\mathbf{V_0}|} \qquad (1)$$

where $\mathbf{V_p}(z)$ is the mean wind component parallel to the surface wind $\mathbf{V_0}$, $\mathbf{V}(z)$ is the mean wind at height $z$, and $<\mathbf{V}(z), \mathbf{V_0}>$ denotes the scalar product between the two vectors $\mathbf{V_0}$ and $\mathbf{V}(z)$. The *surface* wind directly responsible for the onset of wave motion is somewhat difficult to define. In this study we use the wind speed from the upstream radiosonde sounding averaged over a 200 m deep layer centered at the ridge top level.

On 6 March, $\mathbf{V_p}$ decreases with increasing height with a critical level for stationary gravity waves ($\mathbf{V_p} = 0$) at 5 km above sea level (Fig. 1b). Vertical decrease of this wind component can cause amplification and breaking of gravity waves as discussed in later sections. In contrast, $\mathbf{V_p}$ increases with increasing height and critical layer does not exist within the observational domain for 25 March (Fig. 1d).

We mainly investigate the flow on 6 March where low-level wave breaking is expected. The horizontal wind parallel to the direction of the flight, vertical wind, and the potential temperature observed at the 3.3 km level on 6 March are presented in Fig. 2 together with the underlying topography. The most significant feature of the observed flow is the large-amplitude disturbances on a horizontal scale of a few tens of kilometers accompanied by smaller scale turbulence. The strongest disturbances are confined to the lowest first few kilometers above the coastal range.

The larger scale motions are isolated by band-pass filtering the raw records with 10 and 80 km cutoff wavelengths for the lower and upper limits of horizontal length scales, respectively. The wavelengths were chosen based on inspection of the record which includes one major event on the scale of mountain range and smaller scale wave-like motions. The computed fluxes are not sensitive to the exact values of the cutoff wavelengths. These band-pass filtered disturbances will be loosely called the *wave-scale* disturbances. Noticeable peaks of the variance of wave-scale vertical velocity appear above and immediately downstream from the ridge (Fig. 3). Growth and breaking of gravity waves are usually accompanied by significant asymmetry of the shape of perturbation streamlines and the concentrated horizontal gradients of $u$. Such sharp gradients appear as boundaries of ramp-like structures and may indicate the presence of a *frontal* region associated with wave steepening. The strongest events in the records of $u$ and $w$ at the 3.3 km flight level (Fig. 2) are examples of such a structure.

The turbulence occurring on 6 March is strongly related to wave-scale motions. The variance of 1 km high-pass filtered vertical velocity (Fig. 3) is large at locations of large wave-scale variance Turbulence in the wave breaking regions and associated turbulent heat flux will be discussed in more detail in Section 8 Similar horizontal variations occur at other flight levels near and below the critical level on 6 March (not shown).

### 2.1.3. Observed wave momentum flux

The momentum flux due to wave-scale motions on 6 and 25 March for each flight leg is calculated by averaging the product between the band-pass filtered horizontal and vertical velocities as

$$\overline{\tilde{u}\tilde{w}}(z) = \frac{1}{N}\sum_{i=1}^{N}\tilde{u}_i(z)\tilde{w}_i(z)dx \tag{2}$$

$$\overline{\tilde{v}\tilde{w}}(z) = \frac{1}{N}\sum_{i=1}^{N}\tilde{v}_i(z)\tilde{w}_i(z)dx \tag{3}$$

where $\tilde{()}$ represents the wave-scale (band-pass filtered) disturbance, $N$ is the number of points in the averaging region, and the subscript "$i$" denotes the position along the flight path. The averaging is performed for a 80 km section of the flight track above the coastal range where the wave activity is significant. The average momentum flux is somewhat sensitive to the averaging length. This sensitivity may indicate sampling problems as discussed by Lumley and Panofsky (1964), Wyngaard (1972), and Lenschow and Stankov (1986). However, wave-scale motions and associated momentum fluxes observed in each flight leg appear to be stationary and confined to a region directly over the mountain range. Consequently sampling problems for the current study are more related to defining the horizontal length scale of the wave activity than obtaining ensemble averages of random signals.

The wave-scale momentum flux vector on the two days is generally directed in the opposite direction of the surface wind (Fig. 4a) as expected from linear gravity waves induced by terrain. Only on 6 March at higher levels does the direction of wave-scale momentum flux rotate away from this direction and by an angle of less than 45 deg.

For comparison with the wave momentum flux formulations in Section 6, we compute the *wave momentum flux* $\tilde{M}_w$ as the component of band-pass momentum flux in the opposite direction of the surface wind $\mathbf{V_0}$ as

$$\tilde{M}_w \equiv -\frac{<\tilde{M}, \mathbf{V_0}>}{|\mathbf{V_0}|} \tag{4}$$

where $\tilde{M}$ is the vector of wave-scale momentum flux $(\overline{\tilde{u}\tilde{w}}, \overline{\tilde{v}\tilde{w}})$ calculated from (2-3) and $<\tilde{M}, \mathbf{V_0}>$ represents the scalar product of the flux vector $\tilde{M}$ and the surface wind $\mathbf{V_0}$. This wave momentum flux decreases with increasing height on 6 March consistent with the expected occurrence of wave breaking on this day (Fig. 5, open circles). Without wave breaking, conservation of wave stress implies that the wave momentum flux should increase with height due to the decrease of atmospheric density with height. The wave momentum flux is about 2.8 $m^2/s^2$ at 2.4 km level and decreases to about 0.5 $m^2/s^2$ at the 4.5 km level (Fig. 5). This vertical decrease of the wave momentum flux implies deceleration of the mean wind component parallel to the surface wind at a rate of about $9 \times 10^{-4}$ $ms^{-2}$. This deceleration rate is comparable to the magnitude of the Coriolis term. Thus, wave drag appears to be important in the evolution of the low-level flow over the coastal range on this day.

In contrast, the wave momentum flux generally increases with increasing height on 25 March (Fig. 6, open circles). The magnitude of this increase of wave momentum flux with height is predicted by conservation of wave stress (Section 6).

### 2.1.4. Wave equation

In Section 6, we will compare the observed wave momentum flux with that predicted by formulations for linear gravity waves and wave breaking. The following two sections will develop these formulations by combining the nonlinear lower boundary condition of Smith (1977) with wave stress supersaturation theory of Lindzen (1988) after generalizing the wave stress supersaturation theory for height-dependent mean flow. Although portions of the following derivation are completely analogous to Smith (1977) or Lindzen (1988), they are included here in abbreviated form for continuity of the derivation. We will first briefly review the solutions to the linear gravity wave equation with zero- and first-order lower boundary conditions as presented by Smith (1977).

The disturbance field of a streamline for a linear, stationary gravity wave in a steady, incompressible, hydrostatic flow can be expressed by Long's equation (Long, 1953)

$$\nabla^2\delta + \ell^2\delta = 0 \tag{5}$$

where $\nabla^2$ is a two-dimensional Laplacian operator in the $x - z$ plane, $\delta \equiv z - z_0$ is the vertical displacement of the streamline height from its undisturbed upstream value $z_0$, and $\ell$ is the Scorer parameter, or vertical wave number, defined as

$$\ell^2 \equiv -\frac{1}{U^2}\frac{g}{\rho}\frac{d\rho}{dz_0} \equiv \frac{N^2}{U^2}. \tag{6}$$

Assuming that the horizontal wavelength of the motion is much larger than the vertical wave length, which can be justified for the cases considered in this study, we neglect the terms containing second order derivatives in the horizontal while retaining those containing second order derivatives in the vertical. Then, expanding the Laplacian operator, (5) can be approximated as

$$\frac{\partial^2\delta}{\partial z^2} + \ell^2\delta = 0. \tag{7}$$

Assuming further that surface topography is the only source of gravity waves, the radiation boundary condition is applied at the top of the domain. At the bottom of the domain, a kinematic boundary condition

$$\delta(x,\eta(x)) = \eta(x) \tag{8a}$$

is imposed, where $\eta(x)$ is the height of the ground topography and $\delta(x,\eta(x))$ is the vertical displacement of a streamline at the ground level. In (8a), the amplitude of terrain-induced gravity waves is assumed equal to the height of the ground topography.

The lower boundary condition (8a) can be expanded in terms of $\eta_0\ell_0$ (Smith, 1977) as

$$\delta(x,\eta(x)) = \delta(x,0) + \frac{\partial\delta}{\partial z}(x,0)\eta(x) + O(\ell_0^2\eta_0^2) = \eta(x) \tag{8b}$$

where $\eta_0$ is the amplitude of the surface topography and $\ell_0$ denotes the vertical wavenumber at the ground level. The usual linear lower boundary condition is obtained by retaining the lowest order terms from the expanded nonlinear lower boundary condition (8b) as

$$\delta(x,0) = \eta(x). \tag{9}$$

For shallow terrain, (9) may be sufficient to represent the disturbance of the streamline at the ground. However, as the mountain becomes higher, the first-order term in (8b) may become significant (Smith, 1977). Retaining the first-order term on the right-hand side of (8b), the first-order lower boundary condition becomes (Smith, 1977)

$$\delta(x,0) + \frac{\partial\delta}{\partial z}(x,0)\eta(x) = \eta(x). \tag{10a}$$

In this study we will apply the first-order lower boundary condition (10a) since the solution corresponding to zero-order lower boundary condition (9) can be recovered from the final solution

For simplicity, we assume a monochromatic sinusoidal topography with an amplitude $\eta_0$ defined as

$$\eta(x) = \eta_0 \cos(kx). \tag{10b}$$

In the presence of vertical shear and vertically varying stratification, the solution for $\delta(x,z)$ in (7) with the first-order lower boundary condition (10$a,b$) and the WKB approximation can be written as (Smith, 1977)

$$\delta(x,z) = h(z)\left[\cos(kx+\phi) + \frac{h_0\ell_0}{2}\sin(2kx+\phi)\right] \tag{11}$$

where $\phi(z) \equiv \int^z \ell(z')dz'$ is the vertical wave phase, $h(z)$ is the amplitude of the streamline disturbances at height $z$, and $h_0$ is the amplitude of the vertical displacement of the streamline at the ground assumed equal to the amplitude of the surface topography $\eta_0$.

The amplitude of the vertical displacement of the streamline height, $h(z)$, can be estimated from conservation of wave stress (Eliassen and Palm, 1960) or conservation of wave action (Smith, 1977) for linear internal gravity waves. The relationship between the mean flow profile and the amplitude of streamline disturbances for linear monochromatic gravity waves can be expressed as (Smith, 1977)

$$\rho(z)U(z)N(z)k\overline{\delta^2}(z) = constant \tag{12}$$

where $\overline{\delta^2}(z)$ is the mean-square amplitude of the gravity wave at height $z$ and $\overline{()}$ denotes horizontal averaging over one wavelength. The mean-square amplitude $\overline{\delta^2}(z)$ is obtained from (11) as

$$\overline{\delta^2}(z) = \frac{h^2(z)}{2}\left[1 + \frac{(h_0\ell_0)^2}{4}\right]. \tag{13}$$

Combining (12) and (13), the ratio of the amplitude of the streamline displacement at height $z$ above the ground to the amplitude at the ground level, $\gamma(z)$, becomes (Smith, 1977)

$$\gamma(z) \equiv \frac{h(z)}{h_0} = \left(\frac{\rho_0 U_0 N_0}{\rho(z)U(z)N(z)}\right)^{1/2} \tag{14}$$

where the subscript "$_0$" denotes the value at the ground level. Relationship (14) indicates that internal gravity waves amplify during the vertical propagation due to decreasing density, wind speed, and stratification[1] of the mean flow with increasing height.

The average stress exerted by a gravity wave, $\tau_w(z)$, is calculated by

$$\tau_w(z) = -\rho(z)\overline{\tilde{u}\tilde{w}}(z) = -\frac{1}{L}\int_{-L/2}^{L/2} \rho(z)\tilde{u}(x,z)\tilde{w}(x,z)dx \tag{15}$$

---

[1] The amplitude of a gravity wave increases with decreasing stratification in the vertical. However, wave steepening increases for a given value of wave amplitude with increasing stratification with height as shown by (36) and (37) in Section 5.

where $L$ is the horizontal wavelength of the wave, and $\tilde{u}(x,z)$ and $\tilde{w}(x,z)$ are disturbance horizontal and vertical components of wind due to wave activity given as

$$\tilde{u} = -U\left[\frac{\partial\delta}{\partial z}\right](x,z) \tag{16a}$$

$$\tilde{w} = U\left[\frac{\partial\delta}{\partial x}\right](x,z) \tag{16b}$$

where $U$ is the mean wind speed and $\delta(x,z)$ is again the vertical displacement of the streamline (11). Substituting $\tilde{u}$ (16$a$), $\tilde{w}$ (16$b$), and $\overline{\delta^2}$ (13) into (15), the average wave stress for the gravity wave solution with first-order lower boundary condition becomes

$$\tau_w(z) \approx \frac{1}{2}k\rho(z)U(z)N(z)\left[h_0\gamma(z)\right]^2\left[1+\frac{(h_0\ell_0)^2}{4}\right] \tag{17}$$

where $k \equiv 2\pi/L$ is the horizontal wave number of a gravity wave. The wave stress at the ground surface is obtained from (17) by using $\rho$, $U$, and $N$, at the ground level with $\gamma = 1$. In (17), the influence of the height of surface topography enters through the wave amplitude at the ground surface $h_0$ and through the ratio $\gamma(z)$. Recalling that the above development is based on the conservation of wave stress, (17) becomes invalid at the level where wave breaking occurs, which is the subject of the next section.

### 2.1.5. Wave breaking and wave stress supersaturation

As the amplitude of a gravity wave increases with height, the flow modified by the wave activity can become locally unstable, thus, limiting the maximum growth of wave amplitude (saturation hypothesis; Lindzen, 1981). The major mechanism of wave breaking can be either shear-driven Kelvin-Helmholtz instability or convective instability. Thorpe (1973) observed in laboratory experiments that disturbances begin to grow when the gradient Richardson number of the mean flow decreases below 0.25. Klemp and Lilly (1978) adjusted the local flow with respect to the Kelvin-Helmholtz instability criterion and successfully approximated the observed wave disturbance. On the other hand, Smith (1977) and Lindzen (1981) have argued that the growth rate of perturbations by convective instability is much faster than that by Kelvin-Helmholtz instability. As a possible result of this faster growth rate, Delisi and Orlanski (1975) observe well defined convection in wave breaking regions in rotating tank experiments. Pitts and Lyons (1990) also find convective overturning in numerical simulations of stratified flow over topography. In the present study, the convective instability criterion will be used to derive wave breaking conditions.

The saturation hypothesis (Lindzen, 1981) assumes that the maximum slope of a wave streamline will be limited by the onset of convective instability. Parameterizations of gravity wave drag by Palmer *et al.* (1986) and McFarlane (1987) assume that the amplitude of a saturated gravity wave is determined by marginal hydrodynamic stability in wave breaking regions. On the other hand, Smith (1977) and Lindzen (1988) suggest that breaking gravity waves may maintain some degree of convective instability in the wave breaking region.

We will generalize the wave stress supersaturation theory of Lindzen (1988) to include vertically varying mean flows for comparison with our atmospheric data sets. Then the supersaturated wave stress will be estimated for the wave solution with the first-order lower boundary condition. The cases for the zero-order lower boundary condition or wave stress saturation condition can be recovered from this result by neglecting the appropriate terms in the final result.

With supersaturation theory (Lindzen, 1988), the perturbation of a streamline is constrained by the relationship

$$\left(\frac{\partial \delta}{\partial z}\right)_{max}(z) \leq 1 + S(z) \tag{18}$$

where $(\partial \delta / \partial z)_{max}(z)$ is the maximum value of the quantity $(\partial \delta / \partial z)(x, z)$ at a given level and $S(z)$ is the degree of supersaturation at level $z$. When $S(z) > 0$, (18) implies reversal of the slope of the streamline so that some degree of convective instability is maintained in the wave breaking region. When $S(z) = 0$, (18) reduces to the expression for the usual wave-stress saturation condition with respect to the convective instability.

Lindzen (1988) estimates the degree of supersaturation $S(z)$ by considering the balance between the reduction of the wave amplitude due to wave breaking and the growth of the wave amplitude due to vertical variation of the mean flow. Lindzen (1988) also assumes a balance between the rate at which the wave loses its energy to convective instability and the rate at which the wave motion transports energy into the wave breaking region. In the following development, we generalize Lindzen's (1988) approach to include vertically varying mean flows.

The net percentage change of the mean-square amplitude of the wave due to wave breaking in a given layer, $F(\alpha)$, can be obtained as a function of the ***half width of the wave breaking region*** $\alpha$ analogous to Lindzen (1988; his equation 13)

$$F(\alpha) = f(\alpha) g(\alpha). \tag{19}$$

In (19) the reduction factor $f(\alpha)$ is defined as the ratio of the mean-square amplitude with wave breaking to that without wave breaking. The amplification factor $g(\alpha)$ denotes the increase of the mean-square amplitude across the layer due to the height-dependence of the mean flow in the layer in the absence of wave breaking. Assuming complete flattening[2] of the streamline by the action of wave breaking alone, Lindzen (1988) estimates the reduction factor $f(\alpha)$ as (his equation 8a)

$$f(\alpha) \equiv \frac{\left(\int_0^{(3\pi/2)-\alpha} + \int_{(3\pi/2)+\alpha}^{2\pi}\right)\cos^2\beta\, d\beta}{\int_0^{2\pi}\cos^2\beta\, d\beta} \tag{20a}$$

where $\beta \equiv kx + \phi(z)$ is the wave phase and $k$ is the horizontal wavenumber. Integrating (20a), $f(\alpha)$ becomes (Lindzen, 1988; his equation 8b)

$$f(\alpha) = \frac{\pi - \alpha + 0.5\sin(2\alpha)}{\pi}. \tag{20b}$$

The amplification factor $g(\alpha)$[3] for the convectively unstable layer of depth $D$ is obtained from (13) and (14) as

$$g(\alpha) \equiv \frac{\overline{\delta^2}(z+D)}{\overline{\delta^2}(z)} = \frac{\gamma^2(z+D)}{\gamma^2(z)} \tag{21}$$

where $\overline{\delta^2}$ and $\gamma$ again are the mean-square amplitude (13) and the normalized amplitude (14) of the gravity wave, respectively.

The amplification factor $g(\alpha)$ depends on the vertical variations of the atmospheric density, mean wind speed and stratification. To make an analogy to the isothermal atmosphere with constant wind speed where $g(\alpha)$ depends only on the vertical variation of the atmospheric density, we introduce an *equivalent scale height* $H$ defined from local variation of the mean flow. The amplification factor (21) can then be rewritten in terms of an equivalent scale height as

$$g(\alpha) = e^{D/H}. \tag{22}$$

The argument of the exponent in (22) is in terms of $1/H$ instead of $1/2H$ which appeared in Lindzen (1988) because we are concerned with the growth of the mean square amplitude. Accordingly, a height-dependent equivalent scale height $H$ can be determined from (21) and (22) as

$$H = \frac{D}{\ln[\gamma^2(z+D)/\gamma^2(z)]}. \tag{23}$$

---

[2] The streamlines in the wave breaking regions will not be completely flat. Dunkerton (1989) assumes linear slope while Lindzen (1988) does not introduce any particular shape of the streamline. However the amplification factor $g(\alpha)$ in (19) is equivalent to assuming nonzero slope of the streamline when computing the mean-square amplitude.

[3] In Lindzen (1988), the amplification factor (his equation 12) is calculated for the amplitude while the flattening $f(\alpha)$ (or the reduction factor; his equation 9) is calculated for the mean-square amplitude. Hence, the current derivation is more consistent.

For the case of an isothermal atmosphere with constant wind speed, expression (23) for the equivalent scale height reduces to the usual definition of the scale height for an isothermal atmosphere ($RT/g$). If $\gamma^2(z+D) < \gamma^2(z)$, $H$ becomes negative in which case wave breaking does not occur and wave stress is conserved (12). Using the equivalent scale height (23), we can now follow the general procedure presented by Lindzen (1988).

The depth of the convectively unstable region $D$ can be estimated from the shape of the streamline disturbance $\delta(x, z)$ and the half width of the wave breaking region $\alpha$. Neglecting the first order term in the expression for $\delta(x, z)$ in (11), $D$ simplifies to

$$D \approx \mu h(z)\left[\cos\left(\frac{3}{2}\pi + \alpha\right) - \cos\left(\frac{3}{2}\pi - \alpha\right)\right] = 2\mu h(z)\sin\alpha \tag{24}$$

where $h(z)$ is again the amplitude of the streamline disturbance at $z$ and $\mu$ is a positive constant less than unity which accounts for the reduction of the vertical propagation of the wave by convection as proposed by Lindzen (1988). Using the normalized wave amplitude (14), the depth of the convectively unstable region $D$ in (24) can be rewritten as

$$D = 2\mu h(z)\sin\alpha = 2\mu h_0\gamma(z)\sin\alpha. \tag{25}$$

The constant $\mu$ is estimated by equating the convective time scale with the time scale for the vertical propagation of the wave energy across the convectively unstable layer (Lindzen, 1988) as

$$\mu \approx \frac{U}{N}\left(\frac{\sqrt{2}}{6\pi}\frac{k}{H}\right)^{1/2}\frac{H}{h_0\gamma} = \left(\frac{\sqrt{2}}{3}\frac{H}{L}\right)^{1/2}\frac{1}{h_0\gamma\ell}. \tag{26}$$

Assuming that the wave breaking occurs in a region which is narrow compared to the horizontal wavelength ($\alpha << 2\pi$) and that the depth of the convectively unstable layer is small compared to the equivalent scale height ($D << H$), the net percentage change of the mean-square amplitude $F(\alpha)$ and the depth of convectively unstable layer $D$ can be approximated by expanding $\sin\alpha$, $\cos\alpha$, and $e^{D/H}$ in (20b), (25), and (22) for small values of $\alpha$ and $D/H$ to give

$$F(\alpha) \approx \left(1 - \frac{2}{3\pi}\alpha^3\right)\left(1 + \frac{D}{H}\right) \approx 1 + \frac{D}{H} - \frac{2}{3\pi}\alpha^3 \tag{27}$$

where

$$D = 2\mu h_0\gamma\sin\alpha \approx 2\mu h_0\gamma\left(\alpha - \frac{\alpha^3}{6}\right). \tag{28}$$

At an equilibrium state, the reduction factor $f(\alpha)$ balances the amplification factor $g(\alpha)$ for the mean-square amplitude in the wave breaking region so that

$$F(\alpha_c) = 1 \tag{29}$$

where $\alpha_e$ denotes the half width of the wave breaking region at the equilibrium state. This equilibrium half width $\alpha_e$ can then be estimated from (27), (28), and (29) as

$$\alpha_e = \left( \frac{6\mu h_0 \gamma}{\mu h_0 \gamma + 2H/\pi} \right)^{1/2} \tag{30}$$

where $\mu$ is given by (26).

Now $(\partial\delta/\partial z)_{max}$ (or $\bar{A}$ in Lindzen, 1988) for a breaking wave can be obtained from the geometric argument of Lindzen (1988; see his Fig. 1) as

$$\left( \frac{\partial\delta}{\partial z} \right)_{max} = \frac{1}{\cos\alpha_e}. \tag{31}$$

Expanding $\cos\alpha_e$ for small $\alpha_e$ in (31) and substituting $\mu$ from (26) into (30), we obtain an approximate expression for $(\partial\delta/\partial z)_{max}$ as

$$\left( \frac{\partial\delta}{\partial z} \right)_{max} \approx 1 + \frac{3}{2} \frac{(\pi/\ell)(\sqrt{2}H/3L)^{1/2}}{(\pi/\ell)(H/3\sqrt{2}L)^{1/2} + H}. \tag{32}$$

The degree of supersaturation, $S(z) \equiv (\partial\delta/\partial z)_{max} - 1$, is then obtained from (32) as

$$S(z) = \frac{3}{2} \frac{(\pi/\ell)(\sqrt{2}H/3L)^{1/2}}{(\pi/\ell)(H/3\sqrt{2}L)^{1/2} + H}. \tag{33}$$

The first term in the denominator on the right-hand side of (33), which is absent in Lindzen's result, comes from the new expression for the depth of the convectively unstable region $D$ in (24). This term is thought to be smaller than the equivalent scale height $H$. When this term is neglected, the degree of supersaturation estimated in the present study is simply a factor of $\sqrt{2}$ larger than that estimated by Lindzen (1988). This difference is due to the revised estimate of the amplification factor $g(\alpha)$ in (22).

Having estimated the degree of supersaturation, we proceed to calculate the corresponding supersaturated wave stress. From the wave solution with first-order lower boundary condition (11), the quantity $\partial\delta/\partial z$ becomes

$$\frac{\partial\delta}{\partial z}(x,z) = h(z)\ell(z) \left[ -\sin(kx+\phi) + \frac{h_0\ell_0}{2}\cos(2kx+\phi) \right]. \tag{34}$$

Expressing the wave amplitude $h(z)$ in terms of the normalized wave amplitude (14), (34) becomes (Smith, 1977)

$$\frac{\partial\delta}{\partial z}(x,z) = h_0\ell_0\gamma' \left[ -\sin(kx+\phi) + \frac{h_0\ell_0}{2}\cos(2kx+\phi) \right] \tag{35}$$

where $\gamma'$ represents the vertical variation of the mean flow defined as

$$\gamma' \equiv \frac{\gamma(z)\ell(z)}{\ell_0} = \left( \frac{N(z)}{N_0} \right)^{1/2} \left( \frac{U(z)}{U_0} \right)^{-3/2} \left( \frac{\rho(z)}{\rho_0} \right)^{-1/2}. \tag{36}$$

For the wave solution with zero-order lower boundary condition, the second term in the square bracket of (35) is omitted.

The maximum value of $\partial\delta/\partial z$ at height $z$ occurs where $\sin(kx+\phi) = -1$ and is obtained from (35) as

$$\left(\frac{\partial\delta}{\partial z}\right)_{max}(z) = h_0\ell_0\gamma'(z)\left[1-\frac{h_0\ell_0}{2}\cos\phi\right]. \tag{37}$$

Relationships (36) and (37) imply that for a given wave amplitude, $(\partial\delta/\partial z)_{max}$ increase as $\rho$ and $U$ decrease with height and $N$ increases with height. Using (37), the wave breaking condition (18) can be expressed in terms of the vertical profile of the mean flow and the surface wave amplitude as

$$h_0\ell_0\gamma'(z)\left[1-\frac{h_0\ell_0}{2}\cos\phi\right] \leq 1+S(z). \tag{38}$$

If the inequality (38) is satisfied for an arbitrary model layer, the wave stress is conserved and the wave amplitude $h(z)$ varies according to (14) across the layer. If the inequality (38) is not satisfied, then wave breaking occurs and the incident wave stress (17) at the bottom of the layer is reduced to the supersaturated value at the top of the layer.

The supersaturated wave stress can be obtained from (17) as

$$\tau_s(z) \approx \frac{1}{2}k\rho(z)U(z)N(z)\left[h_m\gamma(z)\right]^2\left[1+\frac{(h_m\ell_0)^2}{4}\right] \tag{39}$$

where $h_m$ is the surface wave amplitude resulting from imposing the supersaturation condition corresponding to equality in (38) so that

$$h_m\ell_0\gamma'(z)\left[1-\frac{h_m\ell_0}{2}\cos\phi\right] = 1+S(z) \tag{40}$$

Solving (40) for the positive real value of $h_m\ell_0$, we obtain $h_m$ as:

$$h_m = \frac{1+S}{\ell_0\gamma'} \qquad \cos\phi = 0 \tag{41a}$$

$$h_m = \frac{1}{\ell_0\cos\phi}\left[1-\sqrt{1-\frac{2(1+S)}{\gamma'}\cos\phi}\right] \qquad \cos\phi < 0 \tag{41b}$$

$$h_m = \frac{1}{\ell_0\cos\phi}\left[1+\sqrt{1-\frac{2(1+S)}{\gamma'}\cos\phi}\right] \qquad \cos\phi > 0 \tag{41c}$$

A real solution for $h_m\ell_0$ from (40) exists only for $\cos\phi \leq \gamma'/2(1+S)$. When $\cos\phi > \gamma'/2(1+S)$, the contribution from the first-order lower boundary condition suppresses the wave steepening enough to prevent wave breaking and wave stress is conserved. Solutions for the zero-order lower boundary condition are also given by (41a).

In model calculations, the wave stress is computed from layer to layer beginning at the ground surface. When wave breaking does not occur, the wave stress is constant across the layer. When wave breaking occurs, the supersaturated wave stress is computed from (39) and (41). To replace the supersaturation condition with the saturation condition, $S$ in (41) is set to zero. Dropping the second term in the square brackets of (39) and using (41$a$) for $h_m$, the supersaturated wave stress for zero-order lower boundary condition is recovered. Finally, the deceleration of the mean-flow component parallel to the low-level wind is obtained as

$$\left(\frac{\partial U}{\partial t}\right)_w = \frac{1}{\rho}\frac{\partial \tau_w}{\partial z}. \tag{42}$$

The wave momentum flux profiles computed from this model for 6 and 25 March ALPEX are compared with the observed wave momentum flux in the next section.

### 2.1.6. Modelled wave momentum flux for ALPEX

The wave momentum fluxes are now calculated from the wave momentum flux models with zero- and first-order lower boundary conditions and wave stress saturation and supersaturation conditions as described in the previous section. The parallel wind component and potential temperature profiles observed on 6 and 25 March in ALPEX (Fig. 1b,d) are used as the upstream conditions for model calculations. In this calculation, the coastal range is treated as a two-dimensional. sinusoidal ridge with a horizontal wavelength of 60 km. For the computation of the surface stress, the mountain height $\eta_0$ in (10b) is estimated in terms of an effective mountain height taken as 500 and 120 m for 6 and 25 March, respectively, as will be discussed in the next section.

For 6 March, the modelled wave momentum flux decreases with height below the critical level as a result of wave breaking (Fig. 5). This decrease with height is also observed from the actual aircraft data (Fig. 5). However, the magnitude of the observed momentum flux increases substantially as the record is shortened to include only the inner region of strongest fluxes. Therefore the observations cannot be used to discriminate between the flux magnitudes of the different models. The direct observational evidence of wave induced convection shown in Section 8 will be stronger support for the hypothesis of wave stress supersaturation. The divergence of the modelled wave momentum flux corresponds to mean flow deceleration in the layer between 2.5 to 5 km at a rate of $10^{-3}$ m/s$^2$. For an inflow of 20 m/s, the wind would then decelerate by roughly 4 m/s over the 80 km wide region of such wave stress divergence.

On 6 March, the model predicts the maximum degree of supersaturation to be 18 % at the 3 km above sea level (Fig. 7). The wave momentum flux estimated with the supersaturation condition is about 35 % larger than that estimated with wave stress saturation condition at 3 km level (Fig. 5). For 25 March, wave breaking is not predicted by any combination of lower boundary conditions and wave breaking conditions. The calculated wave momentum flux increases with increasing height for all models in agreement with observations (Fig. 6, solid line).

### 2.1.7. Effective mountain height

Calculation of the wave stress at the ground level requires estimation of the effective mountain height.The actual displacement of the streamline near the ground surface is influenced by terrain-induced disturbances such as the blocking of low-level flow (Klemp and Lilly, 1978; Pierrehumbert and Wyman, 1986), the development of turbulent boundary layer (Pitts and Lyons, 1990), and the formation of stagnant cold-air pools in topographic depressions. To take into account these effects, Palmer *et al.* (1986) limit the value of wave amplitude at the ground level to 400 m or less.

Based on two-dimensional model results, Stern and Pierrehumbert (1988) propose the effective mountain height $\eta_e$ to be

$$\eta_e = \min\left[\eta_0, c\frac{U_0}{N_0}\right] \tag{43}$$

where $\eta_0$ in this equation denotes the actual amplitude of the surface topography and $c$ is a constant estimated to be 0.4 - 0.8 in their study.

We estimate the effective mountain height $\eta_e$ by equating the model-estimated wave stress at ground level with the observed wave stress below the model-estimated wave breaking level since wave stress is conserved below this level. Effective mountain heights of 500 m and 120 m appear to yield the best agreement between the observed and model-estimated fluxes for 6 and 25 March, respectively, although uncertainties in the observed values are large. Examples of the estimated wave momentum flux with various effective mountain heights are shown in Fig. 6 for 25 March. On this day the observed flux profile is simple and the model predicts no wave breaking. Using the above values of $\eta_e$ and substituting the observed upstream wind and stratification into (43), the coefficient $c$ in (43) is predicted to be, perhaps coincidentally, 0.32 for both days.

### 2.1.8. Upward turbulent heat flux in the wave breaking region

Comparison of the wave momentum flux estimated from the linear gravity wave models in the previous section suggests that the difference between the wave momentum flux predicted by wave stress saturation and supersaturation conditions can be locally significant. However, direct observational verification of wave stress supersaturation in the atmosphere has not been previously established.

One indication of wave stress supersaturation and convective instability is upward turbulent heat flux. Turbulent heat fluxes calculated for each flight level on 6 March show a well-defined region of upward turbulent heat flux over the upstream edge of the coastal range (Fig. 8) located approximately where maximum wave steepening is expected.[4] The width of the upward turbulent heat flux region is approximately 10-20 km depending on the altitude.

The occurrence of convectively driven turbulence can be seen from the horizontal variations of vertical velocity and potential temperature in the composite of eddy structures sampled from the upward heat flux region (Fig. 9). The 800 m wide samples are centered at the positive peaks of the Haar-wavelet transform of vertical velocity which is used to detect concentrated eddy-scale gradients (Mahrt, 1991). The selected samples represent about 80 % of the total record length in the upward heat flux region so that most of the record is represented. Similar structures with a factor of 2-3 smaller amplitudes occurred at the 3.7 and 4.4 km levels. In the composited structure, temperature and vertical velocity are almost exactly in phase (Fig. 9) which corresponds to well organized convection and efficient upward heat flux. This convection is consistent with wave stress supersaturation with respect to convective instability.

The estimated magnitude of turbulent heat flux generally decreases with height and varies with the cutoff wavelength for the high pass filter. The upward heat flux at the 3.3 km level reaches a maximum for a 1 km filter cutoff wavelength (Fig. 11). Therefore motions smaller than 1 km are regarded as turbulence scale disturbances. The vertical profile of the heat flux calculated from 500 m high-pass filtered variables is also presented for comparison (Fig. 10).

We now attempt to formulate the upward turbulent heat flux in the wave breaking region using a flux-gradient relationship and the wave stress supersaturation condition. The purpose of this formulation is to document the plausibility of the wave stress supersaturation condition for wave breaking rather than provide a practical tool for modelling.

The upward turbulent heat flux in a wave breaking region will be estimated by assuming a relationship between the turbulent flux and the local wave-modified gradient of the mean flow so that

$$\overline{w'\theta'} = -K\frac{\partial\theta}{\partial z} \tag{44}$$

where $K$ is the eddy diffusivity for heat and $\theta$ is the total potential temperature modified by wave activity. When the wave stress is supersaturated, $\partial\theta/\partial z$ in the wave breaking region is estimated by

---

[4] The upward turbulent heat flux shown in Fig. 10 occurs approximately in the cloud-free region reported by Smith (1987) and, is thus not due to latent heating.

$$\frac{\partial\theta}{\partial z} \approx \frac{\partial\Theta}{\partial z}\left(1 - \left(\frac{\partial\delta}{\partial z}\right)_{max}\right) = -S\,\frac{\partial\Theta}{\partial z} \tag{45}$$

where $\Theta$ is the mean potential temperature (not modified by wave activity) and $S$ is the degree of supersaturation given by (33). In (45), nonzero supersaturation (positive $S$) corresponds to convective instability. With stronger stratification, wave breaking leads to greater convective instability.

The eddy diffusivity in the wave breaking region may be approximated as

$$K \approx \ell_\theta^2 \left|\frac{dV}{dz}\right| \tag{46}$$

where $\ell_\theta$ is the turbulent length scale for heat transfer and $V$ is the wind speed modified by wave activity. In the wave breaking region, the turbulent length scale $\ell_\theta$ is presumably restricted by the depth of the wave breaking region $D$ given by (28).

To estimate the wind shear in the wave breaking region, we estimate the minimum wind speed $u_c$ due to the maximum modification of the flow by gravity waves as

$$u_c \approx U\left[1 - \left(\frac{\partial\delta}{\partial z}\right)_{max}\right] = -SU \tag{47}$$

where $U$ is the unmodified mean wind speed in the direction of the surface wind. Then, the maximum difference of the wave-modified wind speed $\Delta V$ across a depth comparable to the amplitude of the wave streamline displacement is approximated as

$$\Delta V \approx U - u_c = (1+S)U. \tag{48}$$

The corresponding shear of the wave-modified flow in the wave breaking region can be obtained from (48) as

$$\left|\frac{dV}{dz}\right| \approx \frac{\Delta V}{h(z)} = \frac{(1+S)U}{h(z)} \tag{49}$$

where $h(z)$ is, again, the amplitude of the vertical displacement of the streamline and we have assumed that the background mean shear is small compared to the wave-induced shear.

Assuming the mixing length to be proportional to the depth of wave breaking region and using the estimated wind shear (49), the eddy diffusivity in the wave breaking region may be approximated as

$$K = C_K D^2\,\frac{(1+S)U}{h(z)}. \tag{50}$$

where $C_K$ is a constant with expected magnitude less or equal to 1. From (26), (28) and (30), $D^2$ can be estimated to be

$$D^2 = a\left(\frac{H}{L}\right)^{1/2} k\left(\frac{U}{N}\right)^3 \tag{51}$$

where $a \equiv (2^{3/2}/3)^{1/2} \approx 0.97$.

Finally, the turbulent heat flux in the wave breaking region can be estimated from (44), (45), (50) and (51), together with the degree of supersaturation $S$ from (33) to be

$$\overline{w'\theta'} \approx C_K D^2 \frac{(1 + S)U}{h(z)} S\frac{d\Theta}{dz}. \tag{52}$$

Using $C_K = 1$, the model-estimated upward turbulent heat flux decreases with increasing altitude similar to the observed fluxes (Fig. 10). The decrease of upward turbulent heat flux with height results mostly from the decrease of the depth of convection $D$ with height. The comparison between model results and the observations also suggests that the constant $C_K$ in (52) is order of unity.

A wide region of downward turbulent heat flux occurs at the back of the wave immediately downstream from the narrower region of upward turbulent heat flux (Fig. 8). The upward and downward heat flux approximately cancel each other when averaging over the entire record. The wave scale heat flux is also small when averaged over the entire record at different levels. As a result, the total wave and turbulent heat flux and its influence on the mean stratification appears to be small for this day. Similar results are obtained by Delisi and Orlanski (1975) and Dunkerton (1982) from rotating tank experiments. In addition, the turbulent momentum flux is one or two orders of magnitude smaller than the wave momentum flux. Thus the transport of momentum by gravity waves appears to be the primary vertical transport mechanism for the two flow cases studied here.

### 2.1.9. Conclusions

We have studied two distinctly different atmospheric flows over the coastal range of Northern Yugoslavia with aircraft measurements collected during ALPEX. On 6 March, steepening and breaking of orographic gravity waves occur, and the wave momentum flux decreases with increasing height below the critical level. Deceleration of the wind component parallel to the surface wind due to this wave stress divergence appears to be about 9 $\times 10^{-4}$ $ms^{-2}$, a value comparable to the magnitude of the Coriolis term in momentum equations. On 25 March, low-level wave breaking does not occur and the wave momentum flux increases with height. On both days the region of wave activity is 60-70 km wide coinciding with the width of the underlying coastal range.

The wave momentum flux estimated from the linear gravity wave model agree with the observed wave momentum flux on both days. The wave momentum flux with the first-order lower boundary condition is 20 to 30 % smaller than that with zero order lower boundary condition. The generalized wave stress supersaturation condition predicts 20-40 % more wave stress on 6 March compared to application of the wave stress saturation condition. However, the difference between these models may not be significant compared to uncertainties of the flux computed from observations and uncertainties in model-input variables. The estimated effective mountain heights from the observations agree with the formulation suggested by Stern and Pierrehumbert (1988).

The region of observed upward turbulent heat flux on 6 March, 10-20 km wide, contains well defined convective eddies on the turbulent scale. These eddies provide evidence for wave stress supersaturation with respect to convective instability. The vertical profile of the observed upward turbulent heat flux can be approximated by a flux gradient relationship based on the mixing length and vertical shear derived from the generalized supersaturation theory. However the net turbulent heat flux over the entire flight path appears to be small due to cancellation between the upward flux in the convectively unstable region and downward heat flux at the back of the wave. Therefore the turbulent heat flux may not significantly influence the mean stratification at the wave breaking level in agreement with the studies of Delisi and Orlanski (1975), Fritts and Dunkerton (1985), and Dunkerton (1989). The spatially averaged transport of heat by wave-scale motions and transport of momentum by turbulence also appear to be small compared to suspected sampling problems. Therefore vertical transport of momentum by gravity waves is the principle mechanism of vertical transport for both of the flow regimes studied here.

We neglected three dimensionality of the ground topography which could lead to overestimation of the wave momentum flux (Blumen and McGregor, 1976). Nappo (1991) found that wave stress over an idealized three dimensional topography is about half of that over two dimensional topography with the same amplitude and width. However, the detailed influence of the three dimensionality will depend upon the ratio between the along-ridge and cross-ridge length scales (Pierrehumbert and Wyman, 1986). Application of the wave momentum flux formulation to numerical models must also recognize that subgrid-scale topography generally includes mountains with a variety of effective mountain heights and horizontal scales which vary according to the geographical location and grid size. Application of the gravity wave momentum flux formulation to numerical models also requires compatibility with the formulation of the planetary boundary layer (Pitts and Lyons, 1990). Such application may include generation of critical levels in the stable boundary layer (Nappo, 1991) which prevents propagation of gravity waves out of the boundary layer.

## Acknowledgements

We greatfully acknowledge the comments of Tim Dumkerton, and the computational assistance of Wayne Gibson. We also thank Ron Smith for providing the radiosonde data. This work is supported by contract F19628-88-K-0001 from the Geophysics Laboratory.

## References

Blumen, W. and C. D. McGregor, 1976: Wave drag by three-dimensional mountain lee-waves in nonplanar shear flow. *Tellus*, 28. 287-298.

Brown, Phillip R. A., 1983: Aircraft measurements of mountain waves and their associated momentum flux over the British Isles. *Quart. J. Roy. Met. Soc.*,109, 849-865.

Chao, W. C and M. R. Schoeberl, 1984: A note on the linear approximation of gravity wave saturation in the mesosphere., *J. Atmos. Sci.*,41, 1893-1898.

Drazin, P. G., 1961: On the steady flow of a fluid of variable density past an obstacle. *Tellus*, 13. 239-251.

Delisi, D. P. and I. Orlanski, 1975: On the role of density jump in the reflection and breaking of internal gravity waves., *J. Fluid Mech.*,69, 445-464.

Dunkerton, T. J., 1989: Theory of internal gravity wave saturation. *Peleogeophysics*, 130. 373-397.

Eliassen, A. and E. Palm, 1960: On the transfer of energy in stationary mountain waves. *Geophy. Publ.*, 22. 1-23.

Fritts, D. C. and T. J. Dunkerton, 1985: Fluxes of heat and constituents due to convectively unstable gravity waves., *J. Atmos. Sci.*,42, 549-556.

Hoinka, Klaus P., 1985: Observation of the airflow over the Alps during a foehn event. *Quart. J. Roy. Met. Soc.*,111, 199-224.

Holton, James R., 1982: The role of gravity wave induced drag and diffusion in the momentum budget of the mesosphere. *J. Atmos. Sci.*,39, 791-799.

Hunt, B. G., 1990: A simulation of the gravity wave characteristics and interactions in a diurnally varying model atmosphere. *J. Met. Soc. Jap.*, 68, 145-161.

Jasperson, W. H., G. D. Nastrom, and D. C. Fritts, 1990: Further study of terrain effects on the mesoscale spectrum of atmospheric motions. *J. Atmos. Sci.*,47, 979-987.

Klemp, J. B. and D. K. Lilly, 1978: Numerical simulation of hydrostatic mountain waves. *J. Atmos. Sci.*,35, 78-106.

Lenschow, D. H. and B. B. Stankov, 1986: Length scales in the convective boundary layer. *J. Atmos. Sci.*,43, 1198-1209.

Lilly, D. K., J. M. Nicholls, R. M. Chervin, P. J. Kennedy, and J. B. Klemp, 1982: Aircraft measurement of wave momentum flux over the Colorodo Rocky mountains. *Quart. J. Roy. Met. Soc.*,108, 625-642.

Lindzen, Richard S., 1981: Turbulence and stress owing to gravity wave and tidal breakdown. *J. Geophys. Res.*, 86, 9707-9714.

Lindzen, Richard S., 1988: Supersaturation of vertically propagating internal gravity waves. *J. Atmos. Sci.*,45, 705-711.

Long, Robert R., 1953: Some aspects of the flow of stratified fluids I. A theoretical investigation. *Tellus*, 42-58.

Lumley, J. L., and H. A. Panofsky, 1964: *The structure of atmospheric turbulence.*, New York, Interscience. 239pp.

Mahrt, L. and N. Gamage, 1987: Observations of turbulence in stratified flow. *J. Atmos. Sci.*,44, 1106-1121.

Mahrt, L. 1991: Eddy asymmetry in the sheared heated boundary layer.*J. Atmos. Sci.*,48

McFarlane, N.A., 1987: The effect of orographically excited gravity wave drag on the general circulation of the lower stratosphere and troposphere. *J. Atmos. Sci.*,44, 1775-1800.

Nappo, C. J. and G. Chimonas, 1991: Wave exchange between the ground surface and a boundary layer critical level. Submitted to *J. Atmos. Sci.*,.

Palmer, T.N., G.J. Shutts, and R. Swinbank, 1986: Alleviation of a systematic bias in general circulation and numerical weather prediction models through an orographic gravity wave drag parameterization. *Quart. J. Roy. Met. Soc.*,112, 1001-1039.

Pierrehumbert, R.T. and B. Wyman, 1985: Upstream effects of mesoscale mountains. *J. Atmos. Sci.*,42, 977-1003.

Pitts, R. O. and T. J. Lyons, 1990: Air flow over a two-dimensional escarpment. II: Hydrostatic flow. *Quart. J. Roy. Met. Soc.*,116, 363-378.

Smith, Ronald B.,1977: The steepening of hydrostatic mountain waves. *J. Atmos. Sci.*,34. 1634-1654.

Smith, Ronald B.,1987: Aerial observation of the Yugoslavian Bora. *J. Atmos. Sci.*,44, 269-297.

Smolarkiewicz, P. K. and R. Rotunno, 1989: Low Froude number flow past three-dimensional obstacles. Part I: Baroclinically generated lee vortices. *J. Atmos. Sci.*,46, 1154-1164.

Stern, W.F. and R.T. Pierrehumbert, 1988: The impact of an orographic gravity wave drag parameterization on extended range predictions with a GCM. *Eighth conference on numerical weather prediction.*, *Ame. Met. Soc.*, 745-750.

Thorpe, S. A., 1973: Turbulence in stably stratified fluids: A review of laboratory experiments. *Bound.-Layer Met.*,5, 95-119.

Wyngaard, 1972: On surface layer turbulence. *Workshop on micrometeorology.*, 101-150, edited by D. A. Haugan, Boston, Ame. Met. Soc., 392 pp.

## Figure legends

Fig. 1 Vertical profiles of *u*, *v*, the wind component parallel to the surface wind $V_p$, and $\theta$ from the radiosonde over Zagreb, Yugoslavia at 1200 LST on 6 March 1982 (a,b), and at 0900 LST on 25 March 1982 (c,d) obtained by averaging the soundings at 0600 and 1200 LST. Heights are with respect to sea level.

Fig. 2 Detrended observed *u*, *w*, and $\theta$ at the 3.3 km level on 6 March and topography height. The mean flow is northeasterly and directed toward the left.

Fig. 3 Vertical velocity variances of the 10-80 km band-pass filtered data (top) and the 1 km high-pass filtered data (middle) observed on 6 March at the 3.3 km level. The mean flow is northeasterly

and directed toward the left.

Fig. 4 Observed wave-scale momentum flux vectors (thin arrows) and surface wind $V_0$ (thick arrows) for 6 March (a) and 25 March (b).

Fig. 5 Observed momentum flux from the 10-80 km band-pass filtered variables (open circles) and model-estimated wave momentum flux (lines) on 6 March 1982 with the zero-order ("0th") and first-order ("1st") lower boundary conditions and wave stress saturation ("SS") and supersaturation ("SS") conditions.

Fig. 6 Observed momentum flux from 10-80 km band-pass variables (open circles) and model-estimated wave momentum fluxes for different effective mountain heights (lines).

Fig. 7 The degree of supersaturation estimated for 6 March.

Fig. 8 A schematic diagram of the isentropes (after Smith, 1987) and the regions of downward (shaded with lines) and upward (shaded with dots) turbulent heat flux observed on 6 March.

Fig. 9 The composite of $w$ (dashed line) and $\theta$ (solid line) from sampled events in the upward turbulent heat flux region at the 3.3 km level on 6 March.

Fig. 10 The upward turbulent heat flux from high-pass filtered variables with cutoff wavelengths 500 m (cross) and 1 km (open circles) on 6 March and model predicted flux profiles (52).

Fig. 11 The turbulent heat flux for different high-pass filterlengths in the upward turbulent heat flux region at the 3.3 km level on 6 March.

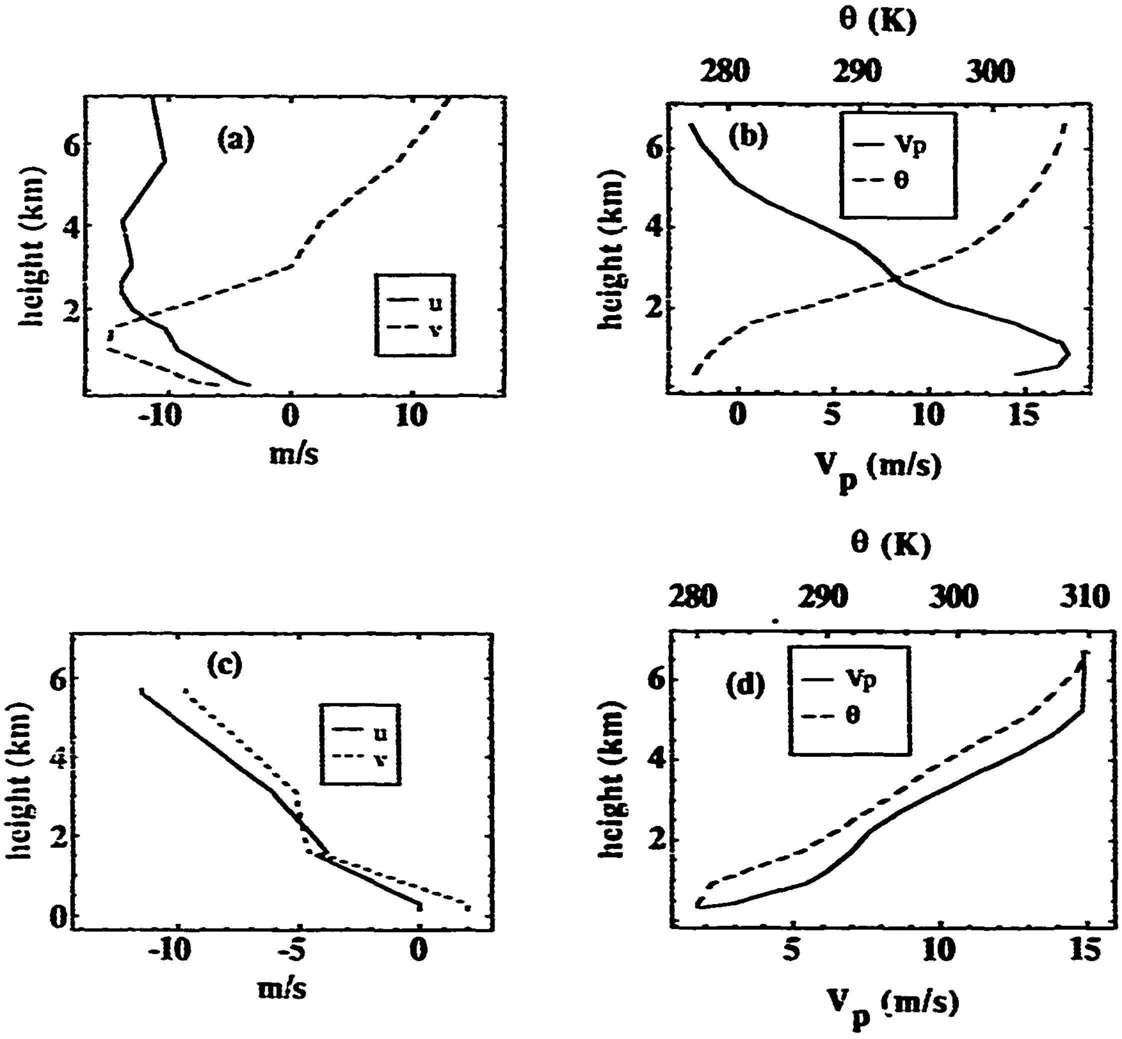
(a)
height (km)
6
4
2
u
v
-10
0
10
m/s
θ (K)
280
290
300
(b)
Vp
θ
height (km)
6
4
2
0
5
10
15
$V_p$ (m/s)
(c)
height (km)
6
4
2
0
u
v
-10
-5
0
m/s
θ (K)
280
290
300
310
(d)
Vp
θ
height (km)
6
4
2
5
10
15
$V_p$ (m/s)

Fig. 1

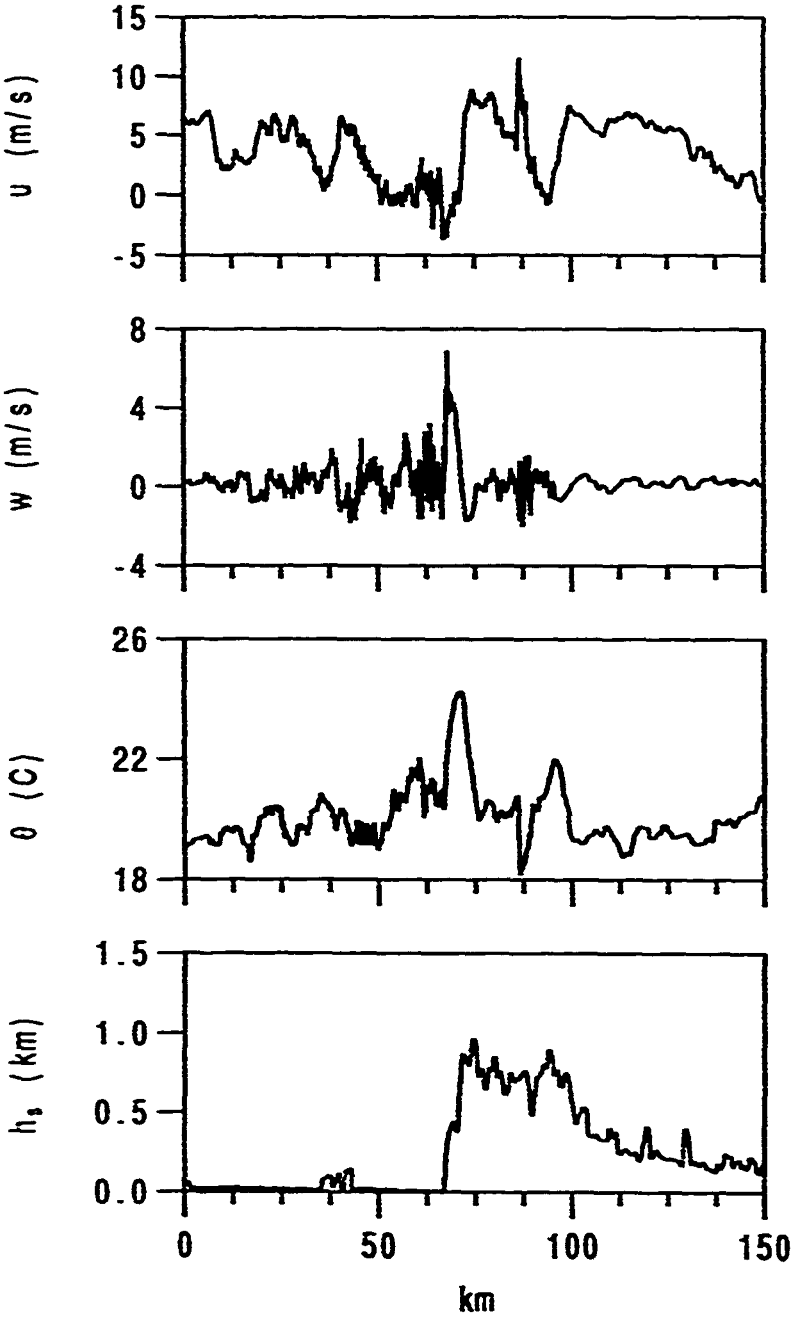

Fig. 2

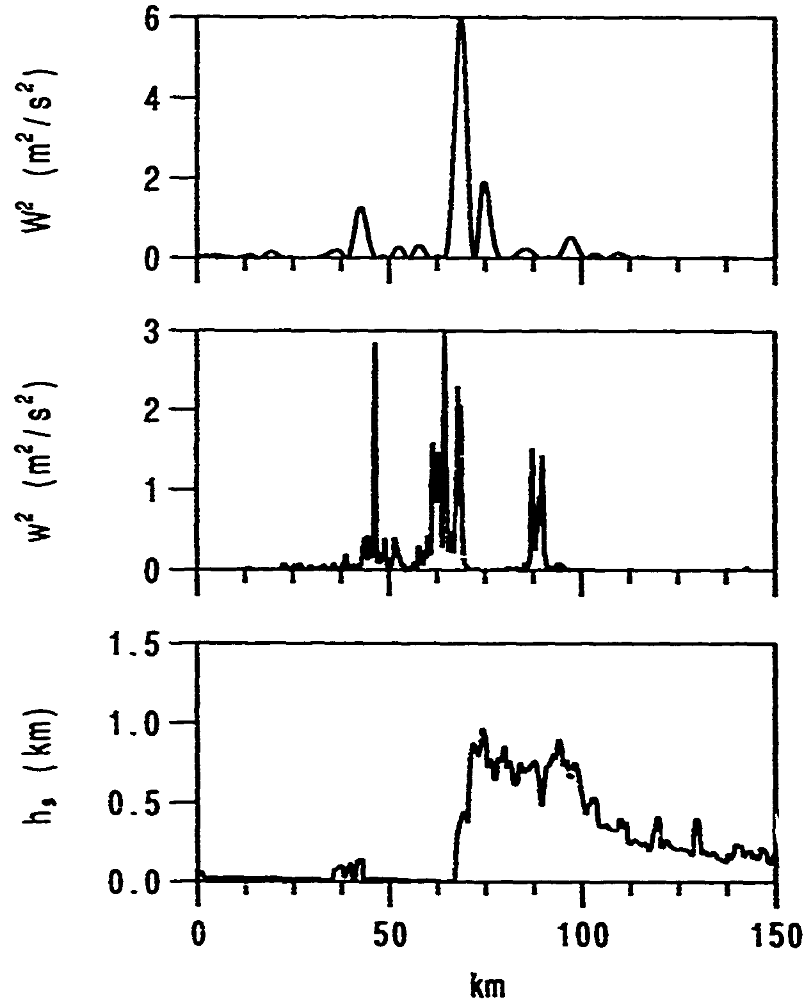

Fig. 3

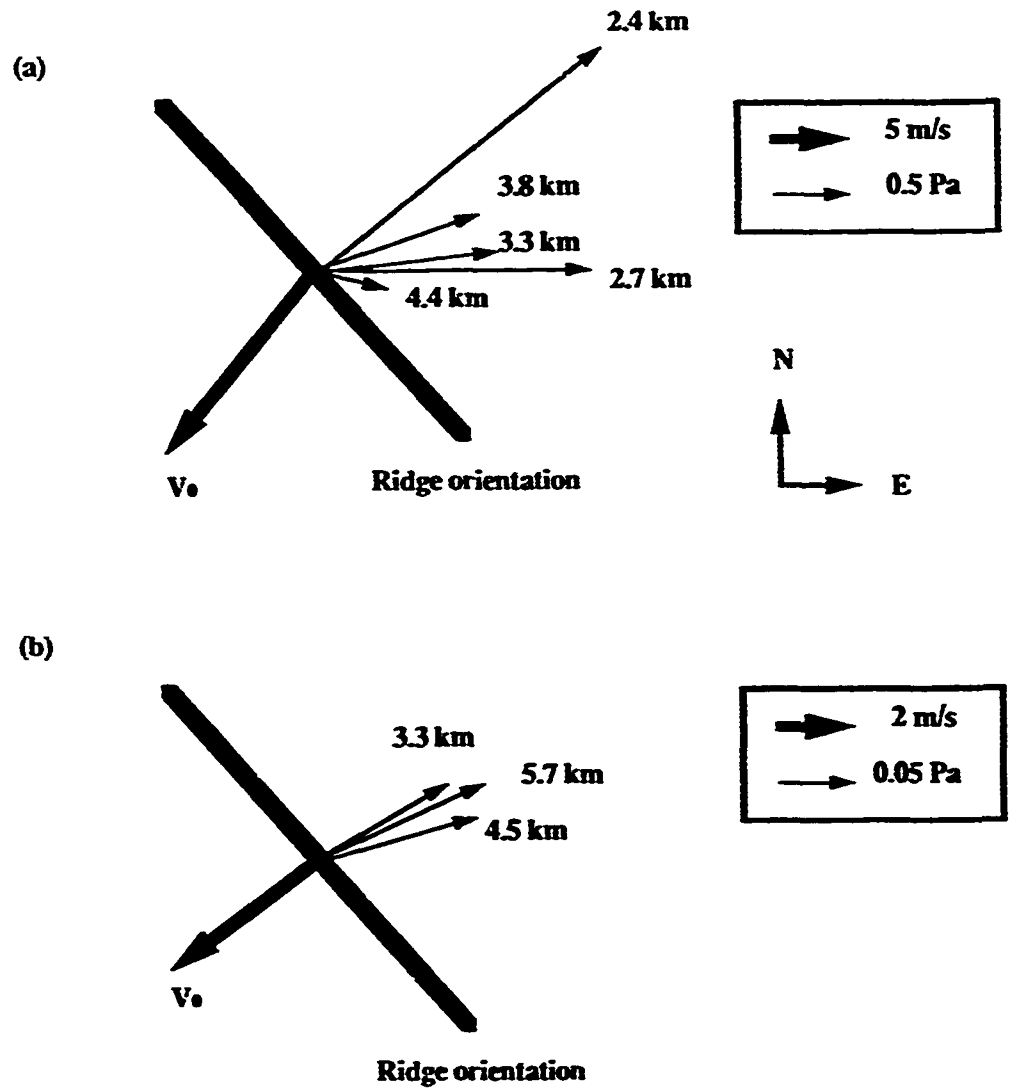
(a)
2.4 km
3.8 km
3.3 km
2.7 km
4.4 km
5 m/s
0.5 Pa
N
E
$V_0$
Ridge orientation
(b)
3.3 km
5.7 km
4.5 km
2 m/s
0.05 Pa
$V_0$
Ridge orientation

Fig. 4

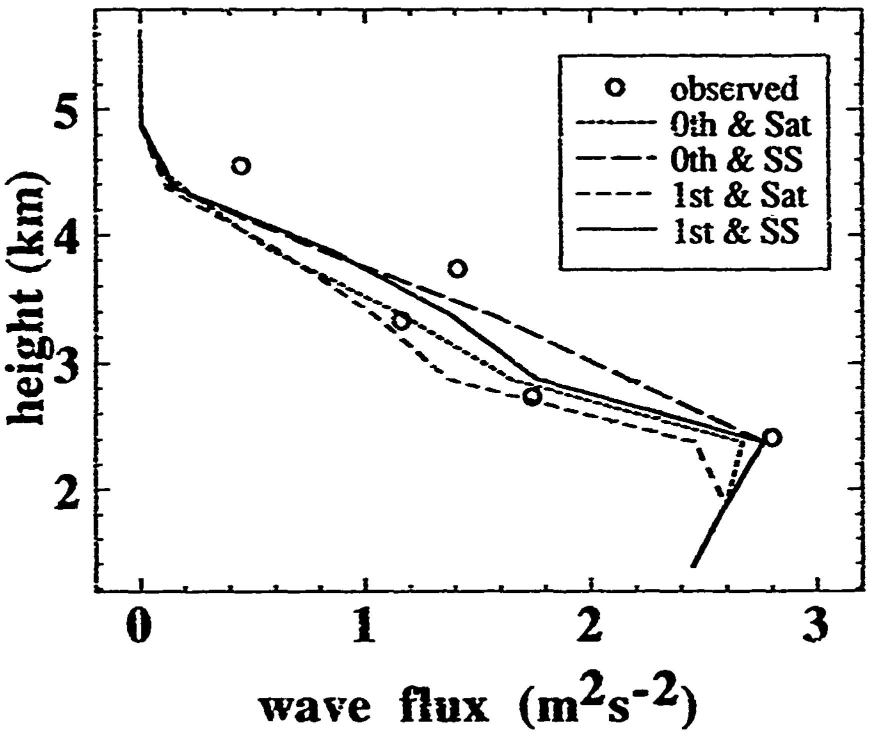

observed
0th & Sat
0th & SS
1st & Sat
1st & SS
height (km)
2
3
4
5
0
1
2
3
wave flux ($m^2s^{-2}$)

Fig. 5

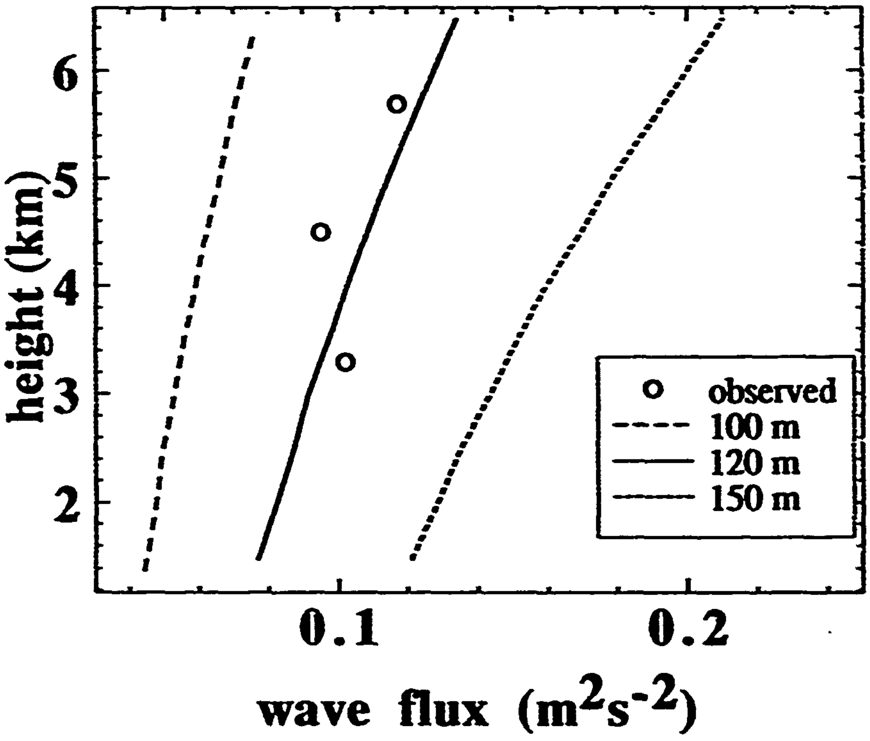

observed
100 m
120 m
150 m
height (km)
2
3
4
5
6
0.1
0.2
wave flux ($m^2s^{-2}$)

Fig. 6

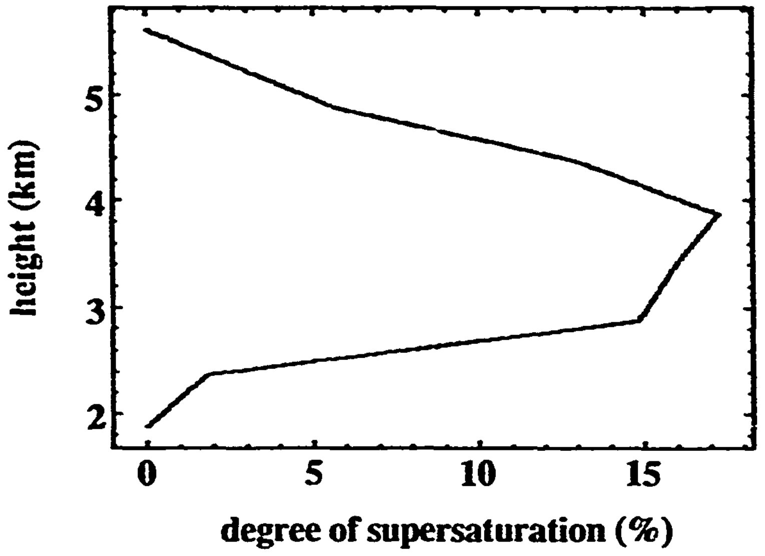

height (km)
2
3
4
5
0
5
10
15
degree of supersaturation (%)

Fig. 7

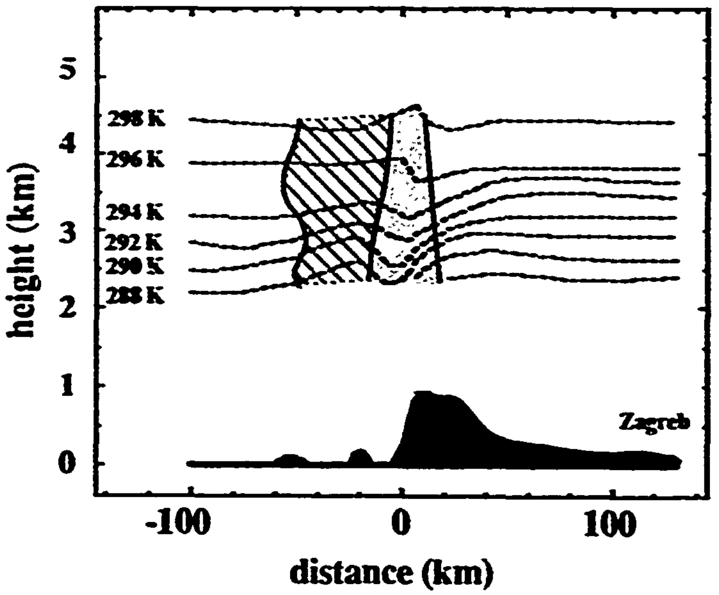

height (km)
0
1
2
3
4
5
298 K
296 K
294 K
292 K
290 K
288 K
Zagreb
-100
0
100
distance (km)

Fig. 8

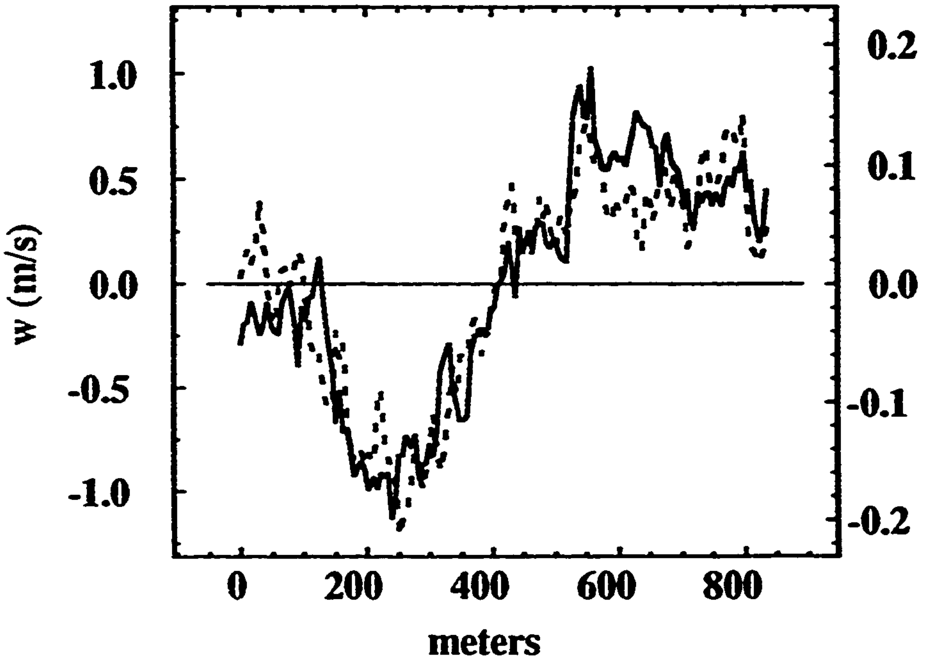
1.0
0.5
0.0
-0.5
-1.0
w (m/s)
0.2
0.1
0.0
-0.1
-0.2
θ (K)
0
200
400
600
800
meters

Fig. 9

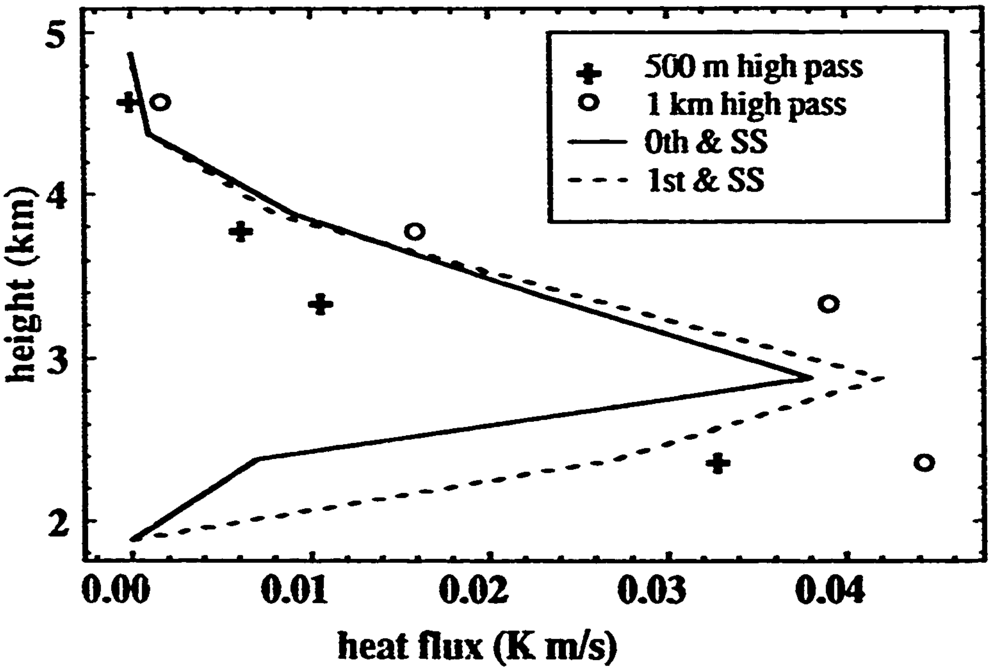
5
4
3
2
height (km)
0.00
0.01
0.02
0.03
0.04
heat flux (K m/s)
+ 500 m high pass
o 1 km high pass
— 0th & SS
- - - 1st & SS

Fig. 10

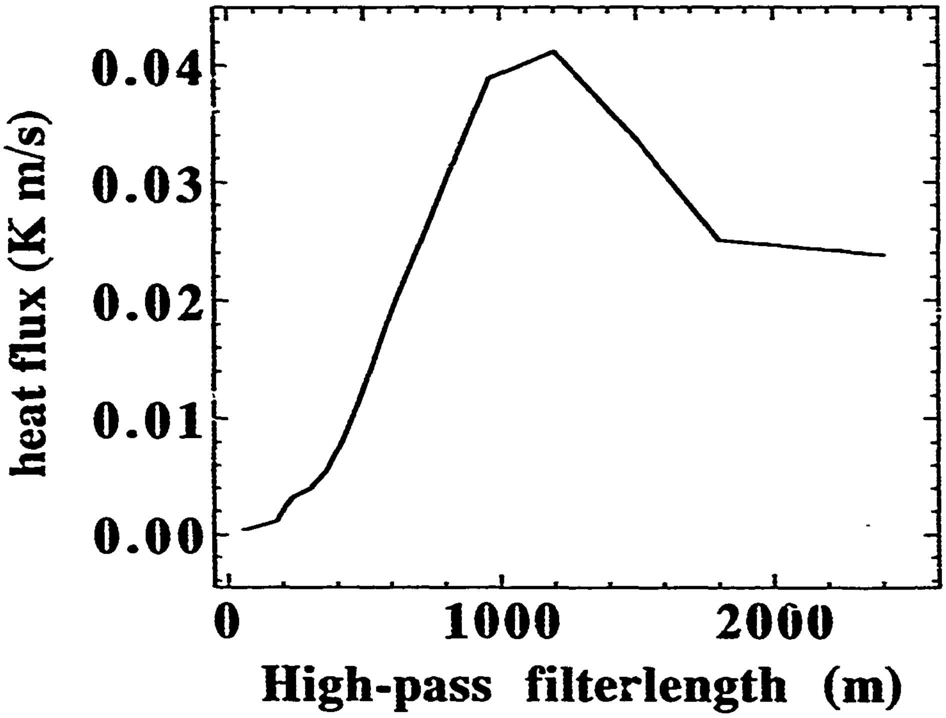
heat flux (K m/s)
0.04
0.03
0.02
0.01
0.00
0
1000
2000
High-pass filterlength (m)

Fig. 11

# Chapter 2.2

## Turbulent Transport in the Free Atmosphere and very stable Nocturnal Boundary Layer

### 2.2.1. Introduction

Previous studies suggest that as much as 25 % of the dissipation of atmospheric kinetic energy occurs through clear air turbulence in the mid- and upper troposphere (Heck *et al.*, 1977). Turbulence in the free atmosphere is usually found in thin and isolated regions of large vertical shear and horizontal temperature gradient, and small Richardson number. Such regions are frequently found near the jet stream and internal fronts (Kennedy and Shapiro, 1975). Clear air turbulence is also induced by smaller scale atmospheric perturbations such as breaking gravity waves and roll vortices (Atlas *et al.*, 1970). Turbulent mixing may occur systematically in the residual layer, a weakly stratified remnant of the daytime mixed layer above the nocturnal boundary layer (Stull, 1990). Observational (Lenschow *et al.*, 1987) and numerical (André *et al.*, 1978; Garratt, 1985; Stull and Driedonks, 1987) studies indicate shear-driven turbulence at the top and/or bottom of what appears to be a residual layer.

Turbulence is often intermittent in the upper part of the surface inversion layer, and seems to be generated by local shear not directly related to the surface stress (Mahrt, 1985). Such turbulence may propagate downward in the form of turbulent bursts (Nappo, 1991). Consequently, models based on boundary layer similarity appear to poorly describe the very stable case.

The modelling studies of Louis *et al.* (1981) show that changing the turbulence parameterization can significantly alter simulated large scale flows. Despite this importance, turbulent mixing in the free atmosphere has received much less attention compared to the surface-based boundary-layer. Operational prediction of atmospheric clear air turbulence sometimes requires the gradient Richardson number to be less than unity (Keller, 1990) or less than some other critical value. Some evidence can be extracted from layers of free turbulence in laboratory and oceanic stratified shear flows (see Fernando, 1991a for a review). For example, laboratory experiments generally support the gradient Richardson number criterion for the onset of turbulence (e.g., Thorpe, 1973). However, the critical value of the Richardson number may increase with the depth of the layer over which it is computed (Lyons *et al.*, 1964). Even with large values of the Richardson number for the resolved flow, the Richardson number on smaller scales may become sufficiently small to initiate turbulence (Padman and Jones, 1985). In addition, values of the fluxes depend on the range of scales included in the estimation. For example, the clear air flux values reported by Kennedy and Shapiro (1980) include scales up to several hundred kilometers and therefore include motions with physics quite different from that of turbulence.

In this study, seventeen aircraft slant soundings obtained on 6, 7, and 24 May 1983 in CABLE (Clear Air Turbulence and Boundary Layer Experiment) and eight soundings and one horizontal leg obtained on 6 May 1979 in SESAME (Severe Environmental Storms and Mesoscale Experiment) are analyzed to estimate the turbulent fluxes above the boundary layer and their relationship to the Richardson number. Based on analyses of this data, we attempt to formulate the eddy diffusivities in the free atmosphere in terms of the turbulent length scale and the eddy Prandtl number (Section 3). In addition turbulent mixing lengths and eddy Prandtl numbers are estimated for 5 and 7 May SESAME from the composite fluxes and mean flows presented in Mahrt (1985) and Lenschow *et al.* (1987). In Section 4, the resulting expressions for the relationships of the mixing length and the Prandtl number to the gradient Richardson number are compared against those suggested by Louis *et al.* (1981) and those used in the medium range forecast model at the U.S. National Meteorological Center (NMC, 1988). In Section 5, the influence of turbulent mixing on the evolution of low-level flow is studied using a column model with emphasis on the evolution of the residual layer above the nocturnal boundary layer.

### 2.2.2 Data

This study analyzes data obtained from 5 May 1983 in CABLE where the NCAR King Air flew from 0600 to 1000 LST in the east-west direction over western Kansas (Fig. 1a). The boundary layer was undergoing transition from the nocturnal surface inversion layer at the beginning of the flight to the mixed layer at the end of the observation. Layers of turbulence occurred above the thin but growing boundary layer. Flights on 24 May 1983 in CABLE extended from Oklahoma City to over the Gulf of Mexico during the period from 1600 to 1900 LST. On this day, clear air turbulence occurs approximately 3 km above the sea surface (Fig. 1b). Based on the isentropic analysis (Fig. 1b), this turbulence apparently occurs in conjunction with mesoscale disturbances.

Data on 6 May 1979 in SESAME were taken in and above a windy, weakly stable nocturnal boundary layer over central Oklahoma (Lenschow *et al.*, 1987). Analyses of turbulence above the surface inversion layer on 5 May in SESAME by Mahrt (1985) and near the top of the residual layer on 7 May in SESAME by Lenschow *et al.* (1987) are also used to compute mixing lengths and the eddy Prandtl number.

After high-pass filtering the aircraft data to partially remove gravity waves and other larger scale disturbances, heat and momentum fluxes and the vertical velocity variances are calculated. Based on cospectra, the cutoff wavelength for the high-pass filtering is approximately 1 km for 5 and 24 May

CABLE and 6 May SESAME. Examples of vertical profiles of potential temperature and variance of high-pass filtered vertical velocity from CABLE 24 May over the ocean are presented in Fig. 2. The observed clear air turbulence is separated from boundary layer turbulence by a layer of relatively small vertical velocity variance (Fig. 2). The bottom of the near-quiescent layer coincides with the capping inversion at the top of the boundary layer as can be seen from the potential temperature profile (Fig. 2). Elevated maxima of downward turbulent heat flux also appear in the same layers as the vertical variance maxima. The variance of the high-pass filtered vertical velocity in the patches of clear air turbulence corresponds to a root-mean-square vertical velocity of 10-60 cm/s for the CABLE cases and 5-40 cm/s for SESAME 6 May. The magnitude of the vertical velocity associated with the stronger updrafts and downdrafts is usually an order of magnitude larger than the root-mean-square vertical velocity.

The vertical profiles of the mean flow are estimated from slant soundings by block-averaging the raw data. The depth of the averaging interval is typically 50 m and is determined for each leg based on a subjective assessment of natural layering and also based on the aircraft ascent or descent rate and the need to reduce the contamination by horizontal variability due to mesoscale motions. To obtain the mean values at the levels corresponding to the top and bottom of the turbulent layer, the averaged variables are interpolated with cubic splines.

The gradient Richardson numbers calculated for the turbulent layers vary from 0.2-1.0 while those calculated outside the turbulent layers are usually larger than 1.5. In a few exceptions the gradient Richardson number drops to about 0.6 in a quiescent layer. When the block-averaging intervals were increased by a factor of two, the resulting gradient Richardson numbers changed by an average amount of approximately 50 % with no preference for the sign of the changes.

### 2.2.3. Eddy diffusivities and the eddy Prandtl number

In this section, we construct an empirical formulation for the eddy diffusivity in the free atmosphere in terms of the large scale stability based on the gradient Richardson number. The gradient Richardson number is approximated by the ***layer Richardson number*** ($R_L$) computed across the bulk turbulent layer as

$$R_L = \frac{g}{\Theta}\frac{\Delta\Theta\,\Delta z}{|\Delta V|^2} \tag{1}$$

where $g$ is the acceleration of gravity, $\Delta\Theta$ is the difference of the mean potential temperature across the turbulent layer of the thickness $\Delta z$, $\Theta$ is the mean potential temperature of the layer, and $\Delta V$ is the magnitude of the wind vector difference across the layer. We express the eddy diffusivity for heat

($K_h$) and momentum ($K_m$) as

$$K_h = \ell_h^2 \left| \frac{\partial V}{\partial z} \right| \tag{2a}$$

$$K_m = K_h Pr \tag{2b}$$

where $\ell_h$ is the turbulent mixing length for heat and $Pr$ is the eddy Prandtl number assumed to be dependent on the Richardson number. These dependencies on the Richardson number will be estimated from the observations. Horizontal velocity fluctuations and associated momentum flux are complicated by pressure fluctuations while temperature fluctuations are not. Therefore we first establish the formulation of the eddy diffusivity for heat and then estimate the eddy diffusivity for momentum from the dependence of the eddy Prandtl number on the Richardson number.

First we compute eddy diffusivities from the observed turbulent fluxes and vertical variation of the mean flow as

$$K_h = -\frac{\overline{w'\theta'}}{\partial \Theta / \partial z} \tag{3a}$$

$$K_m = -\frac{\overline{u'w'}(\partial U/\partial z) + \overline{v'w'}(\partial V/\partial z)}{(\partial U/\partial z)^2 + (\partial V/\partial z)^2} \tag{3b}$$

where primed variables denote the high-pass filtered variables and the overbar designates an average.

The mixing length ($\ell_h$) can be obtained from the eddy diffusivity for heat (3$a$) as

$$\ell_h^2 = \frac{K_h}{|\partial V/\partial z|}. \tag{4}$$

Estimated values of the mixing length decrease rapidly with increasing Richardson number in the range $0 < Ri \leq 0.4$, then decrease more slowly for $Ri > 0.4$ (Fig. 3). The dependence of the estimated mixing length on the Richardson number shows less scatter than the dependence of the eddy diffusivity on the Richardson number (not shown) even though the mixing length is computed from the eddy diffusivity. The mixing length for momentum (not shown) shows more scatter than that for heat.

We will represent the mixing length in terms of an asymptotic mixing length at neutral stability $\ell_{0,h}$, as in Blackadar (1962), and a nondimensional function of the gradient Richardson number $\phi_h(Ri)$ so that

$$\ell_h(Ri) = \ell_{0,h}\phi_h(Ri) \tag{5}$$

The nonlinear least-squares fit of the observed mixing length yields $\ell_{0,h} \approx 52.5$ m for $\phi_h(Ri)$ given by

$$\phi_h(Ri) = \frac{e^{-8.5Ri} + 0.15/(Ri+3.0)}{1.05}. \tag{6}$$

The first term in (6) represents the rapidly decreasing part of $\ell_h$ for the range $0 < Ri < 0.4$ while the second term in (6) represents the more slowly decreasing part of $\ell_h$ for the range $Ri \geq 0.4$. A similar two-regime relationship between $Ri$ and the bulk dimensionless drag coefficient, which is the boundary layer equivalent of $\phi^2$ in (5), is observed by Mahrt (1987). Due to the lack of data for small Richardson numbers ($Ri < 0.2$), some uncertainty is expected in the estimated asymptotic mixing length. Asymptotic mixing lengths used in previous parameterizations of turbulent mixing in the free atmosphere are usually specified to be several hundred meters (Louis, 1979; Louis *et al.*, 1981; NMC, 1988). However, such values are based on desired overall model performance instead of direct observations of clear air turbulence. In actual clear air turbulence, the asymptotic mixing length may depend on the vertical distance from the top or bottom of the turbulent layer. The estimated mixing lengths are typically an order of magnitude smaller than the thicknesses of the turbulent layers. However, the mixing lengths and Richardson numbers do not show a definite relationship to the thickness of the turbulent layers in contrast to near equilibrium turbulence in laboratory experiments (Fernando, 1991b). In geophysical free turbulence layers, equilibrium may be prevented by continual modification of the mean shear by the turbulence.

The eddy Prandtl number is estimated from the observed eddy diffusivities (3*a*,*b*) as

$$Pr = \frac{K_m}{K_h}. \tag{7}$$

The dependence of the Prandtl number on the Richardson number (Fig. 4) shows considerable scatter, especially at Richardson numbers greater than 0.4. The large scatter is partly due to the scatter in the eddy diffusivity for momentum and the usual problems with statistics of ratios. Furthermore, the observed fluxes may be contaminated by large sampling problems particularly with slant soundings. The estimated Prandtl number increases with increasing Richardson number which implies that the contribution of the pressure fluctuations to the vertical transport of horizontal momentum becomes more important as the stability of the mean flow increases. Increasing Prandtl number with increasing Richardson number has also been observed in various laboratory experiments (Arya, 1975; Mizushina *et al.*, 1978; Webster, 1964; Rohr *et al.*, 1988) and seems to be suggested by the atmospheric observations of Merrit and Rudinger (1973), Wittich and Roth (1984) (Fig. 4), and Kondo *et al.* (1978).

The eddy Prandtl numbers estimated from the present analyses are roughly approximated with a least squares linear fit to the gradient Richardson number (solid line, Fig. 4) as

$$Pr(Ri) = 1.5 + 3.08\,Ri. \tag{8}$$

This relationship predicts the Prandtl number at neutral stability to be 1.5 which is larger than some previous laboratory experiments which suggest $Pr_0 \approx 1$ (e.g. Arya, 1975; Mizushina *et al.*, 1978). A nonlinear fit to the data predicts a value of $Pr_0$ closer to one, but a fit more complex than linear cannot be justified with the limited data and large scatter. When $Pr = 1$ at $Ri = 0$ is forced, a linear fit of the current results yields a slope of 3.84, instead of 3.08 in (8) (dashed line in Fig. 4). In the simulations of Section 5, we use (8).

### 2.2.4. Comparison with the other clear air turbulence model

Due to lack of observational evidence, parameterizations for turbulent mixing in the free atmosphere have been based on boundary layer similarity relationships with constant asymptotic mixing length. However, clear air turbulence is not directly influenced by the underlying surface so that the stability dependence computed from actual data (6) may be different from those based on observations in the surface layer. The current model (5,6) will now be compared with mixing length formulations from Louis *et al.* (1981) and NMC (1988) for free atmospheric mixing in operational models.

The nondimensional function of the Richardson number in the Louis model, $f_L$, which is equivalent to $\phi_h$ in (5), is given as

$$f_L(Ri) = [1 + 15\, Ri(1 + 5\, Ri)^{1/2}]^{-1/2} \tag{9a}$$

and that for the NMC model, $f_N$, as

$$f_N(Ri) = [1 + 5\, Ri^2]^{-1/2} \tag{9b}$$

The nondimensional functions $\phi_h(Ri)$, $f_L(Ri)$, and $f_N(Ri)$ all decrease with increasing Richardson number, but $f_N(Ri)$ and $f_L(Ri)$ decreases more slowly than $\phi_h(Ri)$ based on the current observations (Fig. 5). Therefore, for a given asymptotic mixing length, the present formulation will predict smaller eddy diffusivities than the NMC and Louis models.

The eddy Prandtl number for the Louis model is obtained from (1*a*,*b*), (5), and (7) as

$$Pr(Ri) = \frac{\ell_m^2}{\ell_h^2}(Ri) = \frac{\ell_{0,m}^2}{\ell_{0,h}^2}\frac{f_m^2(Ri)}{f_h^2(Ri)} \tag{10}$$

where $\ell_m$, $\ell_{0,m}$, and $f_m$ are the mixing length, the asymptotic mixing length, and the nondimensional function of the gradient Richardson number for the turbulent momentum flux, respectively. Defining a new dimensionless function of the gradient Richardson number $F(Ri)$, (10) becomes

$$Pr(Ri) = Pr_0 F(Ri) \tag{11}$$

where $Pr_0$ is the eddy Prandtl number at neutral stability and is expressed as

$$Pr_0 = \frac{\ell_{0,m}^2}{\ell_{0,h}^2}. \tag{12}$$

We can obtain $F(Ri)$ from $f_h(Ri)$ and $f_m(Ri)$ given in Louis *et al.* (1981) as

$$F(Ri) \equiv \frac{f_m^2(Ri)}{f_h^2(Ri)} = \frac{1+15Ri(1+5Ri)^{1/2}}{1+10Ri(1+5Ri)^{-1/2}}. \tag{13}$$

Based on the sensitivity tests with large-scale models, Louis *et al.* (1981) suggest asymptotic mixing lengths of 150 and 450 m for the momentum and heat transfer, respectively, corresponding to $Pr_0 = 1/9$, much smaller than implied by previous observations. However, such values of asymptotic mixing lengths are quite uncertain so that, for the comparison only, $Pr = 1$ at $Ri = 0$ is assumed for both the Louis model and the present model. NMC (1988) assumes that $Pr = 1$ for stable stratification.

The eddy Prandtl number calculated from the Louis model (dashed line, Fig. 6) increases almost linearly with increasing $Ri$, but faster than the current formulation (solid line, Fig. 6). While the difference between the two formulations may not be significant compared to the large scatter in the data, both relationships predict that the Prandtl number becomes large, 5 or greater for strong stability. Therefore equating the eddy diffusivity for momentum to that for heat in stably-stratified conditions, as in the NMC model, will seriously underestimate the momentum transport for large stability.

### 2.2.5. Turbulence in the free atmosphere: Column model simulations

The influence of clear air turbulence above the nocturnal boundary layer is now investigated using a one-dimensional numerical model with the current eddy diffusivity formulation (2*a*,*b*) based on the stability dependent mixing length (5-6) and Prandtl number (8). Turbulent mixing in the boundary layer is calculated from the model of Troen and Mahrt (1986) except for special modifications developed in Subsection c. Additional features of the column model are detailed in Ek and Mahrt (1990). This model is designed for use within large scale models where simplicity and economy are required.

To eliminate spurious inertial oscillation in the free atmosphere, the initial wind profiles are specified to be geostrophic above 200 m and decrease linearly to zero at the surface. In the experiments presented in Subsections a - c, the mean vertical motion is specified to be zero, and the geostrophic winds are assumed to be time- and height-independent at all levels with a value of 5 m/s.

#### a. Diurnal variation

The model simulation is governed by the growth and decay of the mixed layer and attendant inertial oscillation. As a result, the nocturnal lower atmosphere evolves into three distinctive layers consisting of the nocturnal boundary layer, residual layer, and free atmosphere (Fig. 8a) as also occurs in somewhat different form in the observations of Lenschow *et al.* (1987) plotted in Fig. 7.

The daytime mixed layer begins to collapse at 1700 solartime and yields to a nocturnal boundary layer which is a few hundred meters thick. A residual layer of weak or near zero stratification remains between the top of the nocturnal surface inversion layer and the inversion corresponding to the top of the pre-existing daytime mixed layer (Fig. 8). Modelling studies of André *et al.* (1978), Garratt and Brost (1981), Garratt (1985), and Stull and Driedonks (1987) also show the survival of the residual layer during the nighttime. The weakly stratified layer observed above the surface inversion layer in the early morning of 7 May 1979 in SESAME (Fig. 7) may be an observational example of the residual layer. Weak stratification observed above the nocturnal boundary layer in André *et al.* (1978), Mahrt *et al.* (1979), Hsu (1979), Estournel *et al.* (1986), and Stull and Driedonks (1987) may be additional examples.

Following the mixed layer collapse and development of the inertial oscillation and low-level jet (Buajitti and Blackadar, 1957; Beyrich and Klose, 1988), significant vertical shear of the mean flow develops at the top and bottom of the residual layer (Fig. 8a). In actual atmospheric flows where the geostrophic wind varies spatially, convergence induced by inertial oscillation leads to damping by pressure adjustments (Smith and Mahrt, 1981) and would presumably limit the speed of the low level jet. These effects cannot be included in a column model.

### b. Turbulent diffusion in the free atmosphere

By the early morning, when the modelled low-level jet reaches its full strength, the eddy diffusivity occurs with two distinct maxima above the boundary layer; one located immediately above the low-level wind maximum and the other in the shear layer near the top of the residual layer (Fig. 8b). A local turbulence maximum near the top of the residual layer also occurs in the early morning profile of the turbulence kinetic energy profile on 7 May 1979 SESAME (Fig. 7) and in the model results of André *et al.* (1978) and Garratt (1985). An inferred maximum of turbulence near the low-level jet has been observed by André and Mahrt (1982) and occurs in the modelling studies of André *et al.* (1978) and Garratt (1985).

The modelled clear air turbulence reduces the mean shear near the top of the residual layer but is otherwise unimportant for this flow case. The potential temperature in the residual layer remains well mixed throughout the night and momentum remains partially mixed. As a result the Richardson number and eddy diffusivity are sensitive to slight changes of the mean profiles and can even be altered by changes in the time step; however, the resulting turbulent fluxes are categorically small for these cases and have little effect on the mean flow.

Fig. 7 and previous observations indicate that the residual layer often develops some stratification during the night even if weak. The failure of the model to develop such stratification may be due to underestimation of mixing or neglect of clear air radiative cooling, horizontal advection, the influence of baroclinity (Subsection d), and mean subsidence (Subsection e). Important clear air radiative cooling was inferred from observations for the lower part of the residual layer in André and Mahrt (1982) and occurred in the modelling study of Garratt and Brost (1981). Asymptotic mixing lengths of several hundred meters are usually specified for large-scale numerical models (Louis *et al.*,1981; NMC, 1988) which would produce an order of magnitude larger eddy diffusivity than that estimated from the present observations. The previous model mixing lengths are based on model performance rather than observations and may attempt to include subgrid variability of turbulence (Maryon, 1990). The present analysis of observations includes fluxes on horizontal scales up to 1 km only and does not explicitly include gravity wave induced turbulence nor direct transport of momentum by gravity waves. However application of large mixing lengths of several hundred meters in the present column model still fails to stratify the interior of the residual layer.

### c. Turbulence in the upper part of the nocturnal boundary layer

Models based on boundary layer similarity theory appear to adequately approximate the weakly stratified boundary layer, but poorly describe the very stable boundary layer. Boundary layer similarity theory is based on the assumption that the vertical length scale of large boundary layer eddies is related to the depth of the boundary layer and height above the ground. In the very stable boundary layer, vertical movement of air is restricted and the turbulent eddies can not extend over the entire depth of the boundary layer (Nieuwstadt, 1984) sometimes leading to only intermittent turbulence (Kondo *et al.*, 1978). For example, the formulation for the stable boundary layer used in the current model fails to represent the effect of significant shear in the upper part of the nocturnal surface inversion layer associated with the overlying low level jet. In particular, the nocturnal boundary layer may assume an upside down structure with the main source of shear generation occurring near the top of the surface inversion layer (Mahrt, 1985).

The local scaling model of Nieuwstadt (1984) provides more flexibility but requires the flux to vanish at the top of the boundary layer and cannot accommodate the case where shear at the top of the surface inversion layer is a principle source of turbulence. In an attempt to include local generation of turbulence in the upper part of the nocturnal boundary layer, the current free atmospheric mixing model is now merged with the modelled nocturnal boundary layer. It is arbitrarily assumed that boundary layer similarity is always valid in the lower 30 % of the stable boundary layer. The current boundary layer model predicts maximum eddy diffusivity at approximately $0.3h$ where $h$ is the boundary layer depth. The merged model allows local shear generation of mixing to override the conventional boundary layer prediction in the upper 70 % of the modelled boundary layer if the local prediction of the eddy diffusivity (2, 5, 6) is greater than the boundary layer prediction.

The asymptotic mixing length $\ell_{0,k}$ in (5) is not allowed to exceed $kz$ for the *local* eddy diffusivity formulation where $k$ is the von Kármán constant assumed to be 0.4 and $z$ is the height above the surface. That is, *free* eddies in the stable boundary layer attempting to become larger than $kz$ would become constrained by the surface. Unfortunately there are no observations to study the development of turbulence from elevated shear layers which subsequently becomes influenced by the ground.

The eddy diffusivity estimated by the local prediction significantly exceeds the eddy diffusivity estimated from the boundary layer similarity theory late in the night when shear near the top of the surface inversion layer becomes significant. As a result, the maximum eddy diffusivity in early morning occurs in the upper part of the nocturnal boundary layer (Fig. 9a) as also occurred in Mahrt (1985). For the present numerical experiment the locally generated turbulence reduces the low level wind speed maximum by 10 % but otherwise exerts negligible influence on the mean flow (Fig. 9b). As the specified geostrophic wind speed decreases the influence of local turbulence generation increases. That is, the modelled local generation of turbulence in the stable boundary becomes more important when turbulence in the boundary layer is weak.

### d. Baroclinity

Mean shear and generation of turbulent mixing in the residual layer may be enhanced by baroclinity of the large-scale flow. As an example, the influence of geostrophic wind shear on the generation of turbulence is tested by specifying the geostrophic wind to increase linearly from 4 m/s at the ground to 8 m/s at 2 km above the ground. Horizontal advection of temperature implied by the geostrophic wind shear is neglected.

With the imposed geostrophic wind shear, local generation of turbulence in the upper part of the nocturnal boundary layer smooths the potential temperature profile and reduces the speed of the nocturnal jet by about 20 % (Fig. 10a,b). The nocturnal boundary layer is warmed by the local mixing. The 20 m temperature is about 1.5 deg C warmer when local mixing is included in the upper part of the nocturnal boundary layer (Fig. 10b). Overestimation of surface cooling has been a systematic deficiency of boundary layer models applied to very stable conditions (Ruscher, 1987). Consequently the modelled heat flux from the free atmosphere to the stable boundary layer by inclusion of local shear generation may allow removal of artificial constraints in low resolution large scale models. Such constraints include specification of a minimum low-level wind speed (NMC, 1988) and limitation of the influence of stratification on the surface exchange coefficient (M. Schlesinger and T. Scholtz, personal communications). However, the enhanced mixing due to baroclinity still fails to stratify the residual layer. Unfortunately the present observations do not allow adequate estimation of the geostrophic wind shear to test the column model. The importance of mean vertical motion is discussed in the next section.

### c. Large-scale subsidence

As an example, the influence of large-scale subsidence is studied by arbitrarily specifying the mean vertical velocity profile to be -2.5 cm/s at 3 km and to decrease linearly to zero at the ground. The numerical simulation is otherwise identical to that of Subsection a.

The vertical advection of potential temperature due to subsidence generates some stratification in the residual layer (Fig. 11) and reduces the thickness of the residual layer to less than one half of that without subsidence. These results suggest that subsidence may be an important mechanism for stratifying the residual layer. However a major difficulty for comparing the modelled residual layer with observations now emerges. The depth of the residual layer is sensitive to even modest values of subsidence yet subsidence cannot be accurately estimated from observations.

### 2.2.6. Conclusions

Turbulent fluxes, mixing lengths, and eddy diffusivities in layers of clear air turbulence have been estimated from aircraft data obtained during SESAME and CABLE. For small positive values of the gradient Richardson number, the eddy diffusivity and mixing length decrease rapidly with increasing gradient Richardson number. The eddy diffusivity and turbulent mixing length decrease more slowly at larger values of the gradient Richardson number. This *observed* mixing length is significantly smaller than th • previously used to model clear air subgrid scale flux in large scale models. The observed turbulent Prandtl number tends to increase to values significantly greater than unity with increasing Richardson number although the scatter is large. This indicates that pressure fluctuations enhance the momentum flux at large stability.

Based on the data analyses, this study has constructed a similarity formulation of the stability dependent mixing length and Prandtl number for the free atmosphere. This formulation is applied to a column model sufficiently simple for use in large scale models. During the night, weak turbulence develops at the top and bottom of the residual layer due to shear associated with the inertial oscillation and nocturnal low level jet. The residual layer is located above the thin nocturnal boundary layer and is a remnant of the deeper daytime boundary layer. Large scale subsidence significantly reduces the thickness of the residual layer during the course of the night.

The current formulation for locally generated turbulent mixing is allowed to override the boundary layer scheme in the upper part of the nocturnal surface inversion layer when boundary layer similarity theory fails to represent the impact of the local shear associated with the underside of the nocturnal jet. In the present study, the influence of the locally generated turbulence on the boundary layer mean flow appears to be more significant as the geostrophic wind decreases or as the geostrophic wind shear increases. With weak air flow in the very stable case, the local generation of turbulence at the top of the inversion layer may be the principal cause of diffusion corresponding to an *upside down* boundary layer. Such boundary layers belong to the Type I nocturnal boundary layer class of Kurzeja *et al.* (1991) where much of the variance is due to horizontal meandering and gravity waves. Conventional models of the stable boundary layer are expected to overestimate surface cooling and underestimate dispersion with very stable conditions.

The importance of mean subsidence and baroclinity makes model comparison with observations difficult. Without subsidence, the model fails to stratify the residual layer during the night. Omission of clear air radiative cooling, horizontal temperature advection, or underestimation of mixing may also contribute to lack of stratification of the modelled residual layer. In future work, clear air radiative cooling will be included, which, unfortunately will reduce the model's current utility as an economic package for large scale models.

## Acknowledgements

We greatfully acknowledge Dr. D. Lenschow for supplying the CABLE data. This material is based upon work supported by the Geophysics Laboratory under contract F19628-88-K-0001 and the Physical Meteorology Program of the National Science Foundation under grant ATM-8912736.

## REFERENCES

André, J. C., G. De Moore, P. Lacarrère, G. Therry, and R. Du Vachat, 1978: Modelling the 24 hr evolution of the mean and turbulent structures of the planetary boundary layer. *J. Atmos. Sci.*, 35, 1861-1883.

André, J. C. and L. Mahrt, 1982: The nocturnal surface inversion and influence of clear-air radiative cooling., *J. Atmos. Sci.*, 39, 864-878.

Arya, S. P. S.. 1975: Buoyancy effects in a horizontal flat-plate boundary layer., *J. Fluid Mech.*. 68. 321-343.

Atlas, D., J. I. Metcalf, J. H. Richter, and E. E. Gossard, 1970: The birth of "CAT" and microscale turbulence. *J. Atmos. Sci.*, 27, 903-913.

Beyrich, F. and B. Klose, 1988: Some aspects of modelling low-level jets. *Bound.-Layer Meteor.*, 43. 1-14.

Blackadar, A. K., 1962: The vertical distribution of wind and turbulent exchange in a neutral atmosphere., *J. Geophys. Res.*, , 67, 3095-3102.

Buajitti, K. and A. K. Blackadar, 1957: The theoretical studies of diurnal wind structure variation in the planetary boundary layer. *Quart. J. Roy. Meteorol. Soc.*, 83, 486-500.

Ek, M. and L. Mahrt, 1990: *A user's guide to OSU1DPBL version 1.0.3: A one-dimensional planetary boundary layer model with interactive soil layers and plant canopy,*, Dept. of Atmos. Sci., Oregon State University, Corvallis, OR 97331.

Estournel, C., R. Vehil, and D. Guedalia, 1986: An observational study of radiative and turbulent cooling in the nocturnal boundary layer (ECLATS EXPERIMENT). *Bound.-Layer Meteor.*. 34. 55-62.

Fernando, H. J. S., 1991a: Turbulent mixing in stratified fluids. *Ann. Rev. Fluid Mech.*. 23, 455-493.

Fernando, H. J. S., 1991b: The growth of a turbulent patch in a stratified fluid. submitted to *J. Fluid Mech.*

Garratt, J. R. and R. A. Brost, 1981: Radiative cooling effects within and above the nocturnal boundary layer. *J. Atmos. Sci.*, 38, 2730-2746.

Garratt, J. R., 1985: The inland boundary layer at low altitudes. *Bound.-Layer Meteor.*, 32, 307-327.

Heck, W. J., H. A. Panofsky, and M. A. Bender, 1977: The effect of clear-air turbulence on a model of the general circulation of the atmosphere. *Beiträge zur Physik der Atm.*, 50, 89-97.

Hsu, S. A., 1979: Mesoscale nocturnal jetlike winds within the planetary boundary layer over a flat, open coast. *Bound.-Layer Meteor.*, **17**, 485-494.

Keller, J. L., 1990: Clear air turbulence as a response to meso- and synoptic-scale dynamic processes. *Mon. Wea. Rev.*, **118**, 2228-2242.

Kennedy, P. J. and M. A. Shapiro, 1975: The energy budget in a clear air turbulence zone as observed by aircraft. *Mon. Wea. Rev.*, **10**, 650-654.

Kennedy, P. J. and M. A. Shapiro, 1980: Further encounters with clear air turbulence in research aircraft., *J. Atmos. Sci.*, **37**, 986-993.

Kondo, J., O. Kanechika, and N. Yasuda, 1978: Heat and momentum transfer under strong stability in the atmospheric surface layer. *J. Atmos. Sci.*, **35**, 1012-1021.

Kurzeja, R. J., S. Berman, and A. H. Weber, 1991: A climatological study of the nocturnal planetary boundary layer. *Bound.-Layer Meteor.*, **54**, 105-128.

Lenschow, D. H., X. S. Li, C. J. Zhu, and B. B. Stankov, 1987: The stably stratified boundary layer over the great plains., *Bound.-Layer Meteor.*, **42**, 95-121.

Louis, J., 1979: A parametric model of vertical eddy fluxes in the atmosphere., *Bound.-Layer Meteor.*, **17**, 187-202.

Louis, J., M. Tiedke, and J. F. Geleyn, 1981: A short history of the operational PBL parameterization at ECMWF. *Workshop on planetary boundary layer parameterization*, ECMWF., 59-79.

Lyons. R., H. A. Panofsky, and S. Wollaston, 1964: The critical Richardson number and its implications for forecast problems. *J. Appl. Meteorol.*, **21**, 369-387.

Mahrt. L., R. C. Heald, D. H. Lenschow, B. B. Stankov, and IB Troen, 1979: An observational study of the structure of the nocturnal boundary layer. *Bound.-Layer Meteor.*, **17**, 247-264.

Mahrt, L., 1985: Vertical structure and turbulence in the very stable boundary layer. *J. Atmos. Sci.*, **42**, 2333-2349.

Mahrt. L., 1987: Grid-averaged surface fluxes. *Mon. Wea. Rev.*, **115**, 1550-1560.

Maryon, R. H., 1990: A statistical representation of sub-grid variation in mixing-length models of the turbulent boundary layer. *Bound.-Layer Meteor.*, **53**, 371-399.

Merrit, G. and G. Rudinger, 1973: Thermal and momentum diffusivity measurements in a turbulent stratified flow. *AIAA J.*, **11**, 1465-1470.

Mizushina, T., F. Ogino, H. Ueda, and S. Komori, 1978: Buoyancy effects on eddy diffusivities in thermally stratified flow in an open channel. *Heat transfer 1978, 1*, 91-96, New York, Hemisphere publishing Co.

Nappo, C. J., 1991: Sporadic breakdowns of stability in the PBL over simple and complex terrain. *Bound.-Layer Meteor.*, **54**, 69-87.

Nieuwstadt, F. T. M., 1984: The turbulent structure of the stable, nocturnal boundary layer., *J. Atmos. Sci.*, **41**, 2202-2216.

NMC Development Division Staff, 1988: Documentation of the research version of the Medium Range Forecast model. NMC Documentation Series #1., Development division, NMC, Washington DC. 20233.

Padman, L., and I. S. F. Jones, 1985: Richardson number statistics in the seasonal thermocline. *J Phys. Oceanogr.*, 15(7), 844-854

Rohr, J. J., E. C. Itsweire, K. N. Helland, and C. W. Van Atta, 1988: Growth and decay of turbulence in a stably stratified shear flow., *J. Fluid Mech.*, **187**, 1-34

Ruscher, P. H., 1987: ***An examination of structure and parameterization of turbulence in the stably-stratified atmospheric boundary layer.***, Ph. D thesis, Oregon State University. 170pp.

Smith, B. and L. Mahrt, 1981: A study of boundary layer adjustments. *J. Atmos. Sci.*, **38**. 334-346.

Stull, R. B., and A. G. M. Driedonks, 1987: Applications of the transilient turbulence parameterization to atmospheric boundary layer simulations., *Bound.-Layer Meteor.*, **40**, 209-239.

Stull, R. B, 1990: ***An introduction to boundary layer meteorology.***, Boston, Kluwer academic publishers, 666pp.

Thorpe, S. A., 1973: Turbulence in stably stratified fluids: A review of laboratory experiments., *Bound.-Layer Meteor.*, 5, 95-119.

Troen, IB and L. Mahrt, 1986: A simple model of the atmospheric boundary layers; sensitivity to surface evaporation., *Bound.-Layer Meteor.*, 37, 129-148.

Webster, C. A. G., 1964: An experimental study of turbulence in a density-stratified shear flow. *Fluid Mech.*, 19, 221-245.

Wittich, K.-P., and R. Roth, 1984: A case study of nocturnal wind and temperature profiles over the inhomogeneous terrain of Northern Germany with some considerations of turbulent fluxes. *Bound.-Layer Meteor.*, 28, 169-186.

## Figure legends

Fig. 1 Cross-section of CABLE observational regions for (a) 5 May 1983 and (b) 24 May 1983 including clear air turbulence (shaded), isentropes in 1 deg C intervals (solid lines), the PBL top (dashed line), aircraft flight paths (slant solid lines), and the direction of the mean flow (thick arrows). Height is with respect to sea level.

Fig. 2 Vertical profiles of variance of high-pass filtered vertical velocity (solid line), heat flux × 100 (short dashed line), and potential temperature (long dashed line) observed on 24 May CABLE. Height is with respect to sea level. The computed heat flux in the upper boundary layer was noisy due to sampling problems and omitted from the figure.

Fig. 3 Mixing length and the least square fit given by (5) and (6) with $\ell_{0,h} = 52.5$ m.

Fig. 4 Eddy Prandtl numbers and least-square fit (8) with $Pr_0 = 1.5$ (solid line) and $Pr_0 = 1.0$ (dashed line).

Fig. 5 Nondimensional functions of $Ri$ from (6), the Louis model (9*a*), and NMC model (9*b*).

Fig. 6 $Pr$ estimated from (8), Louis model, and NMC model. $Pr_0 = 1$ is forced for (8) and Louis model.

Fig. 7 Profiles of $\theta$ (dashed line) and turbulence kinetic energy (solid line) observed at 0640 on 7 May in SESAME (after Lenschow *et al.* 1987).

Fig. 8 Model-estimated vertical profiles at 0500 LST for (a) $u$ (solid line) and $\theta$ (dashed line); (b) $K_h$ with free atmospheric mixing.

Fig. 9 Model-estimated vertical profiles at 0500 LST for (a) $K_h$ and (b) $u$ with $U_g = 5$ m/s with (dashed lines) and without (solid lines) local generation in the upper part of the stable boundary layer.

Fig. 10 Vertical profiles at 0500 LST for (a) $u$ and (b) $\theta$ simulated with (dashed lines) and without (solid lines) local generation in the stable boundary layer when geostrophic wind shear is included.

Fig. 11 Vertical profiles of (a) $u$ and (b) $\theta$ with (dashed line) and without (solid line) of subsidence.

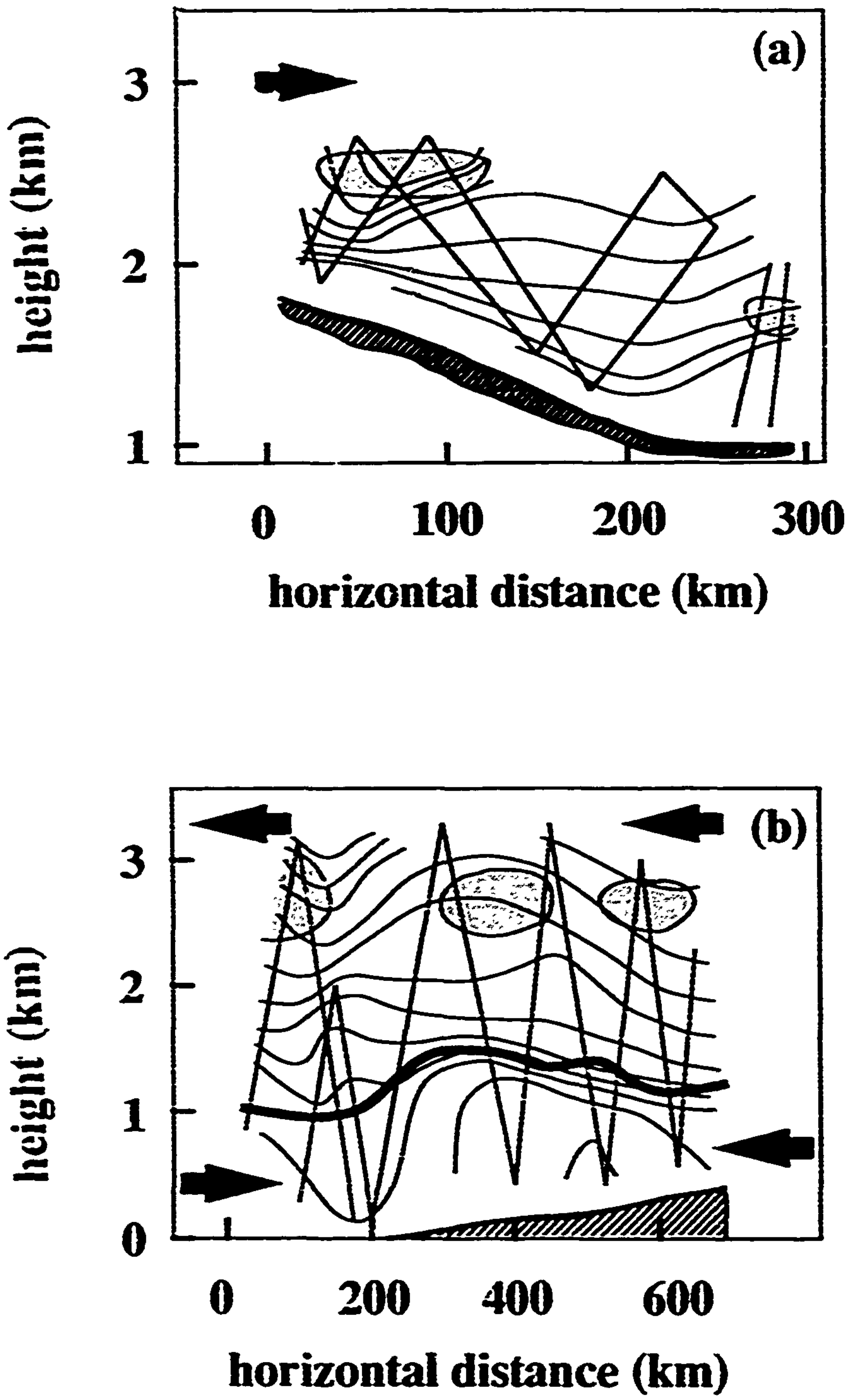
(a)
height (km)
horizontal distance (km)
(b)
height (km)
horizontal distance (km)

Fig. 1

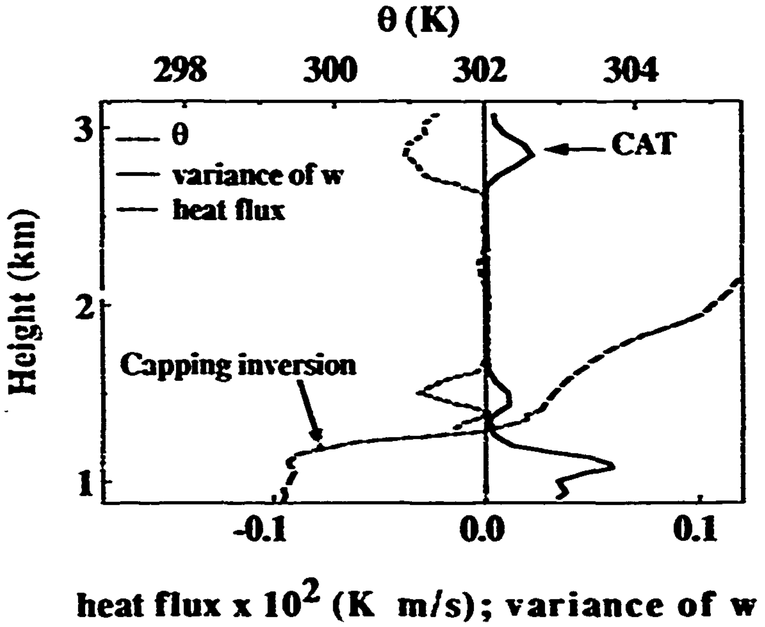
θ (K)
298
300
302
304
— θ
— variance of w
— heat flux
CAT
Capping inversion
Height (km)
3
2
1
-0.1
0.0
0.1
heat flux x 10² (K m/s); variance of w

Fig. 2

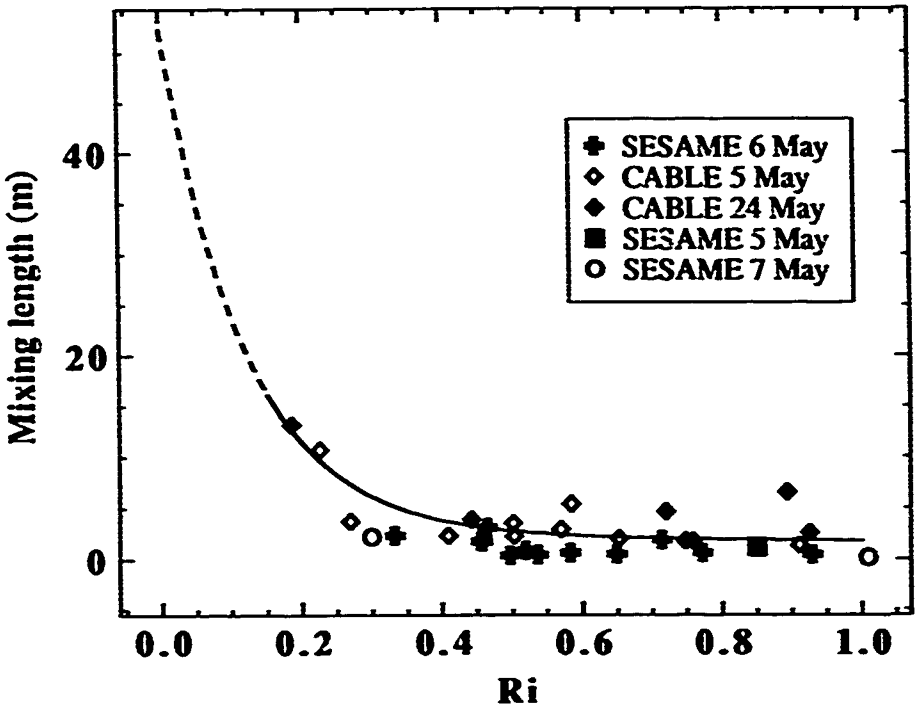

SESAME 6 May
CABLE 5 May
CABLE 24 May
SESAME 5 May
SESAME 7 May
Mixing length (m)
40
20
0
0.0
0.2
0.4
0.6
0.8
1.0
Ri

Fig. 3

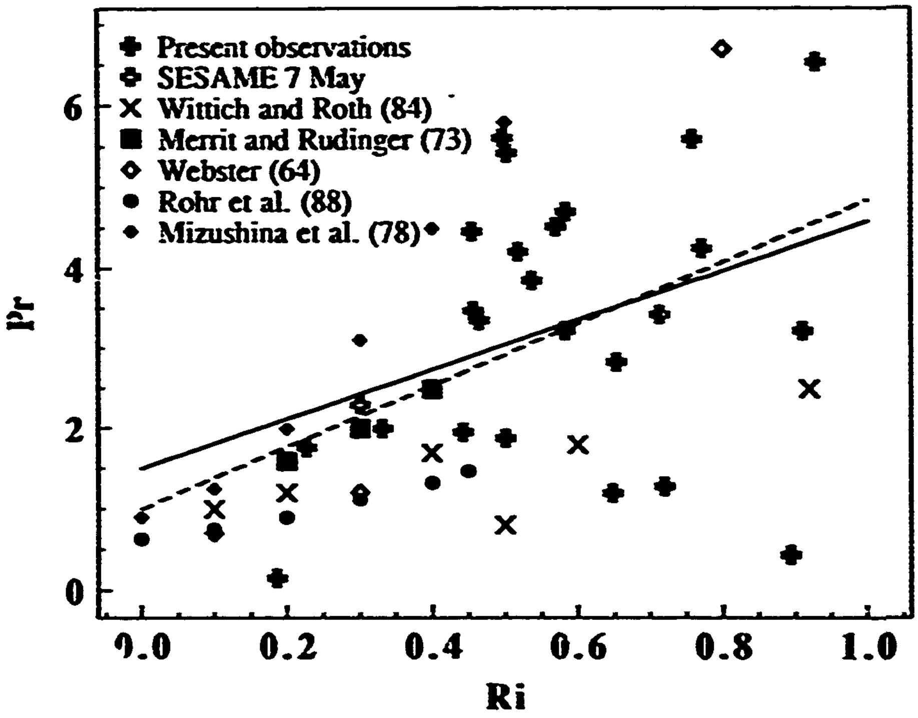

Present observations
SESAME 7 May
Wittich and Roth (84)
Merrit and Rudinger (73)
Webster (64)
Rohr et al. (88)
Mizushina et al. (78)
Pr
6
4
2
0
0.0
0.2
0.4
0.6
0.8
1.0
Ri

Fig. 4

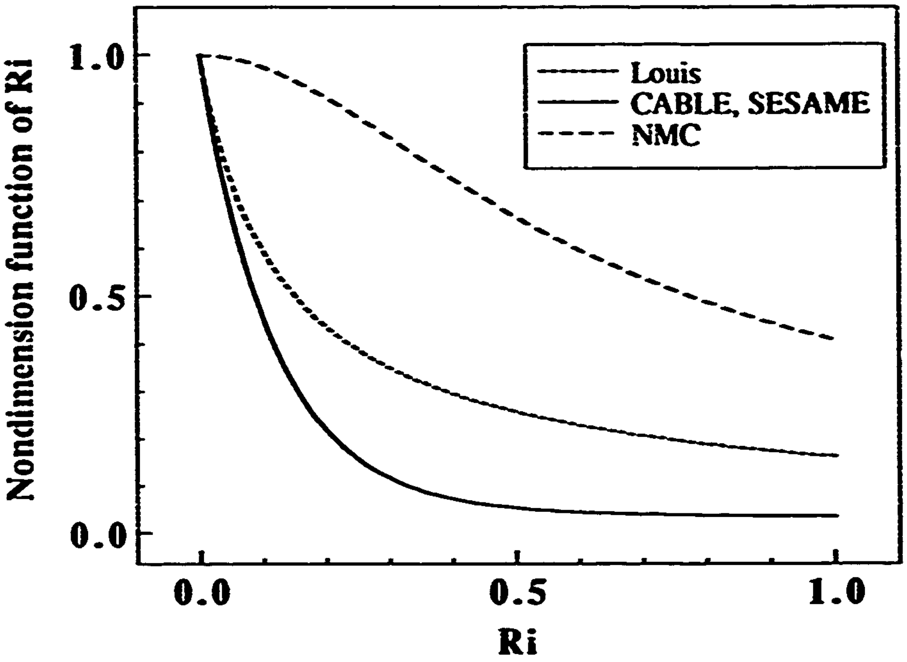

Nondimension function of Ri
1.0
0.5
0.0
0.0
0.5
1.0
Ri
Louis
CABLE, SESAME
NMC

Fig. 5

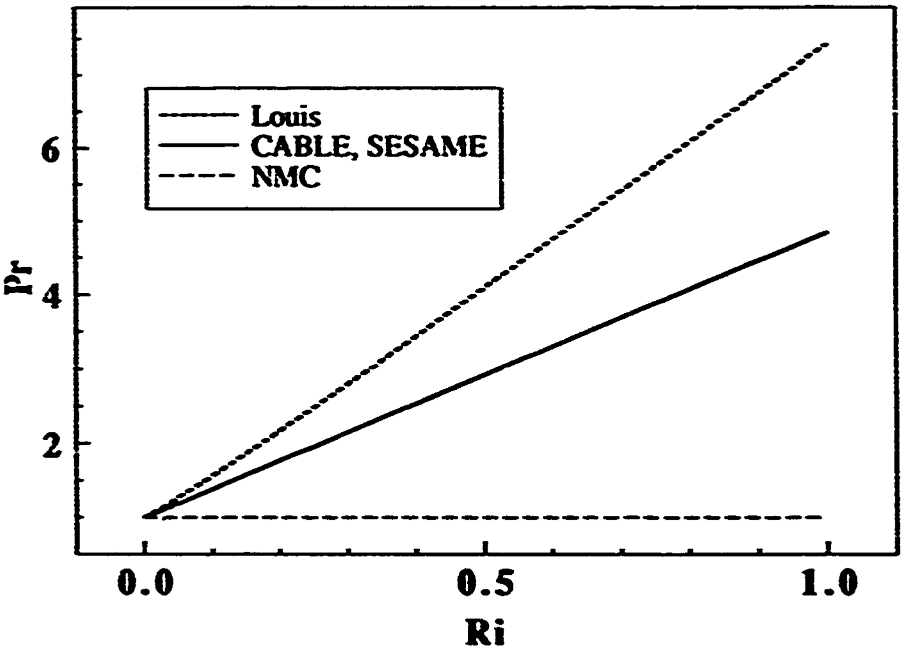

Pr
6
4
2
0.0
0.5
1.0
Ri
Louis
CABLE, SESAME
NMC

Fig. 6

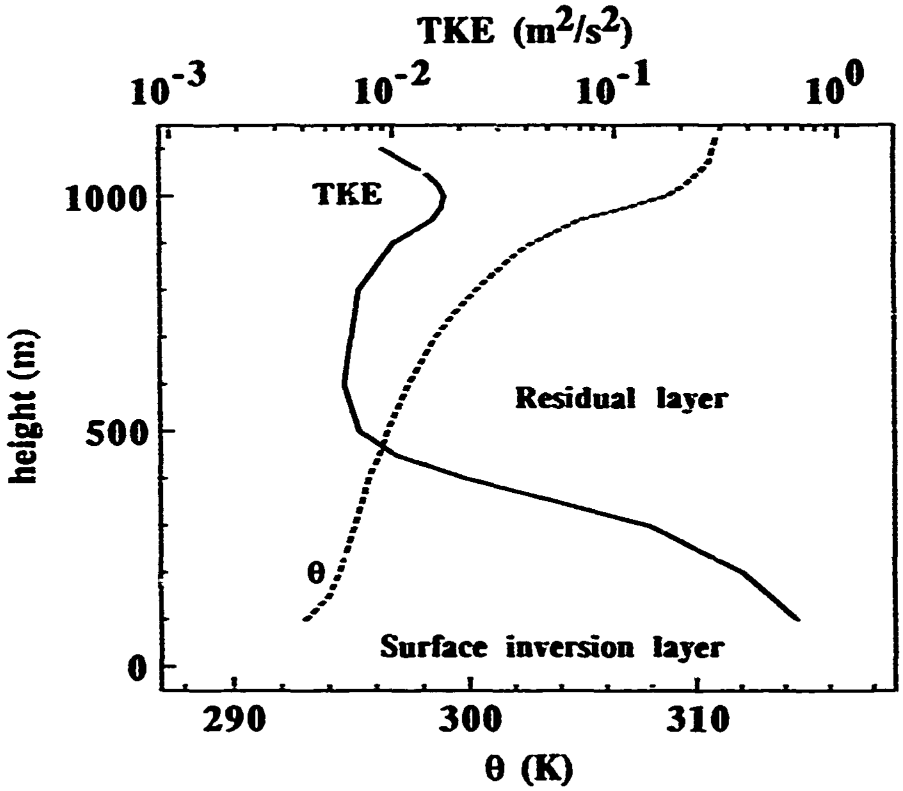
TKE (m²/s²)
10⁻³
10⁻²
10⁻¹
10⁰
1000
500
0
height (m)
TKE
θ
Residual layer
Surface inversion layer
290
300
310
θ (K)

Fig. 7

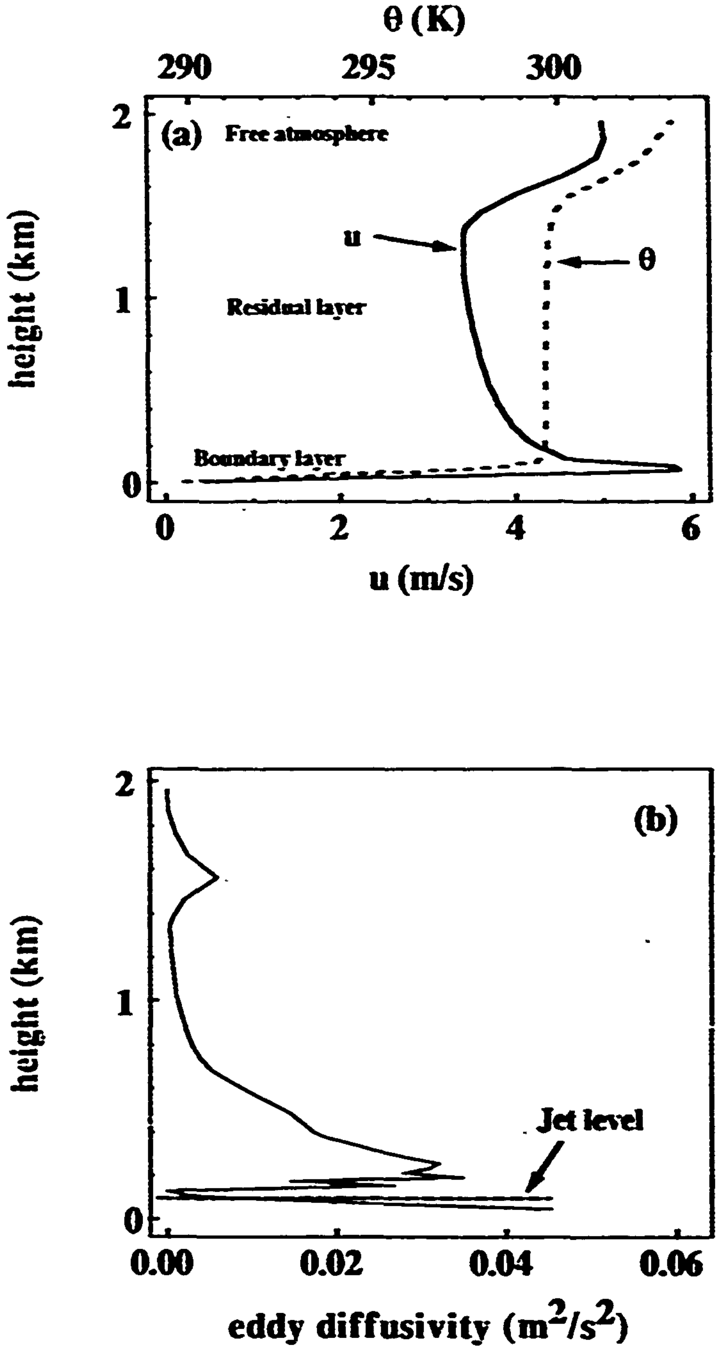
θ (K)
290
295
300
(a)
Free atmosphere
u
θ
Residual layer
Boundary layer
height (km)
2
1
0
0
2
4
6
u (m/s)
(b)
Jet level
height (km)
2
1
0
0.00
0.02
0.04
0.06
eddy diffusivity (m²/s²)

Fig. 8

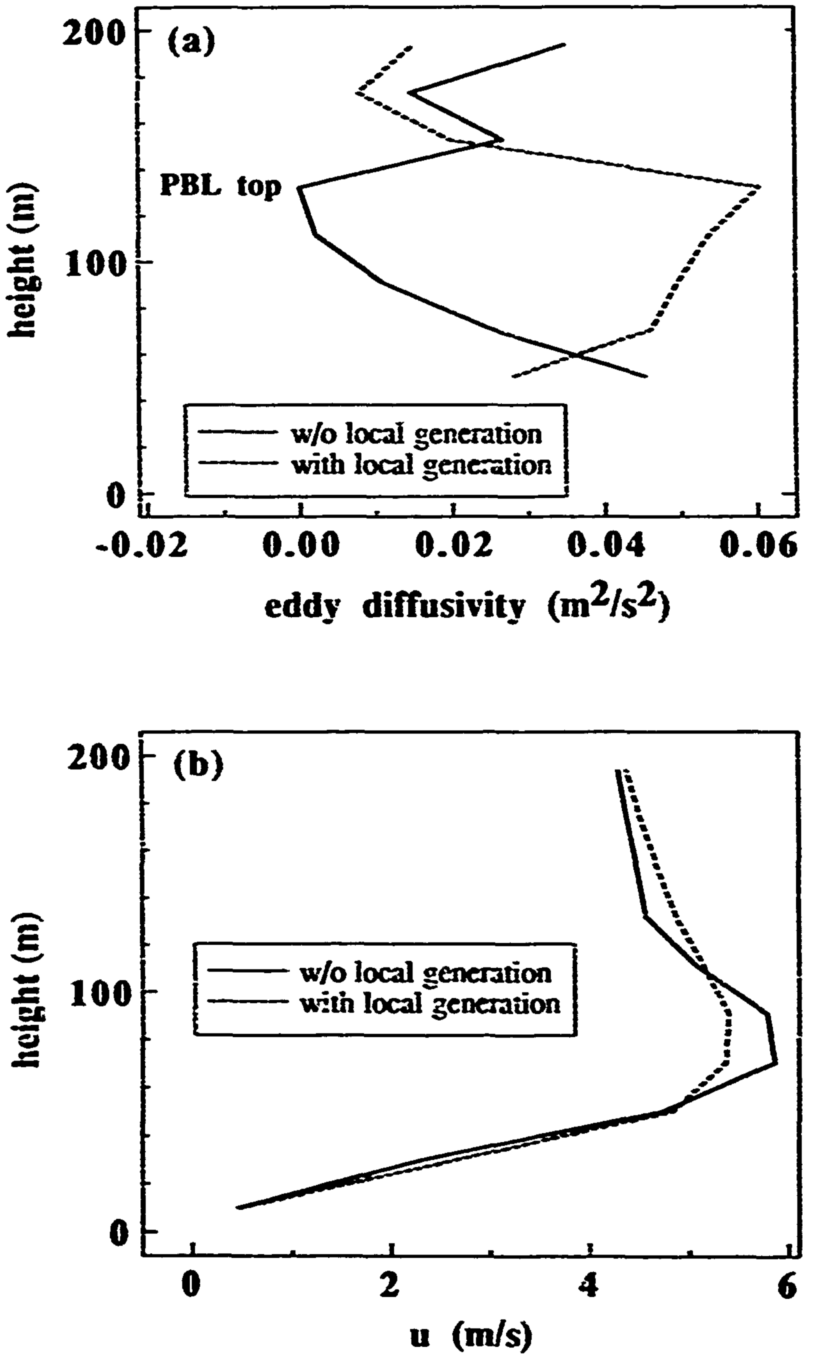
(a)
PBL top
w/o local generation
with local generation
height (m)
200
100
0
-0.02
0.00
0.02
0.04
0.06
eddy diffusivity ($m^2/s^2$)
(b)
w/o local generation
with local generation
height (m)
200
100
0
0
2
4
6
u (m/s)

Fig. 9

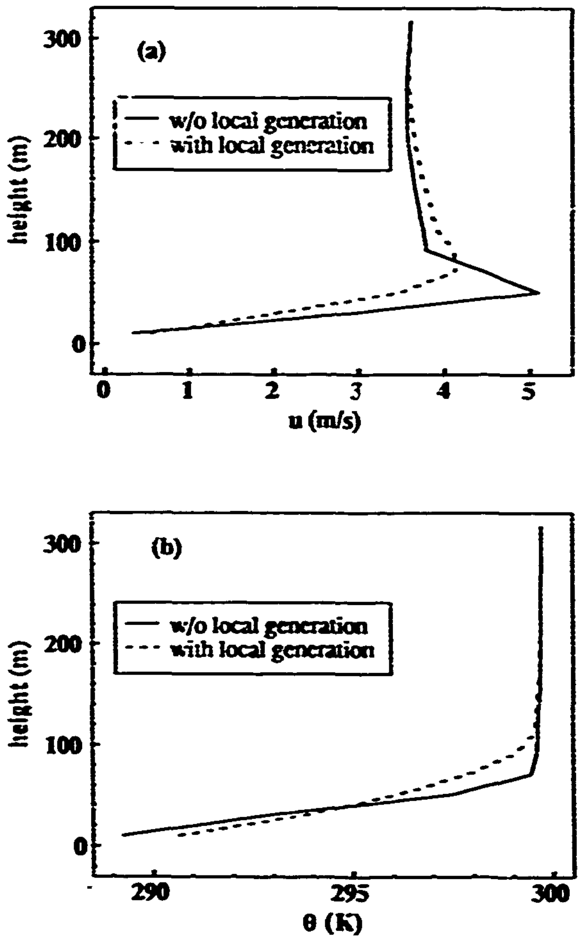
(a)
w/o local generation
with local generation
height (m)
300
200
100
0
0
1
2
3
4
5
u (m/s)
(b)
w/o local generation
with local generation
height (m)
300
200
100
0
290
295
300
θ (K)

Fig. 10

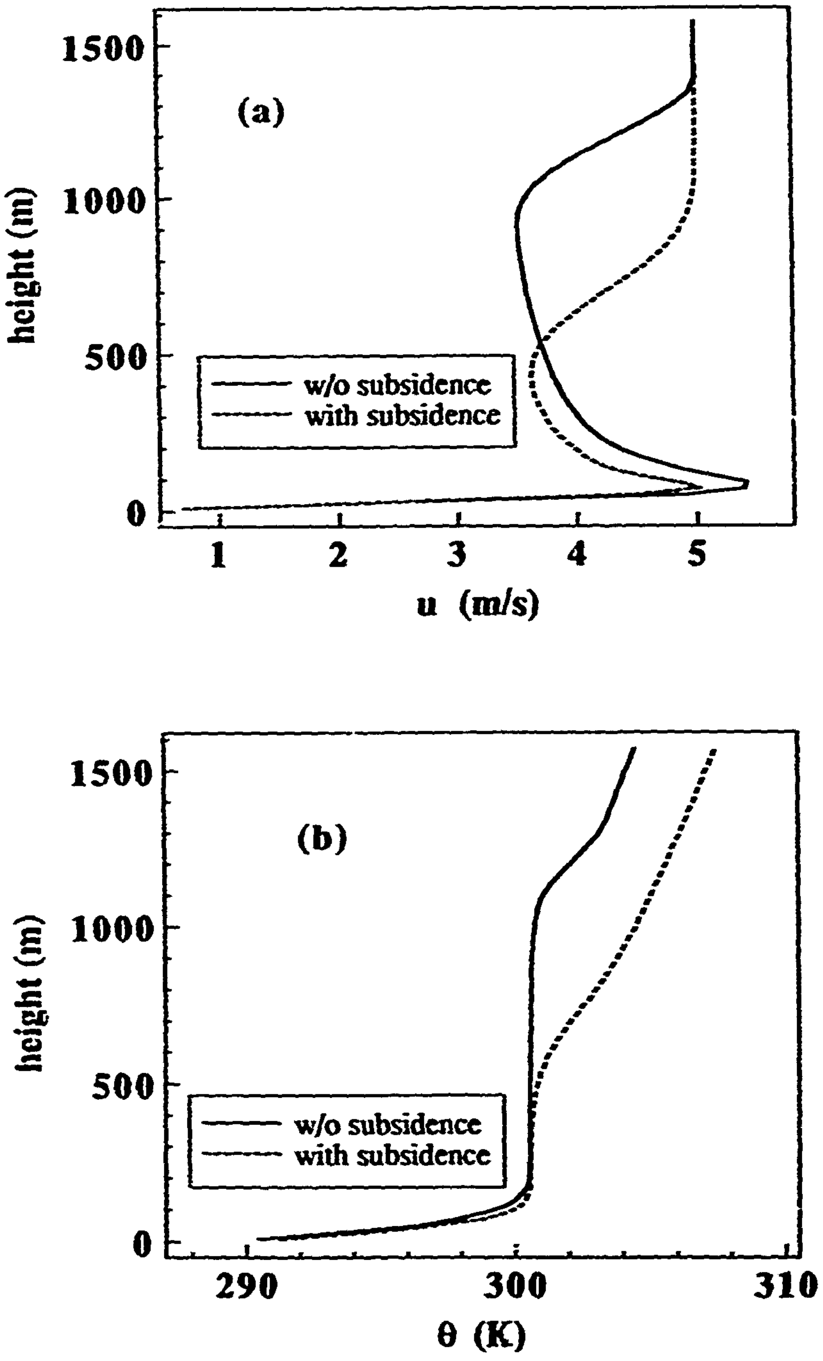
(a)
height (m)
1500
1000
500
0
w/o subsidence
with subsidence
1
2
3
4
5
u (m/s)
(b)
height (m)
1500
1000
500
0
w/o subsidence
with subsidence
290
300
310
θ (K)

Fig. 11

Chapter 3.1

# Boundary-Layer Moisture Regimes

## 3.1.1. INTRODUCTION

Heat and moisture fluxes are normally modelled with the same exchange coefficients. The transfer processes for these two quantities are similar to each other when compared to momentum transport which involves pressure fluctuations (e.g., Garratt and Hicks, 1973). In addition, moisture fluctuations are vulnerable to measurement problems (e.g., Dyer et al. 1983) making distinction between moisture and heat transport tenuous. However certain aspects of transport and organization of moisture in the boundary layer are observed to be distinctly different from that for heat. For example, in the convective boundary layer, Isaka and Guillemet (1983) observe somewhat larger values of the dissipation time scale for moisture fluctuations compared to that for temperature fluctuations. As a second example, Brutsaert (1982) and Brutseart and Kustas (1985) have suggested the need to distinguish between the roughness height for moisture from that of heat.

The most studied aspect of boundary-layer moisture structure is that specific humidity is often not well mixed even when potential temperature is well mixed (Donelan and Miyake, 1973; Betts, 1976; LeMone and Pennell 1976; Johnson 1977; Nicholls and Readings 1979; Nicholls and LeMone 1980; Lenschow et al. 1980; and others). Mahrt (1976) noted that the entrainment moisture flux at the top of the boundary layer acts to dry the boundary layer while moisture fluxes at the surface acts to moisten the boundary layer, thus creating a vertical gradient of moisture which survives mixing in some circumstances. This generation of gradients is in contrast to the case for heat where both the surface flux and the entrainment flux act to warm the boundary layer.

A systematic study of the dependence of the vertical gradient of moisture or scalars on boundary layer scaling variables can be found in André et al. (1979), Mahrt and André (1983), Driedonks and Tennekes (1984) and Kustas and Brutsaert (1987). Kustas and Brutsaert (1987) find that the rate of dry air entrainment controls the vertical gradient of moisture. The fundamental difference between downward mixing from the top and upward mixing from the bottom has been exploited by Wyngaard (1984) and Wyngaard and Brost (1984) in order to model the vertical gradient of passive scalars in the mixed layer.

With sufficiently strong downward mixing of dryer air, the moisture skewness can become negative in the lower part of the boundary layer, even though the skewness of temperature and vertical motion remain positive due to warm moist updrafts (Druilhet et al. 1983). The moisture skewness is just one of several features of boundary layer moisture statistics which varies substantially between boundary layers with different bulk stability, growth rates and surface energy regimes. These features are the subject of Sections 3-6.

Then in Section 7, we study systematic variations of moisture on scales of 10 km and greater. Nicholls and LeMone (1980) found that both larger scale moisture and temperature perturbations seem to have a long lifetime. They allude to large eddy motion and associated downward transport of warm dry air as one possible cause. Further studies by Barnes et al. (1980) and LeMone and Meitin (1984) found organized moisture structure associated with two-dimensional "flat rolls" characterized by horizontal spacing of 10-15 km and aspect ratios of 25: 1 or greater. These flat rolls may be associated with interaction of tropospheric gravity waves with the boundary layer (LeMone, 1989) as in the modelling study of Clark et al. (1986). Motions of a comparable scale are operating in the present study although moisture variations also seem to be influenced by surface inhomogeneity on scales of tens of kilometers and larger as in Malhouf et al. (1987); Segal et al. (1988) and Pinty et al. (1989).

## 3.1.2. THE DATA

The present study focuses on data from the Hydrological and Atmospheric Pilot Experiment (HAPEX) conducted in Southwest France (André et al. 1988: Pinty et al. 1989; Noilhan and Planton, 1989). The HAPEX data (Table 1) are particular useful for moisture studies because extra attention was devoted to the calibration of the sensors and examination of errors in the moisture flux (e.g., Eloranta et al. 1989). Two separate Lyman Alpha hydrometers were flown along with a dew point hygrometer. Independent calibration procedures were carried out before and after each flight.

We begin with two days, each consisting of 6 flights, 120 km long at an elevation of approximately 150 m above a relatively uniform pine forest referred to as Landes. This data set contains one of the largest sample sizes ever accumulated by low-level aircraft flights over relatively homogeneous land surfaces with approximately stationary conditions thus allowing statistical examination of turbulence and some mesoscale motions. The inhomogeneity is limited mainly to occasional clearings in the pine forest whose widths normally appear to be comparable to or smaller than the scale of the main boundary-layer eddies. The forest consists primarily of one species of pine, albeit of varying tree height and some variation of the understory vegetation. The soil type is sandy and relatively uniform compared to typical land sites. The sum of the aircraft-measured latent and sensible heat fluxes is in agreement with the energy available from net radiation as measured at the surface. The other HAPEX days analyzed in this study (Table 1) consist of flight legs over rolling terrain, mixed farmland and part of the pine forest with both north-south and east-west legs. These legs cover a variety of boundary-layer conditions but are characterized by greater sampling problems.

## Table 1. AIRCRAFT FLIGHTS

| Program | Legs | Length | Height | Dir. | Location | Weather |
|---|---|---|---|---|---|---|
| HAPEX | | (km) | (m) | | | |
| 19 May | 6 | 120 | 125 | EW | flat pine forest | Cu < 10% |
| 25 May | 6 | 120 | 160 | EW | flat pine forest | Cu < 10% |
| 13 June | 7 | 40 | 100 | | rolling, mixed | 10% Cu, windy |
| 19 June | 8 | 40 | 100 | | rolling, mixed | clear |
| 22 June | 9 | 40 | 100 | | rolling, mixed | <10% Cu, windy |
| 1 July | 10 | 40 | 100 | | rolling, mixed | vrble Sc |
| FIFE | | | | | | |
| 6 June | 6 | 30 | 100 | EW | hilly grassland<br>Konza Prairie | clear, windy |

A second data set consists of six low level east-west flights above the Konza Prairie in central Kansas, USA carried out during FIFE (First ISLSCP Field Experiment, Sellers et al. 1988). Here the 100 m wind is 11-12 m/s from the south southwest so that most of the shear is directed perpendicular to the flight path. On this day, the surface evapotranspiration is quite large and the surface heating is weak due to wet soil conditions and little stomatal control in the prairie plant community.

Fluctuating and mean quantities for both data sets are computed using the 2-pole Tangent-Butterworth filter with a 5 km wavelength. The choice of the filter length is based on the cospectra of temperature and vertical velocity in order to capture most of the turbulent heat flux.

## 3.1.3. MOISTURE REGIMES

To classify boundary layers in terms of surface fluxes, we define a phase space in terms of the Bowen ratio and the boundary-layer stability parameter -h/L where L is the Obukhov length and h is the boundary-layer depth. The boundary-layer depth is determined from vertical profiles of aircraft measured moisture, temperature and variance of vertical velocity. The Bowen ratio describes the partitioning of the surface energy budget into sensible and latent fluxes while the stability parameter -h/L is roughly proportional to the ratio of buoyancy-generation of turbulence kinetic energy to the shear-generation of turbulence kinetic energy.

In order to help classify different types of boundary layers, four limiting regimes are defined by the Bowen ratio-stability phase space for the heated boundary layer with surface evaporation (main upper right quadrant of Figure 1):

I) Relatively large Bowen ratio of unity or greater and large -h/L, greater than 20 or 30, imply large surface heating and weak surface evaporation and weak winds. Some of the HAPEX data on 13 June and 1 July fall into this category (Figure 1b). Another example is urban centers on sunny days with weak winds (Ching, 1985).

II) Large Bowen ratio and weak boundary-layer instability (small -h/L) implies dry windy conditions. Buoyancy-generation of turbulence kinetic energy is unimportant compared to large shear-generation but is important in the surface energy balance compared to the very weak evaporation. Some of the data for HAPEX 13 June approach such conditions.

III) Small Bowen ratio and small -h/L correspond to moist, windy conditions where surface evaporation is promoted by shear-generated turbulence and leads to weak surface heating. The FIFE data fall into this category as do many maritime examples including Donelan and Miyake (1973), Brost et al. (1982), Grant (1986), and Holt and Raman (1986)

IV) Small Bowen ratio and large -h/L corresponds to weak winds and strong surface evaporation. In this regime, the heat flux term in the surface energy balance is small compared to the latent heat flux term. Yet, the buoyancy-generation of turbulence is large compared to the weak shear-generation. Calm conditions over warm water would be included in this class. The tropical maritime boundary layer examined by Nicholls and LeMone (1980) is an example approaching such conditions.

V). This regime in Figure 1a corresponds to upward heat flux and downward moisture flux implying surface condensation and countergradient moisture flux and is not expected to occur except in transient conditions.

VI). The case of upward moisture flux and downward heat flux can occur in the early evening boundary layer over land with fair weather conditions. This case also occurs with cloudy,windy, wet conditions where the surface evaporation exceeds the incoming net radiation. Another example is the flow of warm air over a cooler wet surface which in weak form can occur climatically over ocean surfaces in summer (Esbensen and Reynolds, 1981).

VII). Downward heat flux and downward moisture flux includes the common case of dew formation induced by nocturnal radiational cooling at the surface.

Most boundary-layer situations probably correspond to an intermediate hybrid of these regimes. For example, the Bowen ratio is typically between 0.4 and 0.8 over temperate forests and grasslands (Oke, 1987). While there is no precise numerical definition to categorize different observed boundary layers, the asymptotic regimes discussed above and the phase space in Figure 1a help organize the different data sets. No cases include very small Bowen ratios where moisture fluctuations dominate the buoyancy even in the lower boundary layer (e.g., Greenhut and Khalsa,1982). In the derivations below, we therefore neglect the differences between the surface heat flux and the surface virtual heat flux although the results can be generalized to include such differences. We also neglect the influence of boundary-layer clouds. Even with such restrictions, the numerical values of Bowen ratio and instability parameter -h/L do not completely describe the flow regime. For example, HAPEX 22 June and FIFE cases are characterized by comparable values of the Bowen ratio and -h/L; however, the fluxes are much weaker on 22 June.

For fixed incoming solar radiation, increasing magnitude of the stability parameter -h/L corresponds to increasing Bowen ratio. That is, less evapotranspiration corresponds to greater sensible heat flux and thus greater instability. This is the tendency for those data sets in Figure 1b which represent primarily sunny conditions. For such days, we can simplify the boundary-layer classification scheme by defining a nondimensional number with isolines that are parallel to the dashed line of Figure 1a. Such a nondimensional number would distinguish between calm wet and windy dry conditions. *Physically such a nondimensional number will combine the constraints of the turbulence energy budget and the surface energy balance.*

We formally develop this combination by beginning with the following simplified form of the surface energy balance

$$E = R_{net} - H \qquad (1)$$

$$H = \rho\, c_p\, [w'\theta']$$

where E is the rate of surface evapotranspiration (Watts $m^{-2}$), H is the heat flux to the atmosphere and $R_{net}$ is the net surface radiation gained at the surface which can be adjusted to include heat flux into the ground, $\rho$ is the averaged value for density, $c_p$ is the specific heat of dry air, primes refer to fluctuating quantities and the bracket refers to an averaging operator.

The simplest possible statement of the turbulence energy budget would be to specify a value of the flux Richardson number

$$R_f = (g/\Theta)\, [w'\theta']/\{[w'v']\text{-}dV/dz\} \qquad (2)$$

which is the ratio of buoyancy-production of turbulence kinetic energy to the shear-production of turbulence kinetic energy where **V** is the horizontal wind vector and $\Theta$ a scale value for the potential temperature.

Solving for the heat flux from (1) and substituting into (2), we obtain the following *moisture energy ratio*

$$M = E/S = -\, R_f + R_{net}/S \qquad (3)$$

where

$$S = [w'V']\text{-}\{d[V]/dz\}\ \rho\, c_p/(g/\Theta)$$

Large values of the moisture energy ratio M correspond to calm wet conditions and small values correspond to windy dry conditions.

For instructive purposes, (3) can be solved for $R_f$, the flux Richardson number at the surface, in which case the moisture energy ratio M represents the relative influence of surface evaporation on the stability through reduction of surface heating. The remaining term, $R_{net}/S$, is proportional to the ratio of the first term of the Penman relationship (radiation term) to the second term of the Penman relationship (so-called advective or aerodynamic term). This term therefore represents the relative importance of evaporation due to net radiational heating relative to the wind-induced evaporation. With large values of this term, the aerodynamic term can be neglected and the Priestley-Taylor model should be a good approximation to the Penman relationship[1]. In other words, the coefficient of the Priestley-Taylor approximation (Priestley and Taylor, 1972) is most likely to require the least adjustment when the moisture energy ratio is large (calm, wet). A more detailed classification scheme based on the Penman equation (Penman, 1948) can be found in Mahrt and Ek (1984). Relating S to the wind speed, the second term in (3) leads to the radiation Richardson number used by Mahrt and Ek (1984) to characterize stability in cases where fluxes are not known.

---

[1] As a short digression, we can instead divide the surface energy balance (1) by the net radiation and obtain

$$E/R_{net} = -H/R_{net} + 1$$

This particular moisture energy ratio is proportional to the nondimensional coefficient $\alpha$ in the Priestley-Taylor model of surface evaporation.

---

Assuming the shear-generation to be proportional to $u_*^3/h$ and introducing the Bowen ratio into (3), the moisture energy ratio can be redefined as

$$\mathbf{M = (-h/L)/\beta} \qquad \mathbf{(4)}$$

where L is the Obukhov length and $u_*$ is the surface friction velocity. *Therefore, the moisture energy ratio can also be interpreted as the boundary-layer stability parameter -h/L divided by the Bowen ratio β.* The HAPEX 13 June case (Table 2) includes some of the smallest values of the moisture energy ratio (10-20) for the present data sets due to windy conditions and only modest evapotranspiration. Even smaller values can be expected in dry windy conditions, perhaps O(1). In fact, small values of M can even be computed from some maritime data sets by using data from Brost et al. (1982), Grant (1986) and Holt and Raman (1986) where winds are significant yet evaporation is small compared to the summertime evaporation over unstressed land surfaces.

HAPEX 19 June is characterized by the largest values of the moisture energy ratio systematically exceeding 100 due to large evapotranspiration and weak winds. Even larger values, exceeding 500, can be computed from the maritime tropical data of Nicholls and LeMone (1980) where significant evaporation occurs with weak winds. The above calculations and Table 2 indicate that the present data sets represent quite different situations but do not cover the realizable sections of the phase space in Figure 1. In the next section, a complementary moisture parameter arises from a relationship for the decay of moisture fluctuations.

### 3.1.4. MOISTURE MEMORY

The data analysis of Sections 5-7 will indicate that the moisture statistics of some boundary layers are strongly influenced by pockets of dry air near the surface with observed widths typically 500 - 1000 m. This dry air at the surface appears to have moisture contents similar to values near the top of the boundary layer but not as dry as air just above the boundary layer. Examples are shown in Figure 2 from HAPEX flights over the pine forest on 19 May. Conditional sampling and compositing indicate that such dry air pockets are statistically associated with sinking cooler air with horizontal divergence. However, the correlation is not strong and the joint frequency distributions (not shown) indicate that dry air fluctuations are often associated with only weak perturbations of temperature and vertical velocity. Under certain conditions, such dry air near the surface appears to survive longer than associated perturbations of vertical velocity and temperature.

To investigate the possibility of longer memory of the moisture perturbations, we define the time scales of the decay of near surface moisture and temperature perturbations as

$$\tau_q = \delta q / \{[w'q']/d\} \qquad (5)$$

$$\tau_\theta = \delta\theta / \{[w'\theta']/d\} \qquad (6)$$

where $\delta q$ and $\delta\theta$ are the initial amplitudes of the perturbations, d is the depth of the perturbations and square brackets indicate averaging of surface fluxes over a larger scale. Here we neglect clear air radiative cooling and feedback of the perturbation flow on the local surface fluxes. This zero order scale argument simply assumes that with weak surface moisture flux, dry air pockets near the surface will retain their moisture deficit for a longer period.

Using the definition of the Bowen ratio for near surface fluxes, the ratio of these two time scales can be written as

$$\tau_q/\tau_\theta = (\delta q/\delta\theta)\ \beta/v \qquad (7)$$

where v is the psychrometric constant. With large Bowen ratio and thus relatively small surface moisture fluxes, the moisture perturbations will survive longer and serve as a tracer or historical indicator for previous circulations.

To interpret (7), consider dry air near the surface originally associated with dry downdrafts of large boundary-layer eddies (Nicholls and LeMone, 1980). The downdrafts upon reaching the warm moist lower part of the boundary layer, are frequently dryer but not warmer than the surrounding warm moist updrafts. This augmentation of the ratio $\delta q/\delta\theta$ has been noticed by Nicholls (1978) and others and seems to also occur in the observations of of this study (Sections 5-6). The dry air is modified but not eliminated by horizontal diffusion because the downdrafts are relatively broad and the small scale turbulence within the downdrafts is relatively weak.

In contrast to the convectively unstable boundary layer with weak winds, significant shear-generation of turbulence in the windy boundary layer apparently leads to mixing on smaller scales rather than boundary-layer scale updrafts and downdrafts. Then the downward transport may require a series of shear-generated overturning events and dry air no longer reaches the surface without major modification. Dry air still reaches the surface but is strongly modified.

If $(\delta q/\delta\theta)$ is proportional to the instability of the boundary layer (large -h/L), then the ratio of time scales (7) becomes proportional to

$$\tau_q/\tau_\theta \sim (-h/L)\ \beta = D^* \qquad (8)$$

This proportionality is only plausible speculation. As circumstantial evidence, Isaka and Guillemet (1983) found the time scale for dissipation for moisture fluctuations to be somewhat larger than the time scale for dissipation of temperature fluctuations in the convective boundary layer. However, the relation between the dissipation time scale and the survival time of larger scale moisture perturbations are not known.

Alternatively, D* can be simply considered as a nondimensional combination of the main parameters which is complementary to the moisture energy ratio (4). Large values of D* correspond to the upper right hand corner of Figure 1a and represent dry free convection while small values of D* represent wet windy conditions. We will refer to D* as a *flux dryness parameter*.

While the above loose arguments provide motivation for using D* to help classify different boundary-layer moisture regimes, a more complete consideration of the moisture fluctuations would directly include the influence of dry air entrainment. We first proceed to examine the relationship between the observed moisture fluctuations and the flux dryness parameter.

As a statistical measure of the occurrence of occasional dry air pockets, we employ the skewness of the fluctuating specific humidity q

$$S_q = [q^3]/[q^2]^{3/2} \qquad (9)$$

where the square brackets indicate simple averaging over the record. Normally, one expects moisture, temperature and vertical velocity fluctuations to be positively skewed due to the influence of narrow, warm, moist updrafts and wider, cool, dry downdrafts. Indeed, temperature and vertical motion are positively skewed for all of the data sets examined here (Table 2). However, the skewness of specific humidity may be positive or negative. Although interpretation of skewness is complex, negative moisture skewness is generally associated with occasional pockets of dry air such as shown in Figure 2

The largest systematic negative values of the moisture skewness occur on HAPEX 19 and 25 May (Table 2, Figure 3) when the flux dryness parameter D* (Eq. 4) is relatively large due to significant surface heating and only modest wind speed and evapotranspiration. The largest systematic positive values skewness occur for the FIFE legs where D* is small due to windy conditions with a relatively moist surface.

For the remaining HAPEX days, the scatter in the skewness-D* relationship is large partly because of shorter, more inhomogeneous, flight legs. The scatter may also be due to the incompleteness of D* which attempts to describe only the survivability of moisture fluctuations and does not contain information on the generation of dry air fluctuations due to entrainment. For example, the flux dryness parameter is large on 1 July, but entrainment-drying and negative moisture skewness do not develop because the air above the boundary layer is moist. The role of dry air entrainment is discussed in Sections 5-6.

A study of the scale dependence of moisture skewness indicates the largest negative values occur on scales between about 400 m and 1100 m which probably corresponds to the cores of the driest air. Even with such conditions, positive moisture skewness sometimes still occurs on scales of 100 m and smaller which probably corresponds to the cores of the moistest updrafts.

### 3.1.5. ENTRAINMENT DRYING BOUNDARY LAYER

Attempts to numerically estimate the moisture flux at the boundary-layer top are made difficult by strong height dependence of the moisture flux with respect to the spatially varying boundary-layer top. In addition, the flux is carried by a larger range of scales compared to the range of scales at surface. This situation at the boundary-layer top leads to both sampling problems and sensitivity to the filter cutoff wavelength. By averaging flux values from two or more available flights near the boundary-layer top for each day, we have been able to establish a rough estimate of $R_q$, the ratio of the moisture flux at the boundary-layer top to the value at the surface. However, these values are quite tentative because the upper level fluxes normally represent a level several hundred meters below the flight level and do not cover exactly the same period as the near surface flights. Finally, Table 3 shows values of the decrease of specific humidity across the inversion subjectively estimated from aircraft soundings. This value is sometimes sensitive to the way in which the sounding is interpreted. For example, the large vertical gradient at the boundary-layer top sometimes extends into the upper boundary layer. As another example, inspection of records near the boundary-layer top in FIFE indicate that the driest entrained air is much moister than predicted by the value of $\Delta q$ reported in Table 3 Apparently, the air is entrained only from the lower part of the capping inversion layer.

Table 3. The value of dq (g/Kg), the three hour change of low level mean specific humidity; $R_q$, the ratio of the averaged values for the moisture flux near the top of the boundary layer to the flux near the surface; $S_q$, the moisture skewness and $\Delta q$ (g/Kg), a rough estimate of the decrease of specific humidity across the capping inversion.

| Data Set | | dq | $R_q$ | $S_q$ | Δq |
|---|---|---|---|---|---|
| FIFE | 8 Jun 87 | 0.2 | 0.3 | 1.2 | 5.0 |
| HAPEX | | | | | |
| | 13 Jun 86 | 0.2 | 0.7 | 1.0 | 1.0 |
| | 19 Jun 86 | -0.1 | 1.2 | -0.7 | 4.0 |
| | 22 Jun 86 | -2.5 | 1.5 | -0.4 | 3.5 |
| | 1 July 86 | 1.5 | 0.4 | 0.8 | 0.0 |

We now attempt to establish a qualitative relationship between the sign of the vertical divergence of the moisture flux, the mean moisture tendency and the moisture skewness. Of the four HAPEX research days where fluxes are available in the upper part of the boundary layer, only the late morning periods on 19 and 22 June HAPEX are characterized by negative moisture skewness (Table 3). These two periods correspond to an *increase* of upward moisture flux with height and decreasing specific humidity with time. This vertical divergence of the moisture flux is associated with large entrainment of dry air and large decrease of moisture across the boundary-layer top. These boundary layers are therefore characterized by entrainment-controlled fluxes which act to dry the boundary layer. The largest systematic negative values of moisture skewness occur on 19 and 25 May when boundary-layer drying was observed throughout the 3-hour observational period; however, measurements were not made in the upper part of the boundary layer on these days. In contrast to the above cases of boundary-layer drying, the FIFE boundary layer and the HAPEX boundary layers on 13 June and 1 July are characterized by positive moisture skewness, decreasing moisture flux with height, and moistening of the boundary layer.

Temporary large entrainment occurs often in late morning when the surface inversion layer is eliminated and the boundary layer grows rapidly into a weakly stratified residual layer from the mixed layer of the previous day. During this rapid growth period in the study of Coulman (1978 a, b), the upward moisture flux increased with height and the negative moisture skewness associated with the entrainment extended down to about $z/h = 0.2$.

The above observations suggest two prototype boundary layers; 1) the *entrainment-drying boundary layer* with large top-down diffusion of dry air and vertical divergence of the moisture flux and 2) the more classical *moistening boundary layer* associated with significant surface evaporation, large bottom-up diffusion of dry air and vertical convergence of the moisture flux.

Some organization of the qualitative relationship between different variables for these two types of boundary layers can be provided by considering the evolution equation for the third moment of moisture fluctuations. Applying the development of Wyngaard and Sundararajan (1979) to moisture instead of potential temperature, we obtain the following equation for the third moment of moisture fluctuations

$$(1/3)d[q^3]/dt = -(d[q]/dz)[wq^2] - (1/3)\, d[wq^3]/dz + [q^2]d[wq]/dz - D \qquad (10)$$

where we have assumed horizontal homogeneity, neglected vertical advection by the mean vertical motion, neglected phase change and where $q$ is the perturbation specific humidity, $w$ is the perturbation vertical velocity, $[q]$ is the mean specific humidity and square brackets again represent an averaging operator. The terms on the right hand side are, respectively, the gradient production term, turbulent transport of $[q^3]$, the moisture flux divergence term and, D, the dissipation of $[q^3]$. These terms are difficult to evaluate because they contain higher moments which require large sample size and contain vertical derivatives which require aircraft flights at multiple levels. However, if we consider limiting cases where either the moisture flux is due primarily to surface evaporation or where the moisture flux is due primarily to dry air entrainment, then this equation provides useful constraints on the relationship between the sign of the third moment, the vertical gradient of moisture and the vertical moisture flux. In turn, the sign of the third moment determines the sign of the nondimensional moisture skewness (9).

Consider the gradient production term by noting that the mean specific humidity almost always decreases with height since both surface evaporation and dry air entrainment cooperatively act to generate such a gradient. In the entrainment-drying boundary layer, the production of moisture variance is mainly at the top of the boundary layer so that the transport of moisture variance is expected to be downward which corresponds to negative $[wq^2]$. Then, the gradient term in (10) produces negative moisture skewness. Conversely, if the moisture variance is generated primarily at the surface due to evaporation, the vertical flux of moisture variance is expected to be upward which corresponds to positive $[wq^2]$. Then the gradient production term in (10) produces positive moisture skewness. Therefore, the evolution equation for the third moment supports the contention that the sign of the skewness reflects the relative importance between moisture flux generation due to surface evaporation and flux generation due to entrainment of dry air.

The second term on the right hand side of (10) redistributes $[q^3]$ through turbulent transport while the last term reduces the third moment through dissipation. Neither of these terms are expected to be the primary influence on the sign of the skewness for the bulk of the boundary layer. They instead act to reduce peak amplitudes of the skewness. The sign of the third term on the right hand side is determined by the sign of the moisture flux divergence because the moisture variance must be positive. In the entrainment-drying boundary layer with positive vertical divergence of the moisture flux, this term is negative and acts to generate negative moisture skewness. Conversely, with vertical convergence of the moisture flux, this term acts to generate positive moisture skewness. These considerations indicate that moisture skewness is a useful measure for differentiating between the entrainment-drying and moistening boundary layers.

In the intermediate cases where both surface evaporation and dry air entrainment are significant, the moisture skewness in the lower part of the boundary layer is expected to depend on the relative magnitudes of the surface and entrainment fluxes. The present observations and those of Coulman (1978 a, b) and Druilhet et al. (1983) suggest that negative moisture skewness can extend into the lower part of the boundary layer if the entrainment moisture flux is greater than the surface moisture flux. In these studies, the moisture variance increases with height because of the strong generation of moisture variance in the entrainment region. This distribution of the moisture variance lends support for the above interpretation of the gradient production of $[q^3]$ (first term on the right hand side of Eq. 10).

While other examples of vertical divergence of the moisture flux and entrainment-drying of the boundary layer can be found in the literature (Deardorff,1974; Betts et al. 1990), moisture skewness is not usually reported. As an alternative indicator, large values of the flux dryness parameter ($D^* > 15$) are found in three of the four entrainment-drying boundary layers studied here. However, values of $D^*$ were not available in the previous studies of the entrainment-drying cited above. The literature does allow computation of $D^*$ from studies of the fair weather marine boundary layer characterized by vertical convergence of the moisture flux, small Bowen ratios, weak instability and small values of the flux dryness parameter; $D^* < 1$ in Donelan and Miyake (1973), $D^* < 0.2$ in Holt and Raman (1986) and $D^* < 0.2$ in Grant (1986, case of 26 Sept.). Significant vertical convergence of the moisture flux also occurred in the strongly heated boundary layer of Wyngaard et al. (1978) where $D^*$ averaged about

7. However, D* is expected to be an incomplete predictor of the entrainment-drying boundary layer because it does not contain direct information about the decrease of moisture with height and dry air entrainment. The enhancement of downward moisture flux by boundary-layer clouds (Nicholls, 1985) is also not included.

The moisture flux profile may assume other forms including near constancy with height as observed in Greenhut and Bean (1981), Milford et al. (1979), Grant (1986) and numerous cases in Kustas and Brutsaert (1987). In the absence of mean advection, height-independent moisture flux corresponds to stationary moisture distributions as might occur over the open ocean in synoptically stationary situations. Finally, moisture flux convergence may occur in one part of the boundary layer and divergence in the other part (Donelan and Miyake, 1973; LeMone and Penell, 1976; Nicholls and Readings, 1979).

Nonetheless, the moistening and entrainment-drying prototype boundary layers discussed above will serve as useful initial organization of boundary-layer situations. This distinction also underscores the limited applicability of models which specify the moisture flux at the top of the boundary layer to be a fixed fraction of the surface moisture flux. The present study and observations cited above show that this fraction may be small compared to unity, or, with large D* and dry air aloft may exceed unity.

## 3.1.6. MOISTURE-TEMPERATURE CORRELATION

In general, the correlation between moisture and temperature is negative in the upper part of the boundary layer due to entrainment of warm dry air (Coulman and Warner, 1977; Wyngaard et al. 1978, Coulman, 1980) and positive in the lower part of the heated boundary layer due to warm moist updrafts. Wyngaard et al. (1978) and Guillemet et al. (1983) describe an intermediate layer where the q-T correlation is negative on the scale of the larger eddies but positive on smaller scales including the inertial subrange.

The decrease of the positive q-T correlation with height and reversal to negative values is associated with an increase of the negative moisture skewness with height (Coulman, 1978b; Druilhet et al. 1983). The effects of entrainment appear to reduce the q-T correlation in the lower boundary layer even if such a correlation does not reverse to negative values, as implied by the significant variability of the q-T correlation near the surface and its relationship to the moisture skewness (Figure 4). Joint frequency distributions near the surface indicate that the some of the very dry air near the surface is associated with little temperature perturbation which reduces the q-T correlation.

Mixed layer scaling laws for the q-T correlation developed by Wyngaard et al. (1978), Lenschow et al. (1980, eq. 45) and Moeng and Wyngaard (1984) and the q-T costructure function developed by Wyngaard and LeMone (1980) correspond to negative correlation in the upper half of the boundary layer and positive q-T correlation in the lower half of the boundary layer with values close to unity near the surface. The observations presented here suggest that these models could be generalized to include the entrainment-drying boundary layer characterized by small q-T correlation near the surface and lower levels for the sign change of the q-T correlation. Generalization might also include the case where buoyancy fluctuations are dominated by moisture fluctuations and buoyant cool updrafts (moistals) as in Nichols and LeMone (1980), which may lead to negative q-T correlation close to the surface.

While few studies report values of the moisture skewness, a number of previous studies allow evaluation of the flux dryness parameter $D^*$. Wyngaard et al. (1978) report high positive values of the q-T correlation near the surface, averaging about 0.7 at $z/h = 0.1$ with an average $D^*$ value of about 7. Chou and Zimmerman (1989, their Table 1 and Figure 3) show q-T correlations of about 0.8 at $z/h = 0.1$ for four cases with an average $D^*$ value of 13 and about 0.25 for two cases with average $D^*$ values of slightly more than 26.

The negative moisture skewness and smaller moisture-temperature correlation generally occur with reduced w-q correlation (Figure 5). The smaller w-q correlation is partly related to some pockets of dry air associated with negligible vertical motion. This observation is consistent with the possibility of slower decay of moisture fluctuations proposed in Section 4 for large values of $D^*$. In conclusion, large $D^*$, negative surface moisture skewness and reduced q-T and w-q correlations all appear to be near surface indicators of the entrainment-drying boundary layer. However, the generality of such a relationship is not known.

### 3.1.7. MOISTURE FRONTS AND MESOSCALE VARIABILITY

#### (a) *Spatial moisture variability*

The repeated 120 km HAPEX flights on 19 and 25 May over the relatively homogeneous pine forest allow *statistical* examination of small mesoscale motions on the horizontal scale of 10 km. Inspection of raw time series (Figure 2) indicates considerable coherent moisture variation on the scale of 10 km and occasional pockets of very dry air on the scale of roughly one kilometer. The dry air pockets are characterized by a specific humidity deficit of more than 1 g/Kg and on rare occasions several g/Kg. The dry air pockets contribute to the negative moisture skewness discussed in the previous section and can occur as part of the 10 km moisture variation or can occur without obvious relation to larger scale variations (Figure 2). These anomalous dry air events are observed with almost identical signature with both Lyman Alpha sensors. The dew point hygrometer measures these events with somewhat weaker amplitude probably due to it's slower response time.

The 10 km moisture variation is characterized by an order of magnitude greater amplitude than the moisture fluctuations on the turbulent scale (say < 1 km) excluding the occasional dry air pockets. In contrast, the 10 km variation of temperature and vertical velocity are weaker and often masked by the stronger smaller scale turbulent fluctuations of temperature and vertical motion (Figure 2). The 10 km moisture structure could be associated with large boundary-layer eddies such as longitudinal roll motions or surface convergence bands (see for example Stull, 1988). The marine boundary-layer studied by Donelan and Miyake (1973) and Nicholls (1978) and some of the boundary layers over land studied by Milford et al. (1979) also show more "mesoscale" variation of moisture than variation of temperature and vertical velocity. In contrast, the tropical boundary layer studied by Nicholls and LeMone (1980) shows considerable variation of both moisture and temperature on the 10 km scale.

Here, the Haar wavelet transform (Appendix) is used to statistically document the greater mesoscale variability of moisture compared to mesoscale variability of other variables in the present data sets (Figure 6). The Haar wavelet transform provides less biased focus on individual scales compared to the structure function and allows better scale resolution at larger scales than do Fourier spectra. For 19 May HAPEX, horizontal temperature variations (Figure 6) show maximum variance at about 500 m while moisture variations continue to increase with scale. Based on this transform, the r.m.s temperature fluctuation at the variance peak is on the order of 0.1 C while the r.m.s moisture fluctuation at 5 km is on the order of 0.1 g kg$^{-1}$.

The same behavior occurs on 25 May except that the peak for temperature gradients occurs on larger scales. This difference is probably due to orientation of the mean shear more parallel to the flight direction and to the somewhat higher level of the aircraft legs on 25 May (Table 1). The stronger shear in the flight direction may elongate the eddies in the direction of the aircraft. The relative importance of moisture and temperature variations at mesoscales varies substantially between the other data sets which contain more variability of the underlying surface conditions.

### (b) *Mesoscale moisture fronts*

The 10 km moisture variation is sometimes associated with sharp gradients occurring in horizontally convergent frontal zones of about 1 km width or narrower (Figure 2). The dry air pockets discussed above are sometimes found just downwind of the mesoscale moisture fronts which leads to concentrated horizontal changes of moisture. The moisture fronts, as observed by aircraft, show no definable preference for orientation with respect to the mean shear. The mesoscale moisture fronts also do not have an obvious relationship with the surface inhomogeneity in that their locations are not correlated with locations of clearings and variations of the surface radiation temperature and albedo.

Since much of the moisture variation seems to have survived longer than any systematic structure in the other variables, compositing will be necessary to identify any tendency for circulations associated with the moisture fronts. To select samples of mesoscale moisture fronts, a time series of horizontal gradients is computed using the Haar wavelet transformation (Appendix). Then samples of about 6 km width were selected centered about peaks of the horizontal gradient of moisture as measured by this transform. The composite of the samples based on negative moisture gradients yielded about the same structure as the composite based on positive gradients. We arbitrarily choose the positive case for the following discussion.

This procedure selects 58 events from the 6 flight legs on 19 May accounting for about half of the total record. The composited structure (Figure 7) indicates strong horizontal convergence at the moisture front. The convergent frontal zone appears to occur on a scale of less than 1 km and is also associated with a narrow zone of rising warm air on the moist side of the front and a narrow zone of a slightly cooler sinking air on the dry side of the front. These variations are confined to within one or two kilometers of the front whereas the coherent changes of moisture often extend five kilometers or more on either side of the front. We infer that the moisture fronts are generated by zones of horizontal convergence in the presence of significant moisture variability. The present analysis is unable to determine if the moisture fronts are related to the surface convergence bands discussed in Stull (1988, p. 446) or other large boundary-layer scale eddies such as longitudinal roll motions. Cellular convection or organization of thermals into spoke patterns (Schmidt and Schumann, 1989) seem to be ruled out by the lack of large scale temperature signature. Moisture fronts occurred on some of the other days with varying degrees of organization.

### (c) *Negative moisture-temperature correlation and the surface energy budget*

On the mesoscale, moisture and temperature are negatively correlated for a wide variety of conditions. For example, the low pass filtered data (5 km wavelength) show negative q-T correlation for almost all of the data sets examined here. This negative correlation is a more general feature than the occurrence of moisture fronts. In contrast to this negative q-T correlation, turbulent scale warm moist updrafts and cool dry downdrafts near the surface correspond to positive correlation between temperature and moisture. This scale crossover is documented in Figure 6 and schematically summarized in Figure 8.

The negative correlation between temperature and moisture near the surface on scales greater than a few kilometers might be attributed to large boundary layer eddies which transport warmer, dryer air toward the surface as suggested by Nicholls and LeMone (1980). On scales greater than a few tens of kilometers, the temperature and moisture patterns vary little between flight legs in spite of 5 m/s airflow. This approximate stationarity is probably related to constraints of the surface energy budget as occurred in Malhouf et al. (1987), Segal et al. (1988), Pinty et al. (1989) and Noilhan et al. (1990). In regions of stronger surface moisture fluxes, the surface energy balance supports weaker heat flux provided that horizontal variations of net radiation and soil heat flux are not more important. Variations of surface evapotranspiration may be forced by spatial variations of stomatal control and soil moisture.

In contrast, on turbulent scales of 1 km or less the correlation between moisture and temperature above heated evaporating surfaces is positive because of dominance by nonstationarity and advection by the turbulent eddies themselves. In other words, local temperature changes are largely due to advection by individual eddy motions, an intrinsic feature of turbulence. Then the vertical decrease of moisture and potential temperature in the surface layer leads to positive correlation between turbulent fluctuations of temperature and moisture.

To statistically document the dependence of the moisture-temperature variations on horizontal scale, we compute the co-wavelet transformation of specific humidity and temperature (Appendix, Eq. A2). The crossover to negative q-T correlation typically occurs at about 2.5 km on 19 May and 4.5 km on 25 May (Figure 6). This negative correlation continues to increase with increasing horizontal scale indicating the importance of the quasi-stationary spatial pattern discussed above. We speculate that for scales greater than a few tens of kilometers, the mesoscale surface energy budget helps maintain the negative correlation between moisture and temperature. The composite of the moisture fronts suggests that the 10 km variation is associated with convergence zones and therefore more likely to be related to large transient eddies. The mesoscale vertical motions associated with the negative moisture-temperature correlation are weak and the overall vertical fluxes of moisture and temperature at such scales are generally either weak upward or not significant as in Nicholls and LeMone (1980).

### (d) *Implications for cloud initiation*

The negative moisture-temperature correlation on scales greater than a few kilometers is of major importance for the initiation of boundary-layer clouds and for the relationship between clouds and the mean relative humidity in the upper part of the boundary layer. The negative correlation between moisture and temperature acts to produce large mesoscale variations of relative humidity and lifted condensation level. For the present data, the standard deviations for relative humidity and lifted condensation level for scales from 5 km to 50 km are typically two or three times larger than the respective standard deviations for scales smaller than 5 km. On the smaller scales, the positive correlation between moisture and temperature act to minimize variations of relative humidity and lifted condensation level.

The negative q-T correlation occurs on scales which will be smaller than the grid size of many numerical models. This variation must be included along with the influence of turbulent fluctuations in the subgrid scale formulation of boundary-layer clouds. For example, the present data suggest that the percentage variation of the LCL used in the Wilde et al. (1985) formulation of boundary-layer clouds might be increased beyond the value attributed to turbulence alone. In a similar manner, the best critical value of the relative humidity above which clouds are inferred in the model of Slingo (1980) might be lower with large mesoscale subgrid variability. That is, with greater variability, some clouds can form at a lower average relative humidity.

## 3.1.8. CONCLUSIONS

This study of boundary layer moisture fluctuations suggests preliminary organization according to two prototype moisture regimes. The *entrainment-drying boundary layer* is characterized by vertical divergence of the moisture flux in association with significant entrainment of dry air at the boundary-layer top and top-down mixing of dryer air. The entrainment-drying boundary layer is more likely to occur with unstable conditions and weak surface evaporation which corresponds to large values of $D^* = (-h/L)\beta$ where $\beta$ is the Bowen ratio. In the entrainment-drying boundary layer, dry air from the upper part of the boundary layer occasionally reaches the surface. This occurrence leads to negative moisture skewness even though positive temperature and vertical velocity skewness are maintained by warm moist updrafts. Since the slowly diffusing dry air pockets more quickly lose their temperature and vertical velocity perturbations, the dry air serves as a tracer and leads to a reduction of the overall positive correlation of moisture with temperature and vertical velocity near the surface.

In contrast, the textbook *moistening boundary layer* is characterized by bottom-up mixing of moisture which corresponds to vertical convergence of the moisture flux, positive moisture skewness, and larger positive correlation between moisture and temperature and between moisture and vertical velocity. Such boundary layers seem most developed with large surface evaporation and significant mean wind shear where the flux dryness parameter $D^*$ is significantly smaller than 10.

The combined results of this study and those from Coulman (1978 a,b) suggest that the diurnal evolution of the heated boundary layer may often begin with a moistening regime in the morning and then experience drying later in the morning. The drying regime occurs when the nocturnal inversion layer has been eliminated and the boundary layer is growing rapidly into a thick weakly stratified layer, probably remaining from the mixed layer of the previous day. The boundary layer may or may not switch back to the moistening regime when the boundary layer growth slows later in the afternoon.

Of course all the various boundary-layer possibilities cannot be simply categorized with only two prototype regimes and one nondimensional parameter $D^*$. A more general approach needs to explicitly include the influence of dry air entrainment and allow for the influence on boundary-layer cumulus on such entrainment. However, the above idealized classification provides a useful initial organization of boundary-layer moisture regimes and indicates that the modelling practice of specifying the moisture entrainment flux to be a fixed fraction of the surface moisture flux is rather restrictive. The present study suggests that this fraction is significantly less than one for small $D^*$ but increases to values greater than unity (entrainment-drying boundary layer) for large $D^*$ and dry air aloft. The entrainment-drying boundary layer appears to be an important stage for counteracting surface evaporation. The failure of models to simulate this phase may account for unrealistic model buildup of moisture in the boundary layer.

Some of the HAPEX data reveal 10 km scale moisture variations with much of the variation often concentrated in narrow zones of horizontal convergence. Since corresponding signatures of vertical velocity and temperature are much weaker, these zones are referred to as "mesoscale" moisture fronts.

As a more general feature, potential temperature and moisture are positively correlated in the lower part of the boundary layer on horizontal scales less than 1 km. This correlation is associated with warm moist updrafts and cool dry downdrafts. However, temperature and moisture near the surface become negatively correlated on scales larger than a few kilometers associated with cool moist regions and warm dry regions. On the 10 km scale, such moisture variations appear to be associated with large boundary-layer eddies and downward transport of entrained warm dry air. However, on larger scales the negative moisture-temperature correlation is quasi-stationary and appears to be related to constraints of the turbulence energy budget.

The negative correlation between moisture and temperature on mesoscales leads to large variations of relative humidity. This variation corresponds to significant subgrid variability in large scale numerical models which implies needed adjustment of coefficients in existing formulations of boundary-layer cloud cover.

## *ACKNOWLEDGMENTS*

The detailed comments of Peggy LeMone, Steve Esbensen, J. C. Weil, Michael Ek, and Shu-Hsien Chou and the extensive comments of the reviewers are greatly appreciated. The computational and graphics assistance of Wayne Gibson, Jacob H. Jensen and Kristin Mahrt are also appreciated. The Computer Services Division of the National Center for Atmospheric Research is acknowledged for computational support and the Research Aircraft Facility of the same institution is acknowledge for all of the aircraft data listed in Table 1 with special appreciation to Dick Friesen. This material is based upon work supported by the Mesoscale Meteorology Program of the National Science Foundation under grant ATM-8820090, the Geophysics Laboratory under contract F 19628-88-K-0001 and the National Aeronautics and Space Administration under contract NAG 5-904.

# APPENDIX: APPLICATION OF THE HAAR WAVELET TRANSFORM

Mahrt (1991) shows that the usual structure function at larger scales is significantly influenced by smaller scale gradients. As a result of this leakage of variance from small scales to larger scales, the structure function is normally not able to define the scale of the main eddies.

In contrast, the Haar wavelet transform (Figure A1) contains spatial averaging which reduces the influence of scales smaller than the window width and appears to yield a variance peak at the scale which corresponds to the main eddies. The wavelet transform is a local transform $W\{f(x),a,b\}$ on the original data $f(x)$ which here is constructed to estimate spatial differences of $f(x)$ as a function of scale (dilation) $a$ and $x=b$ represents the position the local transform within the record. The variable $f(x)$ represents dependent variables such as the velocity components, temperature or moisture With the notation of the wavelet transform (Daubechies, 1988) and scaling in Mahrt (1991), the Haar wavelet transform is defined as:

$$W\{f(x),a,b\} = (1/a)\int h[(x-b)/a]\ f(x)\ dx \qquad \text{(A1)}$$

$$h[(x-b)/a] = \begin{cases} -1 & \text{for } 1/2 < (x-b)/a < 0 \\ +1 & \text{for } 0 < (x-b)/a < 1/2 \\ 0 & \text{otherwise} \end{cases}$$

where the integration is performed over the transformation window of width $a$ and again b is the positioning of the local transform. To compute the *wavelet transform variance*, the square of the local transformation (A1) is summed over the different positions of the local transformation window which sequentially moves through the record. This record variance is computed for different values of the dilation scale $a$ to construct the variance spectra. The details of this calculation can be found in Mahrt (1991).

The transformation operator can be generalized to form a *co-wavelet* transform between gradients of two different variables $f_1(x)$ and $f_2(x)$, mathematically defined as

$$CW\{f_1(x),\ f_2(x),\ a,\ b\} = (1/a)\int \{h[(x-b)/a]\ f_1(x)\}\ \{h[(x-b)/a]\ f_2(x)\}\ dx \qquad \text{(A2)}$$

where again the integration is defined over the width of the transformation window. To compute the covariance for the entire record, (A2) is summed over the entire record separately for each value of the dilation scale *a*. The wavelet covariance for moisture and temperature based on (A2) are shown in Figure 6 as a function of scale *a*.

## REFERENCES

André, J.C., Lacarrere, P. and Mahrt, L. 1979 Sur la distribution verticale de l'humidite dans une couch limite convective. *J. Rech. Atmos.*, **13**, 135-136.

André, J.C.and collaborators 1988: HAPEX-MOBIHLY: First results from the special observing period. *Ann. Geophys. ser. B*, **6**, 477-492.

Barnes, G., Emmitt, G., LeMone, M. Nicholls, S. 1980: The structure of a fair weather boundary layer based on the results of several measurement strategies. *Mon. Wea. Rev.*, **108**, 349-364.

Betts, A. K. 1976 Modeling subcloud layer structure and interaction with a shallow cumulus layer. *J. Atmos. Sci.*, **33**, 2363-2382.

Betts, A. K., Desjardins, R. L., Macpherson, J. I., and Kelly, R. D. 1990 Boundary-layer heat and moisture budgets from FIFE. *Bound.-Lay. Meteor.*, **50**, 109-137.

Brost, R. A., Lenschow, D. H. and Wyngaard, J. C. 1982 Marine stratocumulus layers. Part I: mean conditions. *J. Atmos Sci.*., **39**, 800-817.

Brutsaert, W. H. 1982 *Evaporation into the Atmosphere.* D. Reidel. Dordrecht, 299 pp.

Brutsaert, W. H. and Kustas, W. P. 1985 Evaporation and humidity profiles for neutral conditions over rugged hilly terrain. *J. Climate Appl. Meteorol.*, **24**, 915-923.

Ching, J. K. S. 1985 Urban-scale variations of turbulence parameters and fluxes. *Bound.-Lay. Meteorol.*, **33**, 335-361.

Chou, Shu-Hsien and Zimmerman, J. 1989 Bivariate conditional sampling of buoyancy flux during an intense cold-air outbreak. *Bound.-Lay. Meteorol.*, **46**, 93-112.

Clark, T. L., Hauf, T.and Kuettner, J. P. 1986 Convectively forced internal gravity waves: Results from two-dimensional numerical experiments. *Q. J. R. Meteorol. Soc.*, **112**, 899-925.

Coulman, C. E. 1978a Boundary-layer evolution and nocturnal inversion dispersal-Part I. *Bound.-Lay. Meteorol.*, **14**, 471-492.

Coulman, C. E. 1978b Boundary-layer evolution and nocturnal inversion dispersal-Part II. *Bound.-Lay. Meteorol.* **14**, 493-514.

Coulman, C. E. 1980 Correlations between velocity, temperature and humidity fluctuations in the air above land and ocean. *Bound.-Lay. Meteorol.*, **19**, 403-420.

Coulman, C. E. and Warner, J. 1977 Temperature and humidity structure of the sub-cloud layer over land. *Bound.-Lay. Meteorol.*, **11**, 467-484

Daubechies, I. 1988 Orthonormal bases of compactly supported wavelets. *Comm. Pure and Appl. Math.* **61**, 909-996.

Deardorff, J. W. 1974 Three-dimensional study of the height and mean structure of the heated planetary boundary layer. *Bound.-Lay. Meteorol.*, **7**, 81-106.

Donelan, M. and Miyake, M. 1973 Spectra and fluxes in the boundary layer of the trade-wind zone. *J. Atmos. Sci.*, **30**, 444-464.

Driedonks, A. G. M. and Tennekes, H. 1984 Entrainment effects in the well-mixed boundary layer. *Bound.-Layer Meteorol.*, **30**, 75-105.

Druilhet, A., Frangi, J. P., Guedalia, D. and Fontan, J. 1983 Experimental studies of the turbulence structure parameters of the convective boundary layer. *J Climate Appl. Meteor.*, **22**, 594 - 608.

Dyer, A. J. and colleagues 1983 An International Turbulence Comparison Experiment (ITCE 1976). *Bound.-Lay. Meteorol.*, **24**, 181-211.

Eloranta, D., Stull, R. and Ebert, E. 1989 Test of a calibration device for airborne Lyman-Alpha Hygrometers. *J. Atm and Oc. Tech.*, **6**, 129-139.

Esbensen, S. and Reynolds, R. 1981 Estimating monthly averaged air-sea transfers of heat and momentum using the bulk aerodynamic method. *J. Phys. Ocean.*, **11**, 457-465.

Garratt, J. R. and Hicks, B.B. 1973 Momentum, heat and water vapour transfer to and from natural and artificial surfaces. *Q. J. R. Meteorol. Soc.*, **99**, 680-687.

Grant, A. L. M. 1986 Observations of boundary layer turbulence made during the 1981 KONTUR experiment. *Q. J. R. Meteorol. Soc.*, **112**, 825-841.

Greenhut, G. K. and Bean, B. R. 1981 Aircraft measurements of boundary layer turbulence over the central equatorial Pacific Ocean. *Bound.-Layer Meteorol.*, **20**, 221-241.

Greenhut, G. K. and Khalsa, S. R. S. 1982 Updraft and downdraft events in the atmospheric boundary layer over the Equatorial Pacific Ocean. *J. Atmos. Sci.* **39**, 1803-1818.

Guillemet, B., Isaka, H. and Mascart, P. 1983 Molecular dissipation of turbulent fluctuations in the convective mixed layer Part I: Height variations of dissipation rates. *Bound.-Lay. Meteorol.* **27**, 141-162.

Holt, T. and Raman, S. 1986 Variation of turbulence in the marine boundary layer over the Arabian Sea during Indian Southwest Monsoon (MONEX 79). *Bound. -Lay. Meteorol.*, **37**, 71-87.

Isaka, H. and Guillemet, B. 1983 Molecular dissipation of turbulent fluctuations in the convective mixed layer. part II: Height variations of characteristic time scales and experimental test of molecular dissipation models. *Bound.-Lay. Meteorol.*, **27**, 257-279.

Johnson, R.H. 1977 Effects of cumulus convection on the structure and growth of the mixed layer over south Florida. *Mon. Wea. Rev.*, **105**, 713-724.

Kustas, W.P. and Brutsaert, W. 1987 Budgets of water vapor in the unstable boundary layer over rugged terrain. *J. Climate Appl. Meteorol.* **26**, 607-620.

Lenschow, D. H., Wyngaard, J. C. and Pennell, W. T. 1980 Mean-field and second-moment budgets in a baroclinic, convective boundary layer. *J. Atmos. Sci.*, **37**, 1313-1326.

LeMone, M. A. 1989 The influence of vertical wind shear on the diameter of cumulus clouds in CCOPE. *Mon. Wea. Rev.*, **117**, 1480-1491.

LeMone, M. A. and Meitin, R. 1984: Three examples of fair-weather mesoscale boundary-layer convection in the tropics. *Mon. Wea. Rev.*, **112**, 1985-1997.

LeMone, M. A. and Penneil, W. T. 1976 The relationship of trade wind cumulus distribution to subcloud layer fluxes and structure. *Mon. Wea. Rev.*, **104**, 524-539.

Mahrt, L. 1976 Mixed layer moisture structure. *Mon. Wea. Rev.*, **104**, pp. 1403-1407.

Mahrt, L. 1991 Eddy asymmetry in the sheared heated boundary layer. *J. Atmos. Sci.*, **48**

Mahrt, L. and André, J. C. 1983 On the stratification of turbulent mixed layers. *J. Geophys. Res.*, **88** (C4), 2662-2666.

Mahrt, L. and Ek, M. B. 1984 The influence of atmospheric stability on potential evaporation. *J. Climate Appl. Meteorol.*, **23**, 222-234.

Malhouf, J. F., Richard, E. Mascart, P. 1987 The influence of soil and vegetation development on mesoscale circulations. *J. Climate Appl. Meteorol.*, **26**, 1483-1495.

Milford, J. R., Abdulla, S., and Mansfield, D. A. 1979 Eddy flux measurements using an instrumented powered glider. *Q. J. R. Meteorol. Soc.*, **105**, 673-693.

Moeng, C.-H. and Wyngaard, J.C. 1984 Statistics of conservative scalars in the convective boundary layer. *J. Atmos. Sci.* **41**, 3161-3169.

Nicholls, S. 1978 Measurements of turbulence by an instrumented aircraft in a convective atmospheric boundary layer over the sea. *Q. J. R. Meteorol. Soc.*, **104**, 653-676.

Nicholls, S. 1985 Aircraft observations of the Ekman layer during the Joint Air Sea Interaction Experiment. *Q J. R Meteorol. Soc.*, **111**, 391-346.

Nicholls, S. and Readings, C. J. 1979 Aircraft observations of the structure of the lower boundary layer over the sea. *Q. J. R. Meteorol. Soc.*, **105**, 785-802.

Nicholls, S. and LeMone, M. A. 1980 The fair weather boundary layer in GATE: The relationship of subcloud fluxes and structure to the distribution and enhancement of cumulus clouds. *J. Atmos. Sci.*, **37**, 2051-2067.

Noilhan J. and Planton, S. 1989 A simple parameterization of land surface processes for meteorological models, *Mon. Wea. Rev.*, **117**, 536-549.

Noilhan, J., Lacarrere, P. and Bougeault, P. 1990 A spatial integration of a land surface parameterization within a meso-β-scale model, Part III: Validation against surface network and aircraft flux measurements. To appear in *Bound.-Lay. Meteorol.*

Oke, T. R. 1987 *Boundary Layer Cimates* (second edition), Methuen London, 435 pp.

Penman, H. L. 1948 Natural evaporation from open water, bare soil, and grass. *Proc. Roy. Soc. London.* **A193**, 120-195.

Priestley, C. H. B., and Taylor, R. J. 1972 On the assessment of surface heat flux and evaporation using large-scale parameters. *Mon. Wea. Rev.* **100**, 81-92.

Pinty, J.-P., Mascart, P. Richard, E. and Rosset, R. 1989 An investigation of mesoscale flows induced, by vegetation inhomogeneities using an evapotranspiration model calibrated against HAPEX-MOBILHY data. *J. Appl. Meteorol.*, **28**, 976-992.

Schmidt, H.and Schumann, U. 1989 Coherent structure of the convective boundary layer derived from large-eddy simulations. *J. Fluid Mech.*, **200**, 511-562.

Segal, M., Avissar, R. McCumber, M. C. Pielke, R. A. 1988 Evaluation of vegetation effects on the generation and modification of mesoscale circulations. *J. Atmos. Sci*, **45**, 2268-2292.

Sellers, P. J. Hall, F. G., Asrar, G. Strebel, D. E., and Murphy, R. E. 1988: The first ISLSCP Field Experiment (FIFE). *B. Amer. Meteorol. Soc.*, **69**, 22-27.

Slingo, J. M. 1980 A cloud parametrization scheme derived from GATE data for use with a numerical model. *Q. J. R. Meteorol. Soc.*, **106**, 747-770.

Stull, R. B 1988 *An Introduction to Boundary Layer Meteorology*. Kluwer Academic Publishers. Boston. 666 pp.

| | | |
|---|---|---|
| Wilde, N.P., Stull, R. B., and Eloranta, E. W. | 1985 | The LCL zone and cumulus onset. *J. Climate Appl. Meteor.*, 24, 640-657. |
| Wyngaard, J. C | 1984 | Toward convective boundary layer parametrization: A scalar transport module. *J. Atmos. Sci.*, 41, 1959-1969. |
| Wyngaard, J. C. and Brost, R. A. | 1984 | Top-down and bottom-up diffusion of a scalar in the convective boundary layer. *J. Atmos. Sci.*, 41, 102-112. |
| Wyngaard, J. C. and LeMone, M.A. | 1980 | Behavior of the refractive index structure parameter in the entraining convective boundary layer. *J. Atmos. Sci*, 37, 1573-1585. |
| Wyngaard, J. C., Pennell, W. T., Lenschow, D. H., and LeMone, M. A. *Sci.*, | 1978 | The temperature-humidity covariance budget in the convective boundary layer. *J. Atmos.* 35, 47-58. |
| Wyngaard, J. C. and Sundararajan, A. | 1979 | The temperature skewness budget in the lower atmosphere and its implications for turbulent modeling. *Turbulent Shear Flows*, 1, 319-326. |

## Figure legends

Figure 1. (a) Physical regimes in the Bowen ratio-stability phase space defining asymptotic cases in terms of the moisture energy ratio M (eq. 3) and the flux dryness parameter D* (eq. 8). (b) corresponding location of various aircraft legs in the Bowen ratio-stability phase space for FIFE (+), HAPEX 19 May (open triangles), 25 May (open circles), 13 June (solid diamonds), 19 June (solid circles), 22 June (open diamonds), and 1 July (solid squares).

Figure 2. Two examples of time series of specific humidity, temperature and vertical motion at roughly 150 m above the pine forest on 19 May in HAPEX with east on the right.

Figure 3. Relationship between the skewness of specific humidity and D* (see Eq. 8) based on high pass variables for FIFE (+), HAPEX 19 May (open triangles) and HAPEX 25 May (open circles). Part of the scatter is associated with variation of the vertical moisture gradient and dry air entrainment between observations.

Figure 4. Relationship between the temperature-specific humidity correlation and the skewness of specific humidity of high pass variables

for FIFE (+), HAPEX 19 May (open triangles), 25 May (open circles), 13 June (solid diamonds), 19 June (solid circles), 22 June (open diamonds), and 1 July (solid squares).

Figure 5. Relationship between the correlation between specific humidity and vertical velocity and the skewness of specific humidity based on high pass variables. See Figure 4 for explanation of symbols.

Figure 6. Scale-dependence of the Haar wavelet transform for temperature ($K^2$), specific humidity [$(g/Kg)^2$] and Haar wavelet covariance (K g/Kg) composited over all of the flight legs on (a) 19 May and on (b) 25 May in HAPEX. See Appendix for methodology.

Figure 7. Composite horizontal structure of 6 km samples of sharp horizontal variations of moisture (solid, upper) and associated fields for longitudinal velocity (dashed upper), vertical motion (solid lower) and temperature (dashed lower).

Figure 8. Idealized example of the reversal of the moisture-temperature correlation with increasing scale contrasting turbulent, 10 km and mesoscale energy-controlled regimes.

Figure A1. Application of the Haar wavelet transform to time series for calculation of horizontal variations.

Table 2. Boundary-layer stability -h/L, moisture energy ratio M, flux dryness parameter $D^*$, record mean velocity components ($ms^{-1}$), record mean fluxes based on 5 km high pass variables for momentum ($m^2s^{-2}$), moisture ($ms^{-1}g\ Kg^{-1}$) and virtual heat ($ms^{-1}K$), and correlations based on both high pass and low pass variables.

Table 2

| | Mean values and bulk parameters | | | | | | High Pass Flux | | | | High Pass Correlation | | | | | | Low Pass Correlation | | |
|---|---|---|---|---|---|---|---|---|---|---|---|---|---|---|---|---|---|---|---|
| Data Set | -h/L | M | D* | U | V | Bowen Ratio | W U | W V | Wq | W THv | WU | WV | Wq | TU | TV | Tq | Wq | Tq | WTHv |
| HAPEX 10-MAY-86 | 12.87 | 21.82 | 7.59 | -2.64 | 3.32 | 0.59 | 0.12 | -0.20 | 0.08 | 0.14 | 0.11 | -0.10 | 0.34 | 0.14 | -0.11 | 0.34 | 0.08 | -0.05 | 0.20 |
| | 17.14 | 20.44 | 10.33 | -2.83 | 2.76 | 0.60 | 0.12 | -0.21 | 0.10 | 0.17 | 0.10 | -0.17 | 0.38 | 0.23 | -0.21 | 0.40 | 0.25 | 0.04 | 0.30 |
| | 24.56 | 40.10 | 18.02 | -2.40 | 2.33 | 0.61 | 0.12 | -0.16 | 0.10 | 0.17 | 0.10 | -0.13 | 0.40 | 0.17 | -0.08 | 0.44 | 0.42 | -0.26 | 0.27 |
| | 38.68 | 49.50 | 30.22 | -2.31 | 2.16 | 0.78 | 0.09 | -0.13 | 0.08 | 0.17 | 0.08 | -0.11 | 0.32 | 0.10 | -0.11 | 0.42 | 0.11 | -0.48 | 0.36 |
| | 23.65 | 34.18 | 16.36 | -2.18 | 2.34 | 0.69 | 0.09 | -0.22 | 0.09 | 0.18 | 0.06 | -0.14 | 0.36 | 0.14 | -0.12 | 0.40 | 0.02 | -0.58 | 0.54 |
| | 20.72 | 31.26 | 13.73 | -2.04 | 2.43 | 0.66 | 0.16 | -0.22 | 0.10 | 0.18 | 0.11 | -0.18 | 0.40 | 0.16 | -0.18 | 0.40 | -0.41 | -0.74 | 0.68 |
| HAPEX 25-MAY-86 | 37.15 | 50.31 | 27.43 | -2.90 | -1.68 | 0.74 | 0.08 | 0.10 | 0.06 | 0.12 | 0.09 | 0.10 | 0.34 | 0.05 | 0.13 | 0.79 | 0.16 | -0.80 | 0.10 |
| | 23.86 | 28.69 | 21.31 | -2.94 | 0.33 | 0.89 | 0.10 | -0.08 | 0.06 | 0.14 | 0.17 | -0.06 | 0.41 | 0.17 | -0.06 | 0.60 | 0.11 | -0.73 | 0.12 |
| | 40.65 | 60.37 | 27.30 | -3.43 | -0.76 | 0.67 | 0.14 | 0.00 | 0.07 | 0.15 | 0.12 | 0.00 | 0.30 | 0.02 | 0.00 | 0.30 | 0.14 | -0.70 | 0.22 |
| | 29.09 | 27.44 | [illegible] | -3.66 | -0.04 | 1.09 | 0.17 | 0.02 | 0.05 | 0.14 | 0.14 | 0.02 | 0.26 | 0.14 | -0.06 | 0.32 | 0.20 | -0.70 | 0.17 |
| | 40.45 | 62.46 | 31.20 | -2.97 | 0.18 | 0.77 | 0.13 | 0.01 | 0.06 | 0.13 | 0.11 | 0.01 | 0.32 | -0.06 | 0.06 | 0.36 | 0.22 | -0.62 | -0.24 |
| | 45.22 | 68.86 | 20.69 | -3.17 | -0.60 | 0.66 | 0.11 | 0.07 | 0.07 | 0.13 | 0.09 | 0.05 | 0.20 | 0.09 | 0.01 | 0.26 | 0.19 | -0.43 | 0.19 |
| FIFE 6-JUN-87 | 0.96 | 20.03 | 1.02 | 2.10 | 9.42 | 0.26 | -0.10 | -0.43 | 0.11 | 0.09 | -0.11 | -0.40 | 0.45 | 0.07 | -0.53 | 0.70 | -0.08 | -0.07 | 0.21 |
| | 0.72 | 41.42 | 1.64 | 2.03 | 10.20 | 0.21 | -0.18 | -0.29 | 0.11 | 0.07 | -0.20 | -0.31 | 0.47 | -0.14 | -0.39 | 0.75 | 0.05 | -0.16 | 0.39 |
| | [illegible] | 58.79 | 2.02 | 2.64 | 9.20 | [illegible] | -0.11 | -0.31 | 0.14 | 0.09 | -0.13 | -0.32 | 0.55 | 0.02 | -0.40 | 0.70 | 0.02 | 0.03 | 0.46 |
| | 1.26 | 76.24 | 2.31 | 2.23 | 10.44 | [illegible] | -0.14 | -0.19 | 0.11 | 0.07 | -0.17 | -0.25 | 0.51 | -0.03 | -0.41 | 0.85 | -0.30 | -0.24 | -0.05 |
| | 0.80 | 67.80 | 1.44 | 1.51 | 9.66 | 0.16 | -0.06 | -0.27 | 0.12 | 0.06 | -0.08 | -0.36 | 0.55 | 0.15 | -0.50 | 0.76 | -0.16 | -0.09 | 0.35 |
| | 7.39 | 63.60 | 1.07 | 1.67 | 10.79 | 0.14 | -0.04 | -0.31 | 0.11 | 0.06 | -0.06 | -0.38 | 0.50 | -0.10 | -0.44 | 0.78 | -0.43 | -0.16 | 0.05 |
| HAPEX 13-JUN-86 | 6.91 | 8.11 | 5.89 | 1.25 | -8.43 | 0.86 | -0.12 | 0.57 | 0.07 | 0.16 | -0.06 | 0.31 | 0.44 | -0.21 | 0.43 | 0.86 | -0.09 | 0.08 | 0.07 |
| | 13.01 | 12.86 | 14.00 | 0.74 | -7.62 | 1.07 | -0.17 | 0.45 | 0.07 | 0.10 | -0.09 | 0.24 | 0.51 | -0.15 | 0.31 | 0.91 | 0.40 | 0.06 | 0.76 |
| | 37.44 | 40.69 | 20.21 | 1.01 | -5.67 | 0.75 | 0.00 | 0.20 | 0.07 | 0.15 | 0.05 | 0.14 | 0.54 | 0.01 | 0.00 | 0.90 | 0.22 | -0.01 | 0.82 |
| | 19.49 | 26.90 | 14.00 | 0.13 | -4.79 | 0.72 | -0.06 | 0.33 | 0.08 | 0.15 | -0.04 | 0.19 | 0.51 | -0.07 | 0.29 | 0.88 | 0.34 | 0.19 | 0.30 |
| | 19.32 | 27.18 | 13.73 | 0.27 | -3.20 | 0.71 | 0.05 | 0.31 | 0.07 | 0.13 | 0.04 | 0.22 | 0.82 | -0.01 | 0.22 | 0.88 | 0.14 | 0.73 | 0.80 |
| | 16.90 | 18.21 | 13.09 | -0.12 | -6.00 | 0.67 | 0.06 | 0.36 | 0.06 | 0.14 | 0.04 | 0.24 | 0.40 | 0.02 | 0.24 | 0.87 | 0.36 | 0.63 | 0.69 |
| | 11.69 | 12.22 | 11.10 | 0.00 | -7.50 | 0.96 | 0.01 | 0.51 | 0.07 | 0.16 | 0.00 | 0.27 | 0.40 | -0.00 | 0.29 | 0.90 | 0.82 | 0.10 | 0.76 |
| HAPEX 19-JUN-86 | 27.28 | 40.93 | 14.91 | -0.40 | -1.26 | 0.56 | 0.13 | 0.04 | 0.07 | 0.11 | 0.13 | 0.04 | 0.27 | 0.06 | 0.02 | 0.24 | 0.31 | 0.37 | 0.41 |
| | 99.65 | 160.47 | 59.66 | -1.38 | -1.69 | 0.60 | 0.07 | -0.03 | 0.09 | 0.14 | 0.07 | -0.03 | 0.29 | -0.06 | 0.12 | 0.32 | 0.14 | -0.05 | 0.71 |
| | 262.07 | 524.60 | 131.52 | -0.77 | -0.27 | 0.50 | 0.04 | 0.02 | 0.10 | 0.13 | 0.04 | 0.02 | 0.33 | -0.03 | 0.01 | 0.32 | 0.46 | 0.41 | 0.52 |
| | 102.77 | 155.76 | 67.00 | -0.81 | 0.01 | 0.66 | -0.04 | -0.08 | 0.09 | 0.16 | -0.03 | -0.07 | 0.45 | 0.03 | 0.04 | 0.52 | 0.09 | -0.28 | 0.33 |
| | 425.13 | 703.40 | 250.95 | -0.40 | -0.60 | 0.60 | 0.02 | -0.02 | 0.08 | 0.13 | 0.02 | -0.02 | 0.30 | 0.09 | 0.11 | 0.40 | 0.21 | -0.35 | 0.10 |
| | 41.09 | 70.62 | 23.90 | -0.38 | -2.26 | 0.58 | 0.14 | 0.03 | 0.07 | 0.11 | 0.13 | 0.03 | 0.40 | 0.05 | -0.06 | 0.50 | -0.10 | -0.13 | 0.20 |
| | 95.69 | 174.84 | 52.37 | -0.40 | -2.78 | 0.55 | 0.02 | 0.00 | 0.07 | 0.10 | 0.02 | 0.08 | 0.45 | -0.07 | 0.09 | 0.50 | 0.04 | -0.33 | 0.30 |
| | 40.79 | 92.65 | 17.96 | -0.67 | -0.66 | 0.44 | 0.13 | 0.04 | 0.07 | 0.09 | 0.12 | 0.04 | 0.42 | 0.05 | 0.04 | 0.60 | 0.22 | -0.22 | 0.49 |
| HAPEX 22-JUN-86 | 14.00 | 85.71 | 2.29 | 4.10 | -2.03 | 0.16 | -0.14 | 0.00 | 0.10 | 0.06 | -0.10 | 0.10 | 0.36 | -0.13 | 0.12 | 0.41 | 0.39 | -0.28 | 0.40 |
| | 10.67 | 42.96 | 2.65 | 3.46 | -1.13 | 0.25 | -0.26 | 0.03 | 0.11 | 0.09 | -0.28 | 0.03 | 0.39 | -0.23 | 0.14 | 0.46 | -0.26 | -0.04 | -0.21 |
| | 5.73 | 17.26 | 1.90 | 4.78 | -0.08 | 0.33 | -0.47 | 0.01 | 0.12 | 0.12 | -0.35 | 0.01 | 0.39 | -0.33 | 0.03 | 0.66 | -0.06 | -0.33 | 0.14 |
| | 4.76 | 16.46 | 1.37 | 6.25 | -0.77 | 0.29 | -0.35 | -0.21 | 0.00 | 0.07 | -0.28 | -0.17 | 0.43 | -0.30 | -0.06 | 0.67 | 0.23 | -0.35 | -0.09 |
| | 6.40 | 18.82 | 2.23 | 4.00 | -2.37 | 0.34 | -0.45 | 0.09 | 0.12 | 0.12 | -0.34 | 0.07 | 0.51 | -0.31 | 0.20 | 0.78 | 0.35 | 0.00 | 0.62 |
| | 17.38 | 46.33 | 6.62 | 2.90 | -4.10 | 0.30 | -0.20 | 0.12 | 0.11 | 0.11 | -0.17 | 0.11 | 0.51 | -0.24 | 0.14 | 0.84 | 0.02 | -0.15 | 0.32 |
| | 26.99 | 86.38 | 7.02 | 1.62 | -1.67 | 0.30 | -0.08 | 0.17 | 0.10 | 0.09 | -0.09 | 0.16 | 0.53 | -0.03 | 0.15 | 0.76 | 0.19 | 0.24 | 0.62 |
| | 29.70 | 76.19 | 11.66 | 1.58 | -1.40 | 0.39 | -0.18 | 0.10 | 0.11 | 0.12 | -0.16 | 0.09 | 0.62 | -0.16 | 0.07 | 0.79 | -0.06 | -0.02 | 0.66 |
| | 12.73 | 24.13 | 6.72 | 4.17 | -1.21 | 0.63 | -0.44 | 0.10 | 0.12 | 0.16 | -0.27 | 0.06 | 0.66 | -0.26 | 0.20 | 0.07 | 0.26 | -0.45 | 0.61 |
| HAPEX 01-JUL-86 | 30.93 | 54.79 | 17.46 | -3.06 | -0.26 | 0.66 | 0.09 | 0.09 | 0.06 | 0.09 | 0.12 | 0.11 | 0.40 | 0.15 | 0.13 | 0.72 | 0.24 | 0.13 | 0.53 |
| | 22.02 | 30.11 | 13.30 | -2.69 | -1.08 | 0.59 | 0.14 | 0.13 | 0.07 | 0.12 | 0.15 | 0.14 | 0.59 | 0.11 | 0.10 | 0.83 | 0.04 | -0.60 | 0.17 |
| | 66.06 | 66.36 | 40.08 | -2.43 | -1.04 | 0.83 | 0.10 | 0.05 | 0.06 | 0.12 | 0.12 | 0.06 | 0.45 | 0.17 | 0.30 | 0.60 | 0.43 | -0.20 | 0.61 |
| | 65.81 | 112.76 | 65.30 | -0.33 | -1.47 | 0.76 | 0.07 | 0.03 | 0.05 | 0.10 | 0.00 | 0.03 | 0.53 | 0.02 | 0.05 | 0.78 | 0.00 | -0.61 | 0.62 |
| | 26.80 | 36.60 | 19.31 | -0.57 | -1.00 | 0.73 | 0.18 | 0.06 | 0.07 | 0.14 | 0.16 | 0.05 | 0.60 | 0.06 | -0.05 | 0.84 | 0.39 | 0.00 | 0.32 |
| | 30.33 | 47.43 | 19.40 | -0.84 | -1.54 | 0.64 | 0.14 | 0.07 | 0.07 | 0.12 | 0.16 | 0.06 | 0.54 | 0.08 | 0.07 | 0.87 | 0.46 | -0.02 | 0.34 |
| | 19.07 | 20.07 | 12.66 | 2.36 | -0.93 | 0.66 | 0.22 | 0.08 | 0.07 | 0.13 | 0.21 | 0.07 | 0.58 | 0.20 | 0.04 | 0.89 | 0.33 | 0.05 | 0.35 |
| | 26.08 | 35.36 | 10.24 | -2.58 | -0.93 | 0.74 | 0.20 | 0.06 | 0.08 | 0.15 | 0.18 | 0.04 | 0.59 | 0.21 | 0.05 | 0.84 | 0.37 | -0.49 | 0.54 |
| | 24.83 | 36.89 | 16.71 | -3.42 | -1.02 | 0.67 | 0.16 | 0.13 | 0.08 | 0.14 | 0.15 | 0.12 | 0.63 | 0.10 | 0.23 | 0.85 | 0.27 | -0.13 | -0.34 |
| | 41.79 | 44.26 | 30.41 | -2.60 | -1.42 | 0.94 | 0.12 | 0.10 | 0.08 | 0.15 | 0.09 | 0.09 | 0.52 | 0.08 | 0.13 | 0.78 | 0.18 | 0.05 | 0.61 |

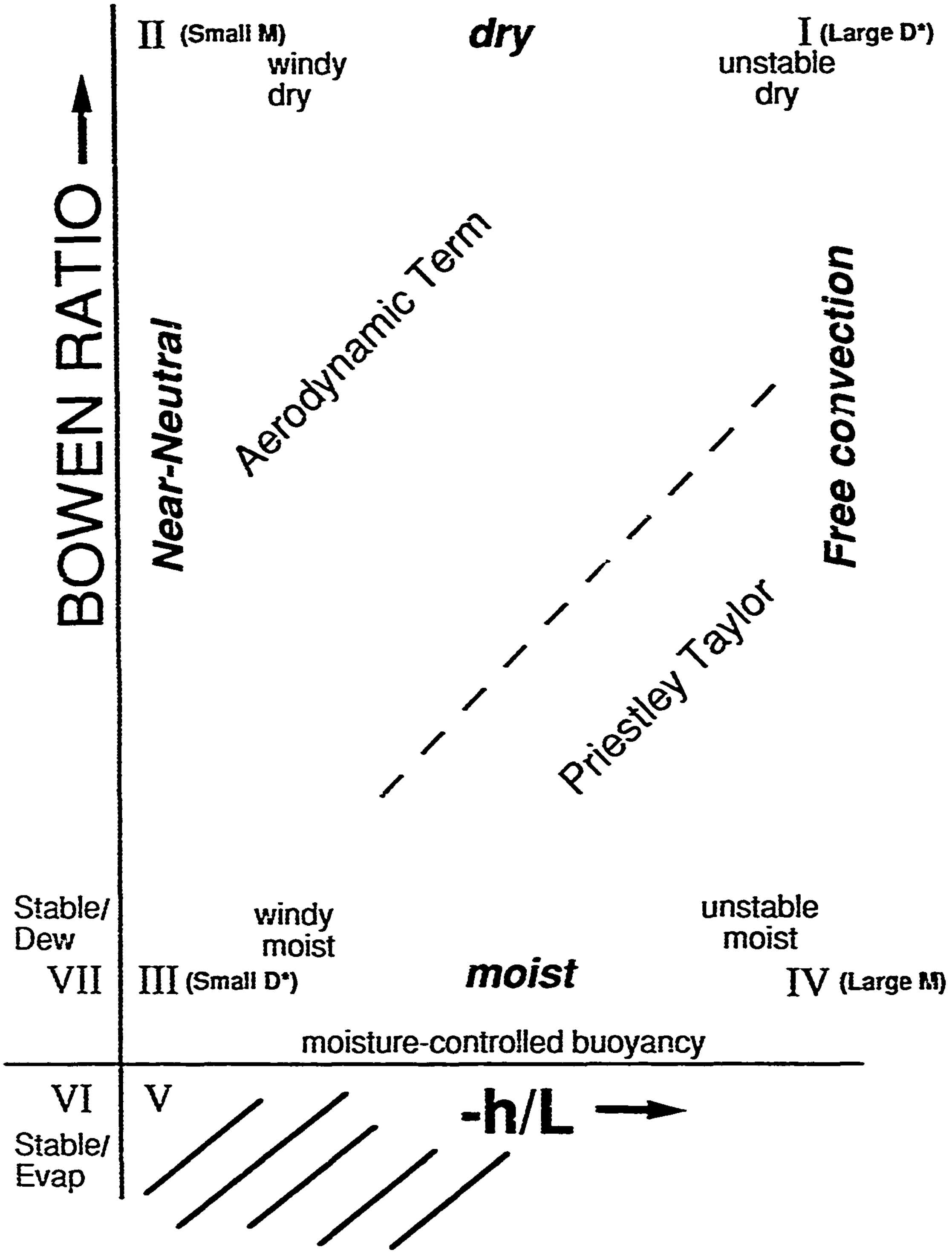
II (Small M)
dry
I (Large D*)
windy
dry
unstable
dry
BOWEN RATIO
Near-Neutral
Aerodynamic Term
Free convection
Priestley Taylor
Stable/
Dew
VII
windy
moist
III (Small D*)
moist
unstable
moist
IV (Large M)
moisture-controlled buoyancy
VI
Stable/
Evap
V
-h/L

Figure 1a

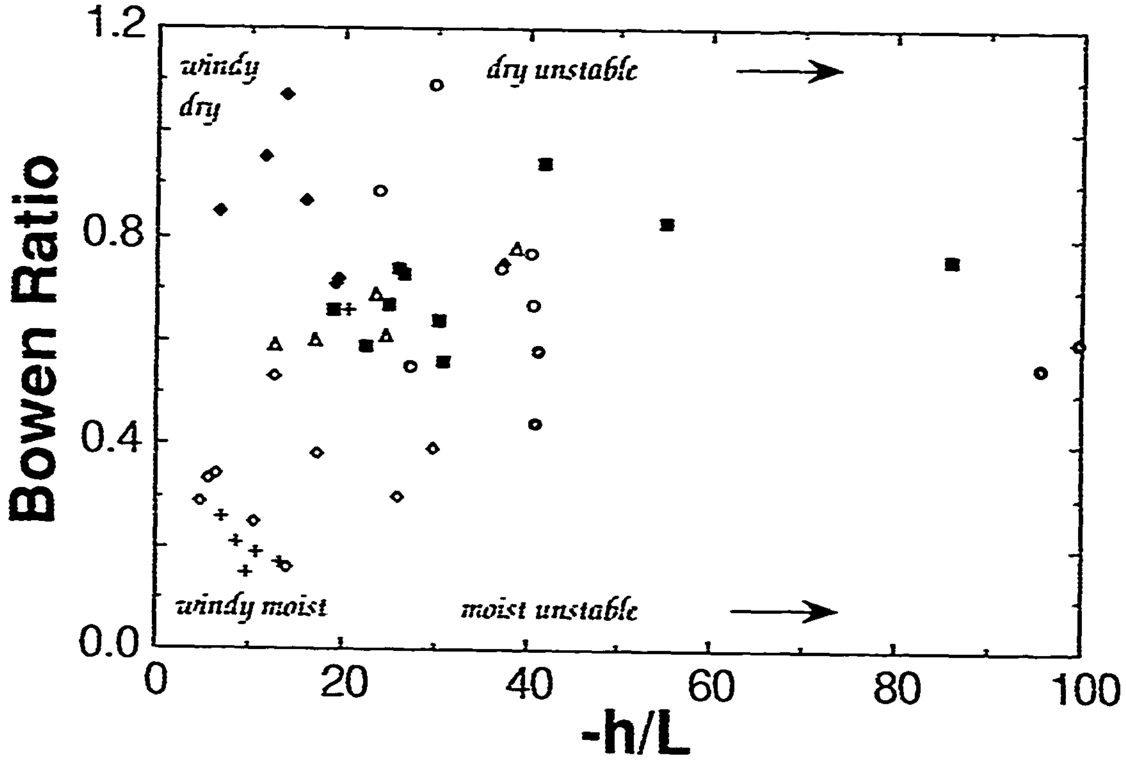
1.2
0.8
0.4
0.0
Bowen Ratio
0
20
40
60
80
100
-h/L
windy
dry
dry unstable
windy moist
moist unstable

Figure 1b

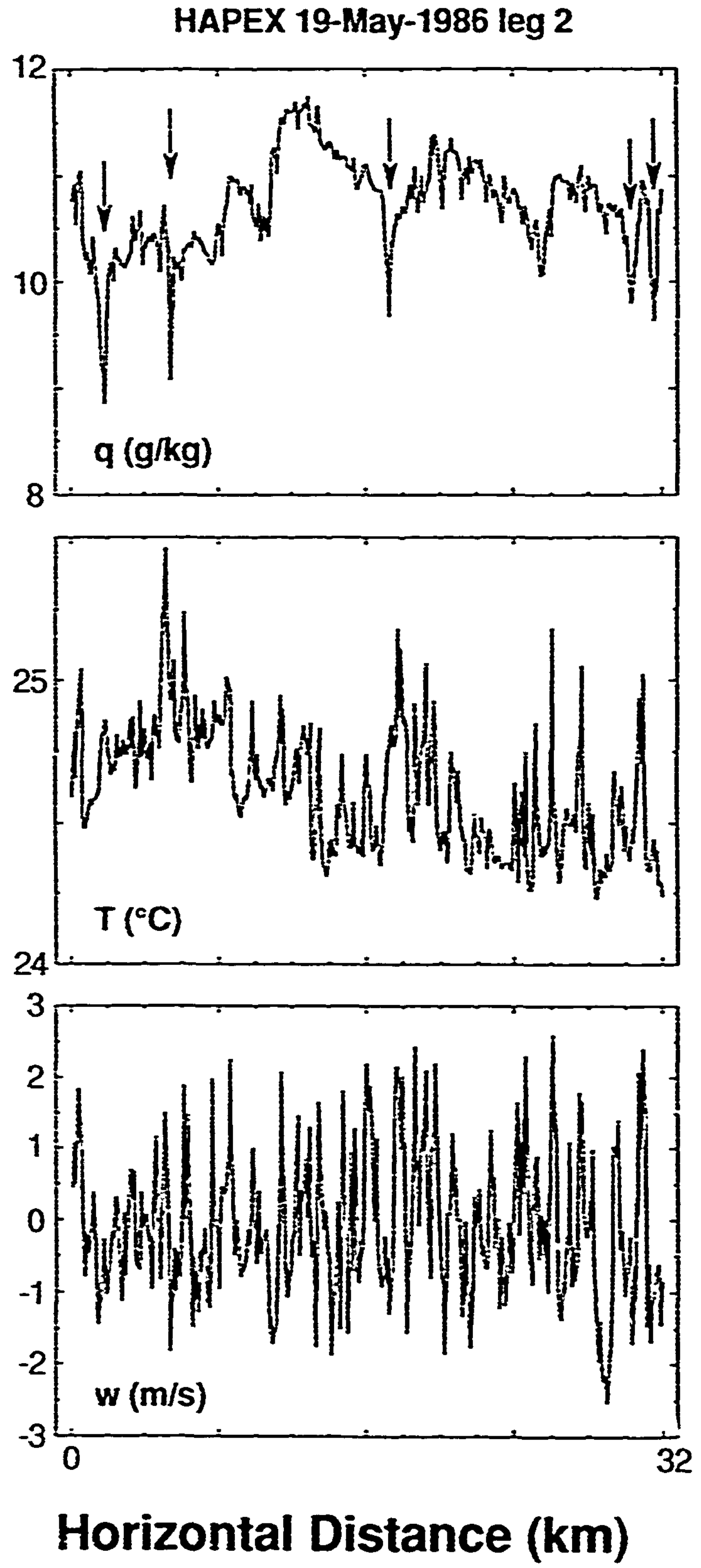
HAPEX 19-May-1986 leg 2
12
10
8
q (g/kg)
25
24
T (°C)
3
2
1
0
-1
-2
-3
w (m/s)
0
32
Horizontal Distance (km)

Figure 2a

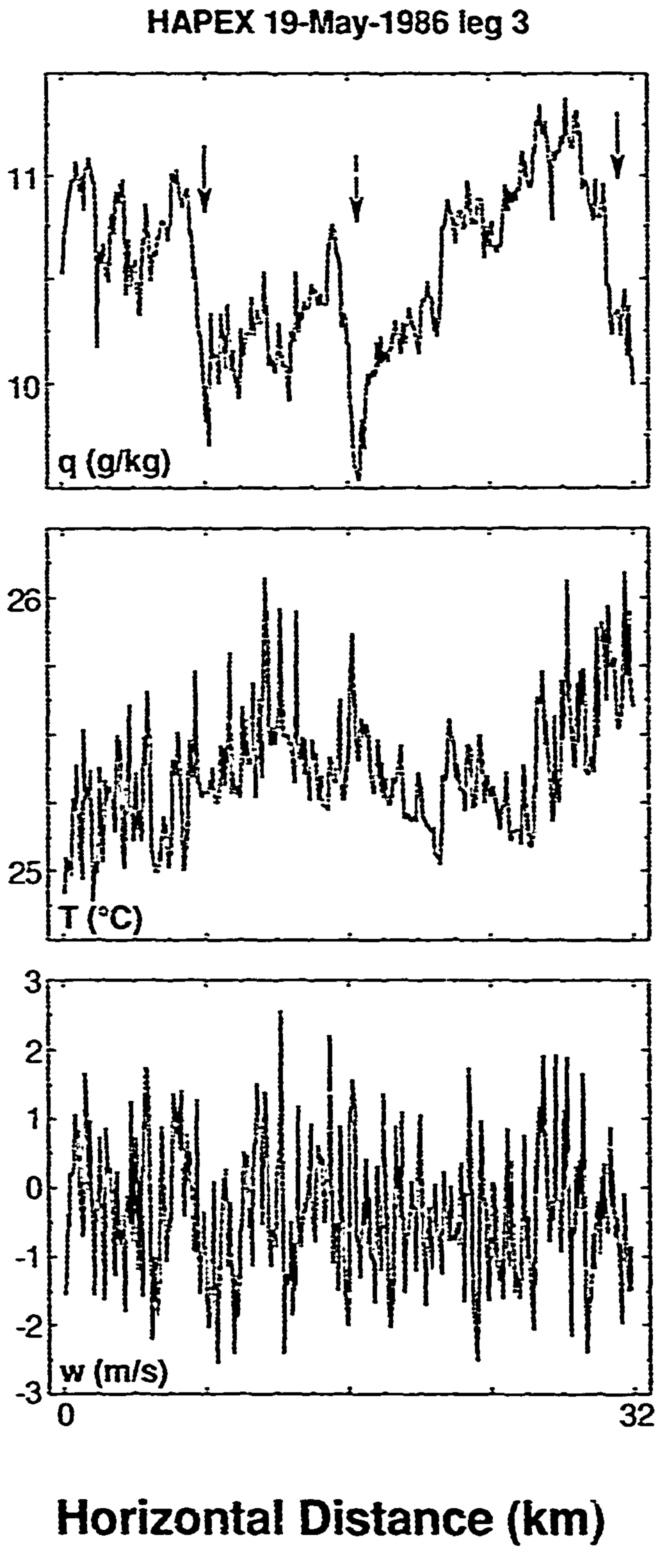
HAPEX 19-May-1986 leg 3
11
10
q (g/kg)
26
25
T (°C)
3
2
1
0
-1
-2
-3
w (m/s)
0
32
Horizontal Distance (km)

Figure 2b

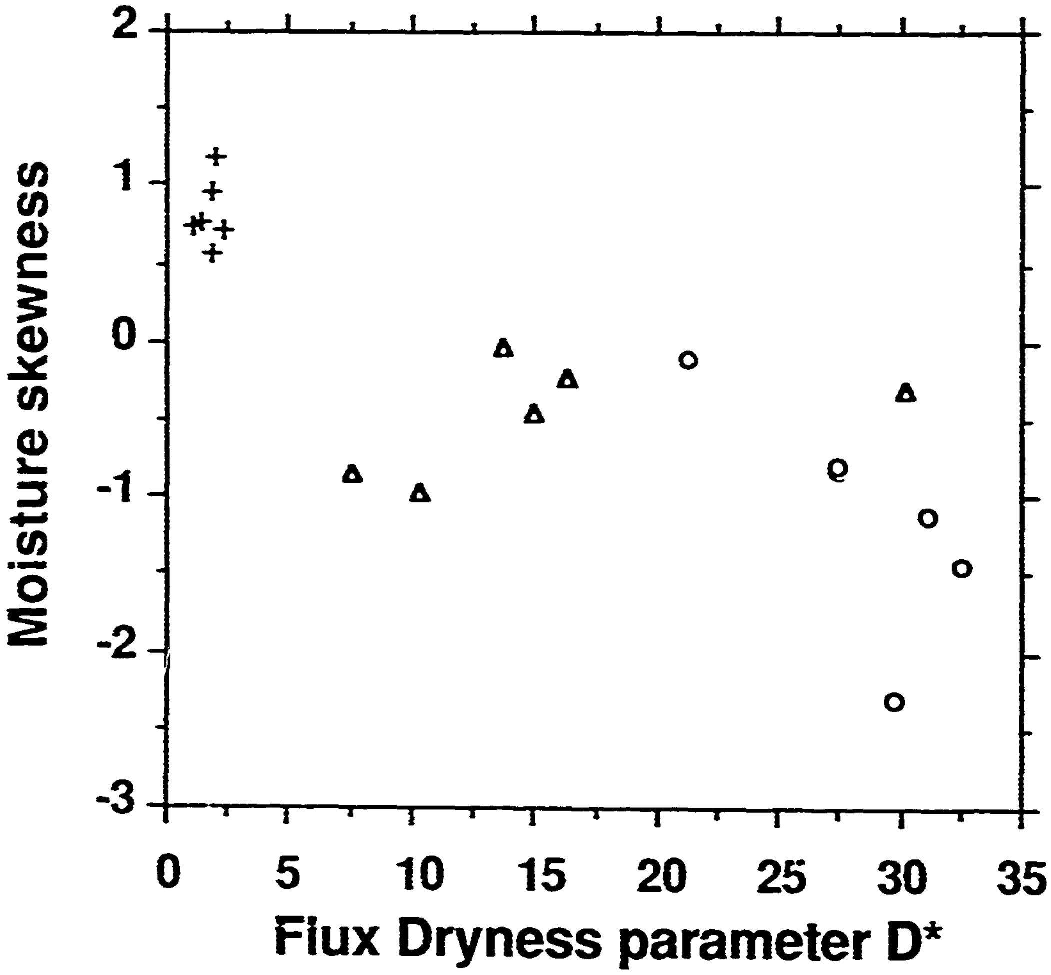

2
1
0
-1
-2
-3
Moisture skewness
0
5
10
15
20
25
30
35
Flux Dryness parameter D*

Figure 3

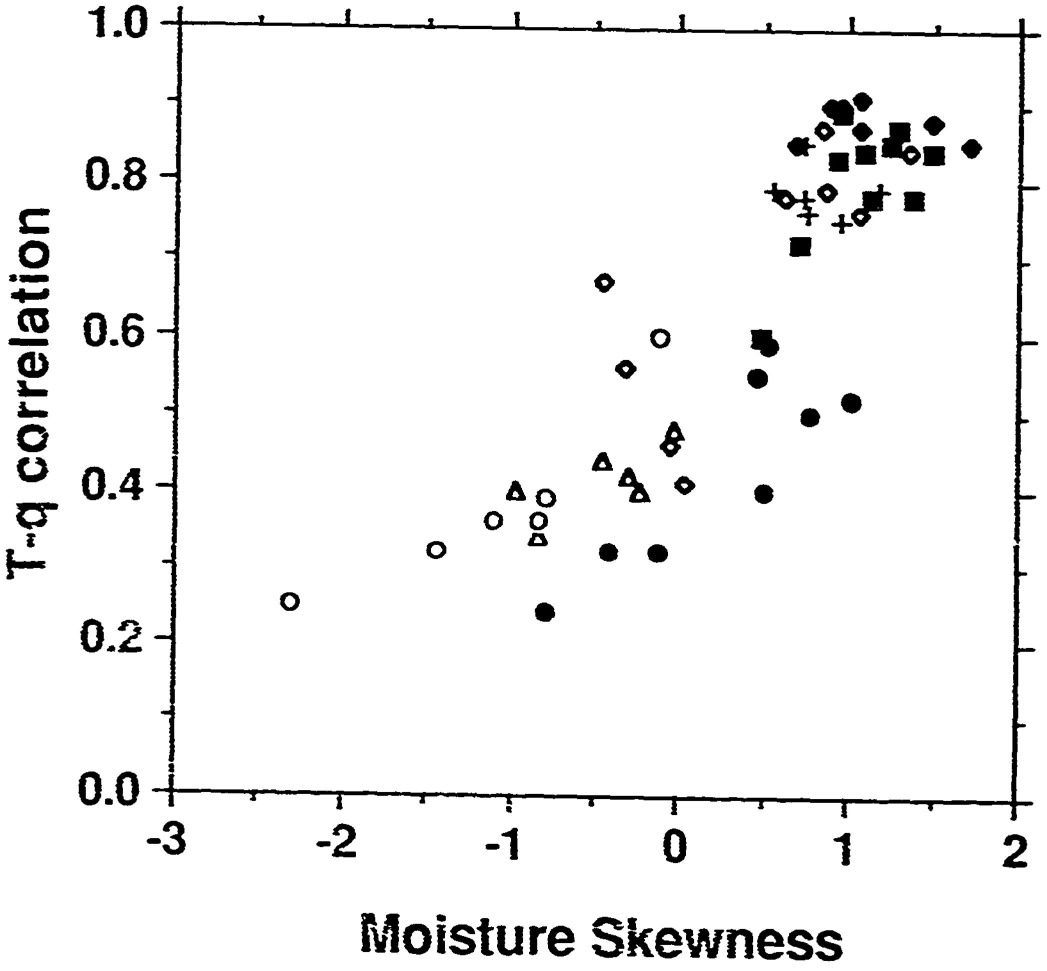

Figure 4

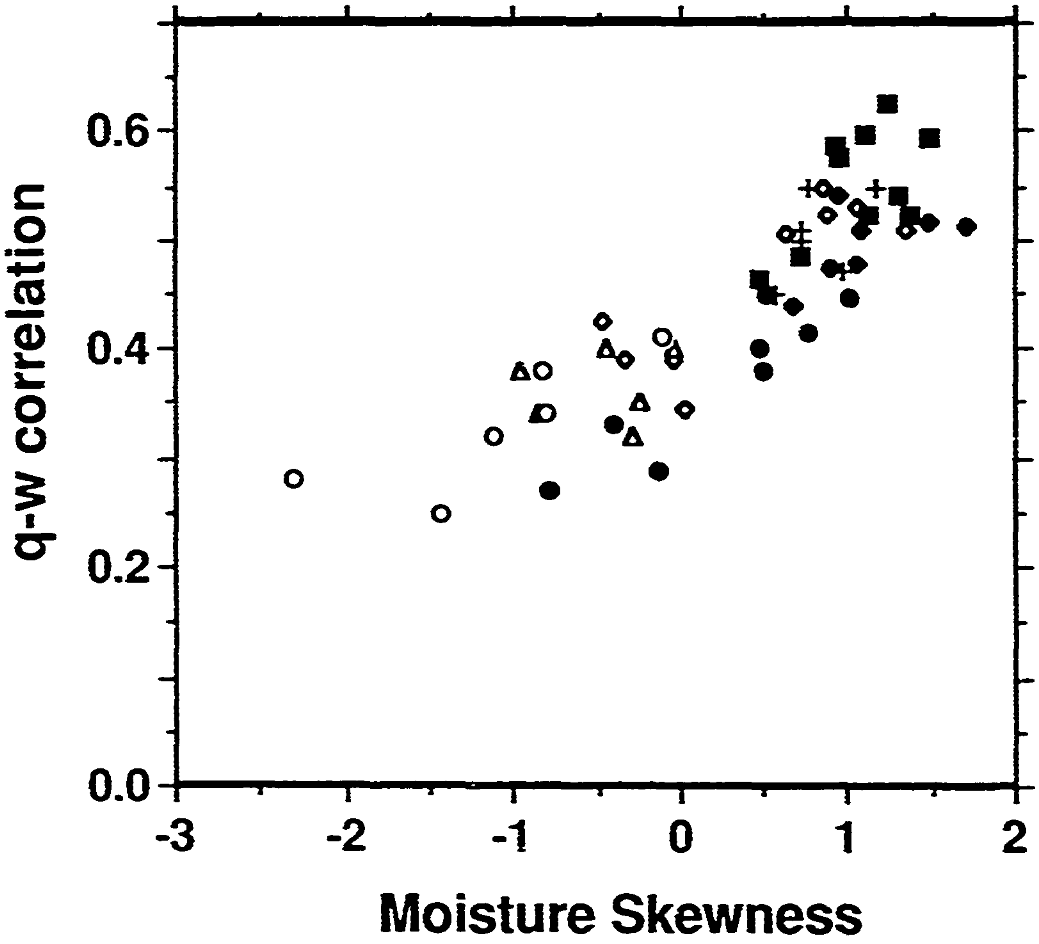

Figure 5

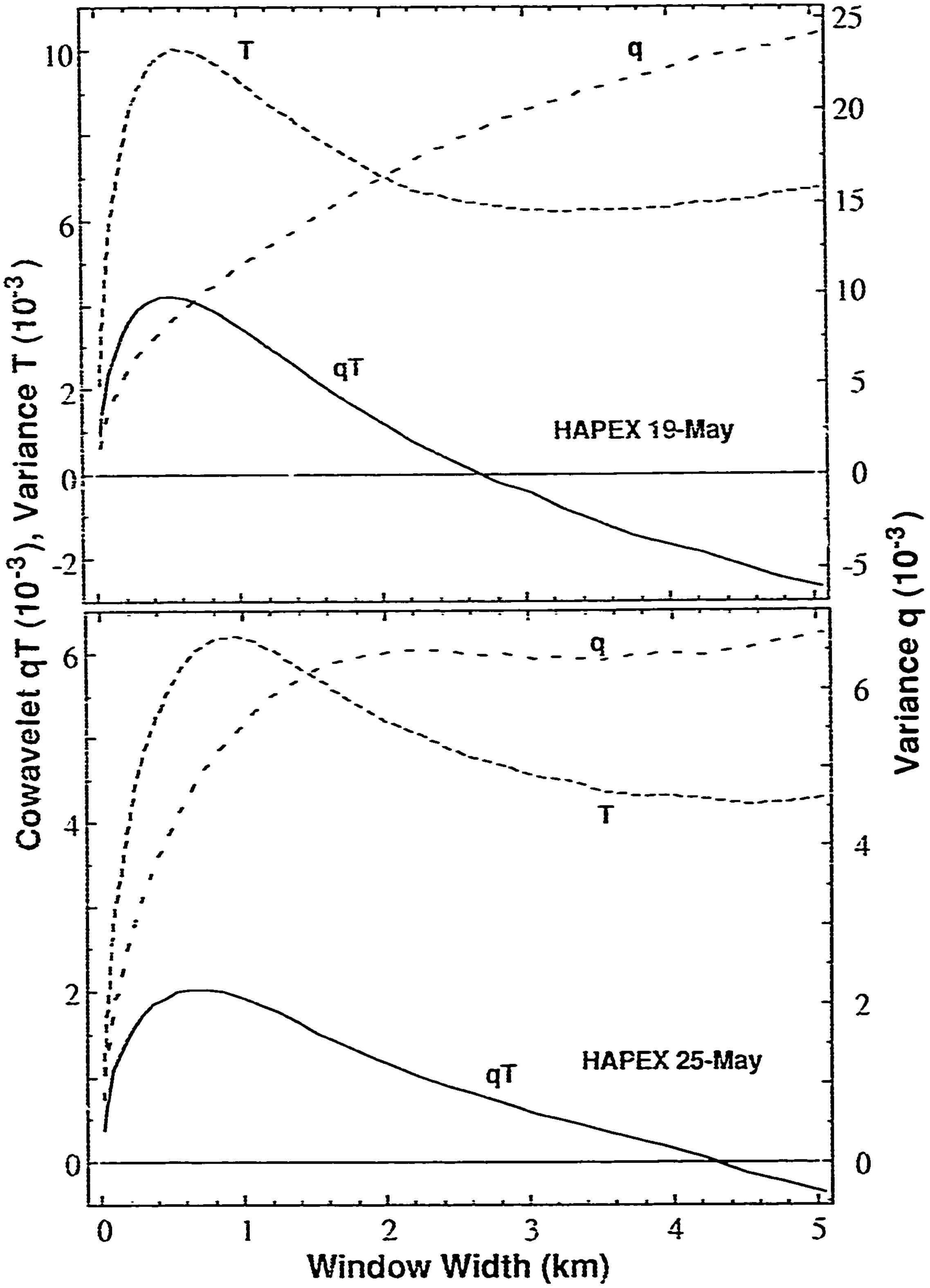

T
q
qT
HAPEX 19-May
q
T
qT
HAPEX 25-May
10
6
2
0
-2
6
4
2
0
25
20
15
10
5
0
-5
6
4
2
0
0
1
2
3
4
5
Window Width (km)
Cowavelet qT ($10^{-3}$), Variance T ($10^{-3}$)
Variance q ($10^{-3}$)

Figure 6

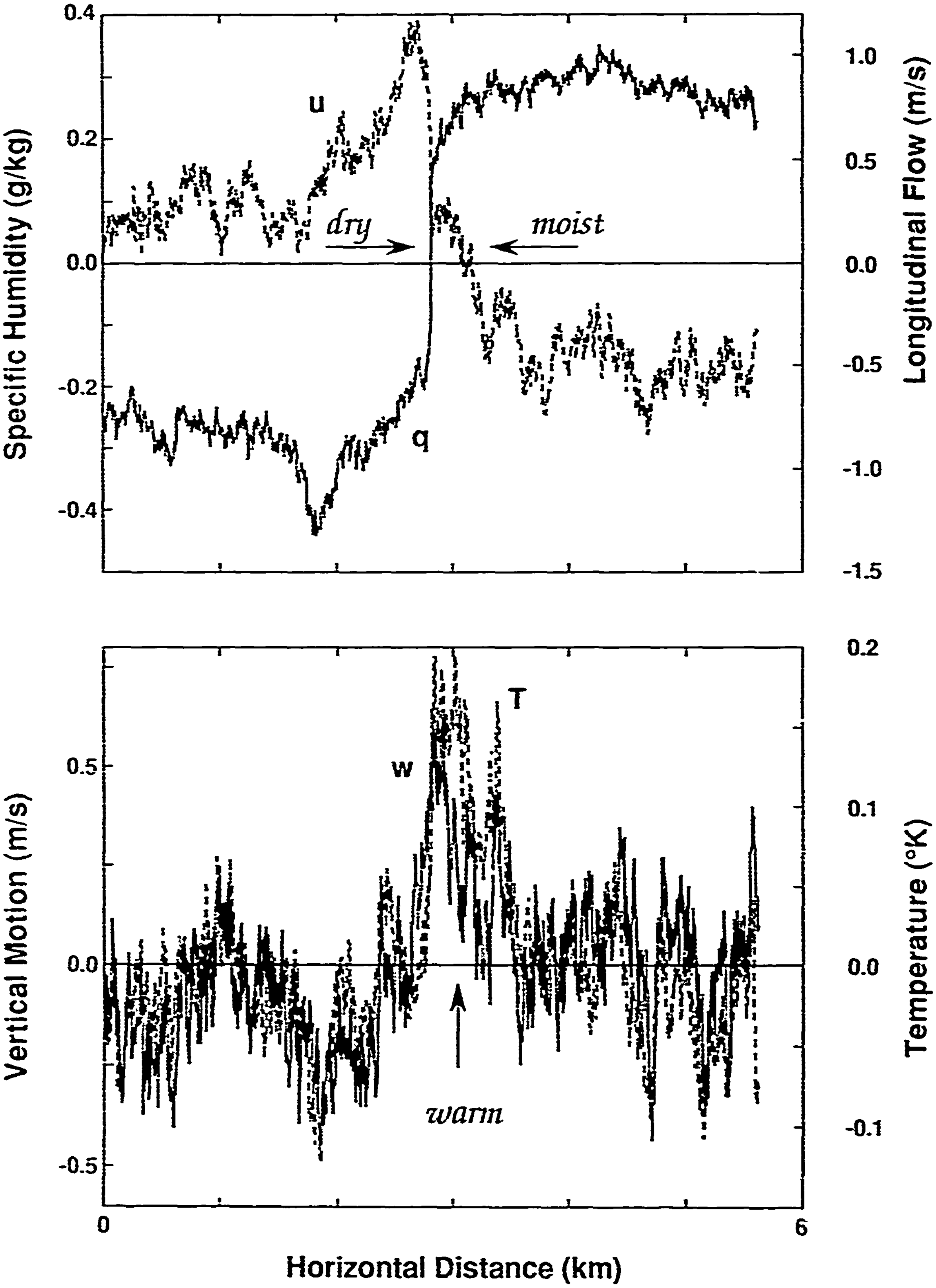
0.4
0.2
0.0
-0.2
-0.4
Specific Humidity (g/kg)
1.0
0.5
0.0
-0.5
-1.0
-1.5
Longitudinal Flow (m/s)
u
q
dry
moist
0.5
0.0
-0.5
Vertical Motion (m/s)
0.2
0.1
0.0
-0.1
Temperature (°K)
w
T
warm
0
6
Horizontal Distance (km)

Figure 7

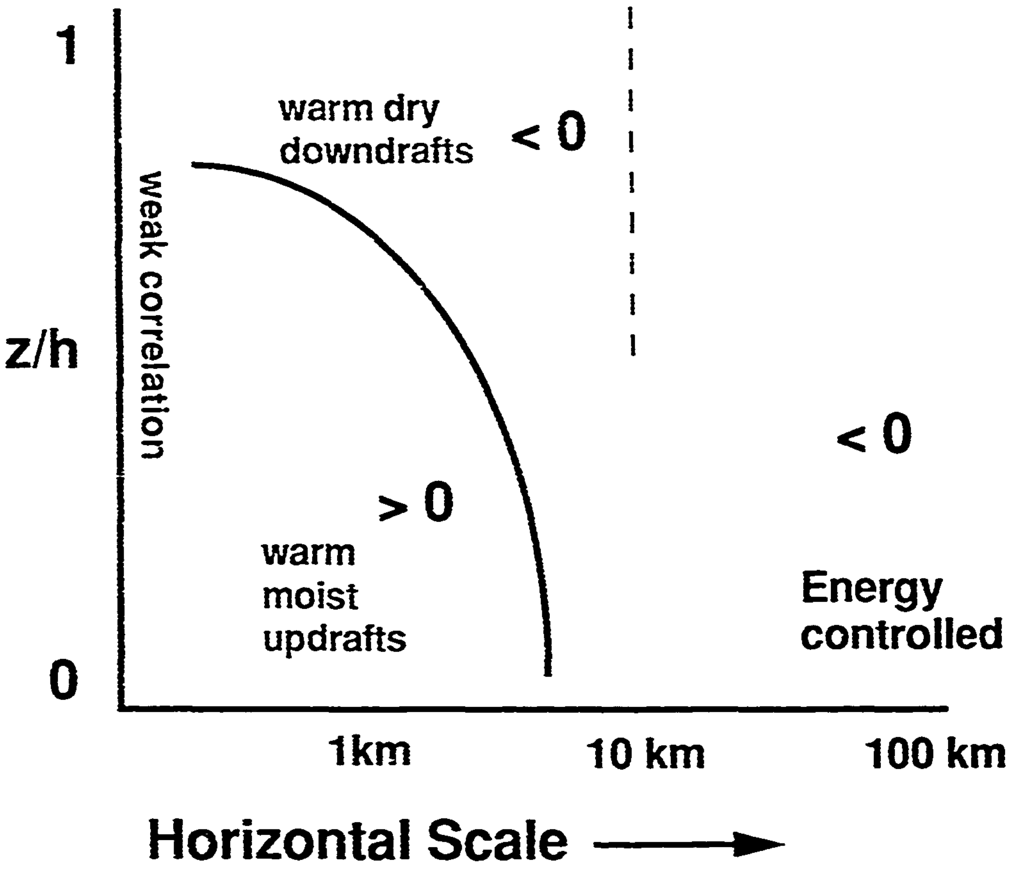

Moisture-Temperature Correlation

1
z/h
0
weak correlation
warm dry
downdrafts
< 0
> 0
warm
moist
updrafts
< 0
Energy
controlled
1km
10 km
100 km
Horizontal Scale

Figure 8

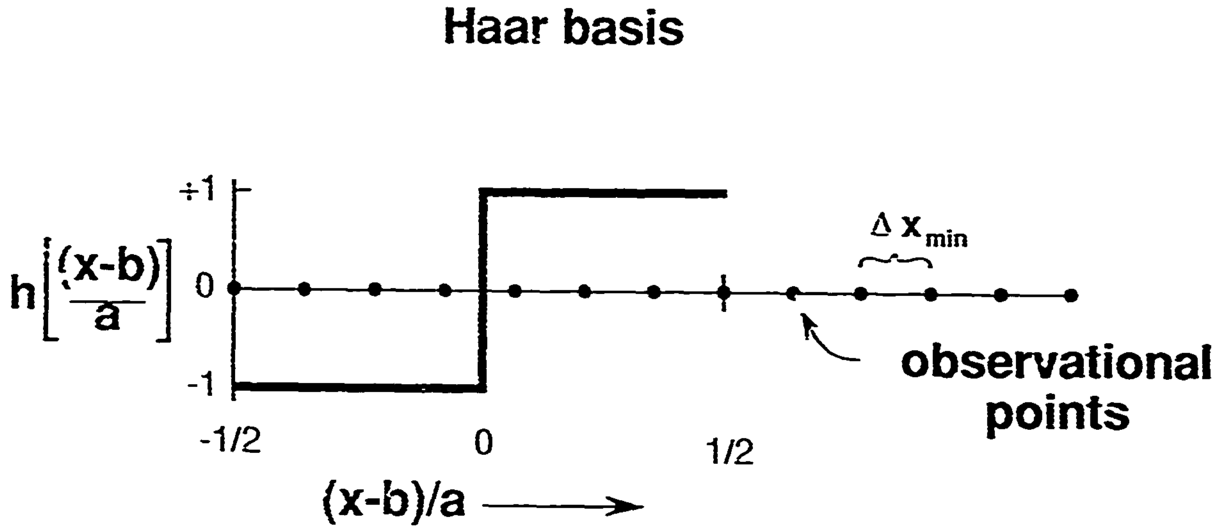
Haar basis
+1
h[(x-b)/a]
0
-1
Δ x_min
observational points
-1/2
0
1/2
(x-b)/a →

Figure A1

## Chapter 3.2

# A formulation for boundary-layer cloud cover

### 3.2.1. INTRODUCTION

Formulation of cloud cover and the associated attenuation of downward solar radiation is an important aspect of practical models of the boundary layer. Development of boundary-layer clouds reduces surface heating and evapotranspiration. Relatively little attention has been devoted to construction of simple formulations of boundary-layer cloud cover.

Most existing simple formulations can be roughly classified into two classes: those formulations based on the relative humidity in the upper part of the boundary layer (Slingo, 1980; Chu, 1986) and those formulations based on a frequency distribution of the lifted condensation level (Betts, 1983; Wilde et al., 1985). The latter class of models seem to possess more physics which can be potentially related to turbulence statistics, whereas the former class is easier to implement in a numerical model. In this investigation, we develop a model of cloud cover which utilizes aspects of both classes of formulations by analyzing data from the Hydrological and Atmospheric Pilot Experiment (HAPEX) conducted in the southwest of France in 1986 (André et al., 1988).

The present study will indicate that turbulent scale variations of relative humidity and subgrid mesoscale inhomogeneity are both important factors in the formulation for grid-averaged cloud cover in large-scale numerical models. The transmission of solar radiation through boundary-layer clouds must also be modelled. We will incorporate this cloud cover formulation into a one-dimensional planetary boundary-layer model and simulate cloud cover development for several days during HAPEX.

### 3.2.2. RELATIVE HUMIDITY MODELS OF CLOUD COVER

The proposed model will follow Slingo (1980) using relative humidity near the boundary-layer top since this quantity is relatively available from numerical models and does not require a link between surface processes and cloud development. We will follow Wilde et al. (1985) and Betts (1983) and assume a frequency distribution of variables (relative humidity for our study) in order to account for variability on turbulent scales. We also include mesoscale subgrid variability to allow for application to large-scale models.

The simplest formulation of cloud cover which is based on relative humidity ($RH$) near the top of the boundary layer can be summarized in a framework based on a "scaled relative humidity"

$$RH^* = [RH - RH_{crit}]/[1 - RH_{crit}] \qquad (1)$$

This function vanishes as $RH$ decreases to the critical relative humidity $RH_{crit}$, and approaches unity when $RH$ approaches 100%. A general model of boundary-layer fractional cloud cover $A_c$ is then formulated as

$$\begin{aligned} A_c &= RH_*^{\,p}, \quad RH^* > 0 \\ A_c &= 0, \quad RH^* \leq 0 \end{aligned} \qquad (2)$$

With formulation (1-2), boundary-layer clouds are first predicted when the grid-averaged relative humidity exceeds $RH_{crit}$. Cloud cover reaches 100% when the grid-averaged relative humidity reaches 100%. The Slingo model uses the average relative humidity in the 950 to 850 mb layer and corresponds to $p=2$ with $RH_{crit} = 0.80$ in (1-2). In this study, average relative humidity will always refer to the relative humidity computed from averaged moisture and averaged temperature. The Chu model corresponds to $RH_{crit} = 0.57$ and $p = 1.32$. The Albrecht (1981) model cannot be expressed in this format without further simplification.

To study the usefulness of (1-2), we estimate the fractional cloud cover using records of downward solar radiation data from aircraft flight legs collected by the NCAR King Air during HAPEX. This data set consists of 12 days with varying cloud amounts in the boundary layer and minimal cloud activity above the boundary layer. Frequency distributions of the downward solar radiation are computed from one-second observations (approximately 80-m segments) along the aircraft flight leg. The resulting frequency distributions (figure 1) indicate a bimodal distribution of solar radiation under a partial cloud cover. As a result, a critical value of solar radiation can be defined for each flight leg to determine the local existence of overhead boundary-layer clouds without suffering significant sensitivity to the exact numerical choice of the critical value.

The relationship between the fractional cloud cover and the average relative humidity observed near the boundary-layer top depends on turbulent scale variability. For example, with moist updrafts and dry downdrafts associated with entrainment at the boundary-layer top, clouds first form with lower average relative humidity compared to the boundary layer with only small turbulent variations of relative humidity.

Observations from the 18 available upper-level flight legs from 10 days in HAPEX (figure 2) indicate that the observed boundary-layer cloud cover is only loosely related to the relative humidity in the upper part of the boundary layer, at least for the data of this study. In our study the upper part of the boundary layer corresponds to $z/h \geq 0.6$ where z is the aircraft flight level and h is the boundary layer depth. Part of the scatter may be due to the variable height of the exact aircraft flight levels with respect to the boundary layer top (table 1). When clouds developed, the aircraft flights were executed immediately below the cloud base. Flights through clouds were avoided because of the uncertainty of temperature and moisture measurements within clouds. For relative humidity less than 100%, the partial cloud cover appears to be greater with significant turbulent scale variability of relative humidity (figure 2). Turbulent fluctuations of relative humidity are computed from the aircraft data using a high-pass filter with a 5 km cutoff wavelength.

A plausible relationship between cloud cover and the variation of relative humidity is posed in terms of a hypothetical frequency distribution of relative humidity in figure 3. Here relative humidity is generalized using total water relative humidity (vapor plus liquid); that is, values greater than 1.0 occur in clouds. For average relative humidity less than 1.0 (figure 3a), greater cloud cover is more likely with larger variation of relative humidity. For an average relative humidity greater than 1.0 (figure 3b), larger variation of relative humidity leads to smaller cloud cover. As an example, in stratocumulus where the fractional cloud cover is large, increased variation of relative humidity corresponds to more dry pockets and decreased cloud cover.

For simplicity we will construct a model of fractional cloud cover which assumes a Gaussian distribution of relative humidity and predicts the mean and variance of relative humidity from variables available from simple boundary-layer models. In actual cloudy boundary layers, the tail of the distribution corresponding to significant liquid water is probably reduced by precipitation. Mathematically, the fractional boundary-layer cloud cover will be predicted by

$$A_c = f\{[RH], \sigma_{RH}\} \qquad (3a)$$

where $[RH]$ is the average relative humidity and $\sigma_{RH}$ is the standard deviation of relative humidity which defines the Gaussian distribution. The fractional cloud cover is the area under the Gaussian curve greater than $RH = 1.0$ (figure 3) and is approximated by a ninth-order polynomial fit to the normal distribution. The relevant variation of relative humidity near the boundary-layer top involves both turbulent scale variations and those mesoscale variations which are on a scale smaller than the horizontal grid size. For simplicity, we assume that the mesoscale and turbulent fluctuations of relative humidity are uncorrelated which requires a distinct separation of scales in which case we can write

$$\sigma_{RH} = [\sigma^2_{RHturb} + \sigma^2_{RHmeso}]^{1/2} \qquad (3b)$$

where $\sigma^2_{RHturb}$ is the turbulent scale relative humidity variance and $\sigma^2_{RHmeso}$ is the mesoscale relative humidity variance.

The turbulent scale relative humidity variance is modelled in Section 3a starting with the variance equation for relative humidity. The subgrid mesoscale variance increases with the horizontal averaging length. With relative humidity significantly less than one and sparse cloud cover, the chance of including some area of high relative humidity and cloud increases with the size of the grid as is suggested by the dependence of the observed cloud cover on averaging length (figure 4). The subgrid mesoscale variance of relative humidity is modelled in Section 3c as an increasing function of grid size.

### 3.2.3. RELATIVE HUMIDITY VARIANCE

Turbulent variations of moisture and temperature near the heated surface are normally positively correlated corresponding to warm moist updrafts and cool dry downdrafts. This correlation leads to relatively small variations of relative humidity. In the upper part of the boundary layer, temperature and moisture tend to be negatively correlated on turbulent scales due to entrainment of warmer drier air between cooler moist updrafts. This negative temperature-moisture correlation corresponds to larger variations of relative humidity compared to lower in the boundary layer.

Mesoscale variations of relative humidity due to variations of the surface energy budget often lead to negative correlations between temperature and moisture (Mahrt, 1991). In regions of moist surface conditions, greater evapotranspiration leads to less energy available to heat the atmosphere; conversely, dry regions correspond to greater sensible heat flux at the surface and warmer air temperatures. With variations between warm dry air and cool moist air, both temperature and moisture variations act in concert to produce significant variations of relative humidity. Since these variations may be on a subgrid scale, they must be considered in the formulation of cloud cover based on relative humidity. Mesoscale moisture variations may be systematically larger over a variety of mesoscale conditions (Mahrt, 1991).

Mahrt (1991) found that the spatial scale of the sign change of the temperature-moisture correlation near the surface occurs typically at roughly 5 km for the HAPEX data. We arbitrarily define turbulent scales as those less than 5 km and mesoscale variations as those greater than 5 km. For this reason, we compute the moisture flux and variances using a 5-km high pass filter. With this partition, dry downdrafts between individual cloud elements are turbulent scale variations. The upper limit to the mesoscale circulations included in this calculation will normally be 100 km corresponding to the length of the record.

The significant mesoscale variation of relative humidity and cloud cover will contribute to the subgrid variability in most large-scale models. This effect decreases the value of relative humidity required for the initial onset of boundary-layer clouds in models of the form (1-2). We now study the variation of relative humidity in the boundary layer by forming an equation for relative humidity variance.

### a) Turbulent scale variation of relative humidity

To compute the turbulent variation of relative humidity near the boundary-layer top, we express the relative humidity ($RH$) in terms of the specific humidity ($q$) and partition variables into record mean and perturbation (') to obtain

$$[RH] + RH' = ([q] + q')/([q_s] + q_S') \qquad (4)$$

Assuming that the perturbation saturation specific humidity $q_S'$ is small compared to the mean value ($[q_s]$), we approximate (4) as

$$[RH] + RH' = (1 / [q_s])([q] + q')(1 - q_s' / [q_s]) \qquad (5)$$

Carrying out the multiplication on the right hand side, rearranging, and subtracting $[RH]$ from both sides, we obtain

$$RH' = - [RH]q_s' / [q_s] + q' / [q_s] - q'q_s' / [q_s]^2 \qquad (6)$$

Squaring (6) and averaging, the turbulent scale relative humidity variance ($\sigma^2_{RHturb}$) becomes

$$\sigma^2_{RHturb} = [RH]^2 \sigma^2_{qs} / [q_s]^2 + \sigma^2_q / [q_s]^2 - \sigma^2_q \sigma^2_{qs} / [q_s]^4$$

$$- 2[RH]q_s'q' / [q_s]^2 + 2[RH] \sigma^2_{qs} q' / [q_s]^3 - q_s' \sigma^2_q / [q_s]^3 \qquad (7)$$

where $\sigma^2_{qs}$ and $\sigma^2_q$ are the variances of saturation specific humidity and specific humidity, respectively. Assuming $q' << [q]$ and $q_s' << [q_s]$ (7) becomes approximately

$$\sigma^2_{RHturb} = [RH]^2 \sigma^2_{qs} / [q_s]^2 + \sigma^2_q / [q_s]^2 - 2[RH][q_s'q'] / [q_s]^2 \qquad (8)$$

The linearized Clasius-Clapeyron equation can be written as

$$q_s' = (dq_s / dT)T' = (\Delta)T'$$
$$[q_s'^2] = (\Delta)^2[T'^2]$$

where

$$\Delta = dq_s / dT = L_v q_s / (R_v T^2).$$

Assigning the perturbation values to be the record standard deviations, the Clasius-Clapeyron equation becomes

$$\sigma^2_{qs} = (\Delta)^2 \sigma^2_T$$

Using this relationship (8) may be rewritten as

$$\sigma^2_{RHturb} = ([RH] \Delta \sigma_T / [q_s])^2 + (\sigma_q / [q_s])^2 - 2[RH] \Delta r_{Tq} \sigma_T \sigma_q / [q_s]^2 \qquad (10)$$

The first term on the right-hand side of (10) is the relative humidity variance due to the temperature variance, the second term is due to the moisture variance, and the third term is due to the correlation between temperature and moisture. In the upper part of the boundary layer, the moisture variance term is much larger than the other two terms (table 1 and figure 5).

Since the contribution from the other two terms in (10) is small, we choose to express $\sigma^2_{RHturb}$ as a function of the moisture variance term. Then (10) reduces to

$$\sigma^2_{RHturb} = f\{(\sigma_q / [q_s])^2\} \tag{11}$$

where $f$ is an undetermined function to be estimated empirically. Unfortunately, simple models of the boundary layer do not predict moisture variance and similarity relationships for moisture fluctuations are unreliable near the boundary-layer top.

We can transform (11) by relating $\sigma_q$ to the moisture flux

$$\sigma_q = [w'q'] / r_{wq}\sigma_w$$

Then (11) becomes

$$\sigma^2_{RHturb} = f\{([w'q'] / (r_{wq}\sigma_w[q_s]))^2\} \tag{12}$$

Boundary-layer models predict $[w'q']$ and $[q_s]$. Relationship (12) is preferable to (11) because similarity expressions for $\sigma_w$ are thought to be more reliable than those formulations for moisture fluctuations. Furthermore $r_{wq}$ in the upper boundary layer appears to be less variable than the moisture variance required for (11). Therefore we proceed to explore the applicability of (12) by assuming $f$ to be a linear function of its argument and ignoring the variation of $r_{wq}$. Then (12) becomes

$$\sigma^2_{RHturb} = C1 + C2\,\{[w'q'] / (\sigma_w[q_s])\}^2 \tag{13}$$

Using the 18 upper-level flight legs from HAPEX, linear regression yields $C1 = 0.00014$, and $C2 = 9.75$ (figure 6) where the single outlying point is not used in the analysis. A comparison of the linear model based on (13) (figure 6) with the relation between the relative humidity variance and the moisture variance term (figure 5) indicates that the parameterization of the moisture variance (12) apparently does not seriously increase the scatter. The coefficient $C1$ in (13) is expected to absorb the smaller contributions from the temperature variance and temperature-moisture correlation terms (first and third terms on the right hand side) in (10). The coefficient $C2$ absorbs the contribution from variations of the vertical velocity-moisture correlation $r^2_{wq}$ in (12).

However, the large percentage of the variance explained by the linear model (13) is of unknown generality. For example, in the case of downward transport of moisture, as occurs with dew formation in the stable nocturnal boundary layer, the second term in (13) must be omitted. Then the turbulent variability of relative humidity is small and large values of average relative humidity are needed to produce cloud cover.

### b) Vertical velocity variance

For unstable conditions, we use the similarity formulation for vertical velocity variance from Lenschow et al. (1980)

$$\sigma^2_w = 1.8 \, (z / h)^{2/3} \, (1 - 0.8 \, z / h)^2 \, w_*^2 \tag{14}$$

where $z$ is height, $h$ is boundary-layer depth, and $w^*$ is the convective velocity scale. For the stable case, we use Stull's (1988) relationship based on the data of Caughey et al. (1979)

$$\sigma^2_w = 2.5 \, [1 - (z / h)^{0.6}] \, u_*^2 \tag{15}$$

where $u^*$ is the friction velocity.

For weakly unstable conditions, we evaluate both (14-15) and take the maximum of these two expressions. This allows $\sigma_w$ to be determined by either mechanical or convective generation of turbulence depending on which one is larger.

### c) Mesoscale variation of relative humidity

Mesoscale variations of relative humidity are related to surface inhomogeneity and transient mesoscale disturbances. With larger horizontal grid size, more of the mesoscale motions become "subgrid" so that we would expect the mesoscale standard deviation $\sigma_{RH meso}$ to increase with grid size. Then for relative humidity significantly less than one, the chance of some cloud cover increases with the horizontal size of the grid area.

To examine the effect of grid size on relative humidity variations, we compute 5-km averages of relative humidity for the 18 upper level flight legs in HAPEX. We then determine the ensemble average of the standard deviations of the 5-km averaged relative humidity ($\sigma_{RHmeso}$) over 10-, 25-, 50- and 100-km segments. An expression for the dependence of $\sigma_{RHmeso}$ on horizontal scale (grid size) is constructed as a least square fit to a logarithmic function (figure 7) and is of the form

$$\sigma_{RHmeso} = a_0 + a_1 \log(\Delta x);\ \Delta x \geq 5\ km. \tag{16}$$

where $a_0$ = -0.0267, $a_1$ = 0.0382 km$^{-1}$, and $\Delta x$ is the horizontal scale in kilometers. We will include this contribution to the relative humidity variation through application of (3b) in the model simulations reported in section 6.

### 3.2.4. CLOUD TRANSMISSION OF SOLAR RADIATION

Transmission of solar radiation through the fractional cloud cover determines the amount of radiation that reaches the surface. The formulation of this transmission may be as important as the prediction of fractional cloud cover itself. Expressions for transmission of solar radiation through clouds (Fairall et al., 1990; Kasten and Czeplak, 1980; Stephens, 1978), are based on functions of solar elevation, cloud thickness, liquid water content, and cloud geometry. In the current simple version of our boundary-layer model, solar elevation is available while the other factors are not. Therefore, we choose a transmission function with an implicitly fixed optical depth following Liou (1976) where the fraction transmitted $t$ is approximated as

$$t = 0.06 + 0.17 \cos\theta \tag{17}$$

where $\theta$ is the solar elevation angle (0° overhead and 90° at the horizon).

### 3.2.5. MODEL TESTING

We incorporate the fractional cloud cover formulation (3a-b, 13, 16) with a simple boundary-layer model which was developed to simulate the interactions of the atmospheric boundary layer, soil, and vegetation (Ek and Mahrt, 1989). The planetary boundary-layer model (Troen and Mahrt, 1986; Holtslag et al., 1990) is coupled with an active two-layer soil model (Mahrt and Pan, 1984) and a primitive plant canopy model (Pan and Mahrt, 1987).

The following comparisons of the boundary-layer model with HAPEX data attempt to study the sensitivity of the cloud cover formulation to less-than-perfect information from the rest of the boundary-layer model. In addition to the various model assumptions, errors in the one-dimensional model result from the external specification of the mean vertical motion and the variable geostrophic wind, and from the omission of horizontal advection of temperature and moisture.

We implement the cloud cover formulation at the level of maximum relative humidity which is normally the first level below the boundary-layer top. We choose the 12 days from the HAPEX data set with minimal cloud activity above the boundary layer for which soundings are available. Only two of these days were previously used in the determination of the coefficients for the cloud cover model. Radiosondes launched from the central site in HAPEX at Lubbon at 0600 LST measured vertical profiles of temperature, pressure, humidity, and winds and provide initial atmospheric conditions for the model simulations. Mean vertical motion is specified to increase linearly with height from zero at the surface and is fitted to a layer averaged value centered at 2 km from the mesoscale analysis of Noilhan (1989). Geostrophic winds are estimated from a layer average of the actual winds at approximately 1500 m from the 0600 LST soundings and are assumed to be height-independent. Equating the initial wind and the geostrophic wind prevents unrealistic inertial oscillations. Other details concerning the model input data are included in Holtslag and Ek (1990). Model simulations begin at 0600 LST and are integrated for 14 hours.

Aircraft observations over the pine forest provide an ensemble average of the spatial averages of fractional cloud cover from several midday flight legs, each approximately 50 km. Surface observations of downward solar radiation in the forest clearing at Lubbon provide an independent assessment of the range of fractional cloud cover for the two-hour period centered at 1400 LST (table 2).

Model simulations of fractional cloud cover averaged over the period 1300-1500 LST are not highly correlated with the observed values (table 2). Investigation of the source of these differences indicates that the modelled fractional cloud cover is sensitive to uncertainties in the mean vertical motion and sensitive to the omission of horizontal advection. In contrast, the modelled prediction of the cloud cover is not sensitive to the values of the coefficients in the cloud cover formulation. For example, changing the values of the coefficients $C1$ and $C2$ in the relationship for $\sigma_{RHturb}$(13) by ±50% alters the modelled fractional cloud cover from the prototype cases by an average absolute value of less than 2% for the 12 days studied, with a 12% maximum absolute difference. The estimated uncertainty of the coefficients $C1$ and $C2$ for the $\sigma_{RHturb}$ formulation (13) is only about ±10% for this data set based on envelopes of the data in figure 6.

Changing the value of $\sigma_{RHmeso}$ (16) by ±50% from the prototype values leads to an average absolute difference of fractional cloud cover of only 1-2%, with a 15% maximum absolute difference. The estimated uncertainty for $\sigma_{RHmeso}$ is probably less than ±15% (except for the 10-km value) as might be surmised from figure 7 for the present data set. If expanded to different geographical regions, $\sigma_{RHmeso}$ may be quite variable.

Model simulations were conducted to test the sensitivity of the fractional cloud cover formulation to changes of the mean vertical motion specified in the one-dimensional model. Incrementally changing the vertical motion from -2.0 cm $s^{-1}$ to +1.0 cm $s^{-1}$ at 1 km causes the fractional cloud cover to increase from zero to complete overcast for all of the 12 HAPEX simulations (figure 8). The change of cloud cover is normally concentrated over a relatively small range of vertical motion values which defines a *cloud transition zone*. The value of the vertical motion defining the cloud transition zone varies from day to day depending on boundary-layer characteristics. For example, an increase in vertical motion from 0.6 to 0.8 cm $s^{-1}$ on 25 May leads to an increase of cloud cover from clear to complete overcast. The range of mean vertical motion values separating clear and cloudy conditions is proportional to the modelled standard deviation of relative humidity (13, 16). Therefore the sensitivity of the modelled cloud cover could depend crucially on the value of this standard deviation if the value of the mean vertical motion is in a transition zone.

These tests underscore the sensitivity of boundary-layer growth and cloud cover to the vertical motion specified in the boundary-layer model. The observed values of cloud cover exhibit more intermediate values (nearer 0.50) than modelled values of cloud cover. This difference between the distribution of cloud covers appears to be the main discrepancy between the observed and modelled cloud cover (table 2). There is some evidence that the mesoscale inhomogeneity of cloud cover was greater on the days being used to test the model compared to the days used to calibrate (16) leading to more intermediate cloud cover values for the observed test days. There is also evidence that the averaging of the aircraft observed cloud cover over the three- to four-hour period, in concert with evolving meso- and synoptic-scale flow (not present in the model) led to more intermediate values of observed cloud cover.

In contrast, the specified vertical motions completely suppress modelled cloud development or initiate complete model cloud development (table 2) on eight of the twelve days studied. Only in cases where the specified mean vertical motion corresponds to values in the cloud transition zone, is partial cloud cover predicted. Because of this sensitivity to vertical motion and the substantial uncertainties of the specified vertical motion, the testing of the cloud model appears inconclusive. The inability to assess the mean vertical motion in field programs may be a generic difficulty for testing models in cloud transition cases.

However, the model tests do indicate interesting interactions between cloud cover and vertical motion. For example, reduced subsidence normally leads to greater boundary-layer growth. However, cloud cover resulting from mean rising motion can eventually lead to *smaller* boundary-layer depths compared to the cloud-free case caused by subsidence. With rising motion and cloud development, boundary-layer growth due to surface heating and entrainment is reduced (figure 9). Since the boundary layer in this case grows primarily due to the rising motion and not to entrainment, drying of the boundary layer by entrainment is reduced and the cloud cover is maintained. Inverting this argument, the boundary layer may be deeper with weak subsidence than with weak rising motion because prevention of cloud cover leads to greater surface heating. Of course, with strong subsidence, the boundary layer becomes shallower in comparison to the cases of weaker subsidence or rising motion (figure 9).

The neglect of horizontal advection in the model can also lead to large model errors for the boundary-layer depth and fractional cloud cover. For example on 22 June, omission of low-level horizontal advection of cool dry air in the model apparently contributes to an overestimation of the boundary-layer depth by 700 m and false prediction of overcast when in fact observed clouds did not develop. On 21 May, omission of low-level horizontal advection of warm dry air may account for the underprediction of the boundary-layer depth by 600 m and prediction of complete overcast compared to the observed cloud cover of 0.40.

Modelled cloud development seems less sensitive to specification of the geostrophic wind for the HAPEX days where variations of boundary-layer growth is more controlled by variations of surface heating.

### 3.2.6. CONCLUSIONS

This study indicates that both the averaged relative humidity and the small-scale variability of relative humidity contribute significantly to the spatially averaged boundary-layer cloud cover. With greater variability of relative humidity, clouds first form at a lower average relative humidity. The averaged relative humidity is computed from spatially averaged variables from aircraft measurements in the upper part of the boundary layer in HAPEX. For this data, turbulent and mesoscale variations of relative humidity contribute about equally to the total subgrid variation of relative humidity and cloud cover for a hypothetical horizontal grid size of about 100 km. In the upper part of the boundary layer, the variability of relative humidity is large partly because of the systematic negative correlation between variations of temperature and moisture on both turbulent scales and mesoscales. However, the moisture variability contributes more to the spatial variability of relative humidity than does temperature variability or temperature-moisture correlations. The turbulent variability of relative humidity at the boundary-layer top is greater with significant surface heating.

From this data analysis, a model of boundary-layer fractional cloud cover is developed by formulating turbulent variations of relative humidity in terms of boundary-layer similarity theory and determining the mesoscale variation to be a function of horizontal grid size. Testing the fractional cloud cover formulation in a one-dimensional boundary-layer model indicates more sensitivity of the modelled cloud cover to the specified vertical motion field than to the adjustable coefficients of the cloud cover formulation. Horizontal advection of heat and moisture appear to be important on some of the days. The model results indicate that the relation of boundary-layer depth and boundary-layer clouds to the mean vertical motion depends on other boundary-layer conditions in a complex way. For example, with sufficient boundary-layer moisture, decreasing mean subsidence or increasing mean rising motion may lead to decreased boundary-layer depth through boundary-layer cloud development and reduced generation of turbulence by decreased surface heating. Otherwise decreased mean subsidence or increased mean rising motion leads to greater boundary-layer growth.

This study should be extended to additional data sets to test the performance of the proposed cloud cover model (3a-d, 13-16) under more diverse geographic and atmospheric conditions. For example, the formulation of the mesoscale subgrid variability undoubtedly depends on the surface inhomogeneity which in turn depends on geographic location.

*Acknowledgements.* The useful help and comments of A. A. M. Holtslag, Sam Chang, Ken Yang, and James Coakley are greatly appreciated, as well as the computational work of Wayne Gibson and technical assistance provided by Susanna M. Bremer and Jacob H. Jensen. This material is based upon work supported by the Geophysical Laboratory under contract F19628-88-K-001, and the National Science Foundation under grant ATM-8820090. The National Center for Atmospheric Research is acknowledged for computer resources and the use of the King Air research aircraft in HAPEX.

**Albrecht, B. A.**, Parameterization of trade-cumulus cloud amounts. *J. Atmos. Sci.*, 38, 97-105, 1981.

**André, J-C. and collaborators**, HAPEX-MOBILHY: First results from the special observing period. *Ann. Geophys. ser.*, **B6** (5), 477-492, 1988.

**Betts, A. K.**, Thermodynamics of mixed stratocumulus layers: saturation point budgets. *J. Atmos. Sci.*, **40**, 2655-2670, 1983.

**Caughey, S. J., J. C. Wyngaard, and J. C. Kaimal**, Turbulence in the evolving stable layer. *J. Atmos. Sci.*, **36**, 1041-1052, 1979.

**Chu, C.-T.**, Parameterization of shallow convection in the boundary layer. Master's Thesis. Oregon State University, Corvallis, Oregon, 1986.

**Ek, M. and L. Mahrt**, A user's guide to OSU1DPBL version 1.0.3: A one-dimensional planetary boundary-layer model with interactive soil layers and plant canopy. Department of Atmospheric Sciences, Oregon State University, Corvallis, Oregon 97331, 1989.

**Fairall, C. W., J. E. Hare, and J. B. Snider**, An eight-month climatology of marine stratocumulus cloud fraction, albedo, and integrated liquid water, *J. Climate*, 3, 847-864, 1990.

**Holtslag, A. A. M., E. I. F. de Bruijn, and H.-L. Pan**, A high resolution air mass transformation model for short-range weather forecasting. *Mon. Wea. Rev.*, **118**, 1561-1575, 1990.

**Holtslag, A. A. M. and M. Ek**, Simulation of surface fluxes and skin temperature: Preliminary results for the pine forest in HAPEX-MOBILHY. Preprint from the American Meteorological Society, Ninth Symposium on Turbulence and Diffusion, 30 April 30 - 3 May, Risø, Roskilde Denmark, 1990, to be submitted to *Bound.-Layer Meteor.*

**Kasten, F. and G. Czeplak**, Solar and terrestrial radiation dependent on the amount and type of cloud. *Solar Energy*, 24, 177-189, 1980.

**Lenschow , D. H., J. C. Wyngaard, and W. T. Pennell**, Mean-field and second-moment budgets in a baroclinic, convective boundary layer. *J.*

*Atmos. Sci.*, 37, 1313-1326, 1980.

**Liou, K.-N.**, On the absorption, reflection and transmission of solar radiation in cloudy atmospheres. *J. Atmos. Sci.*, 33, 798-805, 1976.

**Mahrt, L.**, Boundary-layer moisture regimes. *Quart. J. Roy. Met. Soc.*, 117, 1991.

**Mahrt, L. and H.-L. Pan**, A two-layer model of soil hydrology. *Bound.-Layer Meteor.*, 29, 1-20, 1984.

**Noilhan, J.**. Mesoscale analysis (vertical motion) during HAPEX-MOBILHY 1986 Special Observing Period, CNRM/4M. Toulouse. France, 1989.

**Pan, H.-L. and L. Mahrt**. Interaction between soil hydrology and boundary-layer development. *Bound.-Layer Meteor.*, 38, 185-202, 1987.

**Slingo, J. M.**, A cloud parameterization scheme derived from GATE data for use with a numerical model. *Quart. J. Roy. Met. Soc.*, **106**, 747-770, 1980.

**Stephens, G. L.**, Radiation profiles in extended water clouds. II: Parameterization schemes. *J. Atmos. Sci.*, 35, 2123-2132, 1978.

**Stull, R. B.**, An introduction to boundary-layer meteorology. Atmospheric Sciences Library, Kluwser Academic Publishers, 666 pp., 1988.

**Troen, I. and L. Mahrt**, A simple model of the atmospheric boundary layer: Sensitivity to surface evaporation. *Bound.-Layer Meteor.*, 37, 129-148, 1986.

**Wilde, N. P., R. B. Stull, and E. W. Eloranta**, The LCL zone and cumulus onset. *J. Clim. and App. Meteor.*, 24, 640-657, 1985.

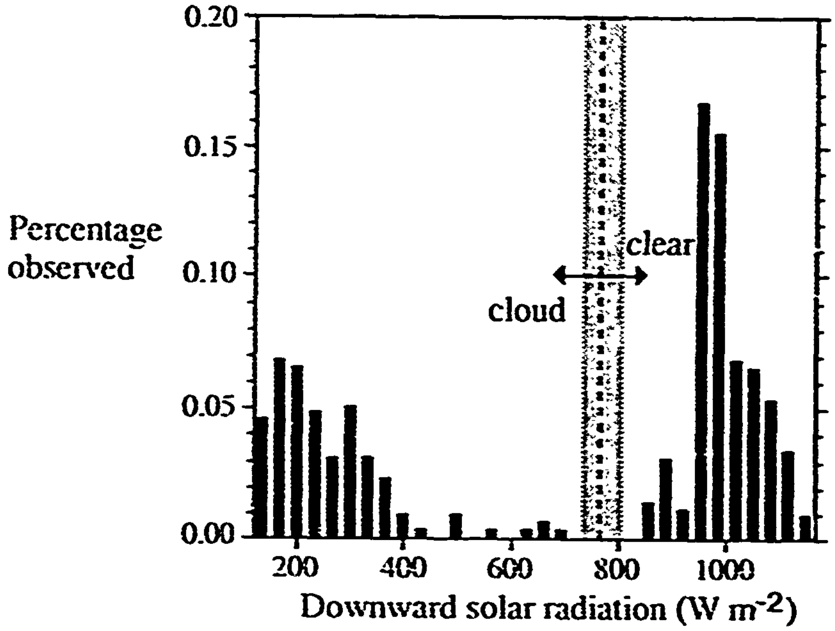

Figure 1.
*Frequency distribution of downward solar radiation from a flight leg in HAPEX on 21 May 1986 with 38% cloud cover.*

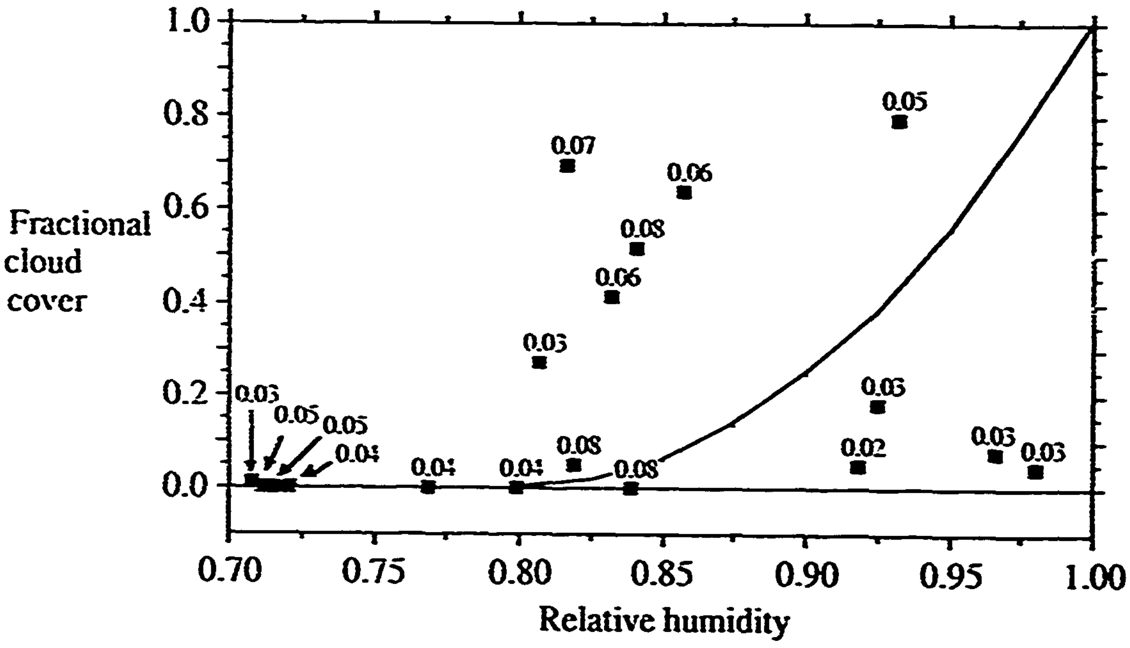

*Figure 2.*
*50-km horizontal averages of cloud cover versus relative humidity (squares). Plotted values of standard deviation of relative humidity indicate greater cloud cover with larger variation of relative humidity for the 18 upper-level flight legs ($z/h \geq 0.6$) from HAPEX; and Slingo (1980) cloud cover model (solid line).*

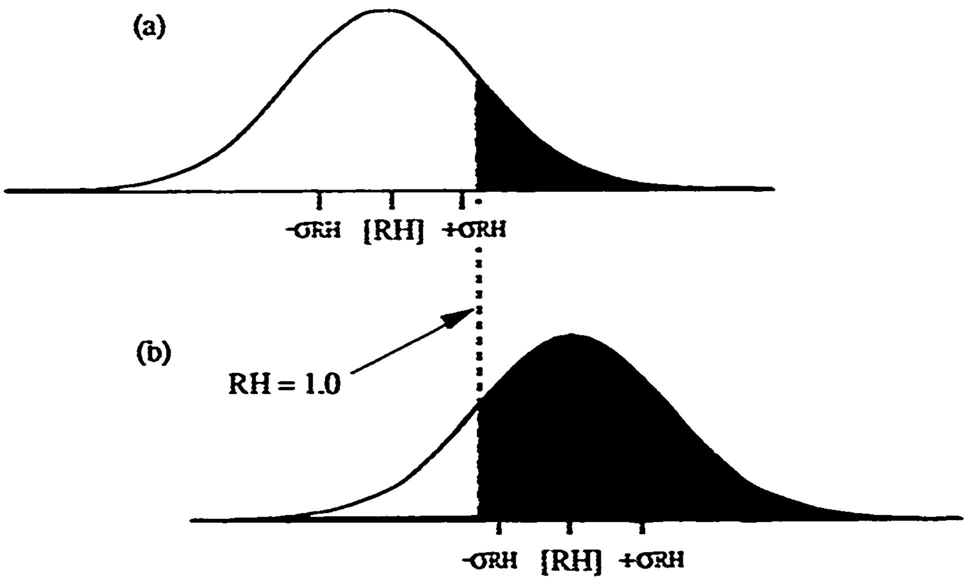

Figure 3.
*Cloud cover (dark region) for a Gaussian distribution of relative humidity with the average total water relative humidity (a) less than 1.0 and (b) greater than 1.0.*

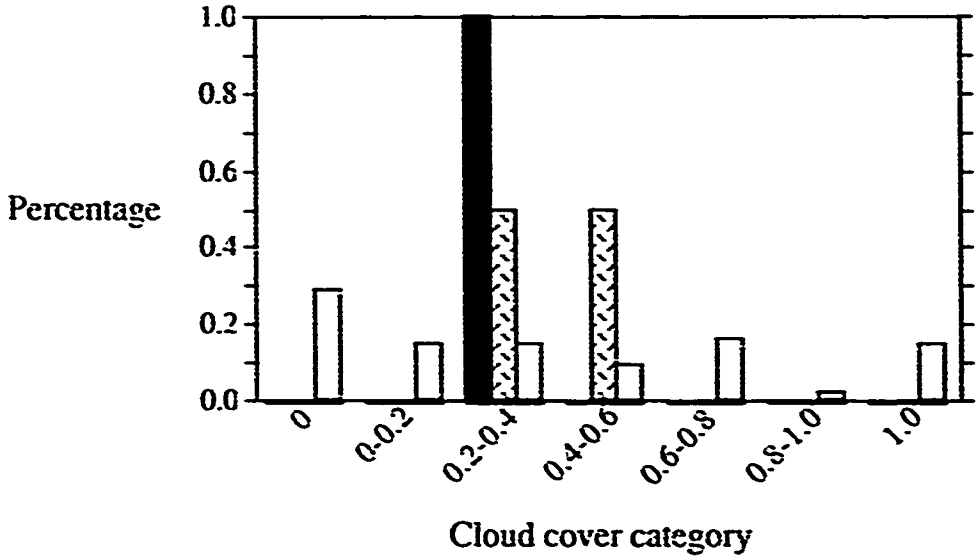

Figure 4.
*Percentage of occurrence for different cloud cover categories from the flight leg in figure 1 for different horizontal scales: 1-km (white), 10-km (hatched) and 50-km (black).*

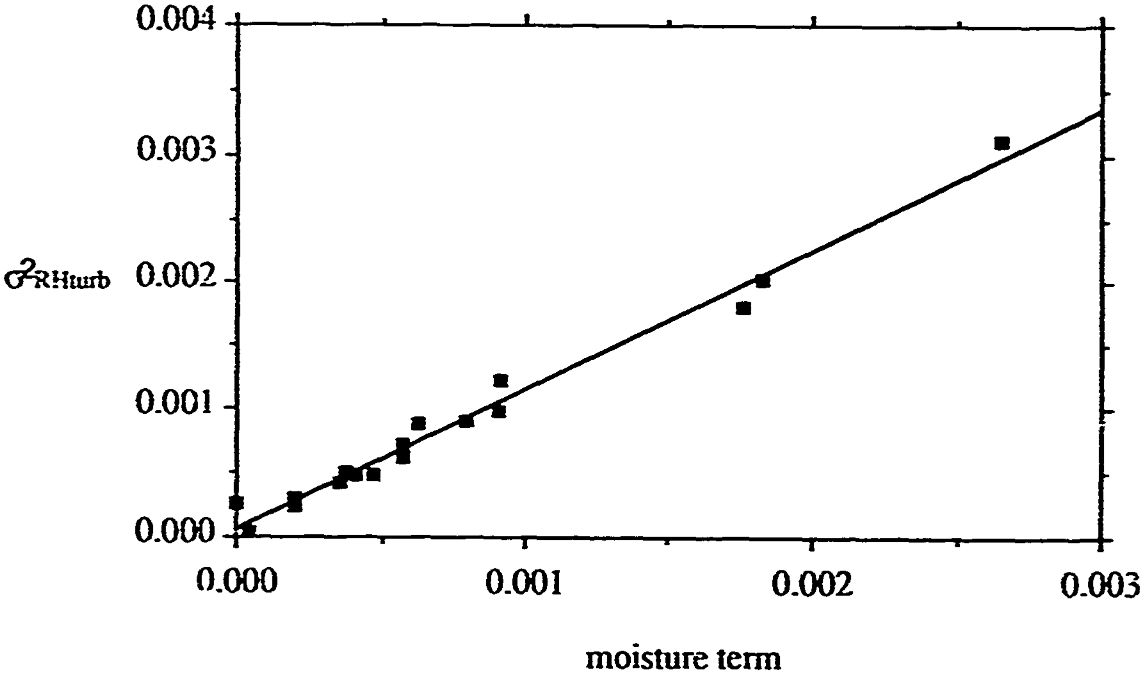

Figure 5.

*Turbulent scale relative humidity variance versus the moisture variance contribution (second term on right-hand side of (10)).*

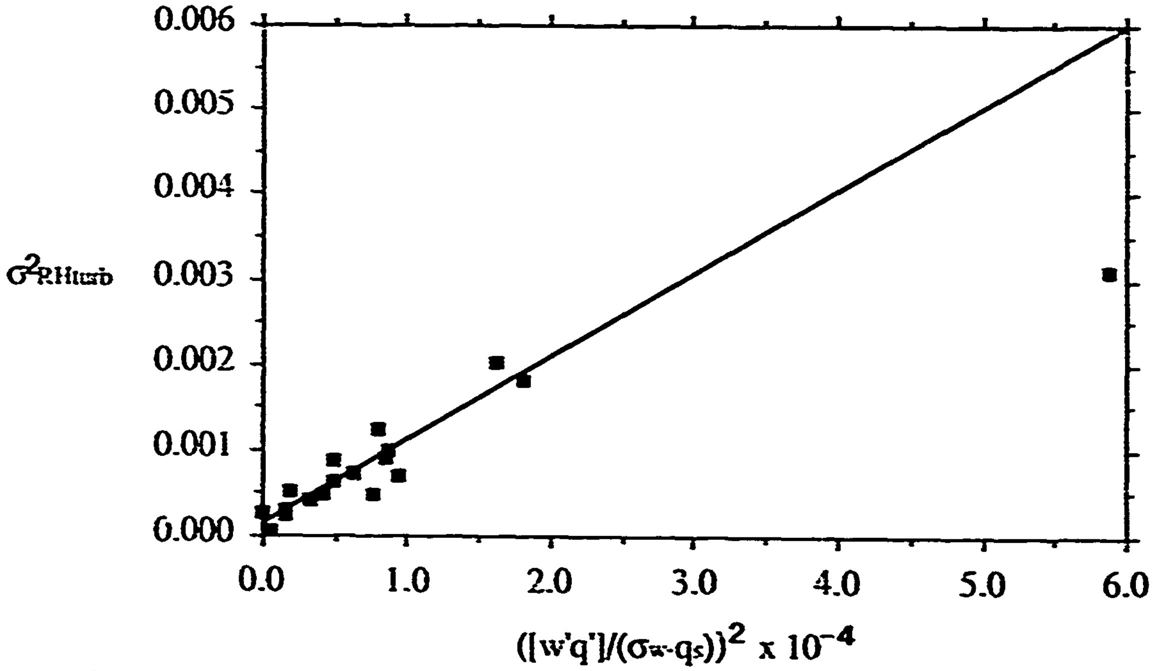

Figure 6.

*Relationship between the turbulent variance of relative humidity and the moisture flux term (2nd term on right hand side in (13)). The y-intercept provides an estimate of C1 while the slope is C2.*

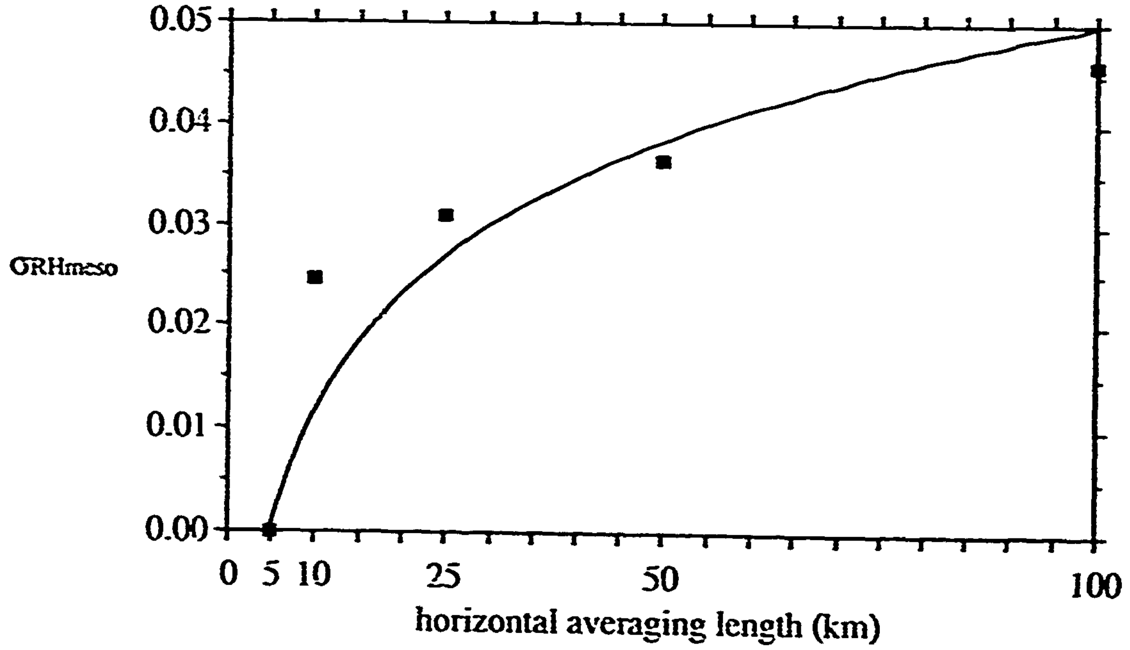

Figure 7.

*Logarithmic fit of the mesoscale standard deviation of relative humidity to the horizontal averaging length.*

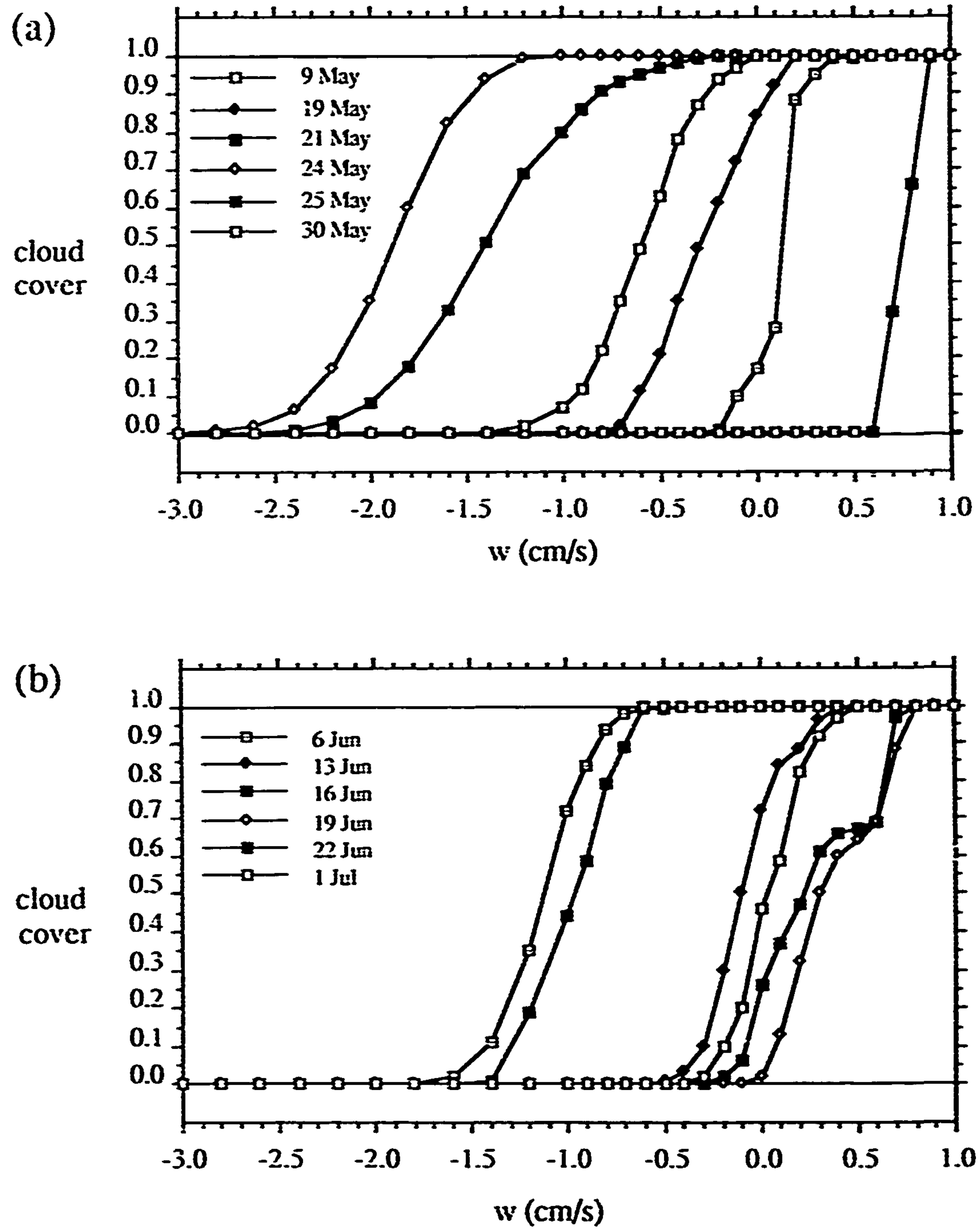

Figure 8

*Fractional boundary-layer cloud cover and vertical motion at 1 km for model simulations during HAPEX in (a) May and (b) June and July. Cloud cover values are averaged from 1300-1500 LST.*

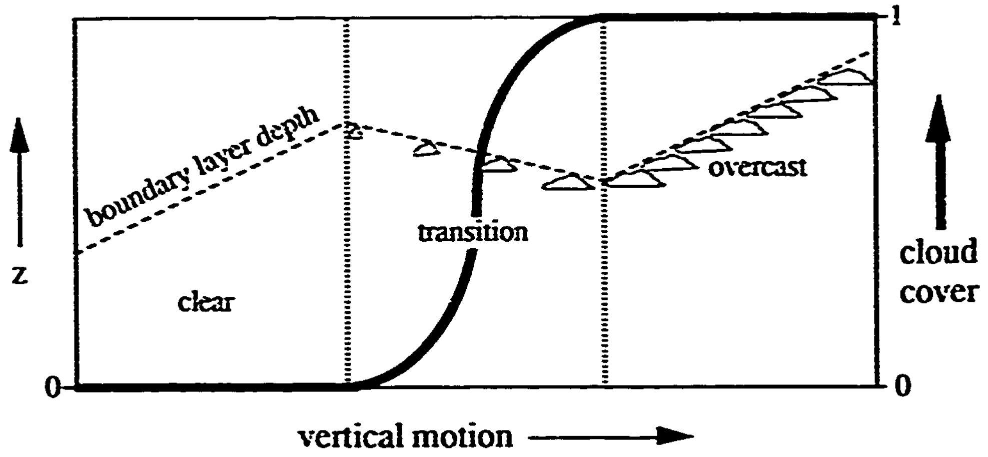
boundary layer depth
z
clear
transition
overcast
cloud cover
0
1
0
vertical motion

Figure 9.
*Schematic relationship of the afternoon cloud cover and boundary-layer depth to the mean vertical motion.*

Table 1.

*Contributions to the variance of relative humidity on the turbulent scale from the three terms in (10) for 18 upper level flight legs in HAPEX.*

| date | cloud cover | z/h | $\sigma_T$-term<br>(x $10^{-5}$) | $\sigma_q$-term<br>(x $10^{-5}$) | $r_{Tq}$-term<br>(x $10^{-5}$) | $\sigma_{RH}^2$turb<br>(x $10^{-5}$) |
|---|---|---|---|---|---|---|
| 9 May | 0.41 | 0.60 | 3.0 | 79.1 | 6.2 | 88.3 |
| 9 May | 0.27 | 0.60 | 2.4 | 46.6 | -0.9 | 48.1 |
| 24 May | 0.79 | 0.60 | 3.4 | 56.7 | 2.9 | 63.0 |
| 6 June | 0.64 | 0.74 | 3.0 | 90.4 | 7.3 | 100.8 |
| 6 June | 0.70 | 0.78 | 2.2 | 175.9 | 6.4 | 184.6 |
| 6 June | 0.52 | 0.80 | 3.8 | 183.0 | 19.8 | 206.6 |
| 13 June | 0.01 | 0.61 | 0.0 | 0.2 | 0.0 | 0.2 |
| 19 June | 0 | 0.72 | 4.3 | 90.7 | 3.2 | 127.4 |
| 19 June | <0.01 | 0.66 | 2.7 | 57.2 | 15.9 | 75.8 |
| 22 June | 0.05 | 0.61 | 4.1 | 265.4 | 46.2 | 315.7 |
| 1 July | 0.05 | 0.60 | 1.3 | 3.7 | 0.1 | 5.1 |
| 2 July | 0 | 0.78 | 2.0 | 36.8 | 11.0 | 49.8 |
| 2 July | 0 | 0.85 | 3.9 | 63.4 | 25.3 | 92.6 |
| 8 July | 0.04 | 0.70 | 3.8 | 20.5 | 6.6 | 30.9 |
| 8 July | 0.08 | 0.66 | 3.4 | 35.7 | 3.5 | 42.7 |
| 8 July | 0.18 | 0.61 | 2.6 | 20.3 | 1.2 | 24.1 |
| 11 July | 0 | 0.60 | 2.8 | 56.9 | 11.0 | 70.8 |
| 11 July | 0 | 0.60 | 1.4 | 41.4 | 5.1 | 48.0 |

Table 2.
*Midday fractional cloud cover from aircraft and surface observations, and from cloud model simulations for 12 HAPEX days.*

| | Boundary-Layer Cloud Cover Observations | | Cloud Model |
|---|---|---|---|
| Date | Aircraft | Surface | Simulations |
| 9 May | 0.37 | 0.00-0.70 | 0.99 |
| 19 May | 0.00 | 0.00 | 0.00 |
| 21 May | 0.40 | 0.00-0.70 | 0.96 |
| 24 May | 0.33 | 0.00-0.75 | 1.00 |
| 25 May | 0.00 | 0.00 | 0.00 |
| 30 May | 0.50 | 0.00-0.85 | 0.35 |
| 6 June | 0.73 | 0.00-0.85 | 1.00 |
| 13 June | 0.03 | 0.00 | 0.37 |
| 16 June | 0.00 | 0.00 | 0.00 |
| 19 June | <0.01 | 0.00-0.20 | 0.15 |
| 22 June | <0.01 | 0.00-0.35 | 1.00 |
| 1 July | 0.48 | 0.00-0.30 | 0.46 |

Chapter 4.1

# Surface Roughness Length

## 4.1.1. Introduction

The surface fluxes of heat, moisture and momentum are of great importance for the correct description of the turbulent structure and mean condition in the atmospheric boundary layer (ABL). Over land, the fluxes are influenced by the interaction of the (vegetated) surface and the atmosphere, and the transport of heat and moisture in the soil. As such the fluxes may play a significant role in the climate system and in the development of weather.

In this study, we simulate the interaction of the atmospheric boundary layer with the soil and canopy system of a pine forest. The simulations are made with a one-dimensional ABL model coupled to a simple description of the soil and vegetation. For this purpose we utilize the model descriptions by Mahrt and Pan (1984), Troen and Mahrt (1986), Pan and Mahrt (1987), and Holtslag et al. (1990).

The surface parameters in the model are chosen to be representative for the meso-$\gamma$-scale (roughly 10 km). Special emphasis is given on the choice for the roughness lengths of heat and moisture. Often these parameters are taken equal to the one of momentum, although studies have shown that actual differences can be at least one order of magnitude over vegetated surfaces (Garratt, 1978; Brutsaert, 1982; Holtslag and de Bruin; 1988; Mason, 1989). Improper choice of the roughness lengths for heat and moisture will especially influence the surface skin temperature and the surface heat flux, which in turn may affect ABL development (Garratt and Pielke, 1989).

The simulations are compared with data from the HAPEX-MOBILHY project, where aircraft measurements are used to represent the proper scale. Special emphasis is placed on the surface fluxes, skin temperature and boundary layer growth.

### 4.1.2. Data from HAPEX-MOBILHY

Data used in this study were taken during the Special Observing Period of the HAPEX-MOBILHY project carried out in southern France from May to July 1986. Data for the days of interest (19 May and 19 June) were obtained from three sources, 1) aircraft, 2) surface observations, and 3) radiosondes. Unfortunately, no data of the forest tower were available on the selected days. The pine forest region in HAPEX is the most homogeneous compared to the other regions and provided the largest data set.

The aircraft data consisted of two sets of flux and sounding data collected by the NCAR King Air aircraft. The 19 May data set follows Mahrt (1989) and the 19 June data set follows Hildebrand (1988). To determine the fluxes of heat, moisture and momentum on the meso-$\gamma$-scale from the aircraft data, they used high pass filters of 5 km for 19 May and 15 km for 19 June. Since the aircraft flew at a height of 100 to 200 m, the fluxes were augmented by 10% to better represent their respective surface values. A surface temperature radiometer on the aircraft was used to obtain the skin temperature; raw observations were then averaged over 5 km to provide representative values over the forest. Aircraft soundings were also taken during these two days of HAPEX, with the vertical profiles of temperature and moisture used to subjectively determine the boundary layer depth. Flight log data (Stull, 1986) were also used as a rough indicator of boundary layer depth.

Surface observations were taken at the central site (Lubbon) in a forest clearing and consisted of sensible heat flux measurements using a flux-gradient relationship, and latent heat flux measurements using the residual method (since the soil heat flux and net radiation were also measured). Data from this site are provided as general estimates only since the site is only marginally representative of the surface fluxes found in the surrounding forest.

Radiosondes launched from the central site measured temperature, pressure and humidity which were used to determine boundary layer depth, and were released on an approximately 3-hour interval from 6.00 to 18.00 UTC for 19 May, and a 2-hour interval from 6.00 to 18.00 UTC for 19 June.

### 4.1.3. Model description and parameter estimation

The model used in this study was developed to simulate the interactions of the atmosphere, soil, and (vegetated) surface. The planetary boundary layer model (Troen and Mahrt, 1986; Holtslag et al., 1990) is coupled with an active two-layer soil model (Mahrt and Pan, 1984) and a primitive plant canopy model (Pan and Mahrt, 1987). The equations used in this composite model are comprehensive enough to approximate the physical processes thought to be most important, yet simple and robust enough to allow both crude and high-resolution model diurnal simulations to be run in a few minutes on a personal computer under a variety of diverse atmospheric conditions. As a stand-alone model it is useful for a number of different sensitivity experiments in local weather forecasting, air pollution, soil chemistry, and soil hydrology. It has also been incorporated into more complex three dimensional global models such as the AFGL global spectral model (Brenner et al., 1984). A modified version of the boundary layer package is used in the KNMI air mass transformation model (Holtslag et al., 1990).

The moisture budget of the coupled atmospheric and soil-vegetation model is schematically depicted in Figure 1. The model allows for a distinction of direct evaporation from the soil, transpiration by the vegetation, and evaporation of precipitation intercepted by the canopy (see Pan and Mahrt, 1987). Transpiration is related to the density of vegetation (the shielding factor), a plant resistance factor, and the soil moisture content. For the pine forest, the shielding factor was estimated effectively at 85% (Pinty et al., 1989). This number reflects the coverage by the pine trees and the under cover of green growing fern. Pan and Mahrt (1987) need to specify the plant resistance factor. In this study the resistance factor is calculated by employing the Penman-Monteith equation. As such we need to specify the canopy resistance, which is taken from the study by Bougeault et al. (1989) to be 100 s/m. The latter value has been found representative for the pine forest near noon time.

The soil moisture content is calculated in the model by solving the diffusion equation for water transport in the soil (Mahrt and Pan, 1984). The wilting point, where root uptake ceases, is specified at 0.07. The soil model consists of a thin upper layer (5 cm thick), which responds mainly to diurnal variation; and a thicker lower layer (95 cm), which participates more in seasonal changes of water storage. The air dry value for the soil moisture content is taken as 0.16 to represent a sandy soil (Pan and Mahrt, 1987). The initial surface moisture content is taken at a value of 0.20

(Bougeault et al., 1989).

In the model, the surface energy balance is solved to derive an effective surface skin (radiation) temperature, where we do not distinguish between the ground temperature and the canopy temperature (Pan and Mahrt, 1987). The solar radiation is estimated with a procedure by Holtslag and van Ulden (1983), the surface albedo of 0.10 is derived from aircraft observations, and the incoming longwave radiation is parameterized according to Satterlund (1979). Finally, the soil heat flux is derived by solving the diffusion equation for heat in the soil, and the surface fluxes for heat and moisture are described with exchange coefficients between the surface and the atmosphere (Holtslag and Beljaars, 1989).

In the present study, the model description is extended with a displacement height. The latter is estimated at 14 m (2/3 of the height of the trees; see Brutsaert, 1982). Furthermore, we distinguish between the roughness lengths for heat and momentum. The effective roughness length for momentum is estimated at 1 m (Bougeault et. al., 1989). The roughness length for heat is varied over two orders of magnitude to show its influence on the surface fluxes, skin temperature and boundary layer growth. The morning soundings at 6.00 UTC are used to derive the initial profiles for temperature, humidity and wind. The vertical resolution of the ABL model is set to 20 m and the model time step is 3 minutes. The vertical motion is obtained by using data from Noilhan (1989) and we assume zero horizontal advection.

## 4.1.4. Results

We now present preliminary results for simulations over the pine forest for 19 May and 19 June 1986. On 19 May the sky was generally clear with some shallow cumulus developing, and some upper level altocumulus and cirrus (less than 30%). In the early morning a cloud cover of about 50% was observed. The boundary layer grew from about 100 m in early morning to about 1200 m by early afternoon.

Figure 2 shows a comparison of three model runs with the data of the aircraft and the SAMER 5 station in the clearing of the forest for the latent heat flux. The model runs have been made with the parameters as discussed above and varying values of the roughness length for heat. Note that the roughness length for moisture is taken equal to that for heat. It is seen that variation of the roughness length of heat over two orders of magnitude has not a great impact on the latent heat flux estimates. This is probably caused by the fact that the latent heat flux is mostly determined by the canopy resistance and shielding factor. The model results compare well with the noontime values of the aircraft data, but not with those of the clearing. This reflects the fact that our choices for the latter parameters are based on mesoscale calibration studies on different days in the same data set (Pinty et al.,1989; Bougeault et al., 1989). It also confirms that the observations in the forest clearing on the SAMER 5 station are not representative for the forest.

Figures 3 and 4 show a comparison of the model runs with the data for the sensible heat flux and surface skin temperature. Observed noontime values of sensible heat flux were nearly 200 W/m2 as recorded from the aircraft (Mahrt, 1989). Note that this is an approximation from the aircraft level of 100 m and includes a 10% augmentation for a crude extrapolation to the surface. Model sensible heat flux is nearly 300 W/m2 for the case where $z_{0M} = z_{0H}$, but slightly greater than 200 W/m2 for the case where $z_{0M} / z_{0H} = 100$. The skin temperatures derived from the aircraft data are reproduced well by the model simulation with $z_{0M} / z_{0H} = 100$.

Figure 5 shows the comparison of the model simulations and the data for the boundary layer height. The data are based on radiosondes, aircraft observer estimates, and aircraft soundings. An uncertainty band for each type of data is given. It is seen that the boundary layer depths were generally overpredicted by the model, but improve by mid afternoon. The case for $z_{0M} / z_{0H} = 100$ has again the best agreement with the data. The boundary layer depths seem to be out of phase by about two hours; this may be due to a significant cloud cover in the early morning which may have delayed the actual boundary layer growth. At the time of this study, the model did not utilize a reduction of solar energy by clouds. In future studies we will incorporate a cloud package which hopefully improves the comparison for the boundary layer height. In addition, since horizontal advection is omitted, it may have influenced the comparison in Figure 5 as well.

Figure 6 shows the comparison of the model runs with the aircraft data for the friction velocity. It is seen that the influence of varying roughness length for heat is small on the model simulations. This can be explained by the fact that the friction velocity is mostly determined by the wind, and roughness length for momentum in unstable conditions. A variation of the sensible heat flux due to the roughness length for heat has less influence.

Finally, Figures 7 and 8 represent simulations for the sensible heat flux and skin temperature on 19 June 1986. On this day the sky was generally clear with some shallow cumulus developing, and some upper level altocumulus and cirrus observed in the late afternoon. Observed values of sensible heat flux between 13.00 and 14.00 UTC averaged from 175 to 225 W/m2 as recorded from the aircraft (Hildebrand, 1988). This also represents an approximation from the aircraft level of 100 m and includes a 10% augmentation for a crude extrapolation to the surface. The model sensible heat flux at noon is over 300 W/m2 for the case where $z_{0M} = z_{0H}$, but about 250 W/m2 for the case where $z_{0M} / z_{0H} = 100$. These values converge to about 200 W/m2 by 15.00 UTC. Both the sensible heat flux and skin temperature are again better simulated with $z_{0M} / z_{0H} = 100$. The affect on the friction velocity, latent heat flux, and boundary layer height are less conclusive (not shown here).

### 4.1.5. Summary and Discussion

In this paper we have studied the interaction between the atmospheric boundary layer with the soil/canopy system of the pine forest in the HAPEX-MOBILHY project. We have shown how the surface fluxes, the skin temperature, and the boundary layer depth respond to variations in the surface roughness length for heat (and moisture). It appears that the skin temperature and especially the sensible heat flux are sensitive to the choice for the roughness length of heat. This is expected to influence the development of the boundary layer. However, this could not be proven definitively from the present simulations.

Our results show that for the sensible heat flux and the skin temperature, the best agreement with the aircraft data is obtained if we use $z_{0M} / z_{0H} = 100$. The latter ratio is one order of magnitude larger than the ratio obtained by Garratt (1978) for a heterogeneous surface covered with scattered live eucalyptus trees and dry dead grass. Recently, Mason (1989) argued on the basis of theoretical ideas and numerical simulations, that for inhomogeneous terrain the effective roughness length for momentum approaches the largest value of the roughness in the area (the trees in our case). On the other hand, the roughness lengths for heat and moisture approach the smaller values in the area (the under cover of fern). As such our results do agree qualitatively with Mason's arguments, although it has to be explained why those of Garratt (1978) differ.

*Acknowledgements* We would like to thank L. Mahrt for numerous discussions, and Susanna M. Bremer and Jacob H. Jensen for technical assistance. The first author would also like to thank the Department of Atmospheric Sciences of Oregon State University for inviting him for a stay during the summer of 1989. This material is based upon work supported by the United States Geophysical Laboratory, Atmospheric Prediction Branch, under contract F19628-88-K-001. The National Center for Atmospheric Research is acknowledged for computer resources and the use of the observations by the King Air research aircraft in HAPEX.

## REFERENCES

Bougeault, P., B. Bret, P. Lacarrere and J. Noilhan, 1989: Design and implementation of a land surface processes parameterization in a meso-β-scale model. Proceed. workshop on parameterization of fluxes over land surface, 24-26 Oct. 1988. European Centre for Medium-Range Weather Forecasts, Reading UK, p. 95-120.

Brenner, S., C.-H. Yang, and K. Mitchell, 1984: The AFGL Global Spectral Model: Expanded Resolution Baseline Version. Rept. No. AFGL-TR-84-0308, Air Force Geophysics Laboratory, Hanscom AFB, 72 pp. [ADA160370]

Brutsaert, W., 1982: *Evaporation into the atmosphere: Theory, History and Applications.* Reidel, Dordrecht NL, 299 pp.

Garratt, J. R., 1978: Transfer characteristics for a heterogeneous surface of large aerodynamic roughness. *Quart. J. Roy. Met. Soc.*, **104**, 491-502.

Garratt, J. R. and R. A. Pielke, 1989: On the sensitivity of mesoscale models to surface-layer parameterization constants. *Bound.-Layer. Meteorol.*, **48**, 377-387.

Hildebrand, P. H., 1988, Flux and sounding data from the NCAR King Air aircraft during HAPEX. NCAR Technical Note - 319, September 1988. Atmospheric Technology Division, National Center for Atmospheric Research, Boulder, Colorado.

Holtslag, A. A. M. and A. P. van Ulden, 1983: A simple scheme for daytime estimates of the surface fluxes from routine weather data. *J. Clim. Appl. Meteorol.*, **22**, 517-529.

Holtslag, A. A. M. and H. A. R. de Bruin: 1988, Applied modeling of the nighttime surface energy balance over land. *J. Appl. Meteorol.*, **27**, 689-704.

Holtslag, A. A. M. and A. C. M. Beljaars, 1989: Surface flux parameterization schemes; Developments and experiences at KNMI. Proceed. workshop on parameterization of fluxes over land surface, 24-26 Oct. 1988. European Centre for Medium-Range Weather Forecasts, Reading UK, p. 121-147 (Also as KNMI Sci. Rep. 88-06, De Bilt NL).

Holtslag, A. A. M., E. I. F. de Bruijn, and H.-L. Pan, 1990: A high resolution air mass transformation model for short-range weather forecasting. *Mon. Wea. Rev.*, 118, 1561-1575, 1990.

Mahrt, L. and H.-L. Pan, 1984: A two-layer model of soil hydrology. *Bound.-Layer Meteorol.*, **29**, 1-20.

Mahrt, L., 1989: Aircraft-measured moisture fluxes in HAPEX. Final report for grant ATM-8812535, Mesoscale meteorology program, National Science Foundation. Atmospheric Sciences, Oregon State University, Corvallis, Oregon 97331 USA.

Mason, P. J., 1989: Boundary-Layer parameterization in heterogeneous terrain. Proceed. IAMAP 89, 31 July - 12 Aug., Reading UK, paper BL-13 (Vol. II).

Noilhan, J., 1989: Mesoscale analysis (vertical motion) during HAPEX-MOBILHY 1986 Special Observing Period, CNRM/4M, Toulouse, France.

Pan, H.-L. and L. Mahrt, 1987: Interaction between soil hydrology and boundary layer development. *Bound.-Layer Meteorol.*, **38**, 185-202.

Pinty, J.-P., P. Mascart, E. Richard, and R. Rosset, 1989: An investigation of mesoscale flows by vegetation inhomogeneities using an evaporation model calibrated against HAPEX-MOBILHY data. *J. Appl. Meteorol.*, **28**, 976-992.

Satterlund, D. R., 1979: Improved equation for estimating long-wave radiation from the atmosphere. *Water Resources Research*, **15**, 1649-1650.

Stull, R. B. (Ed.), 1986: Airborne scientist flight logs, NCAR King Air N312D, HAPEX-MOBILHY, Toulouse, France, 9 May - 15 July, 1986.

Troen, I. and L. Mahrt, 1986: A simple model of the atmospheric boundary layer: Sensitivity to surface evaporation. *Bound.-Layer Meteorol.*, **37**, 129-148.

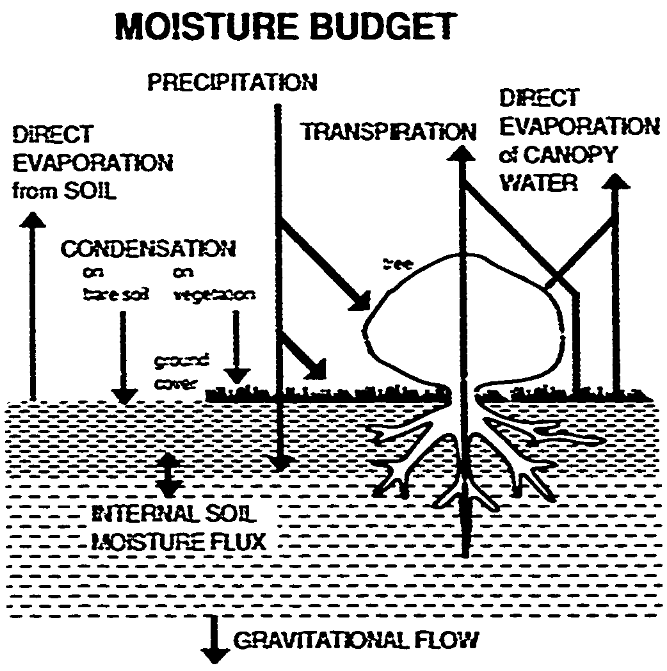
MOISTURE BUDGET
PRECIPITATION
DIRECT EVAPORATION from SOIL
TRANSPIRATION
DIRECT EVAPORATION of CANOPY WATER
CONDENSATION
on bare soil
on vegetation
tree
ground cover
INTERNAL SOIL MOISTURE FLUX
GRAVITATIONAL FLOW

Figure 1. A schematic view of the moisture budget in the present model.

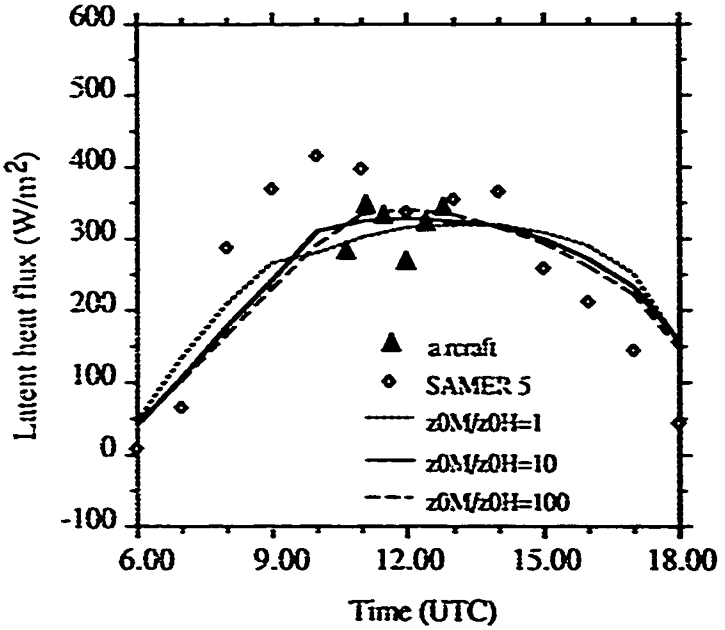

Figure 2. A comparison of model simulations with observations for latent heat flux on 19 May 1986 over the pine forest in HAPEX.

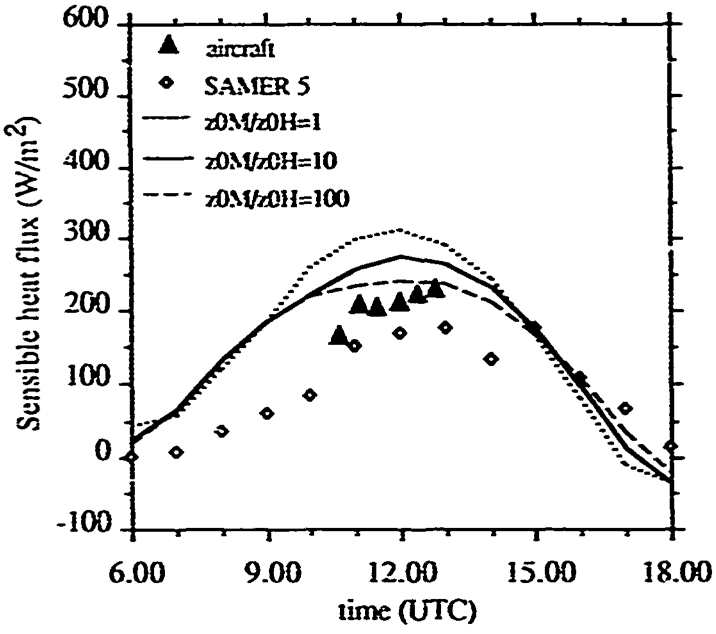

Figure 3. As Figure 2 for the sensible heat flux.

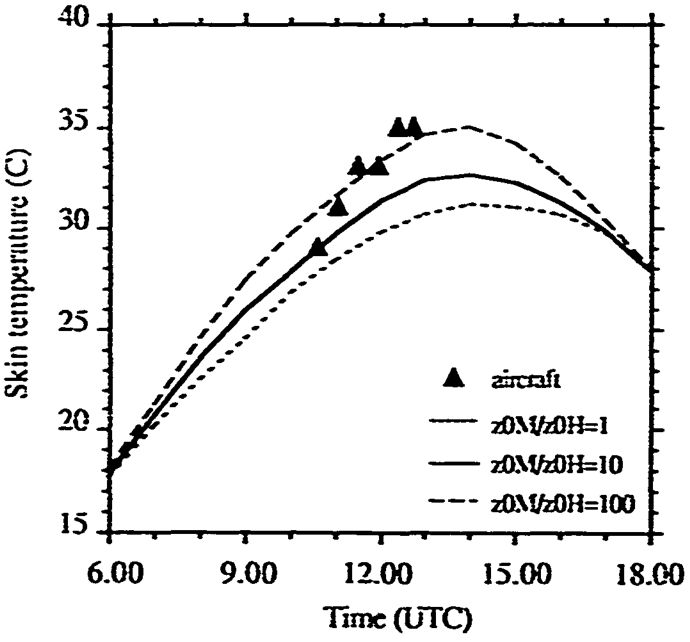

Figure 4. As Figure 2 for the skin temperature.

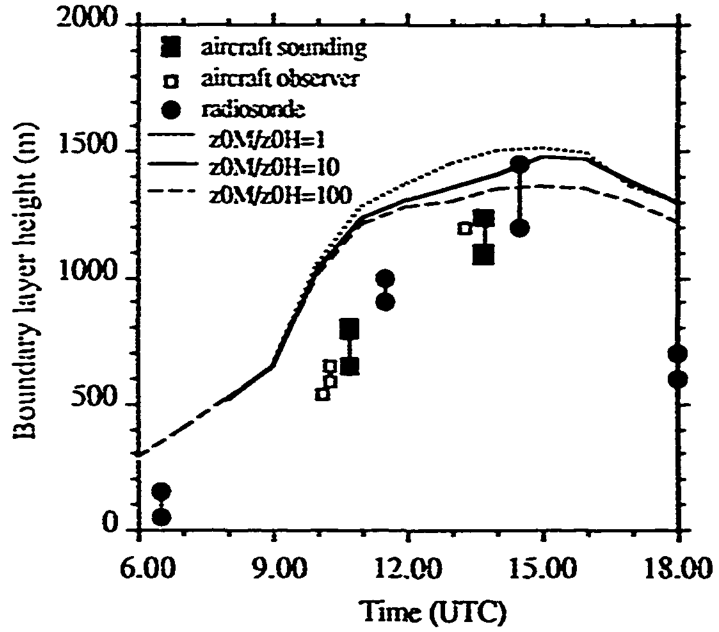

Figure 5. As Figure 2 for the boundary layer height.

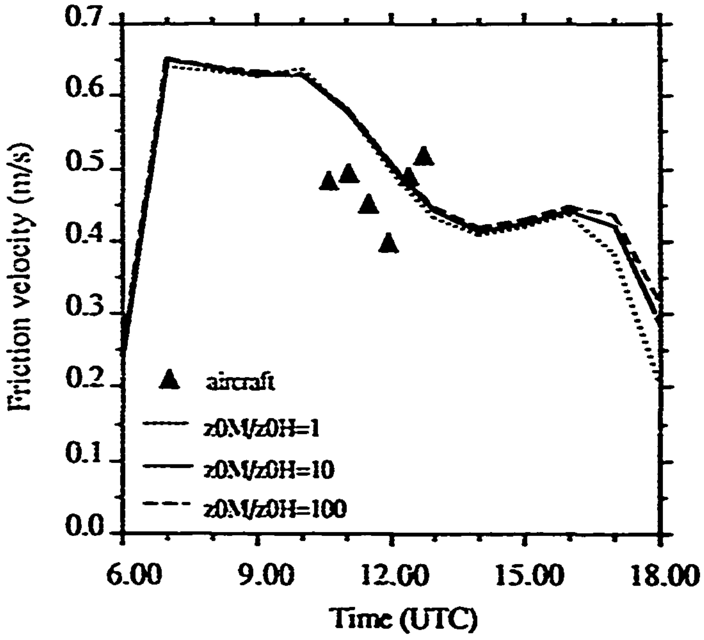

Figure 6. As Figure 2 for the friction velocity.

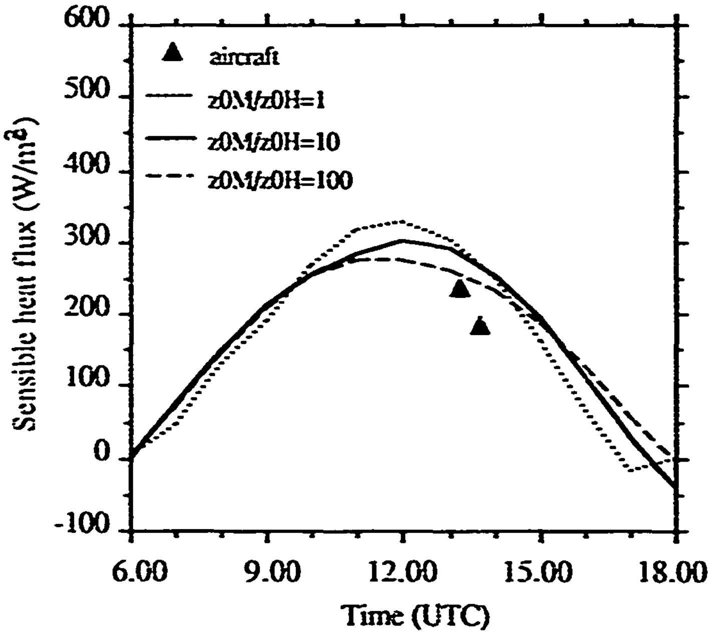

Figure 7. A comparison of model simulations with observations for the sensible heat flux on 19 June 1986 over the pine forest in HAPEX.

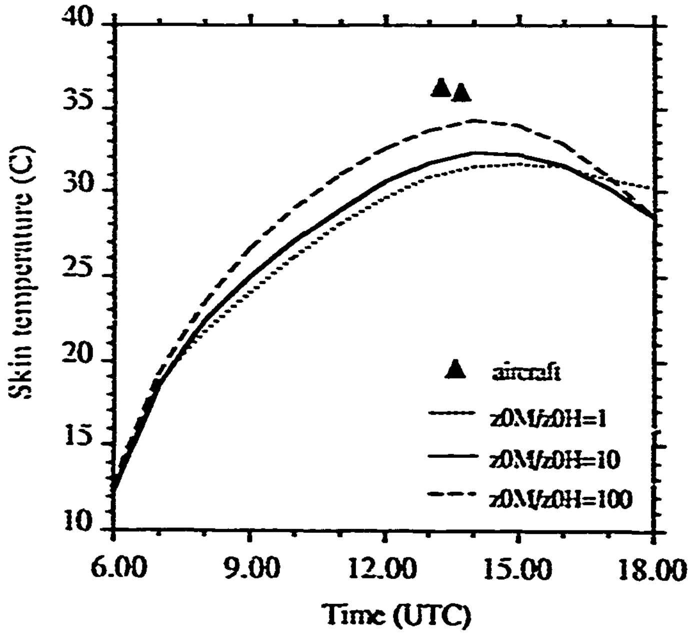

Figure 8. As Figure 7 for the skin temperature.

Chapter 4.2

# Daytime Evolution of Boundary Layer Relative Humidity

## 4.2.1. Introduction

The daytime evolution of the boundary layer moisture field and potential cloud development depends, in part, on soil moisture, the large scale vertical motion field, strength of the inversion capping the boundary layer and the distribution of moisture above the growing boundary layer. The development of near-saturation conditions at the top of the boundary layer depends in a complex way on the above external conditions. This dependence can lead to unexpected nonlinear interactions between soil moisture, surface heating, boundary layer growth and entrainment of dry air. An impression of the complexity is illustrated by the flow chart sketched in Figure 1.

Consider the following two examples. Strong low-level subsidence inversions normally suppress the development of boundary layer clouds. However with a low sun angle and moist soil conditions, boundary layer relative humidity may increase and lead to development of boundary layer stratus or fog. In this case, the increase of relative humidity may result from twenty-four hour radiative cooling and near absence of dry air entrainment.

As a second example, consider the case where boundary layer moisture is limited mainly to the boundary layer with drier air aloft. With a weak capping inversion, wide spread cumulus may develop leading to rapid drying of the boundary layer before precipitating cumulus can develop. With a capping inversion of intermediate strength, boundary-layer clouds are suppressed and boundary layer drying may be prevented. Then a mesoscale disturbance can initiate clouds which then have exclusive rights to the moisture trapped in the boundary layer. This would allow development of precipitation-producing moist convection.

The following study finds other boundary layer interactions where a given influence may assume the expected role, or an unexpected role, depending on the initial boundary layer state and external forcing.

Toward this goal, we examine the daytime evolution of the boundary layer reality humidity field using data from HAPEX (Hydrological and Atmospheric Pilot Experiment, André et al., 1988) and use a simple one-dimensional model of the atmospheric boundary layer, vegetation and soil. The main intention is to examine whether the relative humidity near the top of the growing daytime boundary layer will increase or decrease with time. Given the soil moisture, vegetation properties, large-scale subsidence and vertical distribution of temperature and moisture, will the relative humidity at the top of the boundary layer increase enough to initiate boundary-layer clouds?

The actual development of boundary layer clouds is a complex problem Ek and Mahrt (1991). Our study here concentrates on interactions between boundary layer processes and their influence on the relative humidity near the boundary layer top.

### 4.2.2. Boundary layer relative humidity

To understand the physics of the above examples and other scenarios, we must better understand the diurnal evolution of the moisture field. As an organizational tool, we can frame some of the most important physics in terms of the time rate of change of relative humidity just below the boundary-layer top. In well-mixed conditions, the relative humidity reaches a maximum at this level and becomes an indicator of cloud initiation (Slingo, 1980; Chu, 1986).

The tendency equation for relative humidity (RH) is

$$d/dt(RH) = (dq/dt)/q_{sat,h} - q_h/q^2_{sat,h}\,(dq_{sat}/dT)(dT/dt) \quad (1)$$

where q is the specific humidity, $q_{sat}$ is the saturation specific humidity, h refers to the boundary layer height or the value of a variable at that height. and T is the temperature.

Using the equations for the boundary-layer moisture and thermodynamic budgets

$$dq/dt = -([w'q']_h - [w'q']_{sfc})/h \quad (2a)$$

$$d\theta/dt = -([w'\theta']_h - [w'\theta']_{sfc})/h \quad (2b)$$

where $\theta$ is potential temperature, and $[w'\theta']$ and $[w'q']$ are vertical fluxes of heat and moisture, respectively. Using (2a-b) and the equation of state, the definition of potential temperature, and the hydrostatic approximation, the relative humidity tendency equation becomes

$$d/dt(RH) \;=\; ([w'q']_{sfc} - [w'q']_h)/(h\, q_{sat,h}) \;-\; (RH\, F(T_h)/q_{sat,h}) \cdot$$
$$\{ (p/p_{sfc})^{R/c_p} ([w'\theta']_{sfc} - [w'\theta']_h)/h \;-\; g/c_p\, dh/dt \} \qquad (3)$$

where $p$ is pressure at height $h$, $p_{sfc}$ is surface pressure, $g$ is acceleration due to gravity, $R$ is the gas constant, $c_p$ is specific heat, and

$$F(T) = dq_{sat}/dT$$

To simplify the tendency equation we define

$$C \;=\; -\,[w'\theta']_h/[w'\theta']_{sfc} \qquad (4)$$

$$C_q \;=\; [w'q']_h/[w'q']_{sfc} \qquad (5)$$

The value of $C$ in daytime boundary layers is typically thought to be about 0.2-0.3 but can be much larger in cases of significant shear generation of turbulence. The value of $C_q$ is more variable, exceeding unity in the drying boundary layer and often becoming 0.5 or less in the moistening boundary layer (Steyn, 1990; Mahrt, 1991).

Using (4) and (5), the relative humidity tendency equation (3) becomes

$$d/dt(RH) \;=\; 1/(h\, q_{sat,h}) \cdot \{ [w'q']_{sfc}\, (\overbrace{1}^{(1)}\overbrace{-C_q}^{(2)})$$
$$-\, RH\, F(T_h) \left( \overbrace{(p/p_{sfc})^{R/c_p} [w'\theta']_{sfc}\, (1+C)}^{(3)} \;-\; \overbrace{g/c_p\, h\, dh/dt}^{(4)} \right)\} \qquad (6)$$

The four terms on the right hand side of (6) are

(1) increasing relative humidity due to boundary-layer moistening from surface evapotranspiration, or decreasing relative humidity due to dew

formation,

(2) decreasing relative humidity due to entrainment of dry air from above the boundary layer ($C_q > 0$); or less commonly, increasing relative humidity due to entrainment of moister air from above the boundary layer ($C_q < 0$),

(3) decreasing relative humidity due to surface sensible heat flux and entrainment of warmer air at the boundary layer top, and

(4) increasing relative humidity due to increasing boundary layer depth where for a given potential temperature, the temperature at the boundary layer top decreases with boundary layer deepening. This effect will be loosely referred to as the "adiabatic cooling effect".

Moisture changes normally dictate the change of relative humidity with small Bowen ratio or large $C_q$ corresponding to a large entrainment rate and dry air aloft. Temperature changes normally dominate the changes of relative humidity with large relative humidity or warm temperatures where the nonlinear increase of saturation specific humidity with temperature is rapid (large F(T)).

The influence of external conditions on the development of boundary layer cloud cover can be posed in terms of the above four influences on the relative humidity tendency near the top of the boundary layer. It is not possible to *a priori* predict the influence of an external effect without considering the relative importance of the four effects. For example, less soil moisture is expected to reduce boundary-layer cloud development. However, with moist air and weak stratification aloft, the fourth term on the right hand side of (6) may dominate. Then the enhanced boundary layer growth due to less surface evaporation and more sensible heat flux may lead to higher relative humidity at the boundary layer top. As another example, the influence of increased subsidence on boundary-layer cloud development will in part depend on the importance of entrainment of dry air (term 2) with respect to surface evaporation. These and other possibilities are studied with a one-dimensional boundary-layer model in the next section.

### 4.2.3. Boundary-layer model sensitivity tests

This section studies a number of sensitivity tests using a simple one-dimensional model of the atmospheric boundary layer (Troen and Mahrt, 1986; Ek and Mahrt, 1989), coupled to a primitive plant canopy model (Pan and Mahrt, 1987) and active two-layer soil model (Mahrt and Pan, 1984). We study the effect of various scenarios of large-scale forcing on relative humidity near the boundary layer top by artificially varying moisture aloft and large-scale subsidence. The influence of external forcing and initial state are organized using the relative humidity tendency equation (6).

The simulation for 19 May 1986 over the pine forest in HAPEX is compared with the observed hydrological and meteorological data set from HAPEX where considerable attention was devoted to aircraft moisture measurements (Eloranta, et al 1988). Model results for the 19 May simulation compare favorably with the observed conditions so it is now used as the prototype run. In our model simulations we do not attempt to predict the boundary layer cloud cover since this day was characterized by minimal cloud cover, rather through the sensitivity tests we attempt to predict the effect on the upper boundary layer relative humidity which is then used as an indicator of cloud initiation.

Four stages of moisture development occur on 19 May (Figure 2), and occur to various degrees on other days during HAPEX. Aspects of these stages, especially the first two, are documented in other studies (Segal, 1990).

Stage 1: Early Morning Drying Stage (0800 LST) - Surface fluxes are weak with weak vertical divergence of the turbulent moisture flux and drying of the shallow boundary layer due to entrainment of drier air (second term in (6)).

Stage 2. Rapid Growth Stage (1000 LST) - Boundary layer growth is rapid with stronger vertical divergence of the moisture flux induced by dry air entrainment. This leads to overall boundary layer drying; however, the relative humidity near the boundary layer top increases slightly in the numerical simulations (Figure 3) due to increasing boundary layer depth and associated adiabatic cooling (fourth term in (6)).

Stage 3. The Moistening Stage (1200 LST) This stage occurs after the rapid growth stage. Vertical convergence of the turbulent moisture flux develops due to reduced boundary layer growth, reduced dry air entrainment and increasing surface evapotranspiration (first term in 6)). However in the simulations of Figure 3, this moistening does not lead to increasing relative humidity because the warming effect (third term) is greater.

Stage 4. Decreasing surface fluxes (1500 LST) - Evapotranspiration begins to decrease in the afternoon partly due to drying of the near-surface soil. This leads to slower variation of the moisture flux with height. As a result, relative humidity near the boundary layer top continues to slowly decrease due to the warming effect (third term).

The decrease of relative humidity in the afternoon for the prototype case is largely due to the significant subsidence (about 3 cm $s^{-1}$ at 2 km, linearly decreasing to zero at the surface). This subsidence leads to an approximate balance between the influence of entrainment and larger-scale subsidence on boundary-layer growth. This eliminates the adiabatic cooling associated with boundary layer growth but entrainment of dry air continues. In the case of no subsidence (w=0), modest afternoon growth of the boundary layer occurs and adiabatic cooling (fourth term) is important. As a result, the decrease of relative humidity at the boundary layer top is minimal (Figure 3) and clouds are more likely to occur compared to the prototype case.

If the air aloft is specified to be especially dry (11 g/kg at the surface linearly decreasing to a constant value of 1.0 g/kg above about 600 m), the boundary-layer growth is reduced compared to the no subsidence case (Figure 3). The strong entrainment-drying of the boundary layer leads to greater surface evaporation through larger potential evaporation. This in turn reduces the surface heating and therefore reduces the boundary-layer growth. The relative humidity is less due to the strong drying during the initial growth of the boundary layer. Continued entrainment of the very dry air maintains the lower relative humidity. These interactions are schematically included in Figure 4.

We can invert the above results to show that increased subsidence can decrease the boundary-layer relative humidity under conditions corresponding to the prototype case. However, increased subsidence would increase the boundary layer relative humidity when the air aloft is very dry and the moisture supply is limited to the boundary layer.

### 4.2.4. Conclusions

This study has investigated the dependence of the evolution of relative humidity in the daytime boundary layer on mean subsidence and the vertical distribution of moisture above the boundary layer. This dependence involves complex interactions which prevent formation of simple rules for forecasting the likelihood of boundary layer clouds. For example, increased subsidence may increase or decrease the boundary layer relative humidity depending on the dryness of the air above the entraining boundary layer.

While the model used in this study is simple and incomplete, most boundary layer formulations in larger scale models omit even more physics and necessarily contain cruder vertical resolution. This study indicates that the failure to represent entrainment of dry air and the influence of the atmosphere on the surface evaporation could lead to an incorrect response of the modelled boundary layer to changes in external conditions.

*Acknowledgements.* This material is based upon work supported by the Geophysics Laboratory, under contract F19628-88-K-001. The National Center for Atmospheric Research is acknowledged for the use of the King Air research aircraft in HAPEX.

## References

André , J. C. and collaborators, 1988: HAPEX-MOBILHY: First results from the special observing period. *Ann. Geophys. Ser. B*, **6**, 477-492.

Chu, C.-T., 1986: Parameterization of shallow convection in the boundary layer. Master's Thesis. Oregon State University, Corvallis, Oregon.

Ek, M. and L. Mahrt, 1989: A user's guide to OSU1DPBL version 1.0.3: A one-dimensional planetary boundary-layer model with interactive soil layers and plant canopy. Department of Atmospheric Sciences, Oregon State University, Corvallis, Oregon 97331.

Ek, M. and L. Mahrt, 1991: A formulation for boundary layer cloud cover. Submitted to *Ann. Geophys. Ser. B.*

Eloranta, D., R. Stull, and E. Ebert, 1988: Test of a calibration device for airborne Lyman-Alpha hygrometers. *J. Atm. and Oc. Tech.*, **6**, 129-139.

Holtslag, A. A. M., E. I. F. de Bruin, and H.-L. Pan, 1990: A high resolution air mass transformation model for short-range weather forecasting. *Mon. Wea. Rev .*, **118**, 1561-1575.

Mahrt, L., 1991: Boundary-layer moisture regimes. *Quart. J. Roy. Met. Soc.*, **117**.

Mahrt, L. and H.-L. Pan, 1984: A two-layer model of soil hydrology. *Bound.-Layer Meteor.*, **29**, 1-20.

Pan, H.-L. and L. Mahrt, 1987: Interaction between soil hydrology and boundary layer development. *Bound.-Layer Meteor.*, **38**, 185-202.

Segal, M., Kallos, J. Brown and M. Mandel, 1990: On the morning temporal variations of the shelter-level specific humidity. To be submitted to *J. Appl. Meteorol.*

Slingo, J. M., 1980: A cloud parameterization scheme derived from GATE data for use with a numerical model. *Quart. J. Roy. Met. Soc.*, **106**, 747-770.

Steyn, D. G., 1990: An advective mixed-layer model for heat and moisture incorporating an analytic expression for moisture entrainment. *Bound.-Layer Meteor.*, **53**, 21-31.

Troen, I. and L. Mahrt, 1986: A simple model of the atmospheric boundary layer: Sensitivity to surface evaporation. *Bound.-Layer Meteor.*, **37**, 129-148.

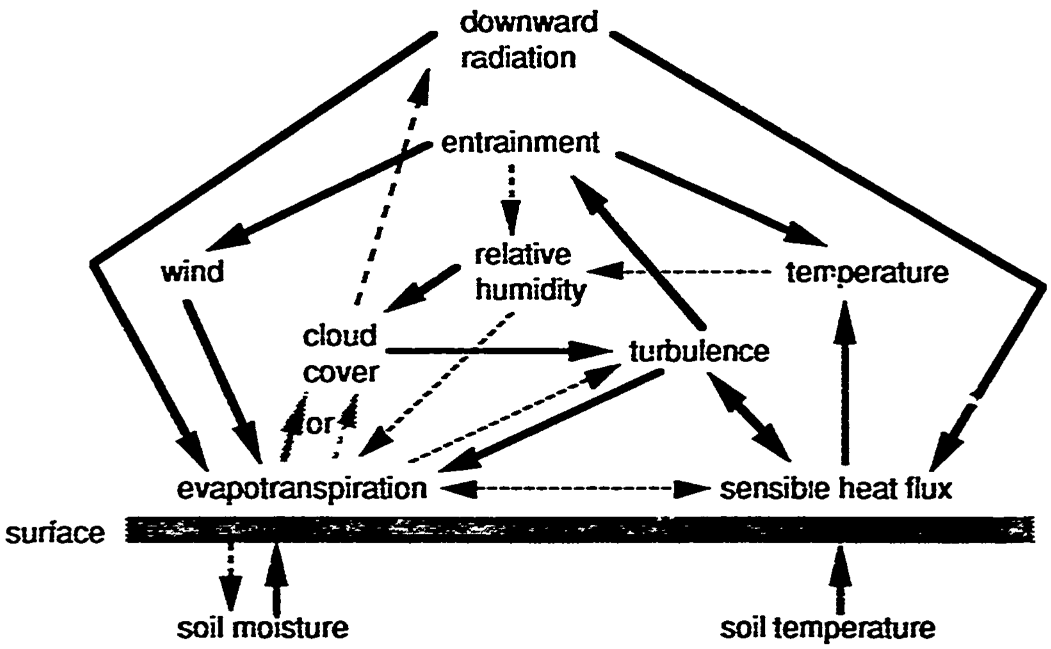
downward radiation
entrainment
wind
relative humidity
temperature
cloud cover
turbulence
or
evapotranspiration
sensible heat flux
surface
soil moisture
soil temperature

Figure 1. Suspected important interactions between the surface and boundary layer for conditions of daytime surface heating. Solid arrows indicate the direction of feedbacks which are normally positive (leading to increases of the recipient variable). Dashed arrows indicate negative feedbacks. Two consecutive negative feedbacks make a positive one. Note that evapotranspiration may lead to increased or decreased cloud cover depending on a number of factors.

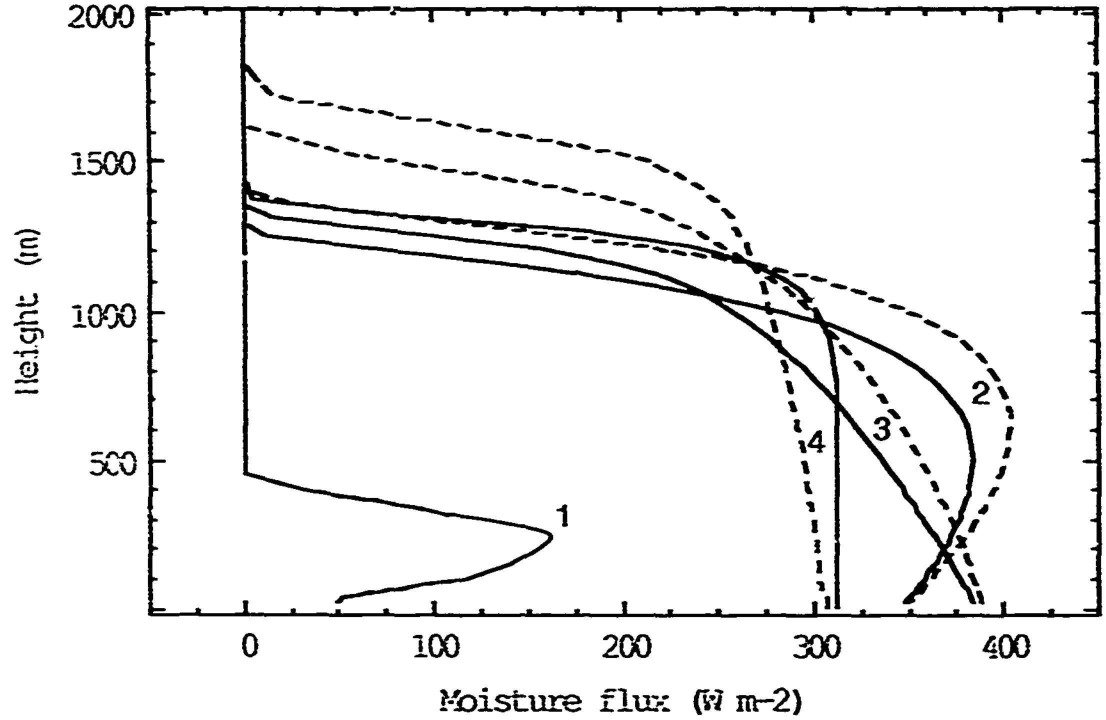

Figure 2. Moisture flux profiles for prototype (solid) and no subsidence (dashed) simulations for different stages of boundary-layer development (1-4), over the pine forest for 19 May 1986 during HAPEX-MOBILHY.

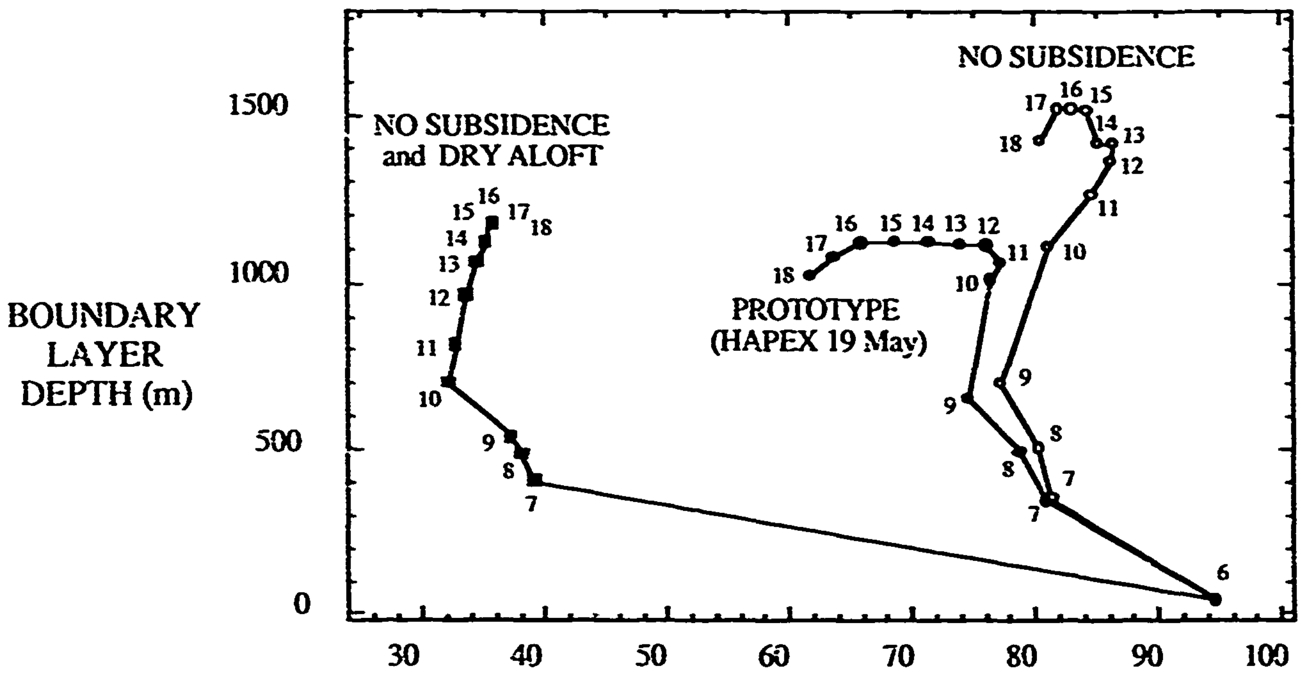

Figure 3. Relative humidity at boundary layer top at different times of day (LST) for prototype (solid circles), no subsidence (open circles), and no subsidence and dry aloft (solid squares) model simulations.

Comparisons at the Moistening Stage

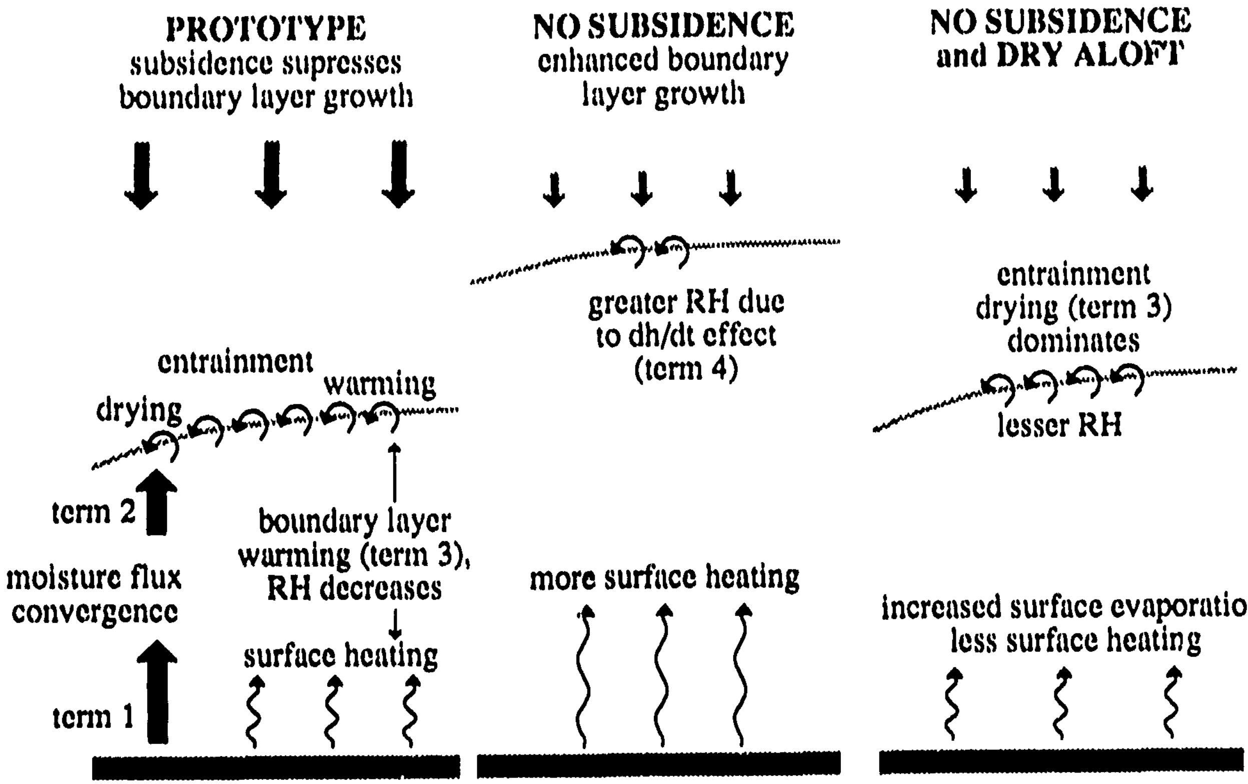
PROTOTYPE
subsidence supresses boundary layer growth
NO SUBSIDENCE
enhanced boundary layer growth
NO SUBSIDENCE and DRY ALOFT
entrainment
drying
warming
term 2
boundary layer warming (term 3), RH decreases
moisture flux convergence
surface heating
term 1
greater RH due to dh/dt effect (term 4)
more surface heating
entrainment drying (term 3) dominates
lesser RH
increased surface evaporation, less surface heating

Figure 4. Comparisons of boundary layer processes at stage 3 for the prototype case and the cases of no subsidence, and no subsidence with dry conditions aloft.

## Chapter 5

# Boundary-Layer Model Physics and Numerical Methods

## 5.1. Introduction

The Oregon State University one-dimensional planetary boundary-layer (OSU1DPBL) model simulates the atmosphere, soil, and vegetated surface. The planetary boundary-layer model (Troen and Mahrt, 1986; Ek and Mahrt, 1989; Holtslag et al., 1990) is coupled with an active two-layer soil model (Mahrt and Pan, 1984) and a primitive plant canopy model (Pan and Mahrt, 1987). While many modifications have been made, the individual components from the original model have been examined previously in the references listed above as well as by Mahrt et al. (1984) and Mahrt et al. (1987). The equations used in this composite model are comprehensive enough to approximate the physical processes thought to be most important, yet simple enough to allow both crude and high-resolution diurnal model simulations to be run in a few minutes on a personal computer under a variety of diverse atmospheric conditions. The model is also robust with respect to atmospheric stability and has been run for long integrations under a variety of diverse conditions for many different locations around the globe. The model is being used by a number of governmental agencies, industrial organizations, and academic institutions for many different sensitivity experiments in local weather forecasting, air pollution, soil chemistry, and soil hydrology, either as a stand-alone model or in concert with larger scale models. The surface evaporation scheme from the model is currently being used in National Weather Service forecast models, and the model has also been incorporated into 3-D global models such as the AFGL global spectral model (Brenner et al., 1984) and the KNMI regional operational air mass transformation model (Holtslag et al., 1990).

## 5.2. Model Equations and Numerical Methods

Here we describe the physics and numerical methods employed in the model. Model equations are described in section 5.2.1. A brief description of the computational procedure follows in section 5.2.2. In section 5.2.3 schematics are presented which describe the general soil, plant canopy, and boundary-layer processes in the model. Section 5.2.4 contains a generalized flowchart of the model. Sections 5.2.5 to 5.2.11 describe numerical methods and other physics used in the model -- the finite differencing methods used for model computations, the snow cover model, the radiation Richardson number, the development of potential evaporation and surface temperature, and the relation between canopy resistance and the plant coefficient. Lastly, a comprehensive list of references for the model is given. Note that equation numbers are sequential within each section.

### 5.2.1 Model Equations

In order to close the system of equations and determine the turbulent mixing, boundary conditions near the earth's surface must be provided. To obtain these conditions, an atmospheric surface-layer parameterization is used. The exchange of sensible and latent heat flux between the surface layer and the underlying surface requires knowledge of the soil and ocean surface conditions.

This section is divided into six subsections, each describing individual aspects of the planetary boundary-layer (PBL) and soil models. Turbulent mixing within the PBL is described in 5.2.1.1; the surface-layer model of the atmosphere is given in 5.2.1.2; the soil model with soil hydrology and thermodynamics, and canopy transpiration and water balance is found in 5.2.1.3; the surface energy balance calculation, used to incorporate the impact of radiative heating effects on both the boundary and soil layers, is discussed in 5.2.1.4; the boundary-layer cloud parameterization follows in 5.2.1.5; and the total downward radiation is given in 5.2.1.6.

Unless otherwise indicated, the units of temperature are in degrees Kelvin (K), velocity in meters per second (m $s^{-1}$), humidity in kilograms per kilogram (kg $kg^{-1}$, nondimensional) and height and length in meters (m). Units for each of the remaining terms are indicated in the text.

### 5.2.1.1 Boundary-layer model

The model forecasts the tendencies due to turbulent mixing of the potential temperature ($\theta$), specific humidity ($q$), and horizontal components of the wind ($\mathbf{v}_h$, or $u$ and $v$). The set of prognostic equations is

$$\frac{\partial \mathbf{v}_h}{\partial t} = \frac{\partial}{\partial z}\left(K_m \frac{\partial \mathbf{v}_h}{\partial z}\right) - w\left(\frac{\partial \mathbf{v}_h}{\partial z}\right) \tag{1}$$

$$\frac{\partial \theta}{\partial t} = \frac{\partial}{\partial z}\left(K_h \left(\frac{\partial \theta}{\partial z} - \gamma_\theta\right)\right) - w\left(\frac{\partial \theta}{\partial z}\right) \tag{2}$$

$$\frac{\partial q}{\partial t} = \frac{\partial}{\partial z}\left(K_h \frac{\partial q}{\partial z}\right) - w\left(\frac{\partial q}{\partial z}\right) \tag{3}$$

To simplify the presentation, only the vertical diffusion terms due to boundary-layer turbulent mixing, and the advection terms due a prescribed vertical motion field are kept in the equations. Details of the complete equations may be found in Troen and Mahrt (1986). Units are m $s^{-2}$ in (1), K $s^{-1}$ in (2), and $s^{-1}$ in (3).

The counter-gradient correction for potential temperature ($\gamma_\theta$, K $m^{-1}$) which is included in (2) following Troen and Mahrt (1986), is parameterized as follows

$$\gamma_\theta = \begin{cases} 0 & \text{, stable} \\ C\dfrac{\overline{(w'\theta')}_s}{w_s h} & \text{, unstable} \end{cases} \tag{4}$$

The counter-gradient correction ($\gamma_\theta$) is evaluated in terms of the surface flux of potential temperature (see section 5.2.1.2 for a discussion of fluxes), the boundary-layer depth (h), a nondimensional constant C, set to 8.5 following Holtslag (1987), modified from the value of 6.5 employed by Troen and Mahrt (1986), and the velocity scale ($w_s$, m $s^{-1}$) of the boundary layer defined as

$$w_s = u_* \phi_m^{-1}\left(\frac{z_s}{L}\right) \tag{5}$$

In (5), $u_*$ (m $s^{-1}$) is the surface friction velocity, $z_s$ is the top of the surface layer (currently 0.1h in the model), and L is the Monin-Obukhov length; $u_*$ and L will also be described in section 5.2.1.2. $\phi_m$ is the nondimensional profile function which is specified in (12) below. In the neutral limit as $L \rightarrow \pm\infty$, the velocity scale $w_s \rightarrow u_*$. In the free convection case as $\mathbf{V} \rightarrow 0$, $u_* \rightarrow 0$ and

$$w_s \rightarrow \left[\frac{7 z_s g k (w'\theta_v')_s}{\theta_{sv}}\right]^{1/3} \tag{6}$$

The coefficient of diffusivity for momentum ($K_m$, $m^2$ $s^{-1}$) in the unstable case is

$$K_m = w_s\, h\, k\, \frac{z}{h}\left(1 - \frac{z}{h}\right)^p \tag{7}$$

with p set equal to 2.0 and $u_* \phi^{-1}(z/L)$ replacing $w_s$ in the stable case. The eddy diffusivity for heat ($K_h$, $m^2$ $s^{-1}$) is related to the eddy diffusivity for momentum in terms of the turbulent Prandtl number (Pr, nondimensional)

$$K_h = K_m \, Pr^{-1} \tag{8}$$

where for the unstable case

$$Pr^{-1} = \frac{\phi_h\left(\frac{z_s}{L}\right)}{\phi_m\left(\frac{z_s}{L}\right)} + C\, k\, \frac{z_s}{h} \tag{9}$$

Pr is determined as the value at the top of the surface layer ($z_s$ = 0.1h) using surface-layer similarity theory. For the stable and neutral cases the Prandtl number is assumed to be a constant (currently 1.0 in the model).

As shown in Eq. 9, the counter-gradient term occurring in the heat equation is also absorbed in the Prandtl number. The nondimensional profile functions ($\phi_m$ and $\phi_h$) have their standard definition and will be defined formally below. The resulting prediction equation for potential temperature will therefore not explicitly contain the counter-gradient term and is actually identical in form to Eq. 1 (Troen and Mahrt, 1986).

The boundary-layer height ($z_i$) is diagnosed as

$$z_i = \frac{Ri_{cr}\theta_{ov}|\mathbf{V}(h)|^2}{g\,(\theta_v(h) - \theta^*_{ov})} \tag{10}$$

where $Ri_{cr}$ (nondimensional) is the critical Richardson number, $\theta_{ov}$ is the reference virtual potential temperature at the first model above the surface, g (m $s^{-2}$) is the gravitational acceleration, $\theta_v(h)$ is the virtual potential temperature at model level h (currently 60 meters for the unstable case and the first model level above the surface for the stable case), and $\mathbf{V}(h)$ is the horizontal wind velocity at level h (the first model level above the surface). This approach to diagnosing the PBL height also requires the specification of a low-level potential temperature ($\theta^*_{ov}$). We define $\theta_{ov}{}^*$ in the following way

$$\theta^*_{ov} = \begin{Bmatrix} \theta_{ov} & \text{, stable} \\ \\ \theta_{ov} + C\dfrac{\overline{(w'\theta_v')}_s}{w_s} & \text{, unstable} \end{Bmatrix} \tag{11}$$

When the boundary layer is unstable, the virtual potential temperature at the top of the surface layer in (11) is enhanced by thermal effects in an amount that is proportional to the surface sensible heat flux. In the neutral limit as $w_s \rightarrow u_*$, the correction to the surface temperature vanishes so that $\theta^*_{ov} \rightarrow \theta_{ov}$ with the result that the modified bulk Ri number (in Eq. 10) reduces to the usual one.

The nondimensional profile functions for the shear and temperature gradients are defined as follows

$$\phi_m = \begin{cases} 6.0 & \text{, very stable} \\ 1.0 + 5.0\dfrac{z}{L} & \text{, stable} \\ \left(1.0 - 15\dfrac{z}{L}\right)^{-1/3} & \text{, unstable} \end{cases} \tag{12}$$

and

$$\phi_m = \begin{cases} 6.0 & \text{, very stable} \\ 1.0 + 5.0\dfrac{z}{L} & \text{, stable} \\ \left(1.0 - 15\dfrac{z}{L}\right)^{-1/2} & \text{, unstable} \end{cases} \tag{13}$$

These formulations are taken from Businger et al. (1971) with modifications by Holtslag (1987), and are functions of the height coordinate (z) and the Monin-Obukhov length scale (L). For the very stable case ($z/L > 1.0$), we set $z/L = 1.0$ so that the profile functions remain constant. In the model code, $\phi_h$ appears implicitly as a form of $\phi_m$ and the Prandtl number.

#### 5.2.1.2 Surface-layer model

The surface fluxes are calculated following Mahrt (1987) for the stable case and following Louis et al. (1982) for the unstable case (with modifications by Holtslag and Beljaars, 1989) as

$$u_*^2 = C_m \left|\mathbf{V}_0\right| \tag{14}$$

$$(\overline{w'\theta'})_s = C_h \left(\theta_s - \theta_0\right) \tag{15}$$

$$(\overline{w'q'})_s = C_h \left(q_s - q_0\right) \tag{16}$$

where $C_m$ and $C_h$ are the surface exchange coefficients for momentum and heat, respectively (m $s^{-1}$). $C_m$ and $C_h$ are defined so that the wind speed factor is absorbed in them. $|\mathbf{V}_0|$ is the wind speed evaluated at the first model level above the surface.

The potential temperature ($\theta_0$) and specific humidity ($q_0$) are taken at the first model level above the surface while the surface potential temperature ($\theta_s$) and specific humidity ($q_s$) are obtained from the surface energy balance.

The surface exchange coefficients are

$$C_m = k^2 \left|\mathbf{V}_0\right| \frac{F1(z, z_{0M}, Ri_B)}{\left(\ln\left(\frac{z}{z_0}\right)\right)^2} \tag{17a}$$

$$C_h = \frac{k^2}{R} \left|\mathbf{V}_0\right| \frac{F2(z, z_{0M}, z_{0H}, Ri_B)}{\ln\left(\frac{z}{z_0}\right)\ln\left(\frac{z}{z_{0H}}\right)} \tag{17b}$$

where k is the nondimensional von Kármán constant (0.40) and R, estimated at 1.0, is the ratio of the drag coefficients for momentum and heat in the neutral limit and is taken from Businger et al. (1971) with modification by Holtslag and Beljaars (1989).

$C_m$ and $C_h$ are functions of the wind speed evaluated at the first model level above the surface ($|\mathbf{V}_0|$), the height of the first model layer above the surface (z), the roughness length for momentum ($z_{0M}$) which depends on surface characteristics, and the bulk Richardson number for the surface layer ($Ri_B$) which will be described later. In addition, $C_h$ is also a function of the roughness length for heat ($z_{0H}$).

For $C_m$, the function F1 is defined as

$$F1 = \begin{cases} e^{-aRi_B} & \text{,stable} \\ 1 - \dfrac{10Ri_B}{1+7.5\left[\dfrac{k^2}{\left(\ln\left(\frac{z}{z_{0M}}\right)\right)^2}10\right]\left(-Ri_B\dfrac{z}{z_{0M}}\right)^{1/2}} & \text{,unstable} \end{cases} \tag{18}$$

and for $C_h$, the function F2 is defined as

$$F2 = \begin{cases} e^{-aRi_B} & \text{, stable} \\ 1 - \dfrac{15Ri_B}{1+7.5\left[\dfrac{k^2}{\ln\left(\dfrac{z}{z_{0M}}\right)\ln\left(\dfrac{z}{z_{0H}}\right)}10\right]\left(-Ri_B\dfrac{z}{z_{0M}}\right)^{1/2}} & \text{, unstable} \end{cases} \quad (19)$$

where a is a constant currently equal to 1.0 in the model.

The bulk Richardson number for the surface layer is defined as

$$Ri_B = \frac{g\ z\ (\theta_{0v} - \theta_{sv})}{\theta_{0v}|\mathbf{V}_0|^2} \quad (20)$$

The bulk-Richardson number is a function of the height (z), the difference between the virtual potential temperature of air at the first model level ($\theta_{0v}$) and the surface virtual potential temperature ($\theta_{sv}$) which corresponds to the surface temperature from the surface energy balance, and the air speed at the first model level ($|\mathbf{V}_0|$).

The length scale for the surface layer is the Monin-Obuhkov length

$$L = -\frac{\theta_{sv}u_*^3}{gk(\overline{w'\theta_v'})_s} \quad (21)$$

The Monin-Obukhov length scale (L) is defined using the surface virtual potential temperature ($\theta_{sv}$), friction velocity ($u_*$), and the virtual heat flux at the surface. It is used in the nondimensional profile functions described in Eqs. 12 and 13.

The tendency equations for the surface layer are the same as those for the boundary layer (Eqs. 1, 2, and 3) except that the eddy diffusivities for the surface layer are

$$K_m = u_* \, k \, z \, \phi_m^{-1}\left(\frac{z}{L}\right)\left(1 - \frac{z}{h}\right)^p \quad (22)$$

$$K_h = K_m \, Pr^{-1} \quad (23)$$

where $\phi_m$ now has a dependence on z/L instead of on $z_s/L$. The dimensionless function $\phi_m$ was defined in Eq. 12. As a modification to surface-layer similarity theory, the term $(1 - z/h)^p$ remains in $K_m$ for proper matching with the mixed layer.

The only variables needed to close the surface-layer model are $q_s$ and $\theta_s$; they are available from the the soil model (5.2.1.3) and the surface energy balance calculation (5.2.1.4), respectively.

### 5.2.1.3 Soil model

The soil model has been described previously by Mahrt and Pan (1984) and Pan and Mahrt (1987). The soil hydrology is modelled with the prognostic equation for the nondimensional volumetric water content ($\Theta$)

$$\frac{\partial \Theta}{\partial t} = \frac{\partial}{\partial z}\left(D(\Theta)\frac{\partial \Theta}{\partial z}\right) + \frac{\partial K(\Theta)}{\partial z} \quad (24)$$

The coefficients of diffusivity (D, $m^2\ s^{-1}$) and hydraulic conductivity (K, $m\ s^{-1}$) are functions of the volumetric water content (Mahrt and Pan, 1984). Through the extremes of wet and dry soil conditions, the coefficients D and K can vary by several orders of magnitude and, therefore cannot be treated as constants. The layer integrated form of (24) for the ith layer is

$$\Delta z_i \frac{\partial \Theta}{\partial t} = \left(D(\Theta)\frac{\partial \Theta}{\partial z} + K(\Theta)\right)_{z_{i+1}} - \left(D(\Theta)\frac{\partial \Theta}{\partial z} + K(\Theta)\right)_{z_i} \quad (25)$$

Eq. 25 is valid for a layer $[z_i, z_{i+1}] = \Delta z_i$. At the surface of the soil, the evaporation is called the direct evaporation. For direct evaporation ($E_{dir}$, $m\ s^{-1}$) at the air-soil interface (z=0), we have

$$E_{dir} = \left[-D(\Theta)\left(\frac{\partial\Theta}{\partial z}\right)_0 - K(\Theta_0)\right](1-\sigma_f) + I(1-\sigma_f) \qquad (26)$$

where I (m $s^{-1}$) is the infiltration rate (which is equal to rainfall less runoff) and $\sigma_f$ (nondimensional, between 0 and 1) is the plant shading factor. The evaporation (E, m $s^{-1}$) can proceed at a potential rate ($E_p$) when the apparent soil moisture at the surface ($\Theta_{sfc}$) is greater than the air dry value ($\Theta_d$), i.e., that is when the soil is sufficiently wet (demand control stage). When the soil dries out, the evaporation can only proceed at the rate by which the soil can diffuse water upward from below (flux control stage) in which case $\Theta_{sfc} = \Theta_d$ and $E < E_p$. ($E_p$ will be discussed below.)

The canopy evaporation of free water ($E_c$) is formulated as

$$E_c = E_p\, \sigma_f \left(\frac{C^*}{S'}\right)^n \qquad (27)$$

where S' (m), the saturation water content for a canopy surface, is a constant usually chosen to be 0.002 meters (2 mm), and n (nondimensional) is taken to be 0.5 (Pan and Mahrt, 1987). The canopy water content ($C^*$, m) changes as

$$\frac{dC^*}{dt} = \sigma_f\ \text{Precip} - E_c \qquad (28)$$

Precipitation increases the canopy water content first while evaporation decreases $C^*$. Eq. 28 is in units of m $s^{-1}$.

The model also incorporates transpiration ($E_t$) in the following manner

$$E_t = E_p\, \sigma_f\, k_v \frac{\sum_{i=1}^{2}[\Delta z_i g(\Theta_i)]\left[1-\left(\frac{C^*}{S'}\right)^n\right]}{\sum_{i=1}^{2}[\Delta z_i]} \qquad (29)$$

where $k_v$ is the nondimensional plant resistance factor or plant coefficient (PC) with a value between 0 and 1. The canopy resistance (RC) may be used instead of the plant coefficient. See section 5.2.10 for a discussion of PC and RC. The nondimensional transpiration rate function $g(\Theta_i)$ is defined as

$$g(\Theta) = \begin{cases} 1 & ,\Theta > \Theta_{ref} \\ \dfrac{\Theta-\Theta_{wilt}}{\Theta_{ref}-\Theta_{wilt}} & ,\Theta_{ref} \geq \Theta > \Theta_{wilt} \\ 0 & ,\Theta_{wilt} \geq \Theta \end{cases} \qquad (30)$$

The transpiration limit $\Theta_{ref}$ and $\Theta_{wilt}$ refer, respectively, to an upper reference value, which is the $\Theta$ value where transpiration begins to decrease due to a deficit of water, and the plant wilting factor, which is the $\Theta$ value where transpiration stops (Mahrt and Pan, 1984).

Total evaporation is obtained by adding the direct soil evaporation, the transpiration and the canopy evaporation

$$E = E_{dir} + E_c + E_t \qquad (31)$$

The total evaporation cannot exceed the potential evaporation ($E_p$, defined in Eq. 39). After obtaining the evaporation, the surface specific humidity ($q_s$) is calculated from

$$q_s = q_0 + \frac{E}{\rho_0 C_h} \qquad (32)$$

This quantity is the specific humidity at the surface which allows E to be calculated from the bulk aerodynamic relationship; $q_s$ is also used in the calculation of vertical profiles of moisture. $\rho_0$ (kg $m^{-3}$) is the air density at the surface, and $C_h$ is the exchange coefficient for moisture, described section 5.2.1.2.

Soil thermodynamics are treated with a prognostic equation for soil temperature (T) such that

$$C(\Theta)\frac{\partial T}{\partial t} = \frac{\partial}{\partial z}\left(K_T(\Theta)\frac{\partial T}{\partial z}\right) \qquad (33)$$

The volumetric heat capacity (C, J $m^{-3}$ $K^{-1}$) and the thermal conductivity ($K_T$, W $m^{-1}$ $K^{-1}$) of the soil are both functions of the soil water content ($\Theta$). The heat capacity (C) is linearly related to $\Theta$, whereas the coefficient of thermal diffusivity ($K_T$) is a highly nonlinear function of $\Theta$ and increases by several orders of magnitude from dry to wet soil conditions. The layer-integrated form of Eq. 33 for the ith layer is

$$\Delta z_i C(\Theta_i)\frac{\partial T_i}{\partial t} = \left(K_T(\Theta)\frac{\partial T}{\partial z}\right)_{z_{i+1}} - \left(K_T(\Theta)\frac{\partial T}{\partial z}\right)_{z_i} \qquad (34)$$

The upper boundary condition for the soil thermodynamic model is the soil heat flux, G (W $m^{-2}$), an important component in the surface energy balance. It is found from

$$K_T(\Theta)\left(\frac{\partial T}{\partial z}\right)_{z=0} = G \qquad (35a)$$

The soil system is closed except for the potential evaporation which is defined in the next section. For the two-level soil model, at 2.5 cm

$$\left(\frac{\partial T}{\partial z}\right)_{z=0} = \frac{\theta_s - T_{1soil}}{\Delta z} \qquad (35b)$$

### 5.2.1.4 Surface energy balance

Surface temperature is calculated from the surface energy balance method

$$(1-\alpha)S\downarrow + L\downarrow - \sigma\theta_s^4 = G + H + LE \qquad (36)$$

where each term is expressed in W $m^{-2}$. The first term on the left-hand side of Eq. 36 is the downward solar radiation (defined as positive downward). The nondimensional coefficient $\alpha$ is the surface albedo and is a function of surface characteristics. The second term on the left-hand side is the downward atmospheric radiation (positive downward). The third term on the left-hand side is the upward terrestrial radiation (positive upward); the coefficient $\sigma$ is the Stefan-Boltzmann constant ($5.6696 \times 10^{-8}$ W m$^{-2}$ K$^{-4}$). The first term on the right-hand side of Eq. 36 is the soil heat flux (positive downward) defined in Eq. 35a. The second term on the right-hand side is the sensible heat flux (positive upward). It is defined as

$$H = \rho_0 \, c_p \, C_h \, (\theta_s - \theta_0) \qquad (37)$$

and is a function of the air density ($\rho_o$), the specific heat for air ($c_p = 1004.5$ J kg$^{-1}$ K$^{-1}$), the exchange coefficient ($C_h$, Eq. 17), and the difference between the surface temperature ($\theta_s$) and the air potential temperature at the first model level ($\theta_o$). The last term on the right-hand side of Eq. 36 is the latent heat flux (positive upward) where L (J kg$^{-1}$) is the latent heat of phase change; E is calculated from Eq. 31.

The potential evaporation is needed to compute the actual evaporation from Eq. 31. The usual Penman relationship cannot be employed since the surface temperature is needed to compute the net radiation. Instead, as a first step, we evaluate the surface energy balance for the reference state of the surface (with the same albedo) but in a saturated condition

$$(1-\alpha)S\!\downarrow + \, L\!\downarrow - \sigma\theta_s'^4 \;=\; G + H' + LE_p \qquad (38)$$

where

$$E_p = \rho_0 \, C_h \, (q_s^*(\theta_s') - q_0) \qquad (39)$$

and

$$H' = \rho_0 \, c_p \, C_h \, (\theta_s' - \theta_0) \qquad (40)$$

The temperature variable ($\theta_s'$) which appears in Eqs. 38-40 is a fictitious temperature the surface would have if the soil is sufficiently wet to evaporate at the potential rate. The variable $q^*_s(\theta_s')$ in Eq. 39 is the saturation specific humidity for this fictitious temperature. Thus $\theta_s'$ should be used for temporary evaluation of $C_m$ in Eq. A3 of Troen & Mahrt (1986).

Over water, the prescribed sea surface temperature (SST) is prescribed so that $q_s$ is the saturated surface specific humidity ($q^*_s$), which is calculated directly from SST. This over-water $q_s$ is then used in the bulk aerodynamic formula for evaporation (Eq. 16 times $\rho_0 L_v$). Since $\theta_s$' (SST in this case) and thus $q^*_s$ are already known, there is no need to evaluate the surface energy balance over water.

A more formal derivation of the potential evaporation ($E_p$) and actual surface temperature ($\theta_s$) can be found in section 5.2.9.

### 5.2.1.5 Boundary-layer clouds

Fractional cloud cover in the boundary layer is determined following Ek and Mahrt (1991). The model predicts cloud cover using the generalized equation

$$\mathrm{CLC} = f(\overline{\mathrm{RH}}, \sigma_{\mathrm{RH}}) \qquad (41)$$

where CLC is the fractional cloud cover, RH (bar) is the maximum relative humidity in the boundary layer, and $\sigma_{RH}$ is the standard deviation of relative humidity which accounts for the turbulent and subgrid mesoscale variations in relative humidity. The turbulent variability of relative humidity is formulated in terms of boundary-layer similarity theory whereas the mesoscale subgrid variability is specified as a function of grid size based on HAPEX analyses. With unstable conditions, boundary-layer clouds first form at lower relative humidities compared to the stable case. The fractional cloud cover is then the area under a Gaussian curve greater than RH = 1.0, and is approximated by a ninth-order polynomial fit to a Gaussian distribution (see the figure describing the cloud cover formulation in section 5.2.3).

### 5.2.1.6 Downward radiation

The model includes a simple radiation package which gives the total downward radiation, a combination of incoming solar (shortwave) plus downward atmospheric (longwave) radiation.

The incoming solar radiation is calculated following the method of Kasten and Czeplak (1980). The clear sky value is reduced due to the solar elevation and presence of boundary-layer clouds. The equation for incoming solar radiation as it reaches the ground is

$$S\downarrow = [1 - (1-t)CLC^n]\ S_{CS}\downarrow \qquad (42)$$

where $S\downarrow$ is the net incoming solar radiation (below clouds but above the ground), t is a fraction dependent on the solar radiation transmitted through the clouds which depends on sun angle following Liou (1976), CLC is the fractional cloud cover, n is an empirically derived coefficient (1.0 in the model), and $S_{CS}\downarrow$ is the clear sky solar radiation adjusted for solar elevation. When n = 1, t is the actual fraction of solar radiation transmitted through the clouds.

Atmospheric (downward longwave) radiation is parameterized using a method from Satterlund (1979) with a modification for clouds following Paltridge and Platt (1976). The expression for atmospheric radiation is then

$$L\downarrow = \varepsilon\ \sigma\ T_{ref}^4 + c_2\ CLC \qquad (43)$$

where $L\downarrow$ is the downward atmospheric radiation (W $m^{-2}$); $\varepsilon$ is the emissivity of the atmosphere, a function of the temperature and moisture at the reference level in the model (currently 200 m); $T_{ref}$ is the temperature at the reference height (200 meters in the model); CLC is the fractional cloud cover; and $c_2$ is an empirically derived constant equal to 60 W $m^{-2}$.

The user also has the option of specifying an effective atmospheric temperature ($T_{eff}$) in order to determine the atmospheric radiation from the simple relation $L\downarrow = \sigma T_{eff}^4$.

### 5.2.2 Computational Procedures

Computationally, we begin by determining the external forcing of the incoming solar radiation (Eq. 42), reduced by a fractional cloud cover (Eq. 41) and calculated for the previous time step. Fractional cloud cover plus profiles of temperature and moisture from the previous time step are then used for the calculation of downward atmospheric radiation (Eq. 43). This gives the total downward radiation.

Next, the fictitious surface energy balance for an open water surface (or a saturated land surface evaporating without resistance) is used to obtain potential evaporation (Eqs. 38-40). The key quantity to be determined in these equations is the skin temperature ($\theta_s'$) which the surface would achieve if it was saturated. Eqs. 38 and 40 are used to form a prediction for $\theta_s'$ which is then used to predict potential evaporation from Eq. 39. Both the soil heat flux G and the exchange coefficients take on their values from the previous time step.

As a test, the potential evaporation is imposed upon the upper part of the soil by requiring the upward flux of water in the soil to equal the potential rate. Eq. 39 is then solved for the surface value of soil moisture which would be required to produce a sufficiently strong gradient for the soil water flux to equal the potential demand. If this test gradient requires the surface soil moisture value to be less than the air-dry value, the potential demand cannot be met. In this case, the evaporative flux is set equal to the maximum value which can be supplied by the soil, that is, Eq. 26 with the surface soil moisture equal to the air-dry value (Eq. 26 serves to determine the top boundary condition for Eq. 25). On the other hand, if the test value of the surface soil moisture is greater than the air-dry value, the test value is retained and the soil moisture flux (bare soil contribution) proceeds at the potential rate. Given the bare soil evaporation and the potential evaporation, the contributions from plant transpiration and reevaporation of canopy water are determined giving the total surface soil moisture flux. The soil hydrology package is then updated.

When precipitation occurs, it wets the plant canopy first until the plant holding capacity is reached, then wets the ground surface by dripping through the plant canopy. Reevaporation from the plant canopy occurs at the potential rate given by Eq. 27 until the canopy water is depleted as determined by Eq. 28. Transpiration from plants is evaluated using Eqs. 29-30 and the potential evaporation determined from (38).

With Eq. 35a, the soil heat flux is obtained using the soil thermodynamic model from Eq. 34. In the finite difference form for Eq. 35a, the skin temperature $\theta_s$ appears as an unknown. Also an unknown in Eq. 36, $\theta_s$ can be solved for, thus allowing the other components of the surface energy balance to be determined. When snow cover is present, changes are needed for the interface; these changes are described in section 5.2.6.

Having obtained $\theta_s$ with Eq. 36 and $q_s$ with Eq. 32, we use the surface-layer parameterization (Eqs. 14-16) to obtain the surface stress, sensible heat flux, and latent heat flux. Variables used in Eqs. 14-16 are further defined in Eqs. 17-20. In addition, we calculate the Monin-Obukhov scale height (Eq. 21) and the similarity diffusivity profiles $K_m$ and $K_h$ (Eqs. 22 and 23) for the surface layer. The nondimensional profile functions for shear- and thermal-gradients are then computed from Eqs. 12 and 13.

In the boundary-layer model, we then determine the height of the boundary layer (Eq. 10). The diffusivity coefficients above the surface layer are obtained with Eqs. 7-9. Finally, the tendencies of wind velocity, potential temperature, and specific humidity are calculated with Eqs. 1-3.

## 5.2.3 Diagrams of OSU1DPBL boundary-layer processes

The diagrams in this section represent some of the physical processes simulated in the OSU1DPBL model.

The diagram below shows the suspected important interactions between surface evapotranspiration and boundary-layer development for conditions of daytime surface heating. Solid arrows indicate the direction of those feedbacks which are normally positive (leading to increases of the recipient variable). Dashed arrows indicate negative feedbacks. Two consecutive negative feedbacks make a positive one.

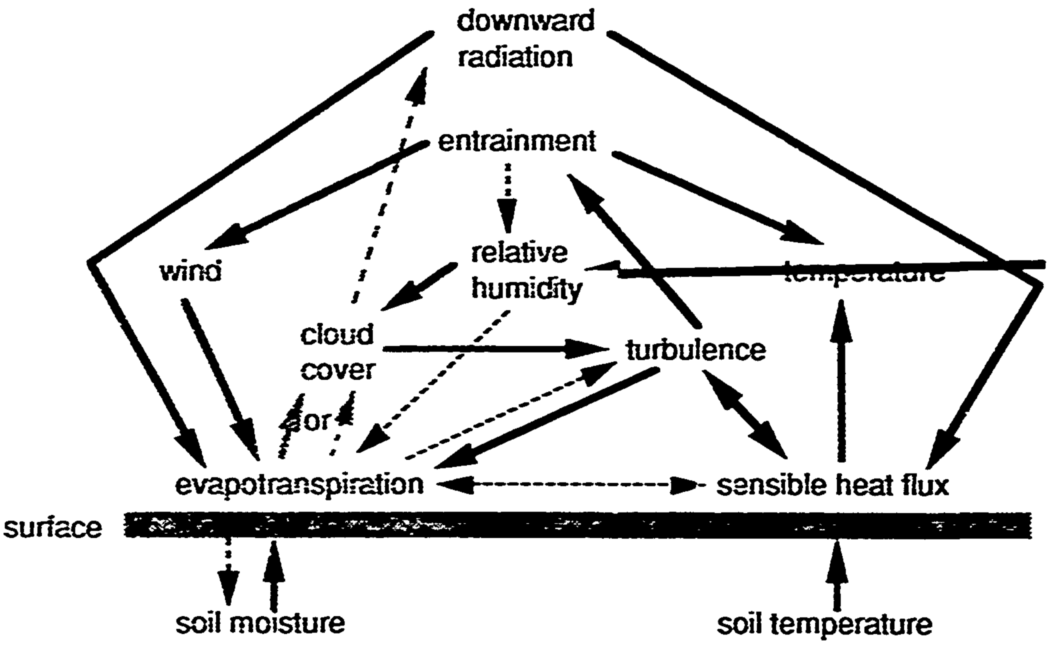
downward radiation
entrainment
relative humidity
wind
temperature
cloud cover
turbulence
or
evapotranspiration
sensible heat flux
surface
soil moisture
soil temperature

The flow chart for moisture is shown in the diagram below. Solid arrows represent the terms in the moisture budget; dashed arrows represent the interaction with the turbulent boundary layer. Ep is potential evaporation, Et is transpiration, Ec is evaporation of water from the plant canopy, and Edir is direct soil evaporation.

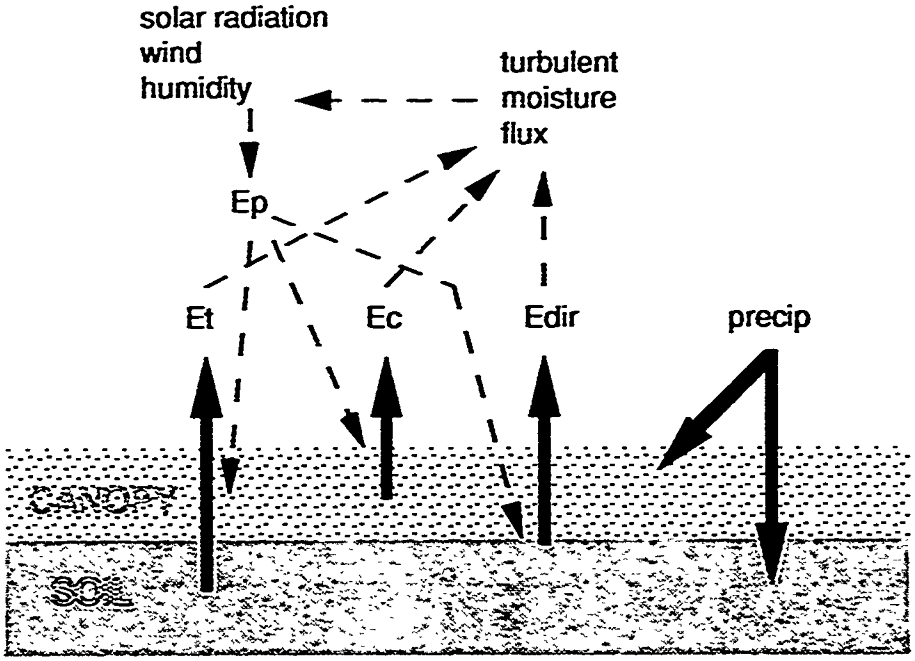

solar radiation
wind
humidity
turbulent
moisture
flux
Ep
Et
Ec
Edir
precip
CANOPY
SOIL

This schematic illustrates the more detailed geometry of the moisture budget in the hydrology model. Arrows indicate fluxes computed by the model; dashed lines indicate the mid-level of each soil layer which is the location of the computed soil water content ($\Theta 1$ at -2.5 cm and $\Theta 2$ at -52.5 cm).

**MOISTURE BUDGET**

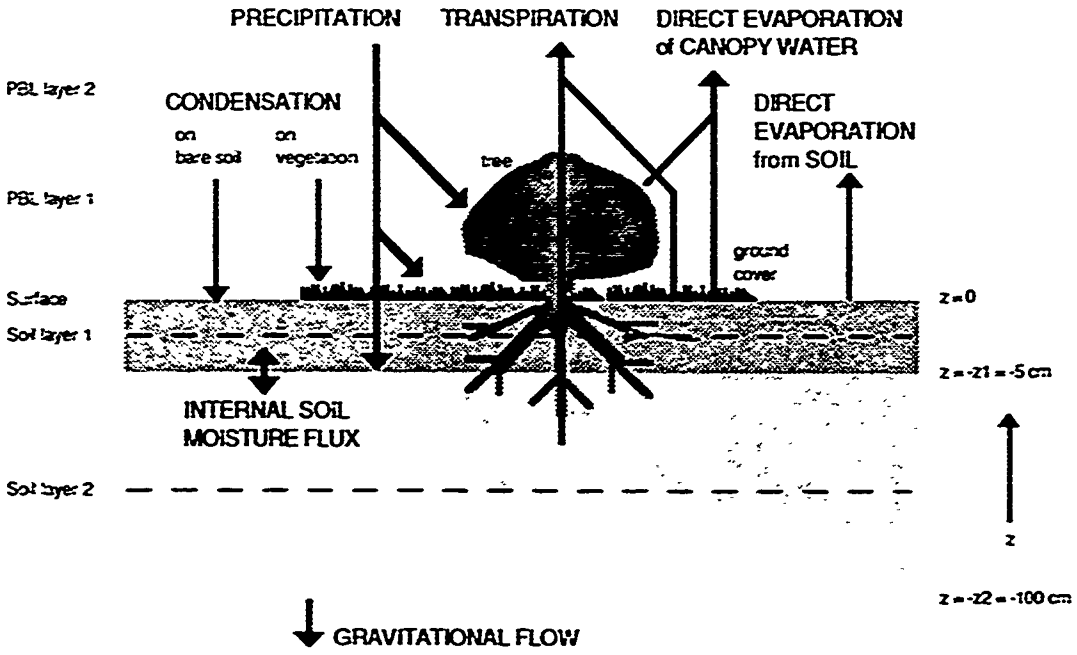
PRECIPITATION
TRANSPIRATION
DIRECT EVAPORATION of CANOPY WATER
PBL layer 2
CONDENSATION
on bare soil
on vegetation
DIRECT EVAPORATION from SOIL
tree
PBL layer 1
ground cover
Surface
Soil layer 1
z=0
z=-z1=-5cm
INTERNAL SOIL MOISTURE FLUX
Soil layer 2
z
z=-z2=-100cm
GRAVITATIONAL FLOW

The flow chart for the surface heat budget is shown in the diagram below. Arrow direction represents the direction of each contribution; arrow size represents relative magnitude.

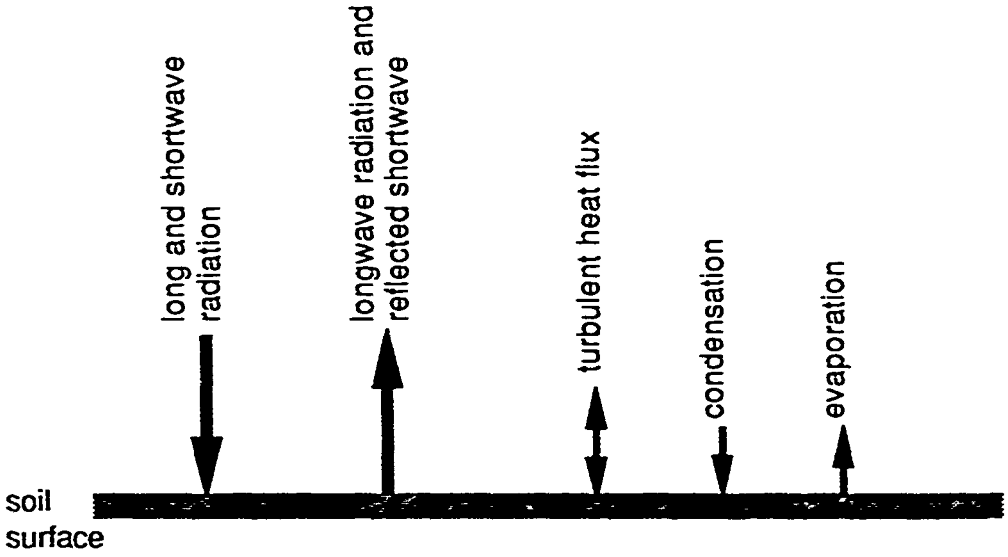
long and shortwave radiation
longwave radiation and reflected shortwave
turbulent heat flux
condensation
evaporation
soil surface

The schematic below illustrates the more detailed geometry of the heat budget used in the model. The terms in UPPERCASE letters represent terms from the surface energy balance. Arrows indicate fluxes computed by the model; dashed lines indicate the mid-level of each soil layer which is the location of the computed soil temperatures (T1 at -2.5 cm and T2 at -52.5 cm).

**HEAT BUDGET**

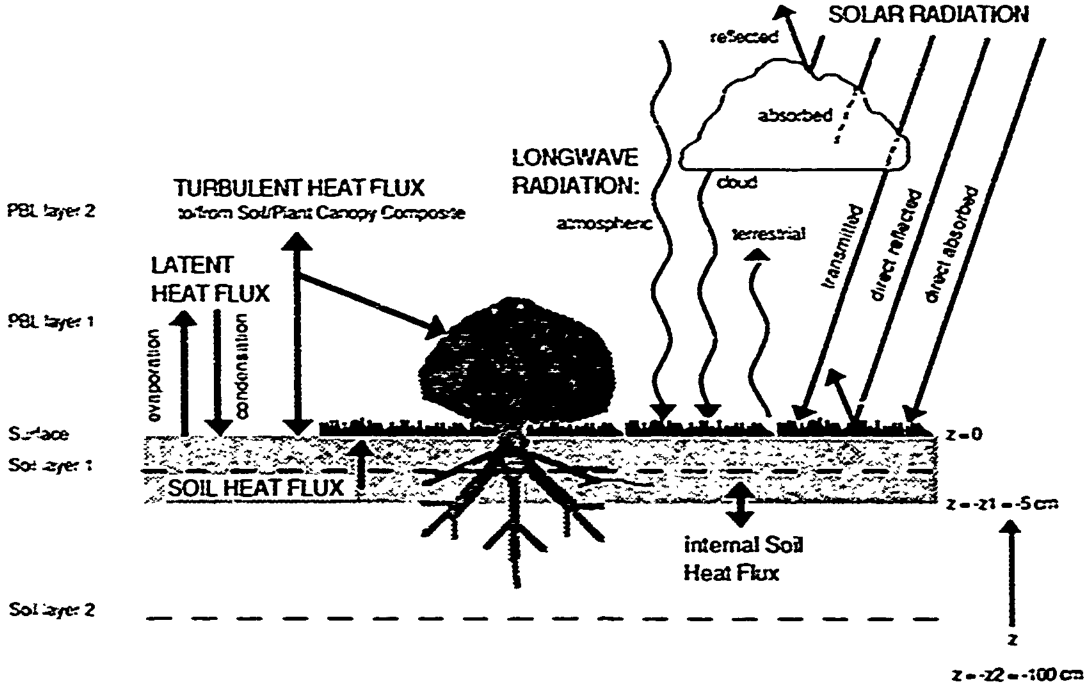
SOLAR RADIATION
reflected
absorbed
LONGWAVE
RADIATION:
cloud
atmospheric
terrestrial
transmitted
direct reflected
direct absorbed
TURBULENT HEAT FLUX
to/from Soil/Plant Canopy Composite
LATENT
HEAT FLUX
evaporation
condensation
PBL layer 2
PBL layer 1
Surface
Soil layer 1
Soil layer 2
SOIL HEAT FLUX
internal Soil
Heat Flux
z = 0
z = -z1 = -5 cm
z
z = -z2 = -100 cm

The graph below shows how the boundary-layer height is determined in OSU1DPBL for unstable and stable cases. Z is height; $\theta_v(Z)$ is the virtual potential temperature at a given height, $\theta_v(Z_1)$ is the virtual potential temperature at the first model level, $\theta_s$ is the surface temperature as determined from the surface energy balance, h is boundary-layer top, $\theta_v(h)$ is the virtual potential temperature at the boundary-layer top, and f(Ri) refers to a function of the layer Richardson number.

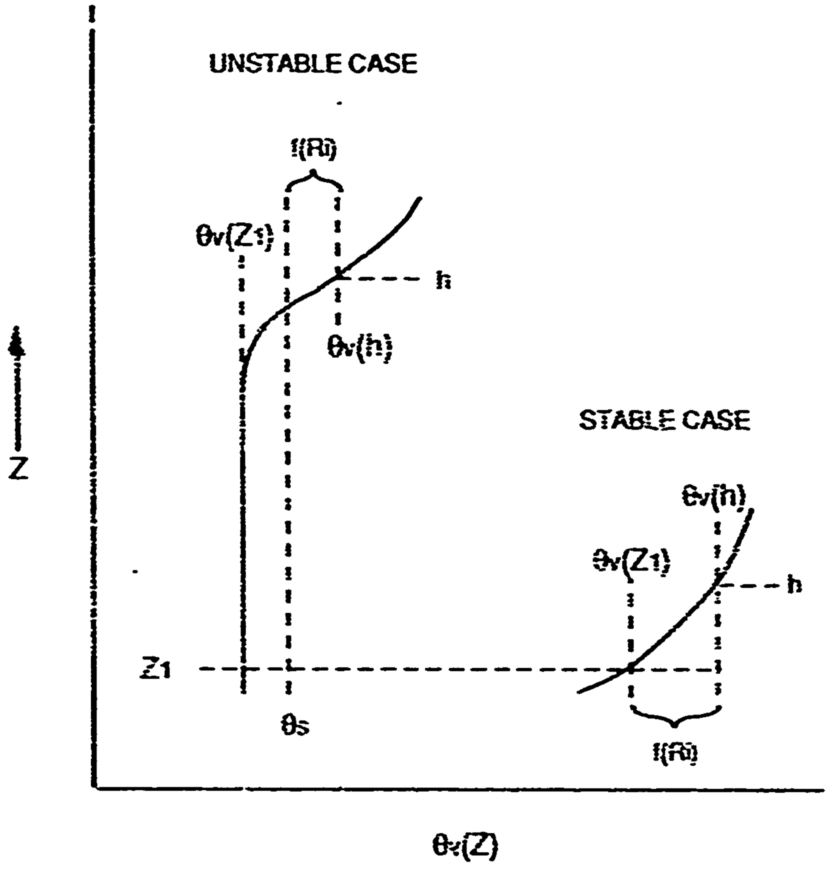
UNSTABLE CASE
f(Ri)
θv(Z1)
h
θv(h)
Z
STABLE CASE
θv(h)
θv(Z1)
h
Z1
θs
f(Ri)
θv(Z)

# Fractional Cloud Cover =
f(maximum RH in PBL, $\sigma_{RH}$ at that level)

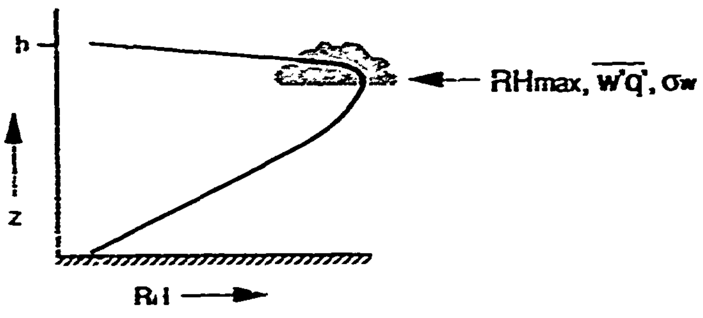

- determine level of maximum RH in PBL
- determine moisture flux at that level
- determine $\sigma_w$ at that level
  - unstable conditions: $\sigma_w = fct(z/h, w^*, u^*)$
  - stable conditions: $\sigma_w = fct(z/h, u^*)$

- $\sigma_{RH\text{-}turb} = a + b * f(\overline{w'q'}, \sigma_w, q_{sat})$

- $\sigma_{RH\text{-}meso} = c + d * f(\Delta x)$, where $\Delta x$ is the horizontal grid size

- $\sigma_{RH} = [(\sigma_{RH\text{-}turb})**2 + (\sigma_{RH\text{-}meso})**2]**0.5$

- Fractional Cloud Cover determined from normal distribution of RH: (use polynomial fit of normal distribution for analytical calculation of cloud cover)

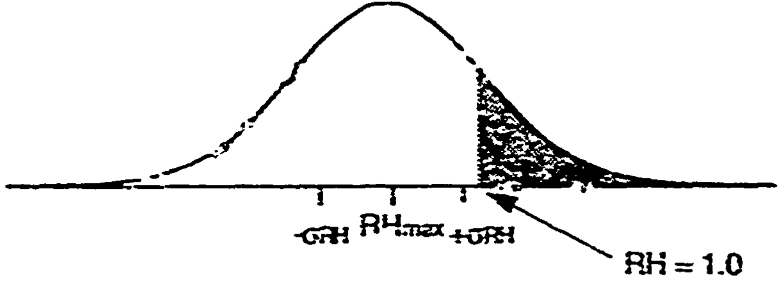

normal distribution of relative humidity

The figure below shows the incoming solar radiation interaction with cloud cover and the terms used in the calculation of the net solar radiation.

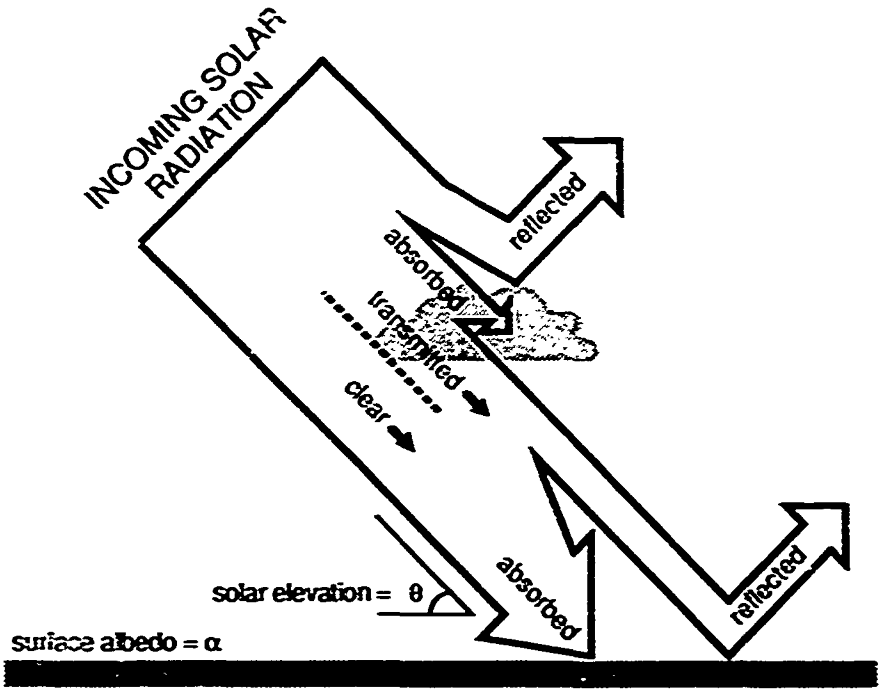
INCOMING SOLAR RADIATION
reflected
absorbed
transmitted
clear
absorbed
reflected
solar elevation = θ
surface albedo = α

INCOMING SOLAR RADIATION = CLEAR

Fractional coud cover = CLC

Fraction of solar radiation transmitted through clouds =
TRANSM = 0.06 + 0.17 sin θ

Fraction of solar radiation reflected/absorbed by clouds =
OPAQUE = 1 - TRANSM

Solar radiation below cloud level =
SOLAR = CLEAR (1 - CLC * OPAQUE)

Solar radiation absorbed at surface = (1 - α) SOLAR

### 5.2.4 OSU1DPBL Flowchart

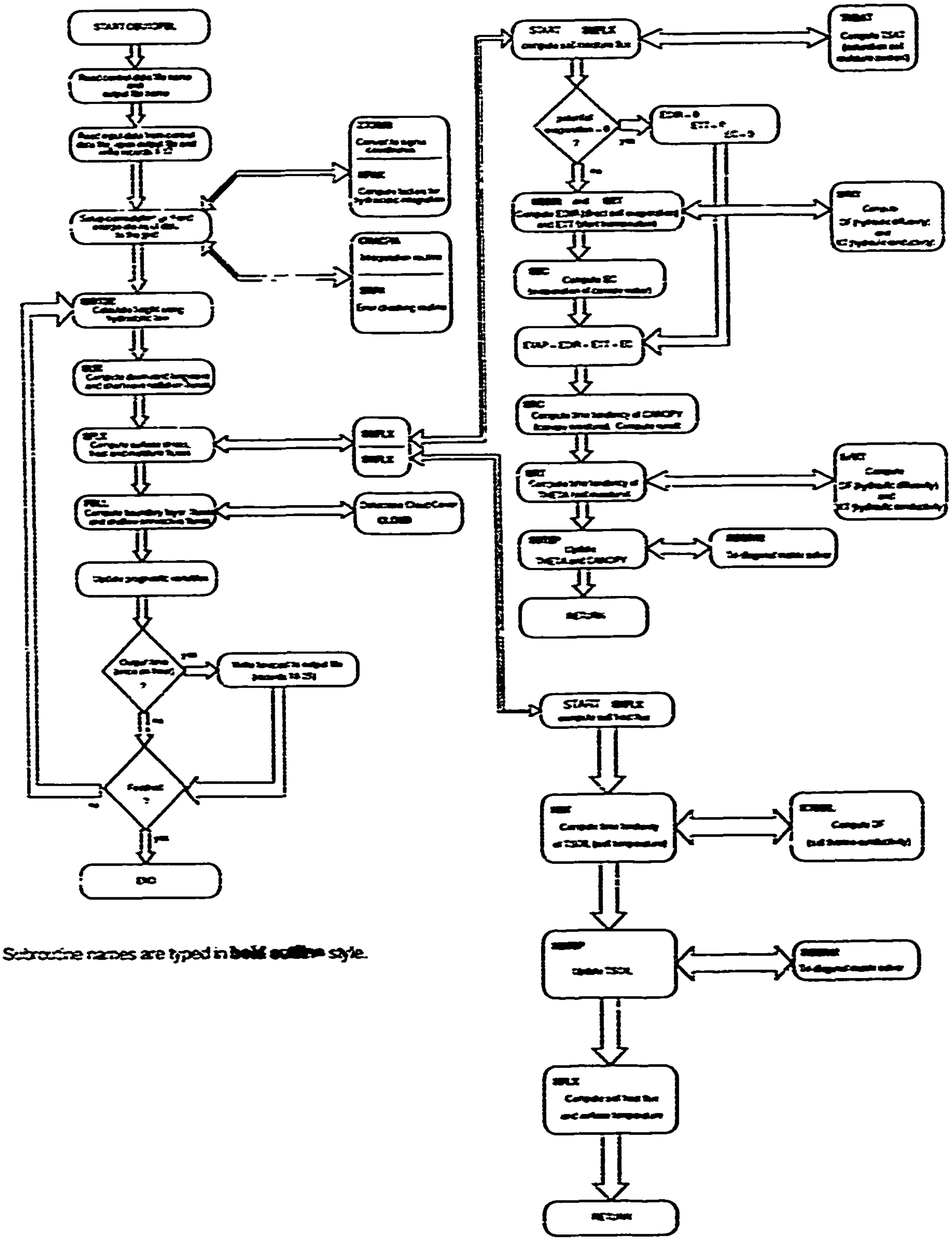
START
compute soil moisture flux
potential evaporation = 0
?
yes
no
Compute
Compute EC
EVAP = EDIR + ETT + EC
Compute time tendency of CANOPY
RETURN
START
yes
no
?
END

Subroutine names are typed in bold outline style.

## 5.2.5 Finite Differencing Techniques

The OSU1DPBL model employs different schemes for the numerical simulation of each of the different physical processes depending on the stability and other characteristics of the terms being approximated. This section contains a description of (1) the Leap-frog method used for time-stepping in the boundary layer, (2) the fully implicit Crank-Nicholson time integration scheme with the Galerkin technique for atmospheric diffusion, (3) the Crank-Nicholson scheme used for time integration in the soil and plant canopy, and (4) the Euler forward differencing scheme used for diffusion in the soil.

### 5.2.5.1 Time-Stepping in the Boundary Layer

To illustrate the method of time-stepping in the boundary layer, we first consider the model equation

$$\frac{\partial \psi}{\partial t} = f(\psi, t) \tag{1}$$

The implicit Leap-Frog scheme (with centered time differencing) for Eq. 1 would then be

$$\frac{1}{2\Delta t}\left(\psi^{n+1} - \psi^{n-1}\right) = f(\psi^{n+1}, t^{n+1}) + \text{error} \tag{2}$$

where the error is $O(\Delta t^2)$.

This method is not self-starting. Thus a first step using the Euler forward scheme is needed to start an integration. This scheme has a computational mode and a special procedure is implemented nominally every 25 steps to reduce this instability problem. Once every few Leap-Frog time-integration steps, the Euler forward scheme is used to prevent separation of the two different branches (Fig. 1).

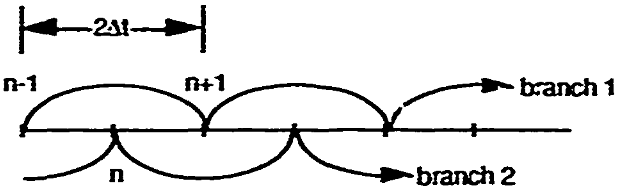

Fig. 1. Grid for the Leap-Frog scheme.

## 5.2.5.2 Finite-Element Formulations for Atmospheric Diffusion

The diffusion equation for the vertical mixing is given as

$$\frac{\partial u}{\partial t} = \frac{\partial}{\partial z}\left(K\frac{\partial u}{\partial z}\right) \qquad (3)$$

where the unknown u can be momentum, potential temperature, moisture, or a (conservative) tracer; t is time; z is the vertical coordinate; and the coefficient of diffusivity K is a function of stability. The fully implicit Cranck-Nicholson scheme (Marchuk, 1974) is selected for time integration; the solution follows closely the procedure in Ahlberg et al. (1967).

The method proceeds as follows. The finite difference form of the diffusion equation (Eq. 3) is

$$\frac{u^{+} - u^{-}}{2\Delta t} = \frac{\partial}{\partial z}\left(K\frac{\partial u^{+}}{\partial z}\right) \qquad (4)$$

where the superscripts + and − denote time level t+Δt and t−Δt, respectively. We now put the equation in the form of the Sturm-Liouville equations where

$$-2\Delta t\frac{\partial}{\partial z}\left(K\frac{\partial u^{+}}{\partial z}\right) + u^{+} = u^{-} \qquad (5)$$

We next expand the variables $u^{+}$ and $u^{-}$ into an element series of a modified Chapeau basis function $\phi_{i,j}$ for which

$$u^+ = \sum U^+_{j,i}\, \phi_{j,i} \qquad (6a)$$

$$u^- = \sum U^-_{j,i}\, \phi_{j,i} \qquad (6b)$$

where j=1,J indicate the basis sets defined for each layer $[z_i, z_{i+1}]$ and $\phi_{i,j}$ is nonzero only in the domain $[z_i, z_{i+1}]$. The summation index (j) runs from 1 to 2 for linear elements since there are only two nonzero elements over each interval. The linear elements are defined as

$$\phi_{i,1} = \frac{z_{i+1} - z}{z_{i+1} - z_i},$$

$$\phi_{i,2} = \frac{z - z_i}{z_{i+1} - z_i}$$

where the superscript denotes the interval over which the element function is to be applied (Figure 2).

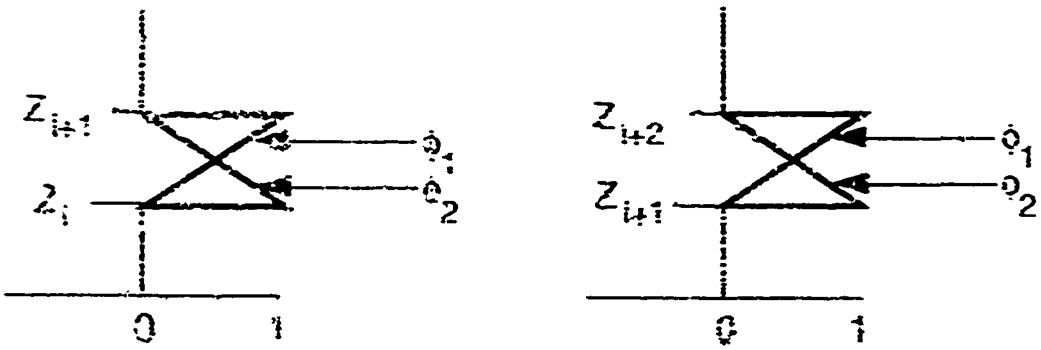

(a) (b)

Figure 2. Basis function used in OSU1DPBL vertical diffusion scheme for the domain (a) $z_i$ to $z_{i+1}$ and (b) $z_{i+1}$ to $z_{i+2}$.

We substitute Eqs. 6a-b into Eq. 5 to form

$$-\Delta t \frac{\partial}{\partial z}\left(K \frac{\partial}{\partial z}\left(\sum U^+_{j,i}\, \phi_{j,i}\right)\right) + \sum U^+_{j,i}\, \phi_{j,i} = \sum U^-_{j,i}\, \phi_{j,i} \qquad (7)$$

Applying the Galerkin criterion, we multiply Eq. 7 by the element of the basis function and integrate to produce

$$-\int_{z_i}^{z_{i+1}} \phi_{i,j} 2\Delta t \frac{\partial}{\partial z}\left(K\frac{\partial}{\partial z}\left(\sum U_{j,i}^{+}\ \phi_{j,i}\right)dz + \int_{z_i}^{z_{i+1}} \phi_{i,j} \sum U_{j,i}^{+}\ \phi_{j,i} dz\right.$$

$$= \int_{z_i}^{z_{i+1}} \phi_{i,j} \sum U_{j,i}^{-}\ \phi_{j,i} dz \tag{8}$$

Integration by parts yields

$$\int_{z_i}^{z_{i+1}} (2\Delta t) K\frac{\partial}{\partial z}\left(\sum U_{j,i}^{+}\ \phi_{j,i}\right)\frac{\partial \phi_{i,j}}{\partial z} dz + \int_{z_i}^{z_{i+1}} \phi_{i,j}\left(\sum U_{j,i}^{+}\ \phi_{j,i}\right)dz =$$

$$\int_{z_i}^{z_{i+1}} \phi_{i,j} \sum U_{j,i}^{-}\ \phi_{j,i} dz + \int_{z_i}^{z_{i+1}} (2\Delta t)\frac{\partial}{\partial z}\left(\phi_{i,j} K\frac{\partial}{\partial z}\left(\sum U_{j,i}^{+}\ \phi_{j,i}\right)\right)dz$$

where the second term on the right-hand side is the boundary-flux term and makes the application of the Neumann boundary conditions a natural procedure. Further,

$$(2\Delta t)\sum_{j=1}^{2} U_j^{+}\int_{z_i}^{z_{i+1}} K\frac{\partial \phi_{j,i}}{\partial z}\frac{\partial \phi_{i,j}}{\partial z} dz + \sum_{j=1}^{2} U_j^{+}\int_{z_i}^{z_{i+1}} \phi_{j,i}\phi_{i,j} dz =$$

$$\sum_{j=1}^{2} U_j^{-}\int_{z_i}^{z_{i+1}} \phi_{j,i}\phi_{i,j} dz - (2\Delta t)(\phi_{i,j}(z_{i+1})\tau(z_{i+1}) - \phi_{i,j}(z_i)\tau(z_i))$$

where the boundary stress at nodes $z_i$ and $z_{i+1}$ are explicitly included as $\tau$. Labelling the vertical coordinate of the grid as $z_1$, $z_2$, ..., $z_n$, we will apply the integration over the interval $[z_i, z_{i+1}]$. Only nonzero terms appear in the equations for i and i+1. For i

$$(2\Delta t)\left(\frac{U_i^{+}}{\Delta z^2}\int_{z_i}^{z_{i+1}} K dz - \frac{U_{i+1}^{+}}{\Delta z^2}\int_{z_i}^{z_{i+1}} K dz\right) + \frac{\Delta z}{3}U_i^{+} + \frac{\Delta z}{6}U_{i+1}^{+} =$$

$$\frac{\Delta z}{3}U_i^{-} + \frac{\Delta z}{6}U_{i+1}^{-} + (2\Delta t)\tau(z_i) \tag{9}$$

where

$$\Delta z = z_{i+1} - z_i$$

while the equation i+1 is:

$$(2\Delta t)\left(-\frac{U_i^+}{\Delta z^2}\int_{z_i}^{z_{i+1}} K dz + \frac{U_{i+1}^+}{\Delta z^2}\int_{z_i}^{z_{i+1}} K dz\right) + \frac{\Delta z}{6}U_i^+ + \frac{\Delta z}{3}U_{i+1}^+ =$$

$$\frac{\Delta z}{6}U_i^- + \frac{\Delta z}{3}U_{i+1}^- - (2\Delta t)\tau(z_{i+1}) \quad (10)$$

Our philosophy has been to transform u in terms of the basis set (modified Chapeau) with the U coefficients substituted into the equation of motion. We will now solve for U using matrix representation and construct the total variable from summing the basis set. In anticipation of a matrix representation of these equations, we will define the following:

$$B_{i,i} = \frac{2\Delta t}{\Delta z^2}\int_{z_i}^{z_{i+1}} K dz,$$

$$B_{i,i+1} = \frac{-2\Delta t}{\Delta z^2}\int_{z_i}^{z_{i+1}} K dz,$$

$$A_{i,i} = \frac{\Delta z_i}{3},$$

$$A_{i,i+1} = \frac{\Delta z_i}{6}, \text{ and}$$

$$\tau_i = \tau(z_i).$$

Eq. 9 now becomes

$$(B_{i,i}+A_{i,i})U_i^+ + (B_{i,i+1}+A_{i,i+1})U_{i+1}^+ = A_{i,i}U_i^- + A_{i,i+1}U_{i+1}^- + (2\Delta t)\tau_i$$

Similarly, Eq. 10 becomes

$$(B_{i,i+1}+A_{i,i+1})U_i^+ + (B_{i,i}+A_{i,i})U_{i+1}^+ = A_{i,i+1}U_i^- + A_{i,i}U_{i+1}^- - (2\Delta t)\tau_{i+1}$$

Adding the second equation for interval $[z_i, z_{i+1}]$ and the first equation for $[z_{i+1}, z_{i+2}]$, we can cancel the internal stress term to close the equation set and obtain

$$
\begin{aligned}
&(B_{i,i+1} + A_{i,i+1})U_i^+ + (B_{i,i} + B_{i+1,i+1} + A_{i,i} + A_{i+1,i+1})U_{i+1}^+ \\
&\quad + (B_{i+1,i+2} + A_{i+1,i+2})U_{i+2}^+ = \\
&\qquad\qquad A_{i,i+1}U_i^- + (A_{i,i} + A_{i+1,i+1})U_{i+1}^- + A_{i+1,i+2}U_{i+2}^-
\end{aligned}
$$

We will define another set of new variables to further simplify the notation

$$A'_{i,i} = (A_{i,i-1} + A_{i,i+1})$$

$$A'_{i,i+1} = A_{i,i+1} = \frac{\Delta z_i}{6}$$

$$A'_{i+1,i} = A'_{i,i+1}$$

$$B'_{i,i} = B_{i-1,i-1} + B_{i,i} = -B'_{i,i-1} - B'_{i,i+1}$$

$$B'_{i,i+1} = B_{i,i+1} = \frac{(2\Delta t)}{\Delta z_i^2}\int_{z_i}^{z_{i+1}} K\,dz$$

$$B'_{i+1,i} = B'_{i,i+1}$$

We now obtain the matrix equation representation

$$(B' + A')\,U^+ = A'\,U^- + \begin{bmatrix} 2\Delta t\tau_1 \\ 0 \\ 0 \\ . \\ . \\ 0 \\ -2\Delta t\tau_N \end{bmatrix}$$

provided we define the coefficients in the first and the last row as

$$A'_{1,1} = \frac{\Delta z_1}{3}$$

$$A'_{1,2} = \frac{\Delta z_1}{6},$$

$$A'_{N-1,N} = \frac{\Delta z_{N-1}}{6}$$

$$A'_{N,N} = \frac{\Delta z_{N-1}}{3}$$

$$B'_{1,1} = \frac{2\Delta t}{\Delta z_1^2}\int_{z_1}^{z_2} K dz$$

$$B'_{1,2} = -B'_{1,1}$$

$$B'_{N,N} = \frac{2\Delta t}{\Delta z_{N-1}^2}\int_{z_{N-1}}^{z_N} K dz$$

$$B'_{N-1,N} = B'_{N,N}$$

Standard methods can now be applied to solve the tridiagonal matrix equation to obtain the updated values of u.

## Application of the Technique for Minimally Diagnosed Boundary Layer

No special modification of the above methodology is required when the boundary layer is at its minimum allowable depth in the OSU1DPBL model (h = the first model level above the surface). The diffusivity profile theoretically vanishes at z = h. In practice, however, K is calculated at intermediate levels and the vertical flux divergence is calculated at the prognostic levels. This is ensured provided that the diffusivity calculation recognizes that the boundary layer is a constant flux layer, with zero diffusion above. Hence the flux divergence is nonzero at the boundary-layer top when the boundary layer is at its minimum allowable depth.

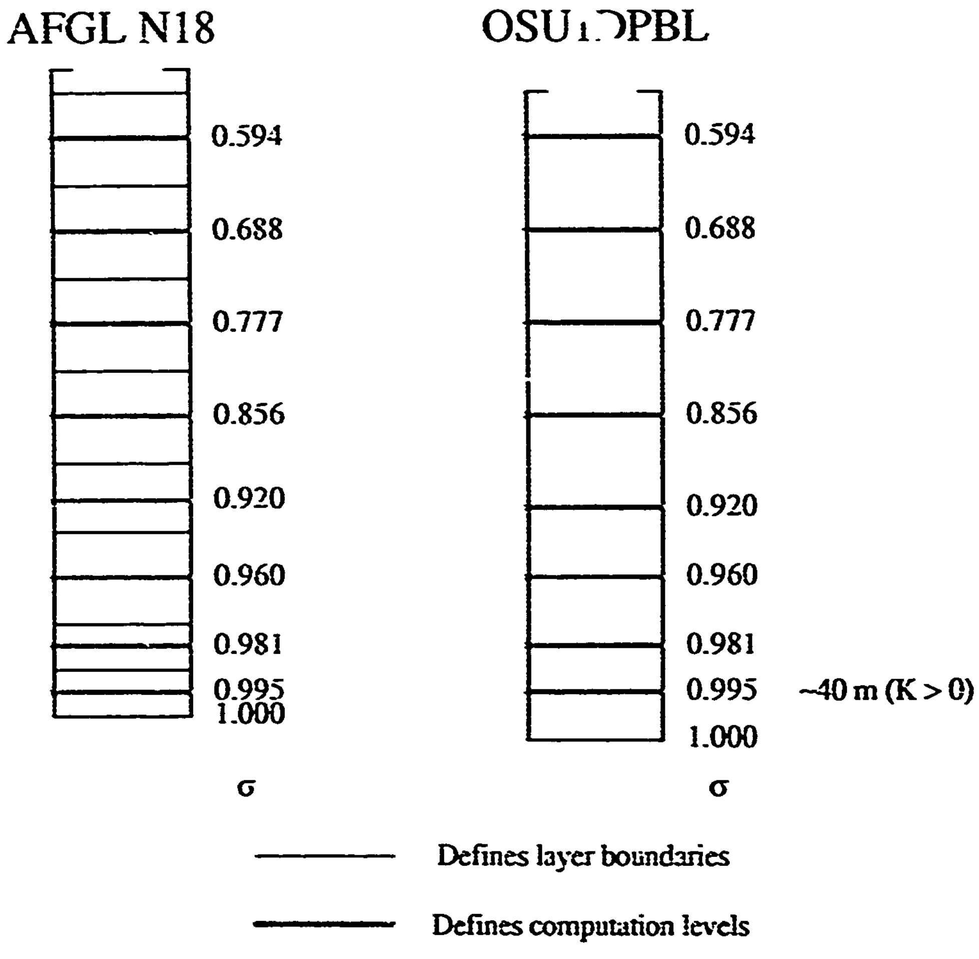
AFGL N18
OSU1DPBL
0.594
0.688
0.777
0.856
0.920
0.960
0.981
0.995
1.000
σ
0.594
0.688
0.777
0.856
0.920
0.960
0.981
0.995
~40 m (K > 0)
1.000
σ
Defines layer boundaries
Defines computation levels

The figure above shows the vertical staggering of the grid for A18 resolution in the AFGL GSM and OSU1DPBL. Note that the computational levels match in sigma coordinates although the GSM uses explicit vertical staggering. OSU1DPBL calculates u, v, $\theta$, and q at the computation levels and K and $\partial/\partial z[u,v,\theta,q]$ at the layer boundaries (between computational levels).

### 5.2.5.3 Time-stepping in the Soil and Plant Canopy

The Crank-Nicholson time integrator is also called the Trapezoidal approximation. It is devised as a "better than Euler" scheme because it is a combination of the Euler forward and Euler backward schemes. Using Eq. 1 to illustrate the method, the Euler forward scheme would be

$$\frac{1}{\Delta t}(\psi^{n+1} - \psi^{n}) = f(\psi^{n},t^{n}) + \frac{1}{2}(\Delta t)\ \psi'' + \text{Error} \qquad (11)$$

The Euler Backward scheme for Eq. 1 would be

$$\frac{1}{\Delta t}(\psi^{n+1} - \psi^{n}) = f(\psi^{n+1},t^{n+1}) - \frac{1}{2}(\Delta t)\ \psi'' + \text{Error} \qquad (12)$$

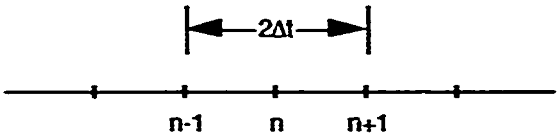

Fig. 2. The grid for the trapezoidal scheme.

The Euler forward scheme overdamps the solution while the Euler backward scheme underdamps it. This observation gives rise to the Crank-Nicholson scheme which can be viewed as an average of the two schemes shown above. The Crank-Nicholson scheme for Eq. 1 would be

$$\frac{1}{\Delta t}(\psi^{n+1}- \psi^{n}) = \frac{1}{2}[f(\psi^{n+1},t^{n+1}) + f(\psi^{n},t^{n})] + \text{Error} \qquad (13)$$

A few comments about the scheme are in order here. The Euler forward scheme and the Euler backward scheme are globally accurate to $O(\Delta t^1)$; the Crank-Nicholson scheme is accurate to $O(\Delta t^2)$. The Crank-Nicholson scheme is also absolutely stable with no computational mode and with slight to moderate phase retardation (see Baer and Simons (1970) for a good graphical representation).

#### 5.2.5.4 Finite Differencing in the Soil Layer

The vertical flux of water at the interface between the two soil layers is computed from the gradient between the midlevels of the two soil layers, and from the hydraulic diffusivity and conductivity evaluated from the soil moisture content of the wetter of the two soil layers. The latter "upstream" diffusivity is invoked because wetting fronts seem to propagate vertically and are based on the hydraulic properties in the wetter soil behind the front. When compared to high resolution models, this procedure reduces truncation errors as effectively as does employing the more complicated finite element approximation. It is also used to determine the soil heat flux.

At the bottom of the model, the hydraulic diffusivity is assumed to be zero so that the soil water flux is due only to the gravitational term $K(\theta)$. The soil heat flux is computed in terms of a vertical temperature gradient determined using a specified temperature at an imaginary level 1 meter below the bottom of the model.

### 5.2.6 Modelling the Snow Cover

The OSU1DPBL combined boundary-layer and soil model was originally developed in an effort to parameterize boundary-layer heat and moisture transport for a global forecast model (Brenner et al., 1984). In order to implement the boundary-layer package in a global model, or as a stand-alone model, it is necessary to include the effects of snow cover (Tuccillo, 1987).

Snow cover serves as the upper boundary of the earth's surface, thereby affecting the boundary layer as well as the soil. Although snow cover reduces the available energy at the surface because of its high albedo for solar radiation and high emissivity in the spectral range of most terrestrial radiation, its insulative properties greatly reduce heat loss from the soil (Gray and Male, 1981). The thermal conductivity of new snow is roughly an order of magnitude less than that of most soils. As snow "ages", its albedo decreases while its thermal conductivity increases which generally remains less than that of moist soil.

The nocturnal cooling which is usually balanced by the soil heat flux (Oke, 1978) may lead to much cooler surface temperatures in the presence of snow. Siberia, northwestern North America, and Antarctica are among the regions where intense radiative cooling occurs which causes the formation of air masses characterized by very low surface temperature and strong surface inversions.

In its present stage, the model does not predict precipitation; rather precipitation is specified as an input to the model. We categorize fallen precipitation as snow when both the temperature at 850 mb is below 0°C and the dew point temperature at the first model level above the surface is below 0°C. The first step in the model is to make an estimate of the heat flux between the soil and the snow by using the relationship

$$G = K_s \frac{T_s - T_{soil}}{h_s} \qquad (1)$$

where $k_s$ is the thermal diffusivity for snow, $T_s$ is the "skin" temperature, $T_{soil}$ is the top-layer soil temperature (in the present model, the top layer is 5 cm thick), and $h_s$ is the depth of the snow layer (assumed to be ten times the water-equivalent snow depth).

The thermal diffusivity for snow depends on the porosity of snow. It can vary from 0.063 $W\ K^{-1}\ m^{-1}$ for new snow with a porosity of 0.95, to 0.71 $W\ K^{-1}\ m^{-1}$ for packed snow with porosity of 0.5 (comparable to clay). Unless we try to resolve the snow surface into many layers and monitor the "age" of each layer, we cannot model the porosity or the snow pack. Here, we choose the value of 0.13 $W\ K^{-1}\ m^{-1}$ for $k_s$ which corresponds to a porosity of 0.8. The soil-surface temperature is assumed to be the same as the top-layer averaged soil temperature. This assumption is supported by observations that the largest thermal gradient below the snow surface is near the top of the snow layer due to weak thermal diffusion within the snow layer (Oke, 1978). When snow falls over warm soil, the snow heat flux may lead to snow melt.

The calculation of the snow heat flux enables one to calculate the potential evaporation $E_p$ using the surface energy balance

$$(1-\alpha)S\downarrow + L\downarrow - \sigma T'^4 = G + \rho_0 c_p C_h |V|(T'-T_0) + LE_p \qquad (2)$$

where

$$E_p = \rho_0 C_h |V|(q_s(T')-q_0) \qquad (3)$$

The albedo ($\alpha$) is assigned a constant value of 0.7; the normal change of snow albedo with age of snow pack is not included. The terms on the left-hand side of (2) are the downward short- and longwave radiative flux and the upward longwave radiative flux. The terms on the right-hand side are the snow, sensible, and latent heat fluxes. The skin temperature $T'$ is the temperature of the surface if the snow surface is evaporating at the potential rate. While the units of $E_p$ in the surface energy balance are kg $m^{-2}$ $s^{-1}$, typical soil hydrological applications use the units m $s^{-1}$. The conversion is accomplished using the density of water ($r_w$ = $10^3$ kg $m^{-3}$). This formula is most appropriate for melted water in the snow. Otherwise, $C_h$ describes sublimation which may depend primarily on solar radiation and snow temperature.

The snow evaporates/sublimates at the following rate

$$E = \begin{bmatrix} E_p, & h_s \geq E_p\Delta t \\ \dfrac{h_s}{\Delta t}, & h_s < E_p\Delta t \end{bmatrix} \qquad (4)$$

where E is in m $s^{-1}$. When the depth of the snow layer is thick, it will evaporate at the potential rate for an entire time step. When the snow layer is thin so that it cannot maintain the potential rate, we assume the snow to evaporate evenly and completely over the time interval $\Delta t$.

When the evaporation rate E is determined, the skin temperature $T_s$ is calculated by solving the surface energy balance (Eq. 2) again

$$(1-\alpha)S\downarrow + L\downarrow - \sigma T_s^4 = D_s \frac{T_s - T_{soil}}{h_s} + \rho_0 c_p C_h |V|(T_s-T_0) + LE \qquad (5)$$

where $T_s$ recognizes evaporation/sublimation of the snow from Eq. 4. If the resulting skin temperature is above the melting point of snow ($T_c$ = 273.16 K), the amount of snow melt $h_m$ is calculated as follows

$$(1-\alpha)S\downarrow + L\downarrow - \sigma T_c^4 = D_s\frac{T_c-T_{soil}}{h_s} + \rho_0 c_p C_h|\mathbf{V}|(T_c-T_0) + LE + L_i h_m \quad (6)$$

where $L_i$ is the latent heat of fusion and $T_c$ is the snow temperature which recognizes both evaporation/sublimation, and melting of snow.

In the model, it is arbitrarily assumed that when precipitation falls, it has the same temperature as that of the lowest atmospheric model layer. Conversion of warm rain to ice or snow may be an important process during warm front passages and is included in the model. Excess snow melt from Eq. 6 is allowed to drip into the top soil layer. Soil temperature is updated by accounting for heat flux (G) across the snow-soil interface.

### 5.2.7 The Radiation Richardson Number

The radiation Richardson number was developed by Mahrt and Ek (1984) in a study which examined the relationship between atmospheric stability and potential evaporation. Although not widely used heretofore, the radiation Richardson number is appealing in that it does not rely on estimates of fluxes to estimate low-level stability; rather, the sensible heat flux is treated as a residual from the surface energy balance. The radiation Richardson number ($Ri_{rad}$) is defined as

$$Ri_{rad} \equiv -\frac{g}{\theta}\frac{(R_n + Q_G)\,z}{u^3} \qquad (1)$$

where $\theta$ is the mean potential temperature, u is a velocity scale, z is the height of the wind speed observation, g is the gravitational acceleration, $R_n$ is the net radiation (defined as positive upwards), and $Q_G$ is the heat flux (to the soil). The radiation Richardson number has been used by Ken Mitchell to compare model predictions with observations where the surface flux information is not available.

The flux Richardson number is

$$\mathrm{Ri}_f \equiv \frac{\frac{g}{\theta}\,\overline{w'\theta'}}{\frac{\partial \overline{V}}{\partial z}\,\overline{w'V'}} \tag{2}$$

with the surface heat flux

$$Q_H = R_n - Q_G \approx \overline{w'\theta'} \tag{3}$$

Typically the radiation Richardson number will have the same sign as other formulations of the Richardson number (such as the flux form above or the low-level bulk form, both of which are available in the model as RIF and RIB, respectively). The range for $\mathrm{Ri}_{rad}$ has been seen to have slightly larger magnitudes, in part due to the role of the soil heat flux. There is no special significance in terms of a known critical radiation Richardson number (of 0.25, for example), and no direct comparisons of the magnitude of $\mathrm{Ri}_{rad}$ to the other forms should be attempted.

A regression relationship between $\mathrm{Ri}_{rad}$ and z/L (Mahrt and Ek, 1984) can be used to estimate $\mathrm{Ri}_f$ for comparison with the model prediction of $\mathrm{Ri}_f$. The cube root of z/L is correlated to $(\mathrm{Ri}_{rad})^{1/3}$ with a correlation coefficient of 0.90 in the unstable case and 0.77 in the stable case. The regression relationship for the unstable case is

$$\left(\frac{z}{L}\right)^{1/3} = -8.64\,(\mathrm{Ri}_{rad})^{1/3} - 0.09 \tag{4}$$

and for the stable case

$$\left(\frac{z}{L}\right)^{1/3} = -15.29\,(\mathrm{Ri}_{rad})^{1/3} - 0.13 \tag{5}$$

Both relationships predict that z/L approaches $\sim -10^{-3}$ as the net radiation vanishes. This small constant has no special significance for the near neutral case but rather improves the fit over the range of the values of the radiation Richardson number. A higher order model is not justified because of the very approximate nature of this development.

### 5.2.8 Stable Boundary Layer

By itself, the usual similarity theory for the stable boundary layer leads to a significant overestimation of surface cooling. This is due to (a) failure to consider subgrid-scale spatial variability where vertical fluxes can occur in part of the grid even with large Richardson number based on grid averaged variables (Mahrt, 1987), (b) poor vertical resolution where turbulence may occur in thinner layers, perhaps intermittently, even when the Richardson number over the model layer is large, (c) neglect of clear air radiative cooling, (d) neglect of gravity wave momentum transport, and (e) use of a temperature from the surface energy balance (instead of temperature at $z_0$) to compute the surface-layer Richardson number.

To compensate for such inadequacies, various mechanisms have been employed (often unreported) which include capping the allowable value of the Richardson number or specifying a minimum wind speed. We use the area-averaged exchange coefficient relationship of Mahrt (1987) where the exchange coefficient for momentum is proportional to $\exp(-Ri_{bulk})$ with the Kondo et al. (1978) modification to the nondimensional gradients.

The above modifications lead to significant improvements of model performance in the nocturnal boundary layer (Ruscher, 1987). However, a future rederivation may include explicit dependence on (a) vertical resolution, (b) wind speed, and (c) subgrid characteristics such as standard deviation of subgrid terrain height (surface inhomogeneity).

### 5.2.9 Potential Evaporation and Surface Temperature

#### 5.2.9.1 Potential Evaporation

The potential evaporation is used to compute the actual evaporation in the model. The derivation of potential evaporation closely follows Mahrt and Ek (1984). Many terms not defined in this section are found in section 5.2.1. The usual Penman relationship is modified since the surface temperature is needed to compute the net radiation. As a first step, we evaluate the surface energy balance for the reference state of a saturated surface.

$$(1-\alpha)S\downarrow + L\downarrow - \sigma\theta_s^4 = G + H' + L_v E_p \tag{1}$$

where $(1-\alpha)S\downarrow + L\downarrow$ is the total downward radiation, the upward longwave radiation, $\sigma\theta_s^4$, is linearized as

$$\sigma\theta_s^4 = \sigma T_0^4 \left(1 + 4\left(\frac{\theta_s - T_0}{T_0}\right)\right)$$

G is the soil heat flux, the sensible heat flux which uses a saturated surface temperature appropriate for the potential evaporation and is defined as

$$\begin{aligned} H' &= \rho c_p C_h(\theta_s - \theta_0) \\ &= \rho c_p C_h[(\theta_s - T_0) - (\theta_0 - T_0)] \end{aligned}$$

and $L_v E_p$ is the potential evaporation ($L_v$ is latent heat). $\theta_s$ is the surface temperature, and $\theta_0$ and $T_0$ are the potential and actual temperatures at the first model level, respectively. The surface energy balance may then be rewritten as

$$\begin{aligned} (1-\alpha)S\downarrow + L\downarrow - \sigma T_0^4 - 4\sigma T_0^4\left(\frac{\theta_s - T_0}{T_0}\right) &= \\ G + \rho c_p C_h[(\theta_s - T_0) - (\theta_0 - T_0)] + L_v E_p \end{aligned} \tag{2}$$

Combining terms and solving for $L_v E_p$

$$\begin{aligned} L_v E_p = {} & (1-\alpha)S\downarrow + L\downarrow - \sigma T_0^4 - G + \rho c_p C_h(\theta_0 - T_0) \\ & - (\theta_s - T_0)\left(\frac{4\sigma T_0^4}{T_0} + \rho c_p C_h\right) \end{aligned} \tag{3}$$

The latent heat flux is approximated as

$$
\begin{aligned}
L_v E_p &= \rho L_v C_h \, (q_s^* - q_0) \\
&= \rho L_v C_h \, [(q_s^* - q_0^*) + (q_0^* - q_0)] \\
&= \rho L_v C_h \left[ \left( \frac{q_s^* - q_0^*}{\theta_s - T_0} \right) (\theta_s - T_0) + (q_0^* - q_0) \right] \\
&\approx \rho L_v C_h \left[ \left( \frac{dq_s}{dT} \right) (\theta_s - T_0) + (q_0^* - q_0) \right]
\end{aligned}
$$

where $q_s^*$ is the surface saturation specific humidity. $q_0$ and $q_0^*$ are the actual and saturation specific humidities at the first model level, respectively. Solving for $\theta_s - T_0$ from the above expression

$$
\theta_s - T_0 = \frac{\left[ \dfrac{L_v E_p}{\rho L_v C_h} - (q_0^* - q_0) \right]}{\left( \dfrac{dq^*}{dT} \right)}
$$

Substituting the above expression for $\theta_s - T_0$ into Eq. 3, noting that $\rho T_0 = p_{sfc}/R_d$, and solving for $E_p$

$$
E_p = \left( \frac{\left[ \dfrac{R_n}{\rho c_p C_h} + (\theta_0 - T_0) \right] \Delta + (r + 1) A}{\Delta + r + 1} \right) \frac{\rho c_p C_h}{L_v}
$$

$$
R_n = (1 - \alpha) S\downarrow + L\downarrow - \sigma T_0^4 - G
$$

$$
\Delta = \frac{dq^*}{dT} \frac{L_v}{c_p}
$$

$$
r = \frac{4 \sigma T_0^4 R_d}{p_{sfc} c_p C_h}
$$

$$
A = (q_0^* - q_0) \frac{L_v}{c_p}
$$

From the notation in the OSU1DPBL model code,

$$\rho c_p C_h = RCH$$

$$L_v = ELV$$

$$\Delta = DELTA$$

$$r + 1 = RR$$

$$A = A$$

$$\frac{R_n}{\rho c_p C_h} + (\theta_0 - T_0) = RAD$$

We define an expression for potential evaporation used in the model as

$$E_p = \left( \frac{RAD \cdot DELTA + RR \cdot A}{DELTA + RR} \right) \frac{RCH}{ELV}$$

### 5.2.9.2 Surface Temperature

To define the surface temperature, $\theta_s$, we start with the surface energy balance similar to Eq. 1 except we use the actual evaporation $E$ instead of the potential $E_p$. Note that $E = \beta E_p$ where $\beta$ is a factor multiplied by the potential evaporation to get the actual evaporation. The surface energy balance then becomes

$$(1-\alpha)S\downarrow + L\downarrow - \sigma\theta_s^4 = G + H + \beta L_v E_p$$

Using similar approximations from the previous section, we can rewrite this surface energy balance as

$$(1-\alpha)S\downarrow + L\downarrow - \sigma T_0^4 - 4\sigma T_0^4 \left( \frac{\theta_s - T_0}{T_0} \right) =$$

$$G + \rho c_p C_h [(\theta_s - T_0) - (\theta_0 - T_0)] + \beta L_v E_p$$

Noting that

$$F = (1 - \alpha)S\downarrow + L\downarrow$$

$$G = K_T(\Theta) \frac{(\theta_s - T_{1soil})}{\Delta z}$$

where the terms in G are defined in the model physics chapter. Using the definition of r from above, we can now write the surface energy balance as

$$\frac{F - \sigma T_0^4}{\rho c_p C_h} - \frac{K_T(\Theta)(\theta_s - T_{soil})}{\Delta z \rho c_p C_h} = (r + 1)(\theta_s - T_0)$$

$$- (\theta_0 - T_0) + \frac{\beta L_v E_p}{\rho c_p C_h}$$

Combining terms and solving for $\theta_s$

$$\theta_s = \frac{T_0 + \dfrac{\dfrac{F - \sigma T_0^4}{\rho c_p C_h} + (\theta_0 - T_0) - \dfrac{\beta L_v E_p}{\rho c_p C_h}}{r + 1} + \dfrac{K_T(\Theta) T_{1soil}}{\Delta z \rho c_p C_h (r+1)}}{1 + \dfrac{K_T(\Theta)}{\Delta z \rho c_p C_h (r+1)}}$$

Using the terms in the OSU1DPBL model code noted in the previous section,

$$EPSCA = \frac{L_V E_p}{\rho c_p C_h}$$

$$\Delta z = -0.5 \cdot ZSOIL(1)$$

$$YY = T_0 + \frac{\dfrac{(F - \sigma T_0^4)}{RCH} + (\theta_0 - T_0) - \beta EPSCA}{RR}$$

$$ZZ = \frac{K_T(\Theta)}{\Delta z \cdot RCH \cdot RR}$$

$$ZZ1 = ZZ + 1$$

The surface temperature $\theta_s$ is now given by

$$\theta_s = \frac{YY + ZZ \cdot T_{1soil}}{ZZ1}$$

## 5.2.10 Canopy Resistance

To account for the reduction in transpiration due to internal plant physiology, OSU1DPBL uses a plant coefficient (PC). The PC is multiplied by the potential evaporation and a value for the soil moisture deficit to obtain plant transpiration. The usual convention in meteorology is to express this reduction in terms of a canopy resistance (RC). The two expressions, PC and RC, can be related to each other by equating the expression for transpiration used in OSU1DPBL and in Monteith (1965). The following relation is obtained for use in the model (Holtslag and Ek, 1990)

$$RC = \frac{\dfrac{(RR + DELTA)}{PC} - (DELTA + RR)}{RR \cdot CH}$$

For $0 < PC \leq 1$,

$$RR = \frac{4\sigma\, T_0^4\, R_d}{p_{sfc} C_h\, c_p} + 1$$

$$DELTA = \frac{L_v}{c_p} \frac{dq_s}{dT}$$

RR and DELTA are dimensionless quantities; $\sigma$ is the Stefan-Boltzmann constant ($5.67 \times 10^{-8}$ W m$^{-2}$ K$^{-4}$); $T_0$ is the air temperature at the first model level; $R_d$ is the gas constant for dry air (287 J kg$^{-1}$ K$^{-1}$); $p_{sfc}$ is the surface pressure (Pa); CH is the surface exchange coefficient for heat and moisture (m s$^{-1}$); $c_p$ is the specific heat for dry air (1004.5 J kg$^{-1}$ K$^{-1}$); $L_v$ is the latent heat of vaporization ($5.2.5 \times 10^6$ J kg$^{-1}$); and $dq_s/dT$ is the slope of the saturation specific humidity curve (K$^{-1}$).

The user has the choice of specifying either a plant coefficient or a canopy resistance in the OSU1DPBL model.

## 5.2.11 References

Al Nakshabandi, G. and H. Kohnke, 1965: Thermal conductivity and diffusivity of soils as related to moisture tension and other physical properties, *Argic. Meteorol.*, **2**, 271-279.

Alhberg, H. J., E. N. Nilson and J. L. Walsh, 1967: *The Theory of Splines and their Applications*, Academic Press, 284 pp.

Baer, F. and T. J. Simons, 1970: Computational stability and time truncation of coupled nonlinear equations with exact solutions. *Mon. Wea. Rev.*, **98**, 665-679.

Brenner, S., C.-H. Yang and K. Mitchell, 1984: *The AFGL Global Spectral Model: Expanded Resolution Baseline Version*. Rept. No. AFGL-TR-84-0308, Air Force Geophysics Laboratory, Hanscom AFB, 72 pp. [ADA160370]

Businger, J. A., J. C. Wyngaard, Y. Izumi and E. F. Bradley, 1971: Flux-profile relationships in the atmospheric surface layer. *J. Atmos. Sci.*, **28**, 181-189.

Charnock, H., 1955: Wind stress on a water surface. *Quart. J. Roy. Meteor. Soc.*, 81, 639-640.

Chu, C.-T., 1986: Parameterization of shallow convection in the boundary layer. M. S. thesis, Department of Atmospheric Sciences, Oregon State University, Corvallis, 83 pp.

Clapp, R. B. and G. M. Hornberger, 1978: Empirical equations for some soil hydraulic properties. *J. Water Resources Res.*, **14**, 601-604.

Dalrymple, P. C., 1966: A physical climatology of the Antarctic plateau. *Studies in Antarctic Meteorology* (M. J. Rubin, ed.). Vol. 9 of the Antarctic Research Series, American Geophysical Union, Washington, 195-231.

Deardorff, J. W., 1966: The countergradient heat flux in the lower atmosphere and in the laboratory. *J. Atmos. Sci.*, **23**, 503-506.

Ek, M. and L. Mahrt,1989: A user's guide to OSU1DPBL version 1.0.3: A one-dimensional planetary boundary-layer model with interactive soil layers and plant canopy. Department of Atmospheric Sciences, Oregon State University, Corvallis, Oregon 97331. An updated user's guide (version 1.0.4) will be available in February 1991.

Ek, M. and L. Mahrt, 1991: A formulation for boundary-layer cloud cover (submitted to *Ann. Geophys. ser. B*).

Fairall, C. W., J. E. Hare and J. B. Snider, 1990: An eight-month climatology of marine stratocumulus cloud fraction, albedo, and integrated liquid water. *J. Climate*, **3**, 847-864.

Gray, D. M. and D. H. Male, 1981: *Handbook of Snow*. Pergamon Press, Toronto, 776 pp.

Holtslag, A. A. M., 1987: Surface fluxes and boundary-layer scaling; models and applications. KNMI Sci. Rep. 87-02.

Holtslag, A. A. M. and F. T. M. Nieuwstadt, 1986: Scaling the atmospheric boundary layer. *Bound.-Layer Meteorol.*, **36**, 201-209.

Holtslag, A. A. M. and H. A. R. de Bruin, 1988: Applied modeling of the nighttime surface energy balance over land. *J. Appl. Meteorol.*, **27**, 689-704.

Holtslag, A. A. M. and A. C. M. Beljaars, 1989: Surface flux parameterization schemes; developments and experiences at KNMI. ECMWF Workshop on Parameterization of Fluxes and Land Surfaces, 24-26 Oct., 1988, pp. 121-147, Reading, England. (Also as KNMI Sci. Rep. 88-06, 1988.)

Holtslag, A. A. M., E. I. F. de Bruijn and H.-L. Pan, 1990: A high-resolution air mass transformation model for short-range weather forecasting. *Mon. Wea. Rev.*, **118**, 1561-1575.

Holtslag, A. A. M. and M. Ek, 1990: Simulation of surface fluxes and skin temperature: Preliminary results for the pine forest in HAPEX-MOBILHY. Preprint Ninth Symposium on Turbulence and Diffusion, Am. Met. Soc., Roskilde, Denmark, 30 Apr - 3 May, pp 188-191. To be submitted to *Bound.-Layer Meteor.*

Kasten, F. and G. Czeplak, 1980: Solar and terrestrial radiation dependent on the amount and type of cloud. *Solar Energy,* **24**, 177-189.

Kondo, J. O., O. Kanechika and N. Yasuda, 1978: Heat and momentum transfers under strong stability in the atmospheric surface layer. *J. Atmos. Sci.,* **35**, 1012-1021.

Liou, K.-N , 1976: On the absorption, reflection and transmission of solar radiation in cloudy atmospheres. *J. Atmos. Sci.,* 33, 798-805.

Louis, J.-F., 1979: A parametric model of vertical eddy fluxes in the atmosphere. *Bound.-Layer Meteorol.,* **17**, 187-202.

Louis, J.-F., M. Tiedtke and J. F. Geleyn, 1982: A short history of the operational PBL-Parameterization of ECMWF. Workshop on planetary boundary-layer parameterization, European Centre for Medium Range Weather Forecasts, Shinfield Park, Reading, Berks, U. K.

Lowe, P. R. and J. M. Ficke, 1974: Computation of saturation vapor pressure. *United States Environmental Prediction Research Facility, Naval Postgraduate School, Monterey, CA., ENVPREDRSCHFAC Technical Paper No. 4-74,* March, 27 pp.

Mahrt, L., 1987: Grid-averaged surface fluxes. *Mon. Wea. Rev.,* **115**, 1550-1560.

Mahrt, L. and M. Ek, 1984: The influence of atmospheric stability on potential evaporation. *J. Clim. Appl. Meteorol.,* **23**, 222-234.

Mahrt, L. and H.-L. Pan, 1984: A two-layer model of soil hydrology. *Bound.-Layer Meteorol.,* **29**, 1-20.

Mahrt, L., H.-L. Pan, P. Ruscher and C.-T. Chu, 1987: *Boundary-layer parameterization for a global spectral model.* Final contract report (AFGL-TR-87-0246) to Atmospheric Prediction Branch, Air Force Geophysics Laboratory, Hanscom AFB, 182 pp. Oregon State University, Corvallis. **ADA199440**

Mahrt, L., J. O. Paumier, H.-L. Pan and I. Troen, 1984: *A boundary-layer parameterization for a general circulation model.* Final contract report (AFGL-TR-84-0063) to Atmospheric Prediction Branch, Air Force Geophysics Laboratory, Hanscom AFB, 179 pp., Oregon State University, Corvallis. **ADA144224**

Marchuk, G. I., 1974: *Numerical Methods in Weather Prediction*, Academic Press, 277 pp.

Monteith, J. L., 1965: Evaporation and environment. *Symp. Soc. Exp. Biol.*, **19**, 205-234.

Monteith, J. L., 1981: Evaporation and surface temperature. *Quart. J. Roy. Meteor. Soc.*, **107**, 1-27.

Oke, T.R., 1978: *Boundary-layer Climates.* Methuen, London, 372 pp.

Paltridge, G. W. and C. M. R. Platt, 1976: Radiative processes in meteorology and climatology in *Developments in Atmospheric Science, 5.* Elsevier Scientific Publ. Co., Amsterdam, 318 pp.

Pan, H.-L. and L. Mahrt, 1987: Interaction between soil hydrology and boundary-layer development. *Bound.-Layer Meteorol.*, **38**, 185-202.

Ruscher, P. H., 1987: An examination of structure and parameterization of turbulence in the stably-stratified atmospheric boundary layer. Ph. D. thesis, Department of Atmospheric Sciences, Oregon State University, Corvallis, 170 pp.

Ruscher, P. H., 1991: A formulation of the very stable boundary layer in a simple atmospheric model. To be submitted to *Mon. Wea. Rev.*

Satterlund, D. R., 1979: Improved equation for estimating long wave radiation from the atmosphere. *J. Water Resources Res.*, 15, 1649-1650.

Troen, I. and L. Mahrt, 1986: A simple model of the atmospheric boundary layer: Sensitivity to surface evaporation. *Bound.-Layer Meteorol.*, 37, 129-148.

Tuccillo, J. J., 1987: Impact of snow cover on NGM forecast temperature. *NWS West. Region Tech. Attach.*, 87, No. 2, 7 pp.

## Chapter 6

# Concluding Remarks

From a historical point of view, the soil-boundary layer model has been developed to include the most important physics yet limited to sufficient simplicity for application to global models. In the early part of the model development, two major advances provided the framework for a successful start.

First, the formula for the boundary-layer depth was developed in terms of a modified bulk Richardson number. This diagnostic approach became more successful than previous mixed layer growth models. The mixed layer growth models required an estimation of the inversion strength (temperature and moisture jumps) at the top of the boundary layer. These jumps are poorly defined in low resolution models and lead to major errors or the need for band-aid auxiliary steps. Furthermore, the simpler diagnostic approach was able to accurately simulate the growth of the heated boundary layer, the forte of the mixed layer growth models. This success results from the overlooked fact that the growth of the heated boundary layer is dictated mainly by simple thermodynamic considerations and can be approximated without considering detailed complications of the turbulent energy budget. An additional advantage of the diagnostic approach based on the modified Richardson number is that it naturally handles the stable boundary layer without requiring transition conditions for switching between the mixed layer growth equations and a stable boundary layer model. I think that the boundary layer depth formulation for the boundary layer package in the GL model has been the most important factor leading to the use of this boundary layer package at more than a dozen institutions in six different western countries. Because of the robustness of the boundary layer depth-mixing formulation, it is now being used successfully in very diverse applications ranging from operational forecast models and long term chemical transport models to global climate change models and different basic research investigations. During the past year, inquiries about the model and adoption of conceptual ideas from the model have increased. We believe this is partly due to the exposure of the model during several presentations made last spring at a meeting of the European Geophysical Society.

The second major advance is the replacement of the usual force-restore equations with the actual water and heat equations for transfer in the soil. These equations are no more complicated than the force-restore substitute constructed by the meteorological community and allow application of the expertise and observations of the soil physics community. The canopy formulation in the boundary-layer package represents the most basic state-of-the-art physics compatible with a prespecified level of complexity. The numerous other components of the boundary-layer soil package have also been selected from conventional wisdom, given the limitations on model complexity.

The model improvements and additions during the past contract period are briefly discussed in the Introduction. I think the most important addition is the boundary-layer cloud formulation. The model can now capture the most important interaction between boundary-layer clouds and boundary layer-development, namely the reduction of incoming solar radiation and its impact on the surface energy balance. Even with this simple inclusion, the subsequent boundary-layer interactions are complex, as detailed in this report. The new formulation of boundary-layer cloud cover includes the influence of turbulent and meso-scale subgrid variability on the averaged boundary-layer cover. Previous research investigations indicated these influences to be the most important ones. Our formulation is the first one to include these influences for application in numerical models. Our analysis of the HAPEX data was crucial to this development.

We feel that our formulation, as well as all existing formulations, for turbulent transport by boundary-layer clouds are inadequate. The interplay between boundary-layer clouds and turbulence varies dramatically between different boundary-layer situations. The failure to understand the basic physics of these situations limits our ability to construct useful parameterizations. As a result we must start with existing and new analyses of observations for relatively simple situations. These are best found over the oceans.

# Reports and articles prepared under this contract

1. Mahrt, L., 1988: Scale dependence of boundary-layer fluxes and subgrid formulations. Parameterization of fluxes over land surface, pp 83-93. Workshop proceedings, ECMWF (European Centre for Medium-Range Weather Forecasts), 24-26 October.

2. Holtslag, A. A. M. and M. Ek, 1990: Simulation of surface fluxes and skin temperature: Preliminary results for the pine forest in HAPEX-MOBILHY. Preprint from the American Meteorological Society, Ninth Symposium on Turbulence and Diffusion, 30 April - 3 May, Risø, Roskilde, Denmark. To be submitted to *Bound.-Layer Meteor.*

3. Kim, J., 1990: Turbulent and gravity wave transport in the free atmosphere. Doctoral dissertation, Department of Atmospheric Sciences, Oregon State University, Corvallis, Oregon, 97331, 103 pp (abstract follows).

4. Mahrt, L., 1991: Boundary-layer moisture regimes. *Quart. J. Roy. Met. Soc.*, 117 (summary follows).

5. Ek, M. and L. Mahrt, 1991: A formulation for boundary layer cloud cover. Submitted to *Ann. Geophys. Ser. B* (abstract follows).

6. Ek, M. and L. Mahrt, 1991: Daytime evolution of boundary-layer relative humidity. To be submitted to *Mon. Wea. Rev.*

7. Kim, J. and L. Mahrt, 1991: Momentum transport by gravity waves. Submitted to *J. Atmos. Sci.* (abstract follows).

8. Kim, J. and L. Mahrt, 1991: Turbulent transport in the free atmosphere. To be submitted to *Bound.-Layer Meteor.* (abstract follows).

9. Ek, M. and L. Mahrt, 1991: A user's guide to OSU1DPBL version 1.0.4: A one-dimensional planetary boundary-layer model with interactive soil layers and plant canopy. Department of Atmospheric Sciences, Oregon State University, Corvallis, Oregon 97331.

10. Ruscher, P. H., 1991: A formulation of the very stable boundary layer in a simple atmospheric model. To be submitted to *Mon. Wea. Rev.*

# AN ABSTRACT OF THE THESIS OF

Jinwon Kim for the degree of Doctor of Philosophy in
Atmospheric Sciences presented on November 29, 1990.
Title: Turbulent and Gravity Wave Transport in the Free Atmosphere

Abstract approved:
Larry Mahrt

Turbulent fluxes and related parameters in the free atmosphere are estimated from aircraft data obtained in SESAME and CABLE. Estimated eddy diffusivities and mixing lengths are found to decrease rapidly with increasing gradient Richardson number (*Ri*) at small *Ri*, and then decrease more slowly at large *Ri*. The eddy Prandtl number increases with increasing *Ri*. This suggests that the generation of TKE by the pressure correlation term becomes more significant as the stability increases.

A simple representation of the eddy diffusivities in the free atmosphere is proposed by using an asymptotic mixing length and a nondimensional function of *Ri*. Tests of this formulation in a column model indicates that nocturnal CAT may become significant near the low-level jet above NBL. This constitutes the first systematic study of the residual layer above NBL.

The momentum flux by orographic gravity waves and the turbulent heat flux in the wave breaking regions are estimated from aircraft data sets from two days in ALPEX. The calculation of these fluxes allows the first direct comparison between gravity wave momentum transport models and observed fluxes.

Toward this goal, the gravity-wave stress supersaturation theory by Lindzen

(1988) is generalized for the application to vertically-varying mean flows. The wave momentum flux estimated from the generalized model agrees well with the observations for both the cases with and without a critical level. The wave breaking leads to convectively unstable regions of 10 - 20 km wide where the magnitude of the observed upward turbulent heat flux can be approximated by using the flux gradient relationship in which the mixing length and modified shear are derived from the generalized wave stress supersaturation condition.

The *effective* height ($h_e$) of the surface topography varies substantially between the two days. Our sensitivity tests tentatively suggest

$$h_e = \min\left[h_0, 0.32\frac{U_0}{N_0}\right],$$

close to that proposed by Stern and Pierrehumbert (1988), where $h_0$ is the mountain height, and $U_0$ and $N_0$ are the surface wind and stratification.

# Boundary-Layer Moisture Regimes

## Summary

Data from fifty-two aircraft legs 100-150 m above ground are analyzed from HAPEX and FIFE to estimate characteristics of boundary-layer moisture fluctuations in boundary layers with different bulk stability and surface energy regimes. In HAPEX, considerable effort was devoted to the quality of measurement of moisture fluctuations. The data include repeated 120 km flight legs flown at 150 m over the same relatively homogeneous terrain, allowing statistical examination of motion characteristics on horizontal scales up to 10 km.

This study finds two prototype boundary-layer regimes. With significant boundary-layer instability, relatively weak surface evaporation and dryer air aloft, the *entrainment-drying boundary layer* may develop. This boundary layer is characterized by vertical divergence of the moisture flux and significant top-down diffusion of dry air. In this type of boundary layer, dry air occasionally reaches the lower boundary layer leading to negative moisture skewness in spite of positive temperature and vertical velocity skewness associated with warm moist updrafts. In contrast, the *moistening boundary layer* associated with greater surface evaporation is characterized by positive moisture skewness near the surface.

In addition to the above turbulent moisture fluctuations, some of the above data are characterized by 10 km moisture variations with horizontal gradients often concentrated in narrow zones of horizontal convergence. Since corresponding signatures of vertical velocity and temperature are weaker, these zones are referred to as "mesoscale" moisture fronts. As a more general feature, moisture variations on scales of 5 km and greater are negatively correlated to temperature variations associated with cool moist regions and warm dry regions. On scales of tens of kilometers and greater, such negative correlation may be due to inhomogeneity of the surface energy budget. The negative moisture-temperature correlation leads to large mesoscale variations of relative humidity and the lifted condensation level.

# A formulation for boundary-layer cloud cover

## Abstract

Subgrid variability of moisture complicates the formulation of boundary-layer cloud cover in large-scale numerical models. Using data from HAPEX we construct a fractional cloud cover formulation which uses relative humidity based on spatially averaged variables and accounts for the important influences of turbulent and subgrid mesoscale variations of relative humidity. With unstable conditions, turbulent fluctuations of relative humidity are large and boundary-layer clouds first form at a lower spatially averaged relative humidity compared to the stable case. The turbulent variability of relative humidity is formulated in terms of boundary-layer similarity theory. The mesoscale subgrid variability is specified as a function of horizontal grid size based on HAPEX analyses. The cloud cover formulation in a one-dimensional boundary-layer model is more sensitive to the specified mean vertical motion than to the adjustable coefficients in the cloud cover formulation.

# Momentum Transport by Gravity Waves

## Abstract

The momentum flux by orographic gravity waves and the turbulent heat flux in wave-breaking regions are estimated from aircraft data from ALPEX. The fluxes on 6 March 1982 are controlled by low-level directional shear of the mean flow and associated critical level. On 25 March 1982 the critical level does not occur. The calculation of these fluxes is the first direct comparison between simple models of gravity wave momentum flux and observed atmospheric fluxes.

Toward this goal, the supersaturation theory for gravity wave stress by Lindzen (1988) is generalized for the application to vertically varying mean flows. The wave momentum flux estimated from the generalized model agrees well with the observations from the two ALPEX days. For the 6 March case, the vertical divergence of wave momentum flux below the critical level is comparable to the Coriolis term in the momentum equation. For the 25 March case, the wave stress is approximately constant with height within the observational domain.

Wave breaking below the critical level leads to convectively unstable regions 10-20 km wide. This region is dominated by well organized turbulent-scale convection. The magnitude of the observed upward turbulent heat flux can be approximated by using the flux gradient relationship in which the mixing length and modified shear are derived from the generalized wave stress supersaturation condition. The net turbulent heat flux across the entire width of the mountain waves appears to be small due to cancellation between the upward heat flux in the convectively unstable region and the downward heat flux at the back of the wave. The spatially averaged wave-scale heat flux is also small for the data analyzed here. The *effective* height of the surface topography required for the formulation of the wave momentum flux at the ground surface is estimated from the data and found to agree with the formulation of Stern and Pierrehumbert (1988).

# Turbulent Transport in the Free Atmosphere
# and very stable Nocturnal Boundary Layer

## Abstract

Clear air turbulence and associated fluxes are analyzed using aircraft turbulence data from SESAME and CABLE. Estimated eddy diffusivities and mixing lengths are found to decrease rapidly with increasing gradient Richardson number (*Ri*) at small *Ri*, and then decrease more slowly at large *Ri*. The eddy Prandtl number increases with increasing *Ri* which implies significant momentum transport induced by pressure fluctuations.

A simple representation of the eddy diffusivities in the free atmosphere is proposed by using an asymptotic mixing length and a nondimensional function of the Richardson number. Application of this formulation in a column model predicts modest clear air turbulence in the residual layer above the nocturnal boundary layer on the upperside of the low-level jet and near the top of the residual layer. For the very stable case, shear generation of turbulence at the top of the nocturnal inversion layer on the underside of the nocturnal jet can become more important than surface-based generation of turbulence. Baroclinity can significantly enhance local generation of turbulence. Typical values of mean subsidence significantly reduce the thickness of the residual layer.